

Experimental Characterization of the Dynamic Behavior of Novel Epoxy Based Composites for Aerospace Applications

Ahmed Elmahdy

Doctoral dissertation submitted to obtain the academic degree of
Doctor of Electromechanical Engineering

Supervisor

Prof. Patricia Verleysen, PhD

Department of Electromechanical, Systems and Metal Engineering
Faculty of Engineering and Architecture, Ghent University

November 2021



**GHENT
UNIVERSITY**

Experimental Characterization of the Dynamic Behavior of Novel Epoxy Based Composites for Aerospace Applications

Ahmed Elmahdy

Doctoral dissertation submitted to obtain the academic degree of
Doctor of Electromechanical Engineering

Supervisor

Prof. Patricia Verleysen, PhD

Department of Electromechanical, Systems and Metal Engineering
Faculty of Engineering and Architecture, Ghent University

November 2021



**GHENT
UNIVERSITY**

ISBN 978-94-6355-545-6

NUR 971, 978

Wettelijk depot: D/2021/10.500/93

Members of the Examination Board

Chair

Honorary Prof. Ronny Verhoeven, PhD, Ghent University

Other members entitled to vote

Prof. Ludwig Cardon, PhD, Ghent University

Pascal Lava, PhD, MatchID

Prof. Giuseppe Mirone, PhD, Università di Catania, Italy

Koen Van Minnebruggen, PhD, Ghent University

Mauro Zarrelli, PhD, Consiglio Nazionale delle Ricerche, Italy

Supervisor

Prof. Patricia Verleysen, PhD, Ghent University

Preface

It was in the year 2010 when the late prof. Abdelhalim Elhabak introduced me to the field of composite materials. During my master thesis, he suggested that I work on impact fatigue behavior of composites. After I finished my master degree in 2014, I realized that I'm actually more interested in the dynamic behavior of composites. So one year later, I joined prof. Patricia Verleysen's DyMaLab group. I always thought of the technical side of the PhD, and little did I know about its mental and personal side. Looking back almost 6 years ago when I started my PhD journey, I believe that I have now become a completely different person, both technically and personally. I ask myself many times: Would I choose to do a PhD again if I go back in time? Despite the many difficulties, the hard work, and the sleepless nights, my answer is always: yes, *definitely*! I encourage anyone with enough will and commitment to pursue a PhD, and embrace a journey of tough intellectual challenges, philosophical and critical thinking, and diving deep into multitudes of intertwining technical topics.

I've learned along the PhD journey that one of the keys to success is the combination of perseverance, self-confidence, and being surrounded by supportive people who believe in you. I was blessed to have all of these combined. I thank God for giving me the necessary perseverance and self-confidence to finish this journey in a good way. I would like to thank my promoter, prof. Patricia Verleysen, for many things: for being always available for discussions and questions, for reading and reviewing every single article, report, and presentation I have prepared during the PhD, for mobilizing your network inside and outside of Belgium whenever I needed any help, for always giving me the opportunity to attend conferences and present my work during project meetings. It has been a pleasure working under your supervision for the past 5 and half years. You have always been scientifically curious, emphasized quality over quantity, and you helped forge some very necessary skills – although sometimes in tough ways – that shaped me as a researcher. Last but not least, thank you for putting together an excellent team of colleagues at DyMaLab, which made the life in the lab much more interesting and fun.

Speaking of the team, I would like to thank my fellow friends and colleagues Dr. Florian Vercryusse and – Drs. to be – Sarath Chandran and Luca Corallo. You guys are the best team I have ever worked with. We have had a really unique working chemistry. You have had my back many times, and supported me during very tough periods. Thanks for all the discussions, the collaborations, and the late working nights in the lab. I will definitely miss our endless discussions in our office around the white board.

I owe a great deal of gratitude to my dear friend and colleague, Dr. Anouar Krairi. You have been a true mentor for me, and believed in me when no one else did. This PhD would have

not been finished if it weren't for your support. Thank you for our endless, and very interesting, daily scientific discussions and for your continuous encouragement.

Special thanks to every single member of the MST group at Ghent University. You have been my second family, and have been with me during my exceptional life events. To Ilse Vercryusse, Roger Van Hecke, and Vitaliy Bliznuk, thank you for the much needed emotional support during the tough times, and for being good friends. Also special thanks to our brilliant team of technicians Luc Van Den Broecke and Pascal Baele from the composites group at MaTCh department, and Wouter Ost from Labo Soete, for spending the time and effort to turn my challenging designs into reality.

To my friends Dr. Khadija Al Cheikh, Dr. to be Khaled Mostafa, and to the late prof. AbdelHalim Elhabak, thank you for talking some sense to me during very difficult and decisive times.

Luckily, this journey was not without its fun moments. Thanks to my fellow DyMaLabers Florian, Sarath, Luca, and Harish for our nice evenings together at the Holy Food Market and our annual outings with Patricia. Thanks to my friends Anouar, Khadija, Ghassan, Amr, and Metwally for our nice trips around Ghent, Brussels, and the Netherlands, and our fun nights playing RISK. Thanks to my fellow MST colleagues for our Fridays cake gatherings.

I would like to thank my father and mother for their endless love, support and continuous encouragement. To my wife, Sarah, thank you for making a lot of effort and taking all the necessary measures so I can focus on finishing this PhD, for your patience to listen to my unintelligible technical gabbing all day, and for enduring the long hours, days and nights, while I stare at the screen instead of you. To my son, Seif, thanks for bringing joy and happiness to my heart.

Finally, I would like to acknowledge the support and collaboration of EXTREME project partners, and the EU Horizon program of research and innovation for funding the project leading to this PhD.

Ahmed Elmahdy
Lommel, April 2021

About the author

Ahmed Elmahdy was born on the 12th of January, 1989 in Giza, Egypt. He obtained his bachelor and master degrees in Mechanical Design and Production Engineering from Cairo University in July 2010 and October 2014, respectively. His master thesis was under the supervision of the late prof. AbdelHalim Elhabak and prof. Mahmoud Adly. During his masters, Ahmed studied the behavior of glass fiber reinforced polyester composites subjected to repeated impact load. His passion for composites and experimental methodologies led him



to receive a full scholarship in September 2015 to pursue his PhD degree at the MST-DyMaLab at Ghent University, under the supervision of prof. Patricia Verleysen. His PhD research was performed in the framework of the EXTREME Horizon 2020 research project, comprising 14 academic and industrial partners in and outside of Europe.

The academic and professional careers of Ahmed span over several years. In 2011, he worked as a piping Engineer at Thyssenkrupp Industrial solutions in Cairo, Egypt. In 2012 he joined the Department of Mechanical Design and Production Engineering at the Faculty of Engineering at Cairo University as a teaching assistant and was later promoted in 2014 to assistant lecturer. During his tenure at Cairo University, he taught and assisted in the teaching activities of a wide range of course and labs such as Strength of Materials, Stress Analysis, and Fundamental of Manufacturing Engineering, among others. During the period of 2013 to 2015, he also worked as a mechanical engineer at the Center of Engineering Studies at Cairo University, where he participated in several research and engineering projects.

Ahmed is currently a research engineer at the Joining and Materials laboratory at Flanders Make, the strategic research center for the manufacturing industry in Flanders, Belgium. He is also the author and co-author of 8 international peer reviewed journal articles, and 10 full conference proceedings articles.

Intentionally left blank

“It is the duty of the one who investigates the writings of scholars – if searching for the truth is his goal – to denounce all what he reads...to use his mind to the core to examine these ideas from every side... and to question the results of his own study as well, in order to avoid falling into any prejudice or indulgence...”

– Alhasan Ibn Alhaytham (Alhazen)

Basra 965 – Cairo 1040

Summary

In today's modern aircrafts, epoxy based composite materials are increasingly replacing the conventional metallic materials in some primary and secondary structures, and also in some engine parts. This is mainly due to their excellent strength-to-weight ratios, good fatigue performance, better corrosion resistance, and their general flexibility in tailoring their properties for specific loading cases, a combination of features which are not yet available in their metallic counterparts such as aluminum or titanium. The result of using composites in aircrafts is lighter, yet strong and stiff, structures which reduce the overall weight of the aircraft and, eventually, reduce the carbon dioxide emissions. However, the current weight percentage of composites in modern aircrafts is still only 50%. Some challenges oppose the widespread use of composites in aircrafts, such as the resistance of composites to impact, their environmental and recycling aspects, and the cost of manufacturing, certification, and airworthiness tests. These challenges can be solved by developing new classes of composite materials which have better impact resistance to extreme events such as bird strike, and can be suitable for low cost manufacturing methods such as wet layup or resin transfer molding. Advanced multiscale material modeling can be used to predict the performance of the structures, and pass the certification tests with the minimum required number of tests. However, in order to build accurate models, the dynamic behavior of such materials at impact rates of strain should be first understood, and accurate experimental material parameters should be measured.

Within the framework of the European H2020 project EXTREME, the objective of this PhD research is to study the mechanical behavior of new classes of epoxy based composites at high strain rates and in different loading conditions. Two novel types of composites were considered for this research: woven basalt fiber reinforced epoxy composite, and epoxy nanocomposite filled with silica nanoparticles and hyper-branched polyester nanoparticles, with different functionalization conditions and weight contents. Both classes of materials were developed for the use of out-of-autoclave manufacturing techniques, i.e., wet layup and resin transfer molding and to address the abovementioned challenges. For the basalt epoxy composites, the in-plane tensile and shear behaviors were studied. Additionally, and with the goal of assessing the replaceability of glass epoxy composites with basalt epoxy composites in aircraft structures, the mechanical behavior of the basalt epoxy composites was compared to that of glass epoxy composites at high strain rates. For the epoxy nanocomposites reinforced with silica nanoparticles and hyperbranched polyester, the compressive behavior was studied.

The split Hopkinson bar technique was used to study the high strain rate behavior of the considered materials in tension, compression, and shear loading. Since the split Hopkinson bar technique was developed primarily to test large deformation materials, certain challenges are imposed when testing polymers and brittle composites with low strain to fracture. Special

attention was paid to the experimental minimization of the wave dispersion effects and the facilitation of the quasi-static stress equilibrium by using polymer impactors. Moreover, the quality of the measured strain signals on the bars and the signal-to-noise ratio were improved by using semiconductor strain gauges. Reference quasi-static testing was also performed using a universal testing machine, in order to study the behavior of the materials over a wide range of strain rates. For these tests, a custom designed system of bars was used to reduce the influence of the heavy grips on the small brittle samples, while keeping the same boundary conditions as in the high strain rate tests.

The classical Hopkinson analysis usually gives inaccurate strain values, particularly in tensile testing. Therefore, the digital image correlation was used as an optical, non-contact measurement technique to accurately and locally measure the full displacement and strain fields during testing. State-of-the-art digital image correlation setups were developed in 2D and stereo 3D configurations at low and high speeds. The optical components and the processing parameters of both systems were optimized for measuring small strains in the small scale polymer and composite samples. The effect of the processing parameters such as subset size, step size, strain window, and subset shape function on the average displacement and strain random error (i.e. noise levels) was studied for both the 2D and 3D DIC systems. It was found that the average displacement and strain noise levels decreased with increasing the subset size, the step size, and the strain window, which was expected considering the smoothing effects of these parameters on the results. First order affine shape function achieved lower displacement and strain random errors compared to quadratic shape functions. Based on these results, the optimum processing parameters were identified to achieve the lowest displacement and strain random errors in testing of the materials under study.

The challenges in testing of polymers and composites using the split Hopkinson bar technique were discussed. Important aspects such as the design of sample geometries, boundary conditions, load introduction, sample clamping, and validating certain testing and material assumptions were investigated. The challenges in compression testing were investigated using RTM6 neat epoxy resin at quasi-static and high strain rates. A novel self-alignment loading attachment was developed specifically to provide good interfacial contact conditions at the start of the high strain rate compression tests. After selecting a suitable sample geometry, the establishment of quasi-static equilibrium was assessed. Additionally, the uniformity of axial strains and the effect of strain rate and lubrication on the interfacial friction were analyzed with the aid of DIC. Furthermore, the assumption of volume conservation during yielding of epoxy was also validated by measuring the instantaneous cross section area of the deforming sample using the DIC. It was found that the selected compression sample geometry achieved an early quasi-static equilibrium at high strain rates, which can enable the extraction of the dynamic elastic modulus and the Poisson's ratio in compression. The interfacial friction showed a decrease with increasing strain rate. This was also confirmed by the nearly homogenous distribution of the axial strains in the compression samples. The assumption of volume conservation was found to be invalid in the yielding and post-yielding stages of compression deformation at low and high strain rates. The DIC technique proved essential in the accurate determination of the stress-strain response of epoxy – and polymers in general – in compression.

Moreover, the challenges in tensile testing of brittle composites were studied based on basalt/epoxy composites using two sample geometries, namely a dog-bone and a straight strip geometry. Both geometries were assessed and compared based on the criteria of establishment of quasi-static stress equilibrium and the uniformity of the axial strain fields with the aid of DIC measurements. Pin/slot end tabs were developed to fix both samples to the bars. A special alignment tool was also developed to accurately align the brittle tensile samples between the end tabs and the bars. Results showed that both sample geometries fulfil requirements of an early quasi-static stress equilibrium and homogeneous axial strain distribution. Both geometries also showed a similar stress-strain response for the basalt/epoxy material. However, the classical Hopkinson analysis overestimated the actual strains and strain rates in the sample by approx. a factor of 3 for both geometries. This overestimation resulted from the contribution of the transitions zones to the total deformation. Local measurement of the strains along the gauge section was, therefore, crucial for the reliability of the characterization of the high strain rate behavior of composites.

Based on the optimized methodologies and testing techniques, the tensile behavior of the basalt epoxy composites in the warp and fill directions and the shear behavior in the off-axis direction were investigated. Additionally, a comparison between the tensile and shear behaviors of the woven basalt and a woven glass fiber reinforced epoxy composites at various strain rates was presented. For this comparison, the same epoxy matrix and manufacturing technique were used. The strain rates covered were 0.0006 s^{-1} up to 154 s^{-1} for tensile experiments and 0.003 s^{-1} up to 645 s^{-1} for shear experiments. Results showed that the woven basalt epoxy composite was strain rate sensitive in both warp, fill, and shear directions. An increase in tensile and shear stiffnesses, ultimate tensile and shear strengths, and ultimate tensile strains was observed with the increase of strain rate. Post mortem analysis of the fractured basalt composite specimens using scanning electron microscopy revealed that the failure morphology was independent of the strain rate. Delamination was present at all strain rates, however, a more homogeneous distribution of delamination over the gauge section was observed with the increase of strain rate. Compared to conventional composites in the literature, the tested woven basalt epoxy composite showed excellent energy absorption capabilities at high strain rates. Furthermore, compared to the woven glass epoxy composites, the normalized results with respect to the material density and fiber volume fraction showed that basalt epoxy composite had higher elastic stiffness, ultimate tensile strength, ultimate tensile strain, and absorbed energy in tension. However, the shear modulus and strength of the glass epoxy composite were higher than those of the basalt epoxy composite. SEM images of the fractured shear samples revealed that the fiber/matrix adhesion was weaker in the basalt epoxy compared to the glass epoxy composites.

The results of this research clearly showed that despite the relatively high void content of the tested basalt epoxy composite and the insufficient adhesion between the basalt fibers and the epoxy matrix, the material still showed superior behavior in tension compared to the tested glass epoxy composites at different strain rates, considering the same volume fiber content. This suggests a promising potential of replacing glass fibers composites with the cheaper and higher performant basalt fiber composites in aircraft secondary structures and, more generally, components prone to impact. However, unlike the glass fiber composites which have been

used in aircrafts for decades, the basalt fiber composites are still new to the aerospace industry. Therefore, further research is still required to improve the manufacturing technique by reducing the void content and improve the adhesion of the basalt fibers to the hosting epoxy matrix. This could increase the shear properties of the basalt epoxy composite, and allow the full exploitation of the promising properties of basalt composites in the design of aircraft secondary structures.

The effect of strain rate and filler content on the compressive behavior of RTM6 epoxy nanocomposites was investigated within a strain rate range of 0.001 s^{-1} up to 1113 s^{-1} . The epoxy nanocomposites were strain rate sensitive in compression. Indeed, results showed that the true peak yield strength showed an increase with increasing strain rates for all types, weight percentages, and sizes of the nanoparticles used. However, the elastic modulus and the Poisson's ratio of the epoxy nanocomposites were independent of the strain rate, and showed a nearly constant behavior at different strain rates for all types, weight percentages, and sizes of the fillers used. The addition of the silica nanoparticles to the RTM6 epoxy resin generally improved both its elastic modulus and its peak yield strength at different strain rates for all the weight percentages of the particles. Increasing the weight percentage of the silica nanoparticles up to 5% also had a positive effect on the true peak yield strength. Moreover, both size and surface functionalization conditions of the silica nanoparticles did not show a significant effect on the compressive behavior of the resin at different strain rates. On the other hand, the addition of the hyperbranched polyester nanoparticles to the resin resulted in an increase in the true peak yield strength of the resin, and a reduction in the compressive stiffness. The highest improvement in the peak yield strength was achieved at 0.1 % weight of the hyperbranched polyester. Further increase in the weight percentage did not result in further improvement in the true peak yield strength.

As for the epoxy based nanocomposites, the results of the research indicated that the addition of silica and hyperbranched polyester nanoparticles generally improve the compressive strength of the RTM6 epoxy resin. The extent of the improvement of the overall mechanical properties of the resin was more pronounced with the addition of the silica nanoparticles. Regarding the hyperbranched polyester filled resin, although they have a potential to be good toughening additives for the epoxy resin, further research is still required to produce hyperbranched polymers which can limit the negative influence on the hosting resin, particularly with regard to the glass transition temperature and the stiffness. Additionally, further research will be required to certify these epoxy nanocomposites as aerospace materials, and to transform their manufacturing from lab scale to industrial scale.

Finally, the digital image correlation technique has proven essential and highly beneficial in the high strain rate testing. Not only were accurate strain measurements locally obtained for the small size samples, but also full field information were obtained which revealed homogeneities and heterogeneities in the strain distribution. Moreover, unique information regarding the interfacial friction conditions at various strain rates were obtained by using full displacement fields on cylindrical samples. Furthermore, the typical materials assumptions which are normally applied to polymers could be checked and validated using the radial displacements obtained by the low and high speed digital image correlation techniques.

Samenvatting

In de nieuwste generatie vliegtuigen vervangen composietmaterialen op epoxybasis in toenemende mate de traditionele metalen in primaire en secundaire constructies, alsook in sommige motoronderdelen. Dit komt voornamelijk door hun uitstekende sterkte-gewichtsverhouding, steeds beter wordende vermoeiingseigenschappen, uitstekende weerstand tegen corrosie, en hun algemene flexibiliteit bij het afstemmen van hun eigenschappen op specifieke belastingsgevallen. Deze combinatie van eigenschappen is niet beschikbaar bij hun metalen tegenhangers zoals aluminium of titanium. Het resultaat van het gebruik van composieten in vliegtuigen is lichtere, maar toch sterke en stijve, constructies die het totale gewicht van het vliegtuig verlagen en uiteindelijk de uitstoot van koolstofdioxide verminderen. Het huidige gewichtspercentage van composieten in moderne vliegtuigen ligt evenwel slechts op 50%. Bepaalde uitdagingen, zoals de bestendigheid van composieten tegen impactbelasting, milieu en recyclage aspecten, en de kosten van fabricage, certificering en luchtwaardigheidstesten, staan nog steeds het wijdverbreide gebruik van composieten in vliegtuigen in de weg. Deze uitdagingen kunnen worden opgelost door nieuwe klassen van composietmaterialen te ontwikkelen die een betere impactbestendigheid hebben tegen extreme gebeurtenissen, zoals vogelimpact, en die geschikt zijn voor goedkopere fabricagemethoden zoals wet lay-up of resin transfer molding. Geavanceerde multischaal-materiaalmodellering kan worden gebruikt om de prestaties van de composietconstructies te voorspellen en de certificeringstesten te doorstaan met een minimaal aantal testen. Voor het ontwikkelen van deze modellen moet evenwel eerst het dynamisch gedrag van dergelijke materialen bij impact vervormingssnelheden worden begrepen, en moeten materiaalparameters heel accuraat experimenteel worden bepaald.

Gerealiseerd in het kader van het Europese H2020 project EXTREME, is het doel van dit doctoraatsonderzoek het mechanisch gedrag van nieuwe klassen van composieten op epoxybasis bij hoge reksnelheden en in verschillende spanningscondities te bestuderen. Voor dit onderzoek werden twee nieuwe soorten composieten doorgelicht: geweven basalt epoxycomposiet en epoxy-nanocomposiet gevuld met silica nanodeeltjes en hyperbranched polyester nanodeeltjes, met verschillende oppervlaktefunctionalisaties en gewichtspercentages. Beide materiaalklassen zijn ontwikkeld voor het gebruik van fabricagetechnieken zonder autoclaaf, namelijk wet lay-up en resin transfer molding, en om de bovengenoemde uitdagingen aan te pakken. Bovendien, en met het doel om de vervangbaarheid van glas epoxycomposieten met basalt epoxycomposieten in vliegtuigconstructies te beoordelen, werd het mechanische gedrag van de basalt epoxycomposieten vergeleken met glas epoxycomposieten bij hoge reksnelheden. Voor de epoxy nanocomposieten met silica nanodeeltjes en hyperbranched polyester werd voornamelijk het drukgedrag bestudeerd.

Om het gedrag van bovenvermelde materialen bij hoge reksnelheid onder trek-, druk- en afschuifspanningen te karakteriseren werd de split Hopkinson bar techniek gebruikt. Speciale aandacht werd besteed aan het experimenteel minimaliseren van golfdispersie en het bereiken van quasi-statisch spanningsevenwicht door gebruik te maken van polymeer impactoren. Bovendien werden de kwaliteit van de gemeten reksignalen op de staven en de signaal-ruisverhouding verbeterd door gebruik te maken van halfgeleider-rekstrookjes. Ook werden quasi-statische referentietesten uitgevoerd met behulp van een universele testbank om het gedrag van de materialen over een breed scala aan reksnelheden te bestuderen. Voor deze testen werden speciaal ontwikkelde stavensystemen gebruikt om de negatieve invloed van zware klauwen op de kleine, brosse proefstukken te vermijden. Het gebruik van de staven garandeerde bovendien dat dezelfde randvoorwaarden werden gehandhaafd als bij de dynamische testen.

De digital image correlation (DIC) techniek werd gebruikt om de volledige verplaatsings- en rekvelen tijdens het testen nauwkeurig te meten. State-of-the-art 2D en stereo 3D DIC opstellingen werden ontwikkeld voor zowel de statische als de dynamische proeven. De optische componenten en de verwerkingsparameters van de DIC systemen werden geoptimaliseerd voor het meten van kleine rekken in de miniatuur polymeer- en composiet proefstukken. Het effect van de verwerkingsparameters zoals subsetgrootte, stapgrootte, rekvenster en subsetvormfunctie op de gemiddelde verplaatsings- en rekfouten (d.w.z. ruisniveaus) werd bestudeerd voor zowel de 2D als de 3D DIC systemen. Hierbij werd vastgesteld dat de gemiddelde niveaus van verplaatsings- en rekruis afnamen met het vergroten van de subsetgrootte, de stapgrootte en het rekvenster. Dit werd verwacht gezien de afvlakkingseffecten van deze parameters op de resultaten. Eerste orde affine vormfuncties bereikten lagere verplaatsings- en rekfouten in vergelijking met kwadratische vormfuncties. Op basis van deze resultaten werden de optimale verwerkingsparameters geïdentificeerd om de laagst mogelijke verplaatsings- en rekfouten te bereiken bij het testen van de onderzochte materialen.

De uitdagingen gerelateerd aan het testen van brosse polymeren en composieten met behulp van de split Hopkinson bar techniek werden besproken. Belangrijke aspecten zoals de keuze van proefstukgeometrieën, rand- en belastingsvoorwaarden, klemmen van de proefstukken en validatie van bepaalde test- en materiaalassumes werden onderzocht. De uitdagingen bij druktesten werden onderzocht met behulp van zuiver RTM6 epoxyhars bij quasi-statische en dynamische reksnelheden. Een nieuw zelfuitlijnend belastingshulpstuk werd ontwikkeld om goede grensvlakcontactcondities te garanderen vanaf de start van de druktesten. Na de selectie van een geschikte proefstukgeometrie, werd het instellen van quasi-statische evenwicht beoordeeld. Daarnaast werden de uniformiteit van axiale rekken en het effect van reksnelheid en smering op wrijving in de contactvlakken van het proefstuk met de opstelling geanalyseerd met behulp van DIC. Bovendien werd de aanname van volumebehoud tijdens het vloeien van epoxy gevalideerd door de dwarsdoorsnede van het proefstuk continu te meten met behulp van de DIC. Met de geselecteerde geometrie van het drukproefstuk werd quasi-statisch evenwicht zeer snel bereikt in de dynamisch proeven. Dit liet toe de dynamische elasticiteitsmodulus en de coëfficiënt van Poisson te bepalen. De wrijving in de grensvlakken vertoonde een afname met toenemende reksnelheid. Dit werd ook bevestigd door de bijna

homogene verdeling van de axiale rekken in de drukproefstukken. De aanname van volumebehoud bleek niet geldig te zijn, zowel voor als na vloeien bij lage en hoge reksnelheden. Voor de nauwkeurige bepaling van de spanning-rekrespons van epoxy - en brosse polymeren in het algemeen - in druk bleek het gebruik van de DIC-techniek essentieel.

De specifieke uitdagingen van dynamische trekproeven op brosse composieten werden bestudeerd voor de basalt epoxycomposieten met behulp van twee proefstuk geometrieën, namelijk een klassiek hondenbeenvormige en rechthoekig proefstuk. Beide geometrieën werden geëvalueerd en vergeleken op basis van criteria gerelateerd met het bereiken van quasi-statisch krachteenevenwicht en de uniformiteit van de axiale rek bepaald met DIC metingen. Pen/groefuiteinden werden ontwikkeld om de trekproefstukken aan de staven te bevestigen. Een speciaal uitlijnhulpstuk werd ontwikkeld om de brosse trekproefstukken nauwkeurig uit te lijnen in de opstelling. De resultaten toonden aan dat beide proefstuk geometrieën voldoen aan de eisen van een vroeg quasi-statisch krachteenevenwicht en een homogene axiale rekverdeling. Beide geometrieën vertoonden ook een gelijkaardige spanning-rek curve voor het basalt epoxy materiaal. De klassieke Hopkinson analyse van de meetresultaten overschatte echter de werkelijke rek en reksnelheden in het proefstuk met een factor van ongeveer 3 voor beide geometrieën. Deze overschatting is het gevolg van de bijdrage van de overgangszones aan de totale vervorming. Lokale meting van de verplaatsing en rek in de gauge sectie was daarom cruciaal voor de betrouwbaarheid van de karakterisering van het hoge reksnelheidsgedrag van composieten.

Op basis van de geoptimaliseerde meet- en testtechnieken werd het trekgedrag van de basalt epoxycomposieten in verschillende richtingen onderzocht, alsook het afschuifgedrag. Bovendien werd een vergelijking tussen het trek- en afschuifgedrag van geweven basalt en glas epoxycomposieten bij verschillende reksnelheden gemaakt. Voor deze vergelijking werden hetzelfde epoxyhars en dezelfde fabricagetechniek gebruikt. De bereikte reksnelheden waren $0,0006 \text{ s}^{-1}$ tot 154 s^{-1} voor de trekexperimenten en $0,003 \text{ s}^{-1}$ tot 645 s^{-1} voor de afschuifexperimenten. De resultaten toonden dat het basalt epoxy composiet gevoelig was voor de reksnelheid in alle richtingen. Een toename in trek- en afschuifstijfheid, en trek- en afschuifsterkten werd waargenomen met de toename van de reksnelheid. Postmortem analyse van gebroken basaltcomposiet proefstukken met behulp van scanning-elektronenmicroscopie toonde aan dat de morfologie van het falen onafhankelijk was van de reksnelheid. Delaminaties werden waargenomen bij alle reksnelheden, maar deze waren meer homogeen verdeeld bij de hogere reksnelheden. Vergelijking van de resultaten van het basalt epoxy composiet met meer conventionele composieten in de literatuur toonde het uitstekende energie absorptie potentieel aan van de eerste bij hoge reksnelheden. Bovendien toonden de resultaten, genormaliseerd ten opzichte van de materiaaldichtheid en het vezelvolumegehalte, in vergelijking met vergelijkbaar glas epoxy composiet, dat het basalt epoxy composiet een hogere elastische stijfheid, treksterkte, breukrek en geabsorbeerde energie had. De afschuifmodulus en sterkte van het glas epoxy composiet waren echter hoger dan deze van het basalt epoxy composiet. SEM-beelden van de gebroken afschuif proefstukken onthulden dat de hechting tussen vezels en matrix zwakker was in basalt epoxy in vergelijking met de glas epoxycomposieten.

De resultaten van dit onderzoek toonden duidelijk aan dat, ondanks het relatief hoge gehalte aan porositeiten in het geteste basalt epoxycomposiet en de eerder slechte hechting tussen de basaltvezels en het epoxyhars, het materiaal nog steeds een superieur trekgedrag vertoonde in vergelijking met de geteste glas epoxycomposieten bij verschillende reksnelheden. Bij de analyse werd rekening gehouden met het vezelvolumegehalte. De resultaten tonen een veelbelovend potentieel om glasvezelcomposieten te vervangen door de goedkopere en beter presterende basaltvezelcomposieten in secundaire constructies van vliegtuigen en, meer in het algemeen, componenten die gevoelig zijn voor impact belasting. In tegenstelling tot glasvezelcomposieten, die al tientallen jaren in vliegtuigen gebruikt worden, zijn basaltvezelcomposieten nog nieuw. Verder onderzoek is nog steeds nodig om de fabricagetechnieken te verbeteren, de porositeit te verminderen en de hechting van de basaltvezels aan de epoxymatrix te verbeteren. Dit zou de afschuifeigenschappen van basalt epoxycomposieten kunnen vergroten en het volledige benutten van de veelbelovende eigenschappen van basaltcomposieten in het ontwerp van secundaire vliegtuigconstructies mogelijk maken.

Het effect van reksnelheid en vulstofgehalte op het drukgedrag van RTM6 epoxy nanocomposieten werd onderzocht binnen een reksnelheidsbereik van $0,0008 \text{ s}^{-1}$ tot 1113 s^{-1} . De resultaten toonden dat de epoxy-nanocomposieten gevoelig waren voor reksnelheid bij drukbelasting. De werkelijke piekvloeisterkte vertoonde een toename met toenemende reksnelheden voor alle types, gewichtspercentages en groottes van de bestudeerde nanodeeltjes. De elasticiteitsmodulus en de coëfficiënt van Poisson van de epoxy-nanocomposieten waren evenwel onafhankelijk van de reksnelheid. De toevoeging van de silica-nanodeeltjes aan het RTM6-epoxyhars verbeterde in het algemeen zowel de elasticiteitsmodulus als de piekvloeisterkte bij verschillende reksnelheden voor alle gewichtspercentages van de deeltjes. Het verhogen van het gewichtspercentage van de silica-nanodeeltjes tot 5% had ook een positief effect op de werkelijke maximale vloeisterkte. Bovendien hadden zowel de grootte als de oppervlaktefunctionalisatie van de silica-nanodeeltjes geen significant effect op het drukgedrag van het hars bij verschillende vervormingssnelheden. Anderzijds resulteerde de toevoeging van de hyperbranched polyester nanodeeltjes aan het hars in een verhoging van de werkelijke piekvloeisterkte van het hars en een vermindering van de drukstijfheid. De grootste verbetering van de piekvloeisterkte werd bereikt bij een gewichtspercentage van 0,1 van het hyperbranched polyester. Een verdere verhoging van het gewichtspercentage resulteerde niet in een verdere verbetering van de werkelijke piekvloeisterkte.

Wat betreft de epoxy nanocomposieten, toonden de resultaten van het onderzoek aan dat de toevoeging van silica en hyperbranched polyester nanodeeltjes in het algemeen de druksterkte van RTM6 epoxyhars verbetert. De mate van verbetering van de mechanische eigenschappen van het hars was meer uitgesproken bij de silica-nanodeeltjes. Alhoewel hyperbranched polyester deeltjes potentieel hebben om de taaiheid van epoxyhars te verbeteren, is verder onderzoek nog nodig naar de productie van hyperbranched polymeren die de negatieve invloed op de epoxymatrix kunnen beperken, in het bijzonder met betrekking tot de glasovergangstemperatuur en de stijfheid. Bovendien zal verder onderzoek nodig zijn om deze

epoxy-nanocomposieten te certificeren als materialen voor vliegtuigen en om hun productie op te schalen van labo naar industriële schaal.

Tenslotte is de DIC techniek niet enkel zeer nuttig gebleken, maar zelfs essentieel voor het testen bij hoge reksnelheden. In de miniatuurproefstukken werden nauwkeurige lokale rekmetingen verkregen. Eventuele heterogeniteiten in de rekverdeling werden aan het licht gebracht. Bovendien werd unieke informatie verkregen over wrijving in de grensvlakken bij verschillende reksnelheden - die normaal verwaarloosd wordt - door gebruik te maken van volledige verplaatsingsvelden bij de cilindrische proefstukken. Verder konden klassieke aannames over het materiaalgedrag van brose polymeren gecontroleerd en gevalideerd worden aan de hand van de radiale verplaatsing verkregen met de ontwikkelde DIC opstellingen.

Intentionally left blank

List of relevant publications

A1 Peer-reviewed international journal articles

1. **Elmahdy, A.**, and Verleysen, P., 2019, “Tensile Behavior of Woven Basalt Fiber Reinforced Composites at High Strain Rates,” *Polym. Test.*, **76**, pp. 207–221.
2. **Elmahdy, A.**, and Verleysen, P., 2020, “Mechanical Behavior of Basalt and Glass Textile Composites at High Strain Rates: A Comparison,” *Polym. Test.*, **81**, p. 106224.
3. Zotti, A., **Elmahdy, A.**, Zuppolini, S., Borriello, A., Verleysen, P., and Zarrelli, M., 2020, “Aromatic Hyperbranched Polyester/RTM6 Epoxy Resin for EXTREME Dynamic Loading Aeronautical Applications,” *Nanomaterials*, **10**(2), p. 188. (*First co-author*).
4. **Elmahdy, A.**, Zotti, A., Zuppolini, S., Zarrelli, M., Borriello, A., and Verleysen, P., “Effect of strain rate and filler content on the compressive properties of silica filled epoxy nanocomposites” (*Submitted to Polymers in 2021 – currently under review*)
5. **Elmahdy, A.**, and Verleysen, P., “In-depth characterization of the dynamic behavior of RTM6 epoxy using digital image correlation” (*To be submitted to Polymer Testing in 2021*)

P1/C1 Peer-reviewed international conference proceedings

1. Zarrelli, M., **Elmahdy, A.**, Zotti, A., Zuppolini, S., Borriello, A., and Verleysen, P., 2018, “Compressive Behavior of Epoxy Resin Filled With Silica Nanoparticles At High Strain Rates,” *Proceedings of the 18th European Conference on Composite Materials ECCM18*, Athens, Greece 24-28 June 2018. (*First Co-author, online proceedings*).
2. **Elmahdy, A.**, Feldman, E., and Verleysen, P., 2018, “Tensile Behavior of Basalt Fiber Reinforced Composites at High Strain Rates,” *Proceedings of the 18th European Conference on Composite Materials ECCM18*, Athens, Greece, 24-28 June 2018. (*Online proceedings*).
3. **Elmahdy, A.**, and Verleysen, P., 2018, “Challenges Related to Testing of Composite Materials at High Strain Rates Using the Split Hopkinson Bar Technique,” *EPJ Web Conf.*, **183**, p. 02021.
4. **Elmahdy, A.**, and Verleysen, P., 2018, “The Use of 2D and 3D High-Speed Digital Image Correlation in Full Field Strain Measurements of Composite Materials Subjected to High Strain Rates,” *Proceedings*, **2**(8), p. 538.
5. **Elmahdy, A.**, and Verleysen, P., 2019, “Comparison between the Mechanical Behavior of Woven Basalt and Glass Epoxy Composites at High Strain Rates,” *Mater. Today Proc.*, **34**, pp. 171–175.

C3 Conference abstracts

1. **Elmahdy, A.**, and Verleysen, P., 2017, “High strain rate testing of fiber-reinforced composites” The First International Workshop on Dynamic Response of Composite Materials IWDRC, Taormina, Italy, 27-28 September 2017.
2. **Elmahdy, A.**, Zarelli, M., Zotti, A., Borriello, A, and Verleysen, P., 2018, “Effect of silica nanoparticles on the compressive behavior of RTM6 epoxy resin at different strain rates” The Second International Workshop on Dynamic Response of Composite Materials IWDRC, Ischia, Italy, 27-28 September 2018.

Participation in international conferences and workshops

1. The 18th European Conference for Composite Materials ECCM18, Athens, Greece, 2018 (*oral presentation*)
2. The 12th International Dymat conference, Arcachon, France, 2018 (*oral presentation*)
3. The 18th International Conference on Experimental Mechanics, Brussels, Belgium, 2018 (*oral presentation*)
4. The 12th International Conference on Composites Science and Technology, Sorrento, Italy, 2019 (*oral presentation*)
5. The 1st International Workshop on the Dynamic Response of Composite Materials, Taormina, Italy, 2017 (*oral presentation*)
6. The 2nd International Workshop on the Dynamic Response of Composite Materials, Ischia, Italy, 2018 (*oral presentation*)

Contents

Preface	i
About the author	iii
Summary	vi
Samenvatting	xi
List of relevant publications	xvi
1. Introduction	
1.1. Composite materials	2
1.2. The use of composites in the aviation industry	3
1.3. Challenges facing the widespread use of composites in modern aircrafts	4
1.4. The EXTREME H2020 Project	5
1.5. Scope of the PhD Research	6
1.6. Layout of the thesis	7
References	9
2. Materials: State-of-the-art	
2.1. Introduction	12
2.2. Basalt fiber reinforced composites	12
2.2.1. Manufacturing of the basalt fibers	12
2.2.2. Mechanical properties of the basalt fibers in comparison with other conventional fibers	13
2.2.3. Mechanical behavior of basalt fiber reinforced composites at different strain rates	16
2.2.4. Comparison between the mechanical behavior of basalt fiber reinforced composites and glass fiber reinforced composites at different strain rates	19
2.3. Epoxy based nanocomposites	20
2.3.1. Silica nanoparticles as fillers of epoxy resins	20
2.3.2. Hyperbranched polymers as fillers of epoxy resin	25
2.4. Conclusions	28
References	29

3. Quasi-static and high strain rate testing methods

3.1. Introduction	36
3.2. High strain rate testing methods: state-of-the-art	36
3.3. Overview of the split Hopkinson bar technique	39
3.3.1. Theoretical background	39
3.3.2. Wave dispersion and pulse shaping techniques	42
3.4. The split Hopkinson bar facility at Ghent University	43
3.4.1. General description	43
3.4.2. Strain measurement on the bars	45
3.5. Quasi-static testing setup	47
3.6. Conclusions	48
References	48

4. Development of Digital Image Correlation techniques

4.1. Introduction	52
4.2. Principles of the digital image correlation technique	53
4.3. Components of a digital image correlation system	54
4.3.1. Optical system	54
4.3.2. Surface texture of the sample and speckle pattern	57
4.3.3. Interpolation, subset size, and step size	59
4.3.4. Correlation criteria and subset matching	60
4.4. Stereo digital image correlation	63
4.4.1. Basics of stereo vision and triangulation	64
4.4.2. Calibration for stereo vision	65
4.4.3. Correlation in 3D	69
4.5. Development of low and high speed 2D and 3D DIC systems	70
4.5.1. Low speed DIC setups	70
4.5.2. High speed DIC setups	71
4.5.3. Calibration of the 2D and 3D DIC setups	73
4.5.4. Data processing software and processing parameters	74
4.6. Comparison between 2D and 3D DIC setups	74
4.6.1. Experimental conditions and DIC processing	75
4.6.2. Results and discussion	80
4.7. Remarks on the 3D DIC technique	85
4.8. Conclusions	86
References	88

5. Challenges in testing of polymers and composites using the split Hopkinson bar technique

5.1. Introduction	92
5.2. Challenges in compression testing of polymers	92
5.2.1. Design of compression sample geometry	92
5.2.2. Boundary conditions and load introduction	93
5.2.3. Material assumptions	93
5.2.4. Experimental testing conditions in compression	94
5.2.5. Results and discussion	101
5.3. Challenges in tensile testing of brittle composites	107
5.3.1. Design of tensile sample geometry	107
5.3.2. Sample clamping and load introduction	108
5.3.3. Experimental testing conditions in tension	109
5.3.4. Results and discussion	113
5.4. Conclusions	118
References	120

6. Mechanical behavior of basalt and glass epoxy composites at different strain rates

6.1. Introduction	124
6.2. Specimen materials and geometries	124
6.3. Experimental testing conditions	125
6.3.1. Quasi-static testing	125
6.3.2. High strain rate testing	127
6.3.3. DIC processing parameters and data reduction	129
6.4. Results and discussion	130
6.4.1. Strain rate evolution	130
6.4.2. Evaluation of the axial strain homogeneity during high strain rate loading	132
6.4.3. Tensile stress-strain response of the basalt/epoxy and glass/epoxy composites in the warp (0°) direction	135
6.4.4. Tensile stress-strain response of the basalt/epoxy composites in the fill (90°) direction	135
6.4.5. Shear stress-strain response of the basalt/epoxy and glass/epoxy composites in the ($\pm 45^\circ$) direction	137
6.4.6. Effect of strain rate on the elastic modulus of the basalt/epoxy composite	139
6.4.7. Effect of strain rate on the ultimate tensile strength of the basalt/epoxy composite	140
6.4.8. Effect of the strain rate on the maximum tensile strain of the basalt/epoxy	141
6.4.9. Comparison of the tensile and the shear moduli for basalt and glass epoxy composites at different strain rates	142
6.4.10. Comparison of the tensile and the shear strengths for basalt and glass epoxy composites at different strain rates	144

6.4.11. Comparison of absorbed energy in tension and ultimate tensile strain for basalt and glass epoxy composites at different strain rates	147
6.4.12. Fractographic analysis and failure morphology	148
6.4.13. Comparison with other conventional composite materials at similar high strain rates from literature	151
6.5. Conclusion	153
References	155

7. Compressive behavior of epoxy based nanocomposites at different strain rates

7.1. Introduction	158
7.2. Specimen materials	158
7.2.1. Synthesis of the silica nanoparticles	158
7.2.2. Synthesis of the aromatic hyperbranched polyester nanoparticles	159
7.2.3. Preparation of the epoxy nanocomposites and testing specimens	160
7.2.4. Dynamic mechanical analysis of the prepared nanocomposites	160
7.3. Experimental testing conditions	162
7.3.1. Quasi-static testing	162
7.3.2. High strain rate testing	162
7.3.3. Data reduction and processing parameters for the DIC	163
7.4. Results and discussion	163
7.4.1. Compressive stress-strain response of RTM6 epoxy nanocomposites at different strain rates	163
7.4.2. Effect of strain rate and weight content on the elastic modulus and Poisson's ratio of hyperbranched polyester filled RTM6 epoxy resin	164
7.4.3. Effect of strain rate and weight content on the peak yield strength of hyperbranched polyester filled RTM6 epoxy resin	168
7.4.4. Effect of strain rate and weight content on the elastic modulus and Poisson's ratio of the silica nanoparticles filled RTM6 epoxy resin	170
7.4.5. Effect of strain rate and weight content on the peak yield strength of the silica nanoparticles filled RTM6 epoxy resin	171
7.4.6. Effect of the silica nanoparticles size and surface functionalization of on the elastic modulus, Poisson's ratio, and peak yield strength of RTM6 epoxy nanocomposite	172
7.5. Conclusions	175
References	176

8. Conclusions and future perspectives

8.1. Summary of conclusions	180
8.2. Future perspectives	183
8.2.1. Basalt fiber reinforced composites	183
8.2.2. Epoxy based nanocomposites	184
8.2.3. Methods	185

1

Introduction

This chapter provides a general introduction to the motivation and background of the PhD research. Section 1.1 gives a brief background on composite materials, followed by an overview of the use of composites in modern aircrafts in section 1.2. Section 1.3. discusses the current challenges facing the aerospace industry, and the possible solutions which could be implemented to address these challenges. Section 1.4. gives a brief introduction to the European project EXTREME H2020 which was funded to implement the solutions to the challenges of the aviation industry in Europe. Section 1.5 gives the scope of the PhD research within the framework of the H2020 project EXTREME. Finally, section 1.6 provides the layout of the PhD thesis.

1.1. Composite materials

Composite materials combine two or more forms of different materials – referred to as reinforcement and matrix – with different properties to create a new material with improved properties compared to the constituents. The combination of these materials can happen at any size scale, i.e., macroscale to nanoscale. The reinforcement is usually the main load carrying component of the composite material, and can take the form of short or continuous fibers, particles, lattices, flakes, etc. The matrix protects and encloses the reinforcement, and helps in transferring the load to the reinforcement. The matrix material can be either metallic, polymeric, or ceramic. The focus of this research, however, is on fiber reinforced polymeric composite materials.

Polymeric matrix materials can be either thermoplastics or thermosets. Thermoplastics are polymers with long chains of monomers, and are processed by heating and cured by cooling. They are generally ductile and can be recycled such as polyamide and polyethylene polyether ether ketone PEEK and the high density polyethylene HDPE. Thermosets are polymers with cross-linking chains, and are processed – i.e., cured – by heat to increase the cross-linking density. Thermosets can also cure at room temperature in the presence of a hardener, which starts an exothermic reaction that causes the curing. Several types of synthetic fibers can be used such as glass, carbon, and aramid fibers, in addition to thermoplastic fibers such as polyamide, polyethylene, and polyester fibers. Reinforced polymeric composites can also take the form of a sandwich structure, i.e., sandwich composites, which are made up of a core material sandwiched between two composite skins. These materials are not considered within the scope of this research.

Fiber reinforced polymeric composites are produced with a bottom up approach, i.e., building up the material. The smallest building block is the lamina which is one ply of fiber/matrix combination. Laminas are layered on top of each other to form laminates. In that sense, the material can be fully designed and tailored for specific structural requirements. For example, the orientation of the fibers can be changed to either increase the strength of the final composite laminate in a specific direction, or create a laminate with nearly similar strength in all directions, i.e., quasi-isotropic.

1.2. The use of composites in the aviation industry

In today's modern aircrafts, advanced composite materials are increasingly replacing the conventional metallic materials. This is mainly due to their excellent stiffness and strength-to-weight ratios, excellent fatigue and corrosion resistance, and their general flexibility in tailoring their properties for specific loading cases, a combination of features which are not yet available in their metallic counterparts such as aluminum or titanium alloys. Figure 1.1 shows an example of the progress of using composites in civilian and military aircrafts. It can be seen that in the last 20 years alone, the use of composites in aircrafts has increased from approx. 15% to 55%, which is a significant increase.

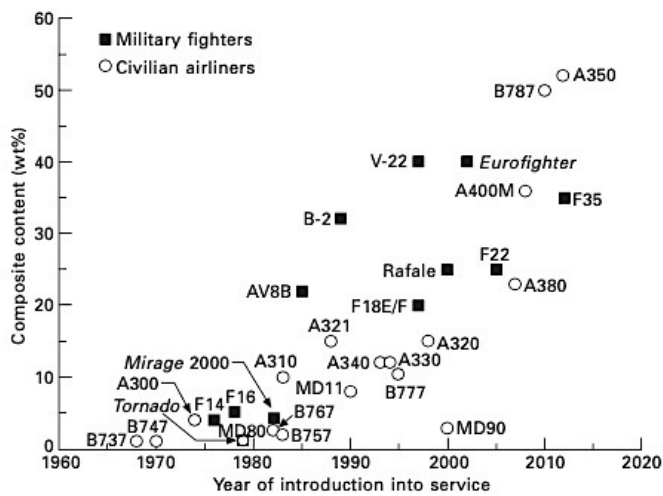


Figure 1.1. The use of composites in aircrafts from 1960 to 2020 [1]

Composite materials are typically used in some primary and secondary structures and also in some engine parts of the aircraft, as shown in Figure 1.2. For instance, the recent Boeing 777x has the longest carbon fiber composite wing span in a commercial aircraft [2]. Additionally, latest jet engines such as GE9x use all carbon fiber composite fan blades [3]. The implementation of composites in aircraft structures and engines provides a significant reduction in the aircraft weight, and, therefore, a reduction in overall fuel consumption as shown in Figure 1.3

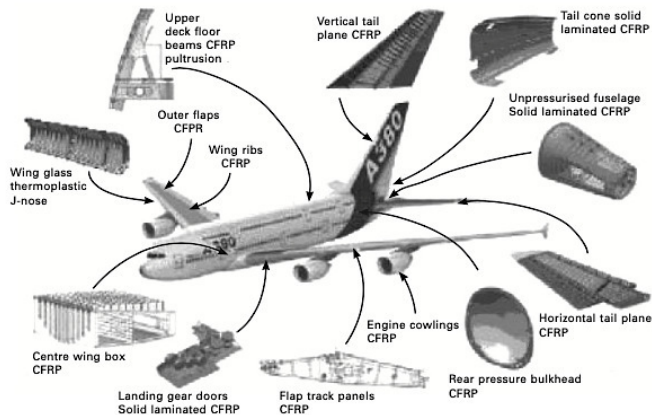


Figure 1.2. Structures which use composites in the Airbus A380 aircraft [1]

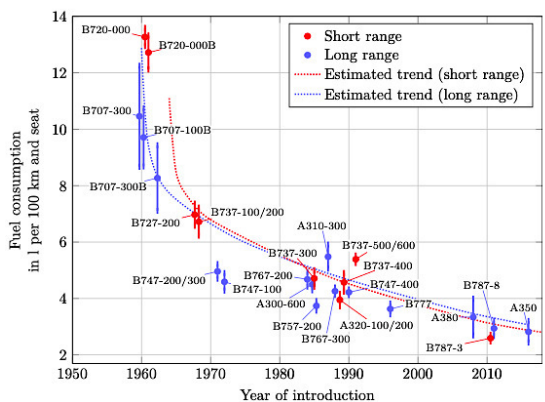


Figure 1.3. Overall fuel consumption of Airbus and Boeing aircrafts from 1950 to 2015 [4]

1.3. Challenges facing the widespread use of composites in modern aircrafts

Despite the current efforts to implement more composites into aircrafts, several issues remain significantly challenging to the widespread use of composites in aircraft structures, namely: the resistance to impact, the environmental aspects related to material recycling, and the costs of manufacturing, certification, and airworthiness testing.

Passenger safety is an utmost priority for aircraft designers. However, composite structures generally have a very low energy absorption capacity and fracture toughness, and are very prone to impact damage from extreme events such as bird strikes, hail strikes, and engine fan

blade-out accidents. The full understanding of the dynamic behavior of composite materials at impact rates of strain is important in designing optimized composite structures for impact events. Additionally, introducing new fiber and resin materials which have the combination of high strength, high stiffness, high energy absorption and high fracture toughness can significantly advance the impact resistance of aircraft structures.

Moreover, the demand for high performance composites, such as carbon fibers, is estimated to rise significantly in the upcoming years, not only driven by the commercial and military aircraft industry, but also by the demand of the new air mobility sectors – also known as air taxis- and heavy duty drones. This expanded use of composites in aircrafts also dictates having an outlook on the recyclability of these materials, considering the environmental responsibility towards the planet. It is, therefore, necessary to develop new classes of composite materials which have a minimum environmental footprint during manufacturing, and have the capacity for recycling.

The cost of manufacturing of aircraft composite structures is mainly affected by the need for expensive high performance prepreg composites. These materials require refrigerated storage, expensive autoclave processing, and have a limited shelf life. Out-of-autoclave techniques such as wet layup or resin transfer molding provide excellent alternatives to autoclave techniques, while maintaining a high fiber volume fraction and low void content.

The cost of certification and airworthiness tests remains one of the biggest challenges in the aviation industry. In order to certify an aircraft to fly, the complete aircraft and its subcomponents undergo rigorous testing with very strict requirements. The design process, the materials, and the manufacturing process are all included in the certification process. Therefore, if a new material or a new manufacturing technique is introduced, the whole certification process has to be followed. Advanced material and structural models can be used as a solution to reduce the certification costs, by accurately and reliably predicting the performance of the components and pass the certification requirements with the minimum required number of tests. However, in order to develop reliable and accurate material models, high quality experimental material data are required for model calibration, especially at impact rates of strain.

1.4. The EXTREME H2020 Project

As part of the efforts of the European Union to address the abovementioned challenges, while reducing the carbon footprint and environmental impact of new aircrafts, the Horizon 2020 program of the European Union Funding for Research and Innovation funded the project “EXTREME dynamic loading: pushing the boundaries of aerospace composites structures”. This PhD research was carried out within the framework of the EXTREME project.

EXTREME received nearly 5 million euros in funding from the period of September 2015 till August 2019. The project included 14 partners from universities, research institutes, and industrial aircraft manufacturers from within and outside Europe. The participating academic

partners were the University of Bath and Brunel University in the United Kingdom, Ghent University in Belgium, Delft University of Technology in the Netherlands, University of Patras in Greece, Technical University of Dresden in Germany, and the National Research Council of Italy – Institute of Polymers, Composites and Biomaterials CNR-IPCB. The participating industrial partners were Rolls Royce – PLC and Dynawave Ltd. in the United Kingdom, DYNAmore GmbH from Germany, e-Xstream Engineering from Belgium, Israel Aerospace Industries from Israel, and Leonardo Helicopters from Italy. The main aims of the project were as follows:

- To develop new classes of composite materials for impact resistance and high fracture toughness.
- To improve the mechanical characterization of novel aircraft composites for impact events.
- To develop advanced multiscale models for aircraft composites materials and structures optimized for impact damage prediction.
- To develop novel structural health monitoring techniques for composite structures.

The project addressed 4 levels of the certification process, ranging from coupon level testing up to validation structure testing. The tasks were distributed over 9 different work packages, including manufacturing the samples and validation structures, developing and optimizing dynamic testing methods for composite materials, developing and validating multiscale material models and computational methods, and developing non-destructive testing techniques and structural health monitoring tools. Within this project, Ghent University was responsible for developing dynamic material testing methods beyond the state-of-the-art, and developing high speed full field optical non-contact measurement techniques for displacements and strains.

1.5. Scope of the PhD Research

The objective of this PhD research is to study the behavior of new classes of epoxy based composites at high strain rates and in different loading conditions. These new classes of composite materials were developed specifically to address the previously mentioned challenges in composite materials of modern aircrafts.

Within the frame work of this research, strain rates of approx. 100 s^{-1} up to 200 s^{-1} were of interest. This value corresponds to the strain rates developed in general bird strike events during normal aircraft take-off and landing. Two novel types of composites were considered for this research. The first type of the developed composites was woven basalt fiber reinforced epoxy composites, which is considered relatively new to the aerospace industry. Basalt fiber composites have the potential to replace glass fiber composites given their similar properties and eco-friendliness. Additionally, basalt fiber composites can have better impact resistance, through increasing the strength and fracture strain of the composite. Since the basalt fiber composites are intended to replace glass fiber composites in aircraft secondary structures, their tensile and shear properties at impact rates of strain were investigated. Moreover, the

mechanical behavior at high strain rates were compared to that of the conventional glass fiber composites. The second type of the developed composites was RTM6 epoxy based nanocomposite, which is an RTM6 epoxy resin filled with silica nanoparticles and hyperbranched polyester nanoparticles. The RTM6 epoxy resin was considered since it is widely used for low volume manufacturing of aircraft components by resin transfer molding. The primary goal of adding these nanoparticles was to improve the fracture toughness of the epoxy resin. However, other mechanical properties of the epoxy resin can be greatly affected by the addition of these nanoparticles, especially at impact rates of strain. Consequently, the compressive properties of these epoxy nanocomposites at high strain rates were investigated. Furthermore, the effect of the weight percentage of these nanoparticles on the compressive behavior of the epoxy resin was also studied. Given the viscoelastic nature of the epoxy resin, the strain rates of interest were increased to approx. 1000 s^{-1} , in order to capture and study the compressive yielding phenomena at high strain rates. Both classes of materials were developed for the use of out-of-autoclave manufacturing techniques, i.e., wet layup and resin transfer molding.

The high strain rate tests were performed using the split Hopkinson bar technique. For these tests, special attention was paid to the applicability of the technique for testing brittle composites and polymers, and to the design of the most suitable sample geometry, since these tests are not standardized. Additionally, new methods of load introduction and sample fixture were introduced. Advanced high speed digital image correlation techniques were developed as full field non-contact displacement and strain measurement tool. Combined with the Hopkinson bar technique, the digital image correlation method was used to provide accurate measurements of the displacements, the strains, and the strain rates locally on the sample's gauge section. Moreover, the use of the digital image correlation technique intended to reveal new information regarding classical assumptions of the Hopkinson testing technique and of material response, such as the homogeneity of the strain fields, the conservation of volume, and interfacial friction effects.

1.6. Layout of the thesis

The PhD thesis is organized as follows:

Chapter 2 discusses the current state-of-the-art of the investigated materials. A brief introduction to the manufacturing of basalt fibers, and the synthesis of the silica and hyperbranched polymer nanoparticles is first presented. Next, a critical review of previous literature studies on the effect of strain rate on the mechanical behavior of basalt fiber composites and epoxy nanocomposites filled with silica nanoparticles and hyperbranched polymers is discussed. Since basalt and glass fibers composites have comparable properties, the critical review is also extended to include the effect of strain rate on the mechanical behavior of glass fiber composites. The chapter concludes with some highlights of the critical analysis of the gaps in the state-of-the-art.

Chapter 3 describes the quasi-static and the high strain rate testing methods used in the research. An overview of the common methods used for high strain rate testing in tension and compression is first discussed. Next, arguments are established to support the use of the split Hopkinson bar technique over the conventional servo-hydraulic testing machines. An introduction to the principles and the theoretical background of the split Hopkinson bar technique is given. A description of the split Hopkinson bar testing facility at Ghent University is presented in detail, together with details on the data acquisition systems and strain measurements used. Finally, a detailed description of the quasi-static setup used in the reference quasi-static experiments is given.

Chapter 4 discusses the development of the digital image correlation techniques used in this research. First, an introduction to the principles and important concepts of the digital image correlation technique is given. This introduction includes the necessary theoretical background, the different optical components and postprocessing schemes required to calculate displacements and strains, concepts of the stereo vision and camera calibration, and some general guidelines for setup construction based on literature. Second, a description of the developed low speed and high speed digital image correlation systems which are used in this research is presented. Special attention is given to optimizing the processing parameters for small strain measurements for both configurations. Finally, a comparison between the 2D and 3D configurations is presented.

Chapter 5 discusses the challenges related to testing of polymers and composites using the split Hopkinson bar technique. First, the classical assumptions of the compression testing at high strain rates are assessed and validated using neat RTM6 epoxy resin samples with the aid of the digital image correlation techniques. These assumptions include the establishment of the quasi-static force equilibrium, the conservation of volume, and the interfacial friction and barreling effects on the compressive strength measurements. Next, the aspects related to the design of the tensile and shear sample geometries for the woven composites are discussed. Two sample geometries based on literature are experimentally assessed, with the aid of digital image correlation technique, in terms of the establishment of the quasi-static force equilibrium and the uniformity of the axial strain fields.

Chapters 6 discusses the experimental results for tensile and shear properties of the woven composite materials at different strain rates. Prior to the formal analysis of the results, the verification of the establishment of the quasi-static equilibrium, the constant strain rate evolution, and the strain homogeneity in high strain rate tensile tests is first discussed. Next, detailed results and analysis of the effect of strain rate on the tensile and shear behavior of the woven basalt/epoxy composite are presented. A detailed comparison between the tensile and shear behavior of the woven basalt/epoxy composite and the woven glass/epoxy composite is also presented. Moreover, fracture morphology and modes of failure for both materials and loading conditions at different strain rates are identified and discussed.

Chapter 7 discusses the experimental results for the compressive behavior of the epoxy nanocomposites at different strain rates. The effect of strain rate on the compressive stiffness, Poisson's ratio and peak yield strength of the tested epoxy nanocomposites is discussed. In

addition, the effect of the weight content of all types of nanoparticles used on the compressive behavior of epoxy nanocomposite at different strain rates is presented. Furthermore, the effect of the size and the surface functionalization conditions of the silica nanoparticles on the compressive behavior of epoxy nanocomposites at different strain rates is also discussed.

Chapter 8 concludes the research with some remarks and future perspectives.

References

- [1] Mouritz, A. P., 2012, *Introduction to Aerospace Materials*, Woodhead publishing.
- [2] Sloan, J., 2019, "Large, High-Volume, Infused Composite Structures on the Aerospace Horizon," Next Gen Aerosp. Adv. Mater. Process.
- [3] Nehls, G., 2020, "GE Aviation GE9X Engine Achieves FAA Certification," Compos. World.
- [4] Theis, J., 2018, "Robust and Linear Parameter-Varying Control of Aeroservoelastic Systems," Technischen Universität Hamburg.

Intentionally left blank

2

Materials: State-of-the-art

2.1. Introduction

This chapter provides a detailed and a critical review of previous literature studies on the effect of strain rate on the mechanical behavior of basalt fiber composites and epoxy nanocomposites filled with silica nanoparticles and hyperbranched polymers. Section 2.2 provides an overview of the basalt fiber reinforced composites. In this section, the manufacturing techniques of continuous and short basalt fibers are presented and compared. Next, the mechanical behavior of the basalt fibers is discussed and compared to other conventional fibers such as glass, carbon, and aramid fibers. The effect of strain rate on the mechanical behavior of basalt fiber composites – in particular the tensile, the compressive, and the in-plane shear behaviors – are critically discussed. Moreover, a comparison of the strain rate effects of both glass fiber composites and basalt fiber composites is discussed. Section 2.3 provides an overview of the epoxy resins filled with silica nanoparticles and hyperbranched polymers. This section begins with presenting the synthesis techniques of the silica nanoparticles and hyperbranched polymers. Next, the effect of the addition of both the silica nanoparticles and the hyperbranched polymers on the mechanical and thermal behavior of epoxy resins is discussed. For the silica nanoparticles, the effect of the particle size of the surface conditions on the mechanical properties of the epoxy resin is also covered. Furthermore, the effect of strain rate on the mechanical properties of epoxy resins filled with both types of nanoparticles is discussed. The chapter concludes with some highlights of the critical analysis of the gaps in the state-of-the-art in section 2.4.

2.2. Basalt fiber reinforced composites

2.2.1. Manufacturing of the basalt fibers

Basalt fibers are made from the volcanic basalt rock, which is the most abundant volcanic rock in the earth's crust [1]. They are chemically made up of various oxides of silicon, aluminum, iron, and calcium, in addition to various other minerals. Figure 2.1 shows a typical composition of basalt fibers. The silicon dioxide content is usually used to classify the basalt material into alkaline basalt (<42% SiO₂), mildly acidic basalt (43% to 46% SiO₂), and acidic basalt (>46% SiO₂) [2]. Due to its high SiO₂ content, the acidic basalt provides suitable levels of flexibility and chemical stability to the produced fibers compared to the other types of basalt material. Therefore, it is the only type used to produce basalt fibers [3].

Basalt fibers are produced in continuous or short forms. Both forms involve melting of the crushed natural volcanic basalt rocks in furnaces up to 1500 °C. Figure 2.2 shows a schematic of the manufacturing processes of basalt fibers. The continuous fibers are produced by the Spinneret method, in which the molten fibers are drawn from heated platinum-rhodium bushings after the sizing application to form strands – see Figure 2.3 (a). Sizing of the fibers is a process of coating the fibers with thin coating layers to give them specific properties and to protect them during handling. The short fibers are produced by the Junkers method, in which the molten rocks are poured onto spinning drums with small compressed air nozzles.

Due to the centrifuge action, the molten fibers are pushed outwards in the form of small droplets, and the compressed air quickly cools these droplets and turns them into elongated short fiber form. However, this technique produces fibers with relatively low mechanical properties due to the presence of large terminating fiber heads [2], as shown in Figure 2.3 (b). The manufacturing technique of continuous basalt fibers is also very similar to the one used for glass fibers. However, as opposed to glass fibers, no other additives are required during production [4]. This results in reduced manufacturing costs and enhanced eco-friendliness of basalt fibers compared to glass fibers, thus giving basalt fibers an economical and environmental advantage [3]. Despite the commercial production of the basalt fibers, they usually do not reach their theoretical tensile strength due to the presence of defects such as cracks and voids on the surface of the fibers [5]. While fiber sizing can help mitigate the surface defects of the fibers, the effect of the composition of the sizing coating on the strength of the basalt fibers is still subject of research [6].

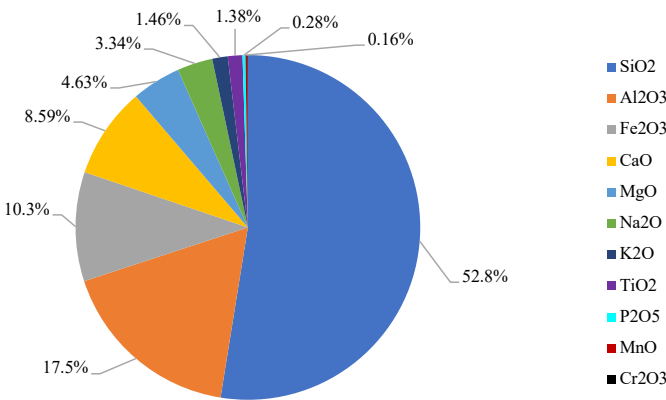


Figure 2.1. Composition of basalt fibers [7]

2.2.2. Mechanical properties of the basalt fibers in comparison with other conventional fibers

Basalt fibers generally have an intermediate position among other fibers in terms of mechanical properties [8], and fall into the same category as the glass fibers [9]. They are only surpassed by the more expensive carbon fibers in terms of strength and stiffness, and by aramid fibers in terms of energy absorption [8,10,11]. Table 2.1 compares the mechanical performance of the basalt fibers with other conventional fibers. One interesting property to note is that the basalt fibers have the second highest maximum strain, and only exceeded by the aramid fibers. Quasi-static tensile stress-strain curves of basalt fibers typically show a linear and brittle behavior without any plastic deformation in a similar fashion as the glass fibers, whereas the fracture surface of the fibers also indicates a brittle fracture, as shown in Figure 2.4.

At high strain rates, the basalt fibers are very sensitive to the variation in strain rate. However, the high strain rate behavior of the basalt fibers is not very well understood. For example, Zhu et al. [11] showed that the stiffness and strength of basalt filament tows increase with increasing the strain rate from 0.001 s^{-1} to 3000 s^{-1} . The failure strain also decreases with increasing the strain rates. Similar results were also obtained by Ou et al. [12], who also showed that the Young's modulus and tensile strength of the basalt fiber bundles increased with increasing the strain rates from 40 s^{-1} up to 160 s^{-1} . The maximum strain also showed a decrease with increasing the strain rates. Yao et al. [8] studied the tensile behavior of unidirectional basalt fabrics at strain rates up to 100 s^{-1} , in comparison with other fabrics (unidirectional glass , unidirectional carbon, and woven aramid fibers) using a servo-hydraulic machine. The results for the basalt fibers showed an increase in tensile strength and maximum strain with increasing strain rates, which partially contradict with the findings of Zhu et al. [11] and Ou et al. [12]. Moreover, basalt fibers generally showed an intermediate strength, stiffness, and maximum strain compared to the glass, carbon, and aramid fibers at high strain rates. Failure of basalt fabric samples was reported to be independent of the strain rate, showing a spread of failure across the entire gauge section.

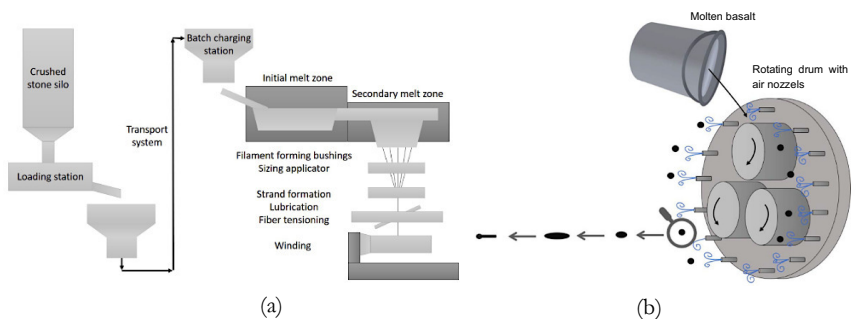


Figure 2.2. Schematic of the manufacturing of basalt fibers: (a) Spinneret method, (b) Junkers method [3]

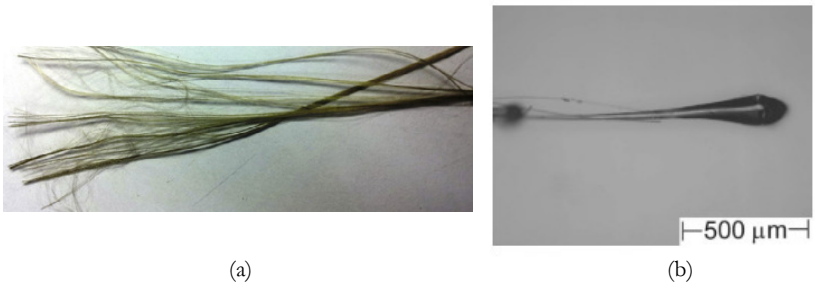


Figure 2.3. Examples of basalt fibers: (a) continuous fiber strands using the Spinneret method [13], (b) short fibers with large terminating heads produced by the Junkers method [2]

Basalt fiber composites show an overall competitive mechanical performance when compared to other composite systems such as glass and carbon composites [14–16]. Hybridization of basalt fibers with other types of fibers such as aramid and carbon fibers can result in composite materials with improved tensile strength [17], fatigue performance [18], and impact resistance [15]. As such, they can substitute a considerable percentage of the rather expensive carbon fibers without a significant decrease in the mechanical properties [19]. Moreover, they show a better sustainability of their mechanical properties at different thermal and environmental conditions compared to glass and carbon composites [10,20]. The previous discussion highlights the great potential of basalt fiber composites as compared to conventional fiber composites, especially for aeronautical applications.

Table 2.1. Comparison between the mechanical performance of basalt fibers with other conventional fibers [8]

Fiber material	Bulk density (g/cm ³)	Elastic modulus (GPa)	Tensile strength (MPa)	Maximum strain	Toughness (mJ/mm ³)
Glass	2.54	62.1	1048	0.0304	20.6
Basalt	2.8	53.5	1427	0.0420	37.2
Carbon	1.8	168.1	2302	0.0278	46.2
Aramid	1.44	47.4	2373	0.0655	92.4

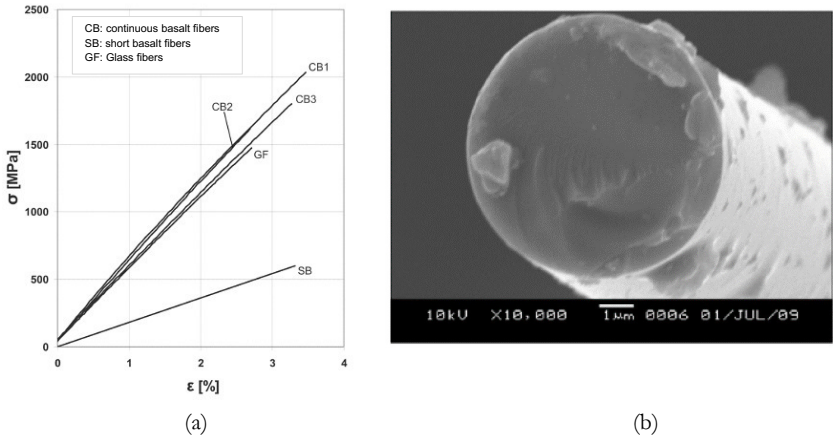


Figure 2.4. (a) Tensile stress-strain curves of basalt fibers in comparison with glass fibers [2], (b) SEM image of a fractured basalt fiber filament after quasi-static tensile test [11]

2.2.3. Mechanical behavior of basalt fiber reinforced composites at different strain rates

2.2.3.1. Tensile behavior

The effect of strain rate on the tensile behavior of the basalt composites was studied by several researchers. Zhang et al. [21] investigated the behavior of unidirectional basalt epoxy composites in tension at strain rates up to 133 s^{-1} and various temperatures using a servo-hydraulic machine. Results showed an increase in tensile strength, maximum strain, and toughness with increasing the strain rates, with percentages of 45.5%, 12.9%, and 17.3% respectively. Ou et al. [12] also studied the effect of strain rate on the tensile behavior of unidirectional basalt epoxy composites using a drop tower impact setup, reaching strain rates up to 160 s^{-1} . Results showed a slight increase in the elastic modulus and maximum strain with the increase in strain rates, and an initial increase followed by a decrease in the tensile strength, which contradicts with the findings of Zhang et al. [21]. Daliri et al. [22] investigated the high strain rate tensile behavior of twill weave basalt fiber epoxy composites using a servo-hydraulic machine, and up to strain rates of 200 s^{-1} . Results showed an increase in tensile strength with the increase in strain rate, however, the authors reported that the dynamically tested samples did not reach a uniform stress condition during the test. Li et al. [23] studied the tensile behavior of basalt/epoxy composites at strain rate range of 10^{-5} s^{-1} to 260 s^{-1} using a servo hydraulic machine. Results also showed an increase in the elastic modulus, the tensile strength, and the tensile strain with increasing the strain rates. However, the sample geometry used in the quasi-static tests was different than that used for the high strain rate tests, which might raise some discrepancies between the two tests due to the sample geometry. It should be noted that the majority of the previously mentioned tests were carried out using servo hydraulic machines, which have some inherent limitations for testing at high strain rates, as will be explained in chapter 3. Among these limitations are: load cell ringing [24], establishment of stress equilibrium [25], and delays in synchronization and data acquisition systems [26]. The Split Hopkinson bar technique is normally used to overcome these limitations [25].

Very few studies, however, are available for the high strain rate tensile behavior of basalt composites utilizing the split Hopkinson bar technique. Sun et al. [27] investigated the tensile behavior of woven basalt vinyl ester composites at high strain rates ranging from 900 s^{-1} up to 2800 s^{-1} . Results indicated a strain rate sensitivity of the basalt composites. An approximately linear increase in stiffness and failure strength was reported with the increase of the strain rate, while an approximately linear decrease in failure strain was noticed with the increase of the strain rate. Electron microscope imaging indicated that failure modes are also strain rate dependent. The main reported failure modes were matrix cracking, fiber pull out and fiber breakage. Gunzenmuller et al. [28] studied the effect of strain rates on quasi-isotropic unidirectional basalt epoxy laminated composites in the range of 10^{-3} s^{-1} up to 10^2 s^{-1} . Results also indicated a strain rate sensitivity of the basalt epoxy composites. The maximum strength increased with increasing the strain rate. However, the stiffness showed a strain rate independency, and the maximum strain showed an increase with increasing the strain rate, both contradicting with the findings of Sun et al. [27].

From the previous review of the literature, it is clear that the data available for the dynamic tensile behavior of basalt fibers and basalt composites are contradicting and no clear trends can be found. This indicates that the effect of the strain rate on the tensile properties of the basalt fibers and their composites is not very well understood.

2.2.3.2. *In-plane shear behavior*

Composite laminates are typically designed such that the fibers are oriented in the direction of the expected stresses. These stresses are often called on-axis stresses. If the actual stresses are applied in a direction other than the on-axis stresses (i.e. off-axis stresses), it will cause shear in the composite laminate. Therefore, next to the tensile properties of basalt composites along the fiber direction, the in-plane shear properties at high strain rates are also very important. Very few studies, however, are available for the in-plane shear behavior of basalt fiber composites at quasi-static and high strain rates. Mengel et al. [29] studied the effect of hybridization of carbon and basalt epoxy composites on the in-plane shear properties at quasi-static rates, and reported an increase in shear strength and modulus of rigidity for the hybrid composites compared to the non-hybrid ones. Liu et al. [30] compared the shear behavior of twill woven basalt and glass epoxy composites at quasi-static strain rates, and reported no significant change in shear strength for both materials. Soares et al. [31] studied the shear response of basalt fiber reinforced polyester composites and reported shear strength and modulus values at quasi-static strain rates. Results indicated a difference in shear modulus obtained using the rail tests and $[\pm 45^\circ]$ tests. Therefore, the author recommended additional testing to be performed in order to determine the actual shear modulus values. Gunzenmuller et al. [28] studied the effect of strain rates on $[\pm 45^\circ]$ unidirectional basalt epoxy laminates in the range of 10^{-3} s^{-1} up to 10^2 s^{-1} . Results showed an increase in shear strength and a reduction in failure strain with increasing the strain rates. Here it is clear that the literature lacks shear data, and the available studies are not enough to provide a complete understanding of the strain rate effect on the shear behavior of basalt fiber composites.

2.2.3.3. *Compressive behavior*

Several researchers studied the effect of strain rate on the compressive behavior of basalt fiber reinforced composites. Zhang et al. [32] investigated the high strain rate compressive behavior of plain weave basalt composites up to 2100 s^{-1} in the out of plane direction. Results showed an increase in stiffness and strength with increasing strain rate. The compressive properties of 3D braided basalt composites at various strain rates and temperatures were investigated by Pan et al. [33,34]. Results showed a decrease of stiffness and maximum strength with the increasing the temperature. Sun et al. [35] studied the compressive behavior of 2D and 3D basalt woven vinyl ester composites up to strain rates of 3500 s^{-1} . Results showed a strong strain rate sensitivity for both material configurations, where the elastic modulus and maximum stress increased with increasing strain rate while the maximum strain decreased. Table 2.2 summarises the experimental results from literature of the basalt epoxy composites at different strain rates.

Table 2.2. Summary of the experimental results from literature of the basalt/epoxy composites at different strain rates

Authors	Materials	Testing mode and method	Strain rates (s ⁻¹)	Main results
Zhang et al. [21]	Unidirectional basalt epoxy	Tension – servo-hydraulic machine	Up to 133	Increase in tensile strength, maximum strain, and toughness with increasing the strain rates
Ou et al. [12]	Unidirectional basalt epoxy	Tension – drop tower impact	Up to 160	A slight increase in the elastic modulus and maximum strain with the increase in strain rates, and an initial increase followed by a decrease in the tensile strength
Daliri et al. [22]	Twill weave basalt fiber epoxy	Tension – servo-hydraulic machine	Up to 200	An increase in tensile strength with the increase in strain rate (no equilibrium reached)
Li et al. [23]	Unidirectional basalt epoxy	Tension – servo-hydraulic machine	10 ⁻⁵ to 260	An increase in the elastic modulus, the tensile strength, and the tensile strain with increasing the strain rates
Sun et al. [27]	Woven basalt vinylester	Tension – Modified split Hopkinson bar	900 to 2800	An increase in stiffness and failure strength and a decrease in failure strain with the increase of the strain rate
Gunzenmuller et al. [28]	Unidirectional basalt epoxy	Tension – split Hopkinson bar	10 ⁻³ to 10 ²	Increase in maximum strength and maximum strain with increasing the strain rate, and a strain rate independency of the stiffness
Mengel et al. [29]	Hybrid carbon/basalt epoxy	In-plane shear – V notched rail on universal testing machine	Quasi-static	An increase in shear strength and modulus of rigidity due to hybridization
Soares et al. [31]	Twill weave basalt polyester	In-plane shear - rail tests and [±45°] tests on universal testing machine	Quasi-static	Inconsistent shear modulus values
Gunzenmuller et al. [28]	Unidirectional basalt epoxy	In-plane shear – split Hopkinson bar	10 ⁻³ up to 10	An increase in shear strength and a reduction in failure strain with increasing the strain rates
Zhang et al. [32]	plain weave basalt vinyl ester	Compression – Split Hopkinson bar	up to 2100	An increase in stiffness and strength with increasing strain rate
Pan et al. [33,34]	3D braided basalt epoxy	Compression – Split Hopkinson bar	Up to 2400	A decrease of stiffness and maximum strength with the increasing the temperature
Sun et al. [35]	2D and 3D basalt woven vinyl ester	Compression – Split Hopkinson bar	up to strain rates of 3500	Increase in elastic modulus and maximum stress and decrease in maximum strain with increasing strain rate

2.2.4. Comparison between the mechanical behavior of basalt fiber reinforced composites and glass fiber reinforced composites at different strain rates

Basalt fibers and basalt fiber composites are often compared to glass fibers and glass fiber composites in terms of stiffness and strength. However, they tend to show higher elastic modulus and strength values compared to glass fibers and glass fiber composites [2,14,36]. Basalt fiber composites also offer a good combination of stiffness, strength, fatigue resistance, and energy absorption compared to glass fiber composites [15,36].

Because of the many similarities in the mechanical properties of basalt fibers compared to glass fibers, (though better in terms of production and environmental issues), several studies were performed to investigate the possibility of replacing glass fibers with basalt fibers in various applications. Liu et al. [30] studied the behavior of basalt composites and their replacement possibility for glass composites in automotive applications, and reported no significant difference between glass and basalt fiber reinforced composites in terms of elastic modulus and tensile strength. Fiore et al. [37] investigated the hybridization of basalt fibers with glass fibers for marine applications, and showed improved bending properties of hybrid basalt/glass composites compared to glass composites alone, suggesting the basalt fibers as an alternative to glass fibers for boat manufacturing. Quagliarini et al. [38] studied the use of basalt fibers for ropes and rods in architectural and civil applications. Results showed that basalt fibers combined the high strength and the low rigidity required for these applications, and concluded that basalt fibers could replace glass fibers for that purpose. Lapena et al. [4] compared the application of basalt and glass fiber composites in tubular structures, and found that basalt fiber composite tubes exhibited 45% higher hoop strength and 11% higher interlaminar shear strength compared to glass fiber composite tubes, assuring the possibility to replace basalt fibers with glass fibers for tubular structures. For aeronautical applications, basalt fiber composites could be an ideal candidate for replacing glass fiber composites in aircraft secondary structures. These aircraft secondary structures are wing leading edges, wing tips, stabilizers, nacelle cowlings, radomes, fairings, etc [39,40].

Since section 2.2.3 covered the previous state-of-the-art studies in the literature of the behavior of the basalt and fiber reinforced composites at high strain rates, here in this section, the focus will be on the behavior of glass fiber reinforced composites at high strain rates. Naik et al. [41] studied the effect of strain rate on the tensile behavior of woven fabric glass epoxy composites up to 400 s^{-1} using the split Hopkinson bar tensile bar technique. Results showed an increase in the tensile strength by 11% along the thickness direction, and by 16% along the fill direction with increasing strain rate. However, the calculation of the strain rate was based on the classical Hopkinson analysis, which is known to overestimate the actual strain rate in the sample gauge section [42]. Ou et al. [43] investigated the tensile behavior of unidirectional glass epoxy composites at strain rates up to 200 s^{-1} and different temperatures using a drop weight tower. Results indicated an increase in tensile strength and toughness at high strain rates. A general reduction in the tensile strength and toughness was also observed with increasing temperature. Shokrieh et al. [44] studied the tensile behavior of unidirectional glass epoxy composites using

a servo-hydraulic machine, and also reported an increase in tensile strength, absorbed energy, and fracture strain with increasing strain rate.

The in-plane shear behavior of glass fiber composites at high strain rate was also studied by several researchers. Gowtham et al. [45] studied the effect of strain rate on the in-plane shear strength of woven glass epoxy composites using the split Hopkinson bar technique. Results indicated an increase in shear strength with the increase in strain rates. Bergmann et al. [46] also studied the in-plane shear behavior of woven glass epoxy composites at high strain rates using a servo-hydraulic machine. Results also showed an increase in shear strength and stiffness with the increase in strain rates, which also agrees with the results of Gowtham [45]. Staab and Gilat [47] investigated the effect of strain rate on the shear behavior of glass epoxy composites using the split Hopkinson bar technique. They also reported an increase in shear strength with increasing strain rate.

It can be seen that the previous research in the literature only studied the high strain rate behavior of both glass and basalt fiber reinforced composites separately without a common framework in which certain aspect of both materials can be kept constant, such as the resin system, manufacturing technique, etc. Therefore, it is important to unify these aspects in order to provide a meaningful comparison between the high strain rate behavior of both materials.

2.3. Epoxy based nanocomposites

Epoxy resins are widely used as matrix material for high performance composites in aeronautical applications. They are generally characterized by a high crosslinking density compared to other thermoset polymers. This gives epoxy resins and their composites many advantages such as high stiffness, good chemical resistance, good performance at high temperatures, and excellent fatigue performance [48]. Additionally, their low curing shrinkage does not cause curing cracks in large aerospace components. However, because of the high crosslinking density, epoxy resins are generally very brittle with a very low fracture strain, and have poor resistance to impact and crack propagation [49]. As a result, efforts were made to improve the mechanical performance of the epoxy resins by the addition of different types of fillers, such as inorganic particles [50–52], elastomer particles [53,54], carbon nanotubes [55,56], hyperbranched polymers [57–59], and recently graphene nanoplatelets [49,60].

2.3.1. Silica nanoparticles as fillers of epoxy resins

Compared to other filler types, the addition of silica nanoparticles to the epoxy resin is widely applied in research. This is related to the marginal effect of the silica based fillers on the glass transition temperature of the hosting epoxy matrix and, hence, its curing temperature [61–64]. Moreover, the advancement in synthesis processes allow the production of these nanoparticles either as precipitates or directly in the epoxy resin itself (in-situ) [65], which can be considered for large scale manufacturing of epoxy nanocomposites with a relatively low cost [66]. In addition, these synthesis techniques allow a very high degree of control over the size and distribution of the formed nanoparticles [53].

2.3.1.1. Synthesis techniques of silica nanoparticles

Several methods are used to synthesize the silica nanoparticles, such as the reverse microemulsion method, the chemical vapor condensation method, and the sol-gel method [67]. In the reverse microemulsion method, silica nanoparticles are produced by the addition of silicon alkoxides and other catalysts to a medium which contains reversed water-on-oil micelles [68]. However, this method is considered expensive and presents some difficulties in obtaining uncontaminated silica nanoparticles [67]. The chemical vapor condensation method relies on high temperature flame decomposition of metal-organic precursors to produce the silica nanoparticles. However, the particle size, morphology, and phase composition cannot be fully controlled using this method [67]. The sol-gel method is the most widely used method to produce silica nanoparticles, due to its ability to precisely control the size range and the composition of the produced nanoparticles [69]. The basic sol-gel method, also known as the Stöber method, uses a tetraethyl orthosilicate (TEOS) and other silicate precursors combined with water, alcohol and ammonia to produce the silica nanoparticles. The size of the silica nanoparticles can be precisely controlled by changing the ratio of the solvents to the TEOS precursors and by controlling the rate of addition of the TEOS precursors [69]. Several modifications to the sol-gel method are also applied to produce different types of silica nanoparticles, such as mesoporous particles, core-shell particles, shaped particles, and etched particles, as depicted in Figure 2.5. The sol-gel and modified sol-gel techniques could also be used to modify the surface of the silica nanoparticles by using alkoxy-silanes/halosilanes [69]. Surface functionalization generally improves the compatibility of the particles with the hosting matrix [67], prepares the silica nanoparticles for specific applications, and improves the dispersion of the particles during the preparation of the nanocomposites [67,69]. Figure 2.6 shows some electron microscopy images from the literature of the silica nanoparticles which can be synthesized by sol-gel techniques.

2.3.1.2. Overall effect of the addition of silica nanoparticles on the thermal and mechanical behavior of epoxy resins

Several authors reported improvements in the overall mechanical properties as a result of the addition of silica nanoparticles to epoxy resin. Chen et al. [70] studied the tensile and fracture toughness behavior of epoxy filled with 12 nm silica nanoparticles at quasi-static strain rates. Results showed an increase in the tensile modulus, tensile strength and fracture toughness up to a filler weight percentage of 25%. Further increase in weight percentages continued to increase the tensile modulus, but decreased the tensile strength and the fracture toughness. Hsieh et al. [62] also investigated the effect of adding silica nanoparticles of size 20 nm on the tensile and fracture toughness behavior of various epoxy resins at quasi-static strain rates. Results indicated that silica nanoparticles increased the tensile modulus, tensile strength and fracture toughness of the epoxy up to filler weight percentages of 20%. The effect of silica nanoparticles of size 20 nm on the compressive behavior of epoxy resins at quasi-static strain rates was studied by Jumahat et al. [71]. Results also showed that the addition of silica nanoparticles up to a filler weight percentage of 25% improved the compressive stiffness and strength of the epoxy without affecting the failure strain. Tian et al. [72] reported that the

addition of silica nanoparticles improved the toughness of the epoxy matrix, which resulted in an increase in interfacial adhesion with carbon fibers. Kothmann [73] reported an increase in the fatigue crack growth behavior of the epoxy by the addition of silica nanoparticles.

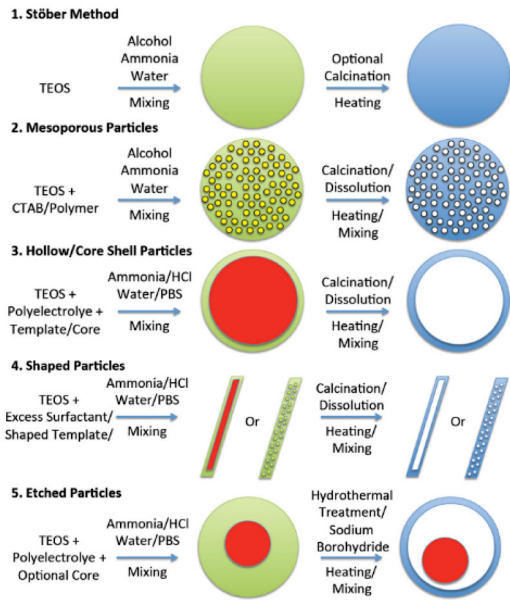


Figure 2.5. Schematic of the sol-gel and the modified sol-gel techniques [69]

2.3.1.3. *Effect of silica nanoparticle size and surface conditions on the properties of the epoxy resin*

The extent of the improvement of the physical and the mechanical properties of epoxy nanocomposites is highly affected by the size and surface functionalization condition of the silica nanoparticles. In terms of nanoparticle size, Macan et al. [74] showed that the addition of silica nanoparticles with a size of 7 nm marginally changed the curing mechanism and glass transition temperature of the epoxy. Liang et al. [63] reported no change in the glass transition temperature and the fracture toughness behavior of silica/epoxy nanocomposites with particle sizes of 20 and 80 nm. Additionally, the authors reported an improved fracture toughness behavior of the epoxy composite with these nanoscale silica particles compared to microscale silica particles of 42 μm . Dittanet et al. [75] showed that for a particle size range of 23 to 170 nm and up to 30% weight content, the elastic modulus, yield strength, glass transition temperature, and fracture toughness remained nearly constant regardless of the silica particle size. Bondioli et al. [76] studied the tensile behavior of epoxy/silica nanocomposites with silica particle sizes of 75 nm and 330 nm. Results showed that after 1% weight content for both

silica particle sizes, the elastic modulus of the 75 nm silica/epoxy became higher than that of the 330 nm silica/epoxy, which partially contradicts the findings of Dittanet et al. [75]. Sun et al. [77] reported a decrease in the glass transition temperature for epoxy filled with 100 nm silica particles after 10% weight, compared to a constant glass transition temperature for the same epoxy filled with 3 μm silica particles, which also contradicts the findings of both Dittanet et al. [75]. Yohanes et al. [78] reported that the addition of silica microparticles with a size of 34 μm improved the dispersion of smaller silica nanoparticle with a size of 17 nm in the epoxy resin. This resulted in an increase in stiffness and energy absorption of the epoxy resin at 5% silica weight content.

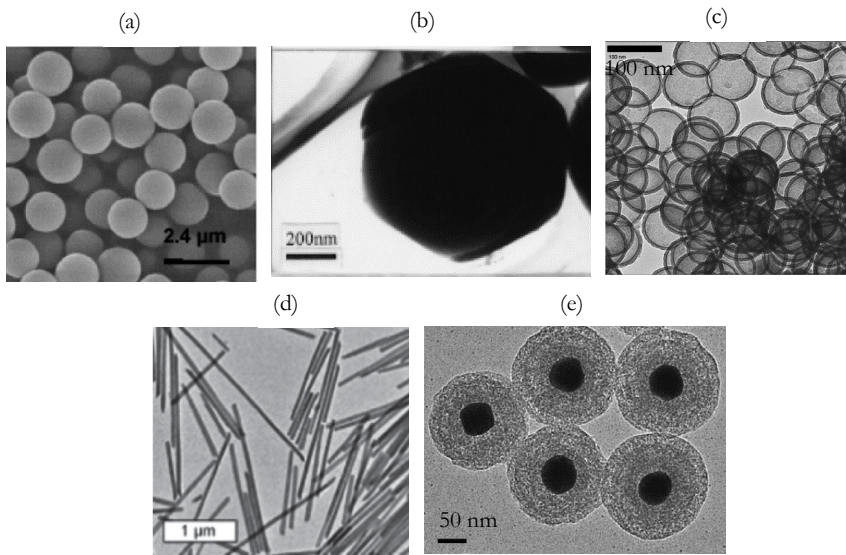


Figure 2.6. Examples of electron microscopy images of silica nanoparticles: (a) spherical particles [79], (b) mesoporous particles [80], (c) core-shell particles [81], (d) shaped particles [82], (e) etched particles [83]

In terms of surface functionalization, Macan et al. [74] showed that surface functionalization of the silica nanoparticles significantly increased the elongation at fracture and the toughness of the resin, without affecting its strength or stiffness. Leon et al. [84] and Karman-Pirzaman et al. [85] reported that surface functionalized silica nanoparticles with size range of 15 to 100 nm and up to 3-5% weight content increased the overall mechanical behavior of the epoxy. Kang et al. [86] showed that surface modified silica nanoparticles of size 400 nm increased the glass transition temperature of the epoxy nanocomposite while a nearly constant glass transition temperature was obtained for surface unmodified particles of the same size regardless of the weight content. In addition, the increase in the weight content of the silica nanoparticles beyond 5% reduced the coefficient of thermal expansion of the epoxy nanocomposite.

2.3.1.4. Mechanical behavior of epoxy resins filled with silica nanoparticle at different strain rates

As mentioned earlier, the main aim of improving epoxy resins is to enhance their use as matrix material and to improve the properties of aeronautical composite components. These components are typically subjected to extreme impact events, such as bird strike or fan blade-out events. Therefore, studying the behavior of epoxy and silica/epoxy nanocomposites at high strain rates is essential. Indeed, it has been shown in literature that epoxy resins have a strong strain rate dependency. For example, Gerlach et al. [87] investigated the tensile and the compressive behaviors of RTM6 epoxy at strain rates up to 104 s^{-1} . Results showed that the RTM6 epoxy resin is strain rate sensitive in both tension and compression. Both yield strength and initial modulus increased with increasing strain rates. Rio et al. [88] and Naik et al. [89] also reported an increase of the elastic modulus and the compressive yield strength for epoxy resins with increasing strain rates up to 2500 s^{-1} .

While several studies report the quasi-static mechanical behavior of silica/epoxy nanocomposites (as discussed in the previous section), few studies are available regarding their high strain rate behavior. Miao et al. [90] studied the compressive behavior of silica/epoxy nanocomposites of size 20 nm and weight content up to 10% at strain rates up to 5000 s^{-1} . Results showed that the silica nanoparticles only marginally improved the yield strength of the epoxy resin regardless of the weight content of the particles. Additionally, the silica/epoxy nanocomposite showed a significant strain rate sensitivity, where the yield strength increased with increasing the strain rate. Tian et al. [91] investigated the compressive behavior of silica/epoxy nanocomposites of 30 nm in size with a weight content of 10% at strain rates up to 3000 s^{-1} . Results showed an increase in compressive modulus and yield strength with increased strain rate and the addition of silica nanoparticles. However, the improvement of the compressive performance was more pronounced in the low strain rate regime compared to the high strain rate regime. Guo et al. [92] also investigated the compressive behavior of silica/epoxy nanocomposite with a particle size of 90 nm and weight contents up to 7% at strain rates up to 10000 s^{-1} . Contrary to the findings of Tian et al. [91], the results showed that the improvement in the compressive strength by the addition of silica nanoparticles was more pronounced at high strain rates, whereas no improvement could be observed at low strain rates. Ma et al. [93] showed that for silica nanoparticles with a size of 50 nm and up to 15% weight, the compressive failure strength increased at strain rates increased up to 200 s^{-1} and higher silica contents. The compressive stiffness, however, showed a reduction at higher silica weight contents. Yohanes [94] found that the addition of silica microparticles with a size of $34 \mu\text{m}$ or silica nanoparticles of 17 nm increased the dynamic stiffness of the epoxy at high strain rates, regardless of the weight content of the particles. However, when a mixture of both particle sizes is used, the dynamic stiffness is significantly reduced. Table 2.3 provides a summary of the experimental data from literature of the silica nanoparticle filled epoxy at different strain rates.

Table 2.3. Summary of the experimental results in compression from literature of the silica nanoparticle filled epoxy at different strain rates

Authors	Silica nanoparticle size and weight %	Strain rates (s ⁻¹)	Main results
Miao et al. [90]	20 nm – up to 10% wt.	up to 5000	Marginal improvement of the yield strength of the epoxy resin with the silica nanoparticles – increase in the yield strength with increasing the strain rate
Tian et al. [91]	30 nm – up to 10% wt.	up to 3000	An increase in compressive modulus and yield strength with increased strain rate and the addition of silica nanoparticles
Guo et al. [92]	90 nm – up to 7 % wt.	up to 10000	Improvement in the compressive strength by the addition of silica nanoparticles was more pronounced at high strain rates compared to low strain rates
Ma et al. [93]	50 nm – up to 15% wt.	up to 200	An increase in strength and a decrease in stiffness, at higher silica weight contents and high strain rates
Yohanes [94]	34 µm and 17 nm – up to 10% wt.	900 to 2800	An increase the stiffness of the epoxy at high strain with either particles are used, but a reduction in the stiffness if mixture of both particles is used

It can be seen that the data in literature are contradicting. No clear trends can be established regarding the effect of the size of the silica nanoparticle on the mechanical behavior of epoxy resins at high strain rates. Despite the contradictions, part of the data still suggests that a lower weight content of silica particles, combined with a submicron size scale of the particles, has the potential to improve the mechanical properties of the epoxy resin without compromising the thermal or the physical properties of the resin. This can be achieved by silica nanoparticle sizes of 300 nm up to 1µm. However, to the best knowledge of the authors, no data are available in the literature regarding the effect of addition of silica nanoparticles within this specific size range on the mechanical behavior of epoxy resins at different strain rates in general, and compressive properties in particular.

2.3.2. Hyperbranched polymers as fillers of epoxy resin

Hyperbranched polymers (HBP) are considered a class of three dimensional polymers with a unique branching, dendritic-like structure, as shown in Figure 2.7. This unique structure, as opposed to the linear polymer chains, allows the hyperbranched polymers to have low melt and solution viscosities, low entanglement and high solvent solubility [57]. Additionally, hyperbranched polymers can be produced in a straightforward manner, and in large quantities, which gives an economical advantage. In terms of mechanical properties, hyperbranched polymers have a lower mechanical strength compared to polymers with linear chains [95].

2.3.2.1. Synthesis techniques of the hyperbranched polymers

The synthesis of the hyperbranched polymers follows 3 main approaches: (1) bottom up approach by polymerization of monomers, (2) top down approach by degradation of giant networks or biomacromolecules, and (3) middle-upon approach by modification of as-prepared hyperbranched polymeric-precursor [95]. Figure 2.8 schematically shows the different synthesis techniques of the hyperbranched polymers. Additional details on the chemical procedure to synthesize hyperbranched polymers can be found in refs. [95–97]. The produced hyperbranched polymers are typically in a powder form, the size of which can range from 2 nm to 15 nm. Additionally, the produced powder does not aggregate in bulk [95]. Hyperbranched polymers have been used in some applications such as additives and coatings in other polymer systems, gene and drug carriers, nanoreactors, and nano capsules [95]. Moreover, hyperbranched polymers filled with various nanoparticles were also considered for optical and dental applications, anti-corrosion coatings, and as dielectric materials [97].

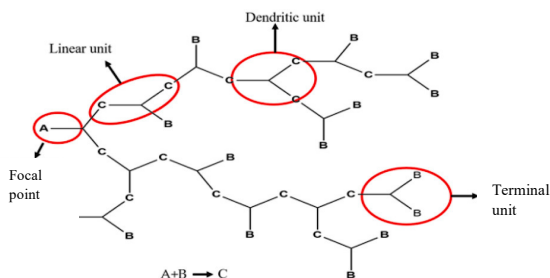


Figure 2.7. Schematic of the structure of hyperbranched polymers [97]

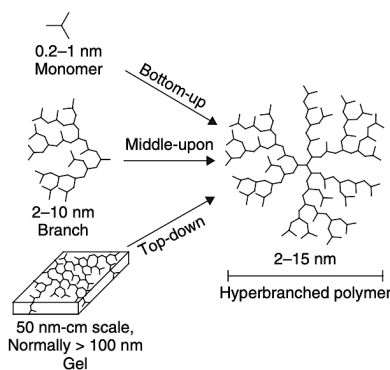


Figure 2.8. Schematic of the different synthesis techniques of hyperbranched polymers [95]

2.3.2.2. Overall effect of adding hyperbranched polymers on the thermal and mechanical behavior of epoxy resins

Because of the characteristic of the hyperbranched polymers, they were considered as modifiers in epoxy resins, particularly for enhancement of fracture toughness and impact resistance [57]. However, the effect of the addition of HBP to epoxy resins on the overall mechanical and thermal performance is not very well understood. Li et al. [98] investigated the effect of adding hyperbranched polymers with different weight percentages to epoxy resin on the impact and flexure strengths. Results showed that both the impact strength and the flexure strength increased with the addition of hyperbranched polymers up to weight content of 8% HBP weight content. Further increase of the HBP weight content to 20% results in an only marginal improvement of the impact strength, and a reduction of the flexure strength. Ratna et al. [99] also investigated the thermomechanical behavior of an epoxy resin filled with HBP up to 20% weight content. Results showed that the impact strength significantly improved at higher HBP content compared to lower HBP content, which contradicts the results of Li et al. [98]. Additionally, the glass transition temperature was reduced with the addition of the HBP up to 20% weight content, as reported by Morancho et al. [100]. Lv et al. [101] reported that the addition of the HBP to epoxy resins up to 10% weight content improved the impact strength and fracture strain, but reduced the glass transition temperature, the storage modulus, the tensile strength, and the flexure strength, which also contradicts with the findings of Li et al. [98]. Both Mezzenga et al. [102] and Boogh et al. [59] reported a significant improvement in the fracture toughness of epoxy resins by the addition of HBP, without reducing the stiffness or the glass transition temperature of the epoxy, which also contradicts the findings of Ranta et al. [99] and Morancho et al. [100]. Inorganic core with HBP shell was also considered for reinforcing epoxy resins, due to the excellent encapsulation properties of the HBP [95]. Li et al. [104] reported an improvement in the tensile and impact strength of epoxy resins filled with 3% of silica/HBP core/shell nanoparticles by weight. Zotti et al. [105] reported a slight increase in the storage modulus and fracture toughness by the addition of silica/HBP core/shell nanoparticles to epoxy resin. However, the glass transition temperature was slightly reduced. Table 2.4 summarizes the experimental data from literature of the HBP filled epoxy.

In addition to the lack of clear trends regarding the overall effect of adding the HBP on the mechanical behavior of epoxy resins, the effect of strain rate on the epoxy resins filled with HBP is also not very well understood. This is due to the lack of studies in the literature of this material at different strain rates.

Table 2.4. Summary of the experimental results from literature of the HBP filled epoxy

Authors	HBP weight %	Main results
Li et al. [98]	Up to 20% wt.	An increase in impact and flexure strengths with the addition of hyperbranched polymers up to 8% and marginal improvement in impact strength and reduction in flexure strength from 8% to 20%.
Ratna et al. [99]	Up to 20% wt.	Improvement in impact strength higher HBP content
Moranco et al. [100]	Up to 20% wt.	A reduction in the glass transition temperature of the resin by the addition of the HBP particles
Lv et al. [101]	up to 10% wt.	An improvement in the impact strength and fracture strain, but a reduction in glass transition temperature, storage modulus, tensile and flexure strengths
Yohanes [94]	34 μm and 17 nm – up to 10% wt.	An increase the stiffness of the epoxy at high strain with either particles are used, but a reduction in the stiffness if mixture of both particles is used
Boogh et al. [59]	5% wt.	An improvement in the fracture toughness of epoxy resins by the addition of HBP, without reducing the stiffness or the glass transition temperature of the epoxy
Mezzenga et al. [102]	10% wt.	An improvement in the interlaminar fracture resistance of epoxy composites by the addition of HBP, without reducing the stiffness, glass transition temperature, viscosity, or processability of the epoxy
Li et al. [104]	3% wt. of silica core with HBP shell	An improvement in the tensile and impact strengths of epoxy resins filled with silica/HBP core/shell nanoparticles
Zotti et al. [105]	Up to 5%wt. of silica core with HBP shell	A slight increase in storage modulus and fracture toughness by the addition of silica/HBP core/shell nanoparticles to epoxy resin

2.4. Conclusions

This chapter covered a detailed and critical review of previous literature studies on the effect of strain rate on the mechanical behavior of basalt fiber composites and epoxy nanocomposites filled with silica nanoparticles and hyperbranched polymers. In the first part of the chapter, the state of the art of the basalt fibers and their composites were discussed in detail. The different manufacturing techniques for short and continuous basalt fibers were presented and compared. Additionally, the position of the basalt fibers with respect to other conventional fibers in terms of mechanical properties was highlighted. A critical review of past studies

covering the strain rate effect on the tensile, in-plane shear, and compression behavior of basalt composites was discussed. Moreover, a comparison between the mechanical behavior of basalt fiber composites and glass fiber composites was presented. In the second part of the chapter, the state of the art covering the epoxy based nanocomposites were discussed. The synthesis of two types of nanoparticles, i.e., silica nanoparticles and hyperbranched polymers, was briefly presented. Furthermore, a critical review of the effect of the addition of both types of nanoparticles on the thermal and mechanical behavior of epoxy resins was presented. Finally, the critical review was extended to the effect of strain rate on the mechanical properties of epoxy based nanocomposites. Based on the analysis of the literature, the following can be concluded:

- 1- The effect of the strain rate on the tensile and in-plane shear properties of the basalt fibers and their composites is not very well understood, either due to the contradiction of the data in the literature (in case of the tensile properties) or the lack thereof (in case of in-plane shear).
- 2- The literature lacks a meaningful comparison between the mechanical behavior of glass fiber composites and basalt fiber composites at different strain rates. The available studies in literature covered the effect of strain rate of both glass and basalt fiber reinforced composites separately without a common framework in which certain aspects of both materials can be kept constant, such as the resin system, manufacturing technique, etc.
- 3- The effect of strain rate on the mechanical behavior of epoxy based nanocomposites is also not very well understood. For epoxies filled with silica nanoparticles, there are no data available in the literature regarding the effect of strain rate and the addition of silica nanoparticles – within the size range of 300 nm up to 1 μ m – on the mechanical properties of epoxy resins. Whereas for the epoxy filled with hyperbranched polymers, no clear trend can be established regarding the effect of the addition of HBP on the overall mechanical and thermal properties of epoxy resins. Additionally, the literature lacks data regarding the effect of strain rate on the mechanical behavior of HBP filled epoxy resins.

References

- [1] Fitton, J. G., 2021, *Basalt and Related Rocks*, Elsevier Ltd.
- [2] Deák, T., and Czígány, T., 2009, "Chemical Composition and Mechanical Properties of Basalt and Glass Fibers: A Comparison," *Text. Res. J.*, **79**(7), pp. 645–651.
- [3] Monaldo, E., Nerilli, F., and Vairo, G., 2019, "Basalt-Based Fiber-Reinforced Materials and Structural Applications in Civil Engineering," *Compos. Struct.*, **214**, pp. 246–263.
- [4] Lapena, M. H., and Marinucci, G., 2017, "Mechanical Characterization of Basalt and Glass Fiber Epoxy Composite Tube," *Mater. Res.*, **21**(1), pp. 226–227.
- [5] Wei, B., Song, S., and Cao, H., 2011, "Strengthening of Basalt Fibers with Nano-SiO₂-Epoxy Composite Coating," *Mater. Des.*, **32**(8–9), pp. 4180–4186.
- [6] Xing, D., Xi, X. Y., and Ma, P. C., 2019, "Factors Governing the Tensile Strength of Basalt Fibre," *Compos. Part A Appl. Sci. Manuf.*, **119**(December 2018), pp. 127–133.
- [7] Dhand, V., Mittal, G., Rhee, K. Y., Park, S. J., and Hui, D., 2015, "A Short Review on Basalt Fiber Reinforced Polymer Composites," *Compos. Part B Eng.*, **73**, pp. 166–180.

- [8] Yao, Y., Zhu, D., Zhang, H., Li, G., and Mobasher, B., 2016, "Tensile Behaviors of Basalt, Carbon, Glass, and Aramid Fabrics under Various Strain Rates," *J. Mater. Civ. Eng.*, **28**(9), p. 04016081.
- [9] Deák, T., and Czirány, T., 2009, "Chemical Composition and Mechanical Properties of Basalt and Glass Fibers: A Comparison," *Text. Res. J.*, **79**(7), pp. 645–651.
- [10] Kessler, E., Gadow, R., and Straub, J., 2016, "Basalt, Glass and Carbon Fibers and Their Fiber Reinforced Polymer Composites under Thermal and Mechanical Load," *AIMS Mater. Sci.*, **3**(4), pp. 1561–1576.
- [11] Zhu, L., Sun, B., Hu, H., and Gu, B., 2010, "Constitutive Equations of Basalt Filament Tows under Quasi-Static and High Strain Rate Tension," *Mater. Sci. Eng. A*, **527**(13–14), pp. 3245–3252.
- [12] Ou, Y., Zhu, D., and Li, H., 2016, "Strain Rate and Temperature Effects on the Dynamic Tensile Behaviors of Basalt Fiber Bundles and Reinforced Polymer Composite," *J. Mater. Civ. Eng.*, **28**(10), p. 04016101.
- [13] Dhand, V., Mittal, G., Rhee, K. Y., Park, S. J., and Hui, D., 2015, "A Short Review on Basalt Fiber Reinforced Polymer Composites," *Compos. Part B Eng.*, **73**(C), pp. 166–180.
- [14] Dorigato, A., and Pegoretti, A., 2012, "Fatigue Resistance of Basalt Fibers-Reinforced Laminates," *J. Compos. Mater.*, **46**(15), pp. 1773–1785.
- [15] Dorigato, A., and Pegoretti, A., 2014, "Flexural and Impact Behaviour of Carbon/Basalt Fibers Hybrid Laminates," *J. Compos. Mater.*, **48**(9), pp. 1121–1130.
- [16] Shishevan, F. A., Akbulut, H., and Mohtadi-Bonab, M. A., 2017, "Low Velocity Impact Behavior of Basalt Fiber-Reinforced Polymer Composites," *J. Mater. Eng. Perform.*, **26**(6), pp. 2890–2900.
- [17] Bozkurt, Ö. Y., 2017, "Hybridization Effects on Tensile and Bending Behavior of Aramid/Basalt Fiber Reinforced Epoxy Composites," *Polym. Compos.*, **38**(6), pp. 1144–1150.
- [18] Wu, Z., Wang, X., Iwashita, K., Sasaki, T., and Hamaguchi, Y., 2010, "Tensile Fatigue Behaviour of FRP and Hybrid FRP Sheets," *Compos. Part B Eng.*, **41**(5), pp. 396–402.
- [19] Chikhradze, N. M., Marquis, F. D. S., Japaridze, L. A., Abashidze, G. S., and Okujava, L. M., 2010, "Polymer Based Composite and Hybrid Materials for Wind Power Generation," *Mater. Sci. Forum*, **654–656**, pp. 2612–2615.
- [20] Liu, Q., Shaw, M. T., Parnas, R. S., Shaw, M. T., Parnas, R. S., and McDonnell, A. M., 2006, "Investigation of Basalt Fiber Composite Aging Behavior for Applications in Transportation," *Polym. Compos.*, **27**(5), pp. 475–483.
- [21] Zhang, H., Yao, Y., Zhu, D., Mobasher, B., and Huang, L., 2016, "Tensile Mechanical Properties of Basalt Fiber Reinforced Polymer Composite under Varying Strain Rates and Temperatures," *Polym. Test.*, **51**, pp. 29–39.
- [22] Daliri, A., Vijayan, A., Ruan, D., and Wang, C. H., 2017, "High Strain Rate Tensile Properties of Basalt-Fibre Reinforced Polymer Composites," *17th Australian Aerospace Congress*, Melbourne.
- [23] Li, Z. X., Zhang, X., and Shi, Y., 2020, "Experimental Study on Dynamic Properties of BFRP Laminates Used for Structural Strengthening under High Strain Rates," *Constr. Build. Mater.*, **251**, p. 118731.
- [24] Xiao, X., 2008, "Dynamic Tensile Testing of Plastic Materials," *Polym. Test.*, **27**(2), pp. 164–178.
- [25] Eriksen, R. N. W., 2014, "High Strain Rate Characterisation of Composite Materials," Springer, Cham.
- [26] Spronk, S. W. F., Verboven, E., Gilibert, F. A., Sevenois, R. D. B., Garoz, D., Kersemans, M., and Van Paeppegem, W., 2018, "Stress-Strain Synchronization for High Strain Rate Tests on Brittle Composites," *Polym. Test.*, **67**, pp. 477–486.
- [27] Yang, Y., Yu, J., Xu, H., and Sun, B., 2017, *Porous Lightweight Composites Reinforced with Fibrous Structures*, Springer.
- [28] Ganzenmüller, G. C., Plappert, D., Trippel, A., and Hiermaier, S., 2019, "A Split-Hopkinson Tension Bar Study on the Dynamic Strength of Basalt-Fibre Composites," *Compos. Part B Eng.*, **171**, pp. 310–319.
- [29] Mengal, A. N., Karuppanan, S., and Ovinis, M., 2017, "In-Plane Shear Properties of Basalt-Carbon/Epoxy Hybrid Composite Laminates," *Materwiss. Werksttech.*, **48**(3), pp. 261–266.
- [30] Liu, Q., Shaw, M. T., Parnas, R. S., and McDonnell, A. M., 2006, "Investigation of Basalt Fiber Composite Mechanical Properties for Applications in Transportation," *Polym. Compos.*, **27**(1), pp. 41–48.
- [31] Soares, B., Preto, R., Sousa, L., and Reis, L., 2016, "Mechanical Behavior of Basalt Fibers in a Basalt-UP Composite," *Procedia Struct. Integr.*, **1**(C), pp. 82–89.
- [32] Zhang, F., Wu, L., Wan, Y., Gideon, R. K., Gu, B., and Sun, B., 2014, "Numerical Modeling of the Mechanical Response of Basalt Plain Woven Composites under High Strain Rate Compression," *J. Reinf. Plast. Compos.*, **33**(12), pp. 1087–1104.
- [33] Pan, Z., Gu, B., and Sun, B., 2014, "Longitudinal Compressive Behaviour of 3D Braided Composite under Various Temperatures and Strain Rates," *Appl. Phys. A Mater. Sci. Process.*, **118**(4), pp. 1315–1337.
- [34] Pan, Z., Gu, B., and Sun, B., 2015, "Experimental Investigation of High-Strain Rate Properties of 3-D Braided Composite Material in Cryogenic Field," *Compos. Part B Eng.*, **77**(C), pp. 379–390.
- [35] Baozhong, S., Zhilin, N., Lytao, Z., and Bohong, G., 2010, "Mechanical Behaviors of 2D and 3D Basalt Fiber Woven Composites under Various Strain Rates," *J. Compos. Mater.*, **44**(14), pp. 1779–1795.

- [36] Lopresto, V., Leone, C., and De Iorio, I., 2011, “Mechanical Characterisation of Basalt Fibre Reinforced Plastic,” *Compos. Part B Eng.*, **42**(4), pp. 717–723.
- [37] Fiore, V., Di Bella, G., and Valenza, A., 2011, “Glass-Basalt/Epoxy Hybrid Composites for Marine Applications,” *Mater. Des.*, **32**(4), pp. 2091–2099.
- [38] Quagliarini, E., Monni, F., Lenci, S., and Bondioli, F., 2012, “Tensile Characterization of Basalt Fiber Rods and Ropes: A First Contribution,” *Constr. Build. Mater.*, **34**(C), pp. 372–380.
- [39] Mouritz, A. P., 2012, *Introduction to Aerospace Materials*.
- [40] Dutton, S., Kelly, D., and Baker, A., 2004, *Composite Materials for Aircraft Structures, Second Edition*.
- [41] Naik, N. K., Yernamma, P., Thoram, N. M., Gadipatri, R., and Kavala, V. R., 2010, “High Strain Rate Tensile Behavior of Woven Fabric E-Glass/Epoxy Composite,” *Polym. Test.*, **29**(1), pp. 14–22.
- [42] Verleysen, P., and Degrieck, J., 2004, “Experimental Investigation of the Deformation of Hopkinson Bar Specimens,” *Int. J. Impact Eng.*, **30**(3), pp. 239–253.
- [43] Ou, Y., Zhu, D., Zhang, H., Huang, L., Yao, Y., Li, G., and Mobasher, B., 2016, “Mechanical Characterization of the Tensile Properties of Glass Fiber and Its Reinforced Polymer (GFRP) Composite under Varying Strain Rates and Temperatures,” *Polymers (Basel)*, **8**(5), p. 196.
- [44] Shokrieh, M. M., and Omid, M. J., 2009, “Tension Behavior of Unidirectional Glass/Epoxy Composites under Different Strain Rates,” *Compos. Struct.*, **88**(4), pp. 595–601.
- [45] Gowtham, H. L., Pothnis, J. R., Ravikumar, G., and Naik, N. K., 2013, “High Strain Rate In-Plane Shear Behavior of Composites,” *Polym. Test.*, **32**(8), pp. 1334–1341.
- [46] Bergmann, T., Heimbs, S., and Maier, M., 2015, “Mechanical Properties and Energy Absorption Capability of Woven Fabric Composites under $\pm 45^\circ$ Off-Axis Tension,” *Compos. Struct.*, **125**, pp. 362–373.
- [47] Staab, G. H., and Gilat, A., 1995, “High Strain Rate Response of Angle-Ply Glass/Epoxy Laminates,” *J. Compos. Mater.*
- [48] Mallick, P. K., 1997, *Composites Engineering Handbook*, CRC Press.
- [49] Domun, N., Hadavinia, H., Zhang, T., Liaghat, G., Valid, S., Spacie, C., Paton, K. R., and Sainsbury, T., 2017, “Improving the Fracture Toughness Properties of Epoxy Using Graphene Nanoplatelets at Low Filler Content,” *Nanocomposites*, **3**(3), pp. 85–96.
- [50] Duan, Z., He, H., Liang, W., Wang, Z., He, L., and Zhang, X., 2018, “Tensile, Quasistatic and Dynamic Fracture Properties of Nano-Al₂O₃-Modified Epoxy Resin,” *Materials (Basel)*, **11**(6), pp. 905–917.
- [51] Naik, N. K., Pandya, K. S., Kavala, V. R., Zhang, W., and Koratkar, N. A., 2014, “Alumina Nanoparticle Filled Epoxy Resin: High Strain Rate Compressive Behavior,” *Polym. Eng. Sci.*, **54**(12), pp. 2896–2901.
- [52] Gurusideswar, S., Velmurugan, R., and Gupta, N. K., 2016, “High Strain Rate Sensitivity of Epoxy/Clay Nanocomposites Using Non-Contact Strain Measurement,” *Polymer (Guildf)*, **86**, pp. 197–207.
- [53] Sprenger, S., 2013, “Epoxy Resins Modified with Elastomers and Surface-Modified Silica Nanoparticles,” *Polymer (Guildf)*, **54**(18), pp. 4790–4797.
- [54] Kausar, A., 2020, “Rubber Toughened Epoxy-Based Nanocomposite: A Promising Pathway toward Advanced Materials,” *J. Macromol. Sci. Part A*.
- [55] Bie, B. X., Han, J. H., Lu, L., Zhou, X. M., Qi, M. L., Zhang, Z., and Luo, S. N., 2015, “Dynamic Fracture of Carbon Nanotube/Epoxy Composites under High Strain-Rate Loading,” *Compos. Part A Appl. Sci. Manuf.*, **68**(C), pp. 282–288.
- [56] Gómez-Del Río, T., Rodríguez, J., and Pearson, R. A., 2014, “Compressive Properties of Nanoparticle Modified Epoxy Resin at Different Strain Rates,” *Compos. Part B Eng.*, **57**, pp. 173–179.
- [57] Buonocore, G. G., Schiavo, L., Attianese, I., and Borriello, A., 2013, “Hyperbranched Polymers as Modifiers of Epoxy Adhesives,” *Compos. Part B Eng.*, **53**(C), pp. 187–192.
- [58] Zotti, A., Elmahdy, A., Zuppolini, S., Borriello, A., Verleysen, P., and Zarrelli, M., 2020, “Aromatic Hyperbranched Polyester/RTM6 Epoxy Resin for EXTREME Dynamic Loading Aeronautical Applications,” *Nanomaterials*, **10**(2), p. 188.
- [59] Boogh, L., Pettersson, B., and Månson, J. A. E., 1999, “Dendritic Hyperbranched Polymers as Tougheners for Epoxy Resins,” *Polymer (Guildf)*, **40**(9), pp. 2249–2261.
- [60] Wang, F., Drzal, L. T., Qin, Y., and Huang, Z., 2016, “Enhancement of Fracture Toughness, Mechanical and Thermal Properties of Rubber/Epoxy Composites by Incorporation of Graphene Nanoplatelets,” *Compos. Part A Appl. Sci. Manuf.*, **87**, pp. 10–22.
- [61] Kinloch, A. J., Mohammed, R. D., Taylor, A. C., Eger, C., Sprenger, S., and Egan, D., 2005, “The Effect of Silica Nano Particles and Rubber Particles on the Toughness of Multiphase Thermosetting Epoxy Polymers,” *J. Mater. Sci.*
- [62] Hsieh, T. H., Kinloch, A. J., Masania, K., Taylor, A. C., and Sprenger, S., 2010, “The Mechanisms and Mechanics of the Toughening of Epoxy Polymers Modified with Silica Nanoparticles,” *Polymer (Guildf)*, **51**(26), pp. 6284–6294.
- [63] Liang, Y. L., and Pearson, R. A., 2009, “Toughening Mechanisms in Epoxy-Silica Nanocomposites (ESNs),” *Polymer (Guildf)*, **50**(20), pp. 4895–4905.
- [64] Linec, M., and Mušić, B., 2019, “The Effects of Silica-Based Fillers on the Properties of Epoxy Molding

- Compounds," *Materials* (Basel), **12**(11), pp. 1–11.
- [65] Bondioli, F., Darecchio, M. E., Luyt, A. S., and Messori, M., 2011, "Epoxy Resin Modified with in Situ Generated Metal Oxides by Means of Sol-Gel Process," *J. Appl. Polym. Sci.*, **122**(3), pp. 1792–1799.
- [66] Aliofkhazraei, M., 2015, *Handbook of Nanoparticles*.
- [67] Rahman, I. A., and Padavettan, V., 2012, "Synthesis of Silica Nanoparticles by Sol-Gel: Size-Dependent Properties, Surface Modification, and Applications in Silica-Polymer Nanocomposites Review," *J. Nanomater.*, **2012**.
- [68] Finnie, K. S., Bartlett, J. R., Barbé, C. J. A., and Kong, L., 2007, "Formation of Silica Nanoparticles in Microemulsions," *Langmuir*, **23**(6), pp. 3017–3024.
- [69] Liberman, A., Mendez, N., Troglér, W. C., and Kummel, A. C., 2014, "Synthesis and Surface Functionalization of Silica Nanoparticles for Nanomedicine," *Surf. Sci. Rep.*, **69**(2–3), pp. 132–158.
- [70] Chen, C., Justice, R. S., Schaefer, D. W., and Baur, J. W., 2008, "Highly Dispersed Nanosilica-Epoxy Resins with Enhanced Mechanical Properties," *Polymer (Guildf.)*, **49**(17), pp. 3805–3815.
- [71] Jumahat, A., Soutis, C., Jones, F. R., and Hodzic, A., 2010, "Effect of Silica Nanoparticles on Compressive Properties of an Epoxy Polymer," *J. Mater. Sci.*, **45**(21), pp. 5973–5983.
- [72] Tian, Y., Zhang, H., and Zhang, Z., 2017, "Influence of Nanoparticles on the Interfacial Properties of Fiber-Reinforced-Epoxy Composites," *Compos. Part A Appl. Sci. Manuf.*, **98**, pp. 1–8.
- [73] Kothmann, M. H., Bakis, G., Zeiler, R., Ziadeh, M., Breu, J., and Altstädt, V., 2017, "Fatigue Crack Growth Behaviour of Epoxy Nanocomposites—Influence of Particle Geometry," *Springer Series in Materials Science*.
- [74] Macan, J., Paljar, K., Burmas, B., Špehar, G., Leskovic, M., and Gajović, A., 2017, "Epoxy-Matrix Composites Filled with Surface-Modified SiO₂ Nanoparticles," *J. Therm. Anal. Calorim.*, **127**(1), pp. 399–408.
- [75] Dittanet, P., and Pearson, R. A., 2012, "Effect of Silica Nanoparticle Size on Toughening Mechanisms of Filled Epoxy," *Polymer (Guildf.)*, **53**(9), pp. 1890–1905.
- [76] Bondioli, F., Cannillo, V., Fabbri, E., and Messori, M., 2005, "Epoxy-Silica Nanocomposites: Preparation, Experimental Characterization, and Modeling," *J. Appl. Polym. Sci.*, **97**(6), pp. 2382–2386.
- [77] Sun, Y., Zhang, Z., Moon, K. S., and Wong, C. P., 2004, "Glass Transition and Relaxation Behavior of Epoxy Nanocomposites," *J. Polym. Sci. Part B Polym. Phys.*, **42**(21), pp. 3849–3858.
- [78] Yohanes, and Sekiguchi, Y., 2018, "Synergistic Effects of Mixed Silica Micro-Nanoparticles on Compressive Dynamic Stiffness and Damping of Epoxy Adhesive," *J. Dyn. Behav. Mater.*, **4**(2), pp. 190–200.
- [79] Nozawa, K., Gailhanou, H., Raison, L., Panizza, P., Ushiki, H., Sellier, E., Delville, J. P., and Delville, M. H., 2005, "Smart Control of Monodisperse Stöber Silica Particles: Effect of Reactant Addition Rate on Growth Process," *Langmuir*, **21**(4), pp. 1516–1523.
- [80] Cai, Q., Lin, W.-Y., Xiao, F.-S., Pang, W.-Q., Chen, X.-H., and Zou, B.-S., 1999, "The Preparation of Highly Ordered MCM-41 with Extremely Low Surfactant Concentration," *Microporous Mesoporous Mater.*, **32**(1–2), pp. 1–15.
- [81] Yang, J., Lind, J. U., and Troglér, W. C., 2008, "Synthesis of Hollow Silica and Titania Nanospheres," *Chem. Mater.*, **20**(9), pp. 2875–2877.
- [82] Rieter, W. J., Taylor, K. M. L., and Lin, W., 2007, "Surface Modification and Functionalization of Nanoscale Metal-Organic Frameworks for Controlled Release and Luminescence Sensing," *J. Am. Chem. Soc.*, **129**(32), pp. 9852–9853.
- [83] Wong, Y. J., Zhu, L., Teo, W. S., Tan, Y. W., Yang, Y., Wang, C., and Chen, H., 2011, "Revisiting the Stöber Method: Inhomogeneity in Silica Shells," *J. Am. Chem. Soc.*, **133**(30), pp. 11422–11425.
- [84] León, L. M., Laza, M., Puchol, V., Torrents, F., Abad, C., and Campos, A., 2009, "Dynamic Mechanical Measurements of Epoxy Matrix-Silica Nanocomposites II," *Polym. Polym. Compos.*, **17**(5), pp. 313–324.
- [85] Kamran-Pirzaman, A., Rostamian, Y., and Babatabar, S., 2020, "Surface Improvement Effect of Silica Nanoparticles on Epoxy Nanocomposites Mechanical and Physical Properties, and Curing Kinetic," *J. Polym. Res.*, **27**(1).
- [86] Kang, S., Hong, S. Il, Choe, C. R., Park, M., Rim, S., and Kim, J., 2001, "Preparation and Characterization of Epoxy Composites Filled with Functionalized Nanosilica Particles Obtained via Sol-Gel Process," *Polymer (Guildf.)*, **42**(3), pp. 879–887.
- [87] Gerlach, R., Siviour, C. R., Petrinic, N., and Wiegand, J., 2008, "Experimental Characterisation and Constitutive Modelling of RTM-6 Resin under Impact Loading," *Polymer (Guildf.)*, **49**(11), pp. 2728–2737.
- [88] Gómez-del Río, T., and Rodríguez, J., 2012, "Compression Yielding of Epoxy: Strain Rate and Temperature Effect," *Mater. Des.*, **35**(C), pp. 369–373.
- [89] Naik, N. K., Shankar, P. J., Kavala, V. R., Ravikumar, G., Pothenis, J. R., and Arya, H., 2011, "High Strain Rate Mechanical Behavior of Epoxy under Compressive Loading: Experimental and Modeling Studies," *Mater. Sci. Eng. A*, **528**(3), pp. 846–854.

- [90] Miao, Y. G., Liu, H. Y., Suo, T., Mai, Y. W., Xie, F. Q., and Li, Y. L., 2016, "Effects of Strain Rate on Mechanical Properties of Nanosilica/Epoxy," *Compos. Part B Eng.*, **96**(9), pp. 119–124.
- [91] Tian, Y., Zhang, H., Zhao, J., Li, T., Bie, B. X., Luo, S. N., and Zhang, Z., 2016, "High Strain Rate Compression of Epoxy Based Nanocomposites," *Compos. Part A Appl. Sci. Manuf.*, **90**(C), pp. 62–70.
- [92] Guo, Y., and Li, Y., 2007, "Quasi-Static/Dynamic Response of SiO₂-Epoxy Nanocomposites," *Mater. Sci. Eng. A*, **458**(1–2), pp. 330–335.
- [93] Ma, P., Jiang, G., Li, Y., and Zhong, W., 2015, "The Impact Compression Behaviors of Silica Nanoparticles—Epoxy Composites," *J. Text. Sci. Technol.*, **01**(01), pp. 1–11.
- [94] Yohanes, and Sekiguchi, Y., 2017, "Effects of Mixed Micro and Nano Silica Particles on the Dynamic Compressive Performances of Epoxy Adhesive," *Appl. Adhes. Sci.*, **5**(1), pp. 1–12.
- [95] Chao, D., Gao, Y., and Frey, H., 2011, *Hyperbranched Polymers: Synthesis, Properties, and Applications*, John Wiley & Sons, Inc.
- [96] Zhang, X., 2010, "Hyperbranched Aromatic Polyesters: From Synthesis to Applications," *Prog. Org. Coatings*, **69**(4), pp. 295–309.
- [97] Suraj Belgaonkar, M., and Kandasubramanian, B., 2021, "Hyperbranched Polymer-Based Nanocomposites: Synthesis, Progress, and Applications," *Eur. Polym. J.*, **147**(February), p. 110301.
- [98] Li, S., Cui, C., Hou, H., Wu, Q., and Zhang, S., 2015, "The Effect of Hyperbranched Polyester and Zirconium Slag Nanoparticles on the Impact Resistance of Epoxy Resin Thermosets," *Compos. Part B Eng.*, **79**, pp. 342–350.
- [99] Ratna, D., and Simon, G. P., 2001, "Thermomechanical Properties and Morphology of Blends of a Hydroxy-Functionalized Hyperbranched Polymer and Epoxy Resin," *Polymer (Guildf.)*, **42**(21), pp. 8833–8839.
- [100] Morancho, J. M., Cadenato, A., Ramis, X., and Salla, J. M., 2010, "Thermal Curing and Photocuring of an Epoxy Resin Modified with a Hyperbranched Polymer," *Thermochim. Acta*, **510**(1–2), pp. 1–8.
- [101] Lv, S., Yuan, Y., and Shi, W., 2009, "Strengthening and Toughening Effects of Layered Double Hydroxide and Hyperbranched Polymer on Epoxy Resin," *Prog. Org. Coatings*, **65**, pp. 425–430.
- [102] Mezzenga, R., Boogh, L., and Manson, J. E., 2001, "A Review of Dendritic Hyperbranched Polymer as Modifiers in Epoxy Composites," *Compos. Sci. Technol.*, **61**(5), pp. 787–795.
- [103] Morancho, J. M., Cadenato, A., Ramis, X., and Salla, J. M., 2010, "Thermal Curing and Photocuring of an Epoxy Resin Modified with a Hyperbranched Polymer," *Thermochim. Acta*, **510**(1–2), pp. 1–8.
- [104] Li, S., Wu, Q., Zhu, H., Lin, Q., and Wang, C., 2017, "Impact Resistance Enhancement by Adding Core-Shell Particle to Epoxy Resin Modified with Hyperbranched Polymer," *Polymers (Basel)*, **9**(12), p. 684.
- [105] Zotti, A., Zuppolini, S., Borriello, A., and Zarrelli, M., 2019, "Thermal Properties and Fracture Toughness of Epoxy Nanocomposites Loaded with Hyperbranched-Polymers-Based Core/Shell Nanoparticles," *Nanomaterials*, **9**(3), p. 418.

Intentionally left blank

3

Quasi-static and high strain rate
testing methods

3.1. Introduction

This chapter covers the quasi-static and high strain rate testing methods used in the PhD research. Section 3.2. gives an overview of the common methods used for high strain rate testing in tension and compression, and highlights the advantages of the split Hopkinson bar technique compared the other techniques. Section 3.3 provides a theoretical background on the split Hopkinson bar technique, with the calculation of average stress, the average strain, and the strain rate in the sample. This section also briefly highlights some key concepts such as pulse shaping requirements, wave dispersion, and data processing. A detailed description of the split Hopkinson bar facility used in the PhD research is provided in section 3.4, together with the modifications made to increase the quality of the measurements. Section 3.5 gives a detailed description of the quasi-static setup used in the reference quasi-static experiments. The conclusions are summarized in section 3.6.

3.2. High strain rate testing methods: state-of-the-art

Impact rates of strain are generally considered to be within the range of 0.1 s^{-1} up to 10^6 s^{-1} , and with typical short testing durations – i.e. characteristic times – ranging from 0.1 s to 10^{-8} s , as depicted in Figure 3.1 [1]. This range can be further divided into: (a) intermediate strain rates which range from 0.1 s^{-1} to 100 s^{-1} , (b) high strain rates which range from 160 s^{-1} to 10^4 s^{-1} , and (c) very high or shock strain rates which range from 10^4 s^{-1} to 10^6 s^{-1} [1,2]. For this PhD research, the intermedial and high strain rate range are of interest, and the very high and shock strain rates are out of scope of this work. As opposed to the static and quasi-static testing conditions, the effect of inertia forces and wave propagation in the high strain rate regime cannot be ignored. The most common testing methods used at different ranges of strain rate are also shown in Figure 3.1. Servo-hydraulic and high speed servo-hydraulic machines are typically used for intermediate strain rate testing, while bar impact systems – either mechanically, gas gun, or explosives driven – are used for high strain rate testing. Important representatives in the high strain rate test category are the Hopkinson bar tests. The ultimate goal of Hopkinson bar tests is to determine the dynamic stress-strain response of the tested material. Considering the propagation of stress waves inside the specimen, even though the loading or deformation of the sample is applied in a continuous way, the stress fields in the sample evolve in a stepwise fashion as a result of wave reverberations at sample boundaries. However, if the characteristic time of the reverberations is considerably shorter than the loading duration, the stresses in the sample can be considered uniform, and a state of dynamic force equilibrium is established. In that case, the average or uniform stress in the sample can be calculated. If only few wave reverberations occur inside the material before failure, the calculation of the average stress inside the sample cannot be considered a valid representation of the sample stress, due to the lack of force equilibrium at the loading interfaces. The time required to achieve these wave reverberations is dependent on the dimensions and the material of the sample.

Testing of brittle materials, including certain polymers and composites, at high strain rates is considered challenging. Brittle materials are characterized by a very low fracture strain. Therefore, the achievement of an early dynamic force equilibrium before the sample fracture is very important to accurately measure the stresses in brittle samples. Additionally, the very small strain to failure can be difficult to measure, given the additional strains which occur in the clamps and the loading frame of conventional testing machine. In this case, local strain measurement techniques, using strain gauges or optical techniques, should be considered. Moreover, brittle polymers, are characterized by a low stress wave speed. Therefore, it can take a longer time to reach a sufficient number of reverberations in polymer samples in order to have a deformation under dynamic equilibrium conditions. As such, the selection of the testing technique to be used, the proper design of the sample geometry, and the correct establishment of dynamic force equilibrium during testing are crucial for these tests.

Additionally, during testing in quasi-static and high strain rate regimes, the mechanical work done to irreversibly deform the sample is partially converted into heat, resulting in a temperature rise of the sample material. In quasi-static regimes, the generated heat has enough time to dissipate to the surroundings, thus, isothermal test conditions can be assumed. On the other hand, high strain rate experiments typically involve adiabatic heating effects which result from the inability of the generated heat to dissipate to the surroundings due to the very short test duration, and thus, affecting the response of the material.

An overview of some of the state-of-the-art methods used in literature for tensile and compression testing at intermediate and high strain rates for polymers and composites is presented in Table 3.1. It can be seen that the most frequently used testing methods for tension and compression are servo-hydraulic machines, drop tower machines, split Hopkinson bar devices, and other variations based on the Hopkinson technique such as the crossbow bar systems. The use of these methods at the strain rates of 100 s^{-1} to 200 s^{-1} in tension, which is the strain rate range of interest in this work, tends to overlap. In the case of high strain rate compression testing, the split Hopkinson bar is the most used technique. However, servo hydraulic and drop tower systems have some inherent limitations for testing at high strain rates. One limitation is the load cell ringing, which occurs when the duration of the applied load is smaller than the response time of the load cell. This results in a wavy load signal which is inaccurate for the measurement of the applied load. It is often recommended that the minimum test duration should be at least 10 times the periodic time of a given load cell [1,3]. This, in turn, adds a limitation on the achievable strain rate [4]. In addition to the load cell ringing, the presence of several interfaces - due to clamps, machine cross head, etc.- between the sample and the load cell causes disturbance and interferences with the propagating wave. Another limitation is the difficulty in establishing a dynamic stress equilibrium. The establishment of stress equilibrium – despite being mainly dependent on the sample material and length as mentioned earlier– is also affected by the testing technique. In most high rate servo-hydraulic machines, the application of a high speed deformation is usually achieved by accelerating a metallic sleeve over a slack rod connected to the sample. This impact creates undesired oscillations which causes further system ringing and affects the state of stress equilibrium during early stages of deformation. The addition of a damping material or damper is usually proposed as a solution [4]. However, several researchers reported difficulties in

achieving a state of stress equilibrium in their tests even with damping material [3,5,6]. Furthermore, the maximum value of strain rates which could be achieved by these machines is limited, due to the relatively short length of the slack rods, and hence, limited impact speeds. Other factors which could affect the quality of the results when using servo-hydraulic machines are delays in stress-strain synchronization and data acquisition systems [1,3]. When considering the wave propagation effects for brittle polymers and composites as mentioned earlier, the accuracy of the servo-hydraulic machines becomes even more critical.

Table 3.1. Summary of the popular methods used in high strain rate testing of polymers and composites

Author	Material	Loading type	Strain rate range (s ⁻¹)	Testing method
Koerber et al. [7]	Carbon/epoxy	Tension	113 – 300	Split Hopkinson tension bar
Spronk et al. [3]	Carbon/epoxy and glass/polyamide	Tension	Up to 200	Hydraulic pulse test machine
Chen et al. [8]	Glass/epoxy	Tension	Up to 115	High speed Servo-hydraulic machine
Ou et al. [9]	Basalt/epoxy	Tension	Up to 160	Drop tower impact
Martin et al. [10]	Glass/polypropylene	Tension	Up to 437	Crossbow/bar impact system
Bernard et al. [11]	Epoxy resin	Compression	900 – 1770	Split Hopkinson pressure bar
Lu et al. [12]	Carbon/epoxy	Compression	200 – 1000	Split Hopkinson pressure bar
Schmack et al. [13]	Carbon/epoxy	Compression	Up to 70	Servo-hydraulic machine

In contrast, the dynamic split Hopkinson bar testing technique is based on different principles. In a split Hopkinson bar facility, the sample is fixed between two long bars and loaded with a mechanical wave. One bar guides the loading wave towards the sample, another bar guides the transmitted wave – which results from the interaction with the sample – away from the sample. Adequate design of the sample geometry and clamping gives rise to an early state of quasi-static equilibrium in the sample, even though it is deformed at a high speed. Additionally, straightforward strain gauge measurements of the waves travelling in the bars allow to determine the force and deformation histories imposed to the sample. As such, the split Hopkinson bar tests do not suffer from the above mentioned limitations of the servo-hydraulic machines. To summarize, when directly compared to the split Hopkinson bar technique for testing of polymers and brittle composites, the servo-hydraulic machines achieve a limited maximum values of strain rate, the stress equilibrium is not always reached, and a constant strain rate cannot be reached during deformation [5]. Therefore, the split Hopkinson bar technique can be considered the most suitable technique for characterizing the mechanical behavior of polymers and composites at high strain rates.

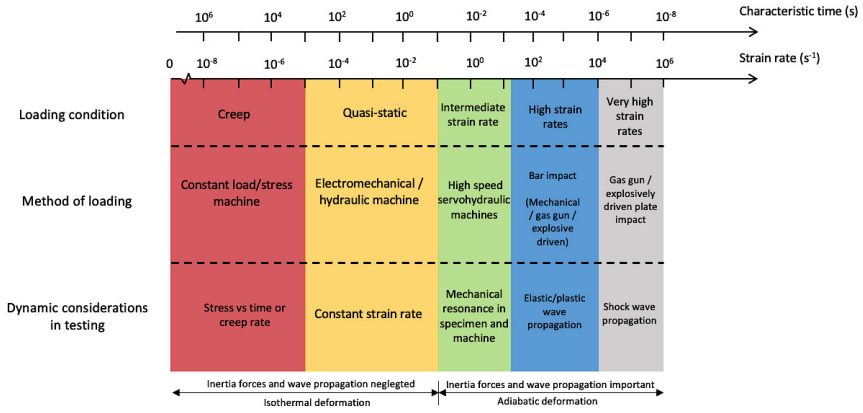


Figure 3.1. Ranges of strain rates in material testing and associated testing methods (adapted from ref. [1])

3.3. Overview of the split Hopkinson bar technique

3.3.1. Theoretical background

Kolsky pioneered the split Hopkinson bar technique in 1949 [7]. The technique was initially developed for compression testing of several materials, such as plastics, rubber, and metals. In 1983, Harding and Welsh [8] proposed the first modifications of the split Hopkinson technique for tensile testing, and introduced the technique for testing of brittle composites. A split Hopkinson bar setup typically consists of two long bars – referred to as input bar and output bar – which are free to move in the axial direction on multiple supports. The sample is placed between the input and output bar ends. An impactor is used to generate an incident dynamic stress wave (e.g. tension or compression), which travels inside the input bar to the specimen/bar interface. When the incident wave reaches the sample, it is partly reflected back into the input bar and partly transmitted to the output bar. This reflection is due to the mechanical impedance mismatch between the bars and the sample. The wave propagation inside the bars and the sample can be illustrated by a Lagrangian position-time diagram, as shown in Figure 3.2. Several stress wave reverberations take place inside the sample, so that the deformation can be considered uniform and under a state of quasi-static stress equilibrium. The required number of wave reverberations is at least three [9]. The time histories of the incident, the reflected, and the transmitted strain signals are measured using strain gauges attached on the input and output bars. The location of the strain gauges on the input bar is carefully selected so that there is no interference between the incident and the reflected waves. Time shifting from the location of the strain gauges to the specimen/bar interfaces is performed to synchronize the incident, the reflected, and the transmitted strain signals during data processing, as detailed in ref. [10].

The validity of split Hopkinson bar experiments is based on the following assumptions:

- The input and output bars remain elastic during the whole experiment. In order to guarantee the fulfillment of this assumption, the bar and specimen dimensions should be carefully selected and the bars should be made from a material with a sufficiently high yield strength relative to the specimen's material.
- The loading interfaces between the bars and the specimen guarantee a proper transfer of the dynamic loads. For compression tests, the loading interfaces of the input and output bars remain plane during the whole experiment.
- The one-dimensional elastic wave propagation theory is valid for the wave propagation in the bars. As such, wave dispersion effects are ignored, i.e. the shape of the waves does not change while travelling along the bars.
- A state of quasi-static stress equilibrium is achieved in the sample from the early stages of deformation, i.e. the forces imposed at both interfaces between the bars and the sample are equal. This assumption imposes a limitation on the length of the sample. Indeed, the time needed to establish quasi-static equilibrium can be estimated as equal to the time needed for a wave to travel three times back and forth in the sample [1,9], which depends on the wave speed of the specimen's material, and the length of the specimen.
- The friction effects at the sample/bar interface and the inertia effects in the specimen – in case of compression loading – are minimum.

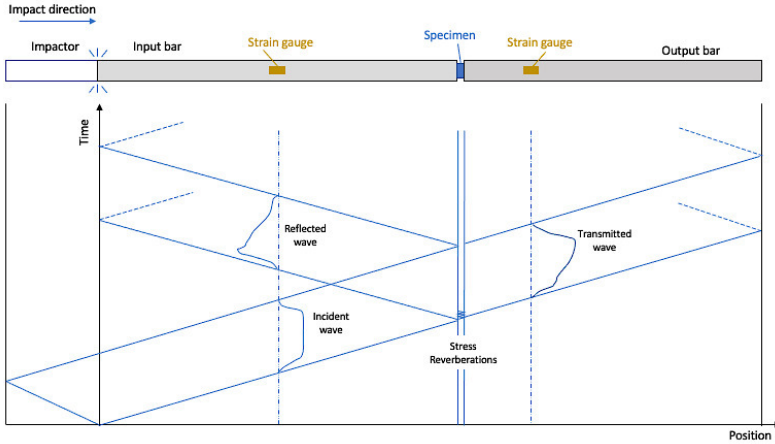


Figure 3.2. Time-position diagram of the wave propagation for a split Hopkinson bar setup

Considering a compression sample between the input and output bars, as seen in Figure 3.3, and the abovementioned assumptions, the particle velocities at the input bar/sample interface v_1 and sample/output bar interface v_2 can be determined based on the one-dimensional wave propagation theory as follows:

$$v_1 = C_b(\varepsilon_i - \varepsilon_r) \quad (3.1)$$

$$v_2 = C_b \varepsilon_t \quad (3.2)$$

Where C_b is the elastic wave speed in the bars, assuming that both bars are made from the same material. ε_i , ε_r , and ε_t are the incident, the reflected, and the transmitted strain signals measured on the bars, respectively. The elastic wave speed of the bar material C_b can be calculated based on the elastic modulus E_b and the density ρ_b of the bar material as follows:

$$C_b = \sqrt{\frac{E_b}{\rho_b}} \quad (3.3)$$

The average engineering strain rate $\dot{\varepsilon}$ and average engineering strain ε in the sample can be determined as follows:

$$\dot{\varepsilon} = \frac{v_2 - v_1}{L_s} = \frac{C_b}{L_s} (\varepsilon_i - \varepsilon_r - \varepsilon_t) \quad (3.4)$$

$$\varepsilon = \int_0^t \dot{\varepsilon} dt = \frac{C_b}{L_s} \int_0^t (\varepsilon_i - \varepsilon_r - \varepsilon_t) dt \quad (3.5)$$

Where L_s is the gauge length of the sample between the bar/sample interfaces. The stresses in the sample at the interfaces of the input bar σ_1 and the output bar σ_2 can be determined as follows:

$$\sigma_1 = \frac{A_b}{A_s} \cdot E_b (\varepsilon_i + \varepsilon_r) \quad (3.6)$$

$$\sigma_2 = \frac{A_b}{A_s} \cdot E_b \cdot \varepsilon_t \quad (3.7)$$

Where A_b and A_s are the cross section areas of the bars and the sample, respectively. Here is it assumed that both bars have the same cross section area. Since the sample is assumed to be under a state of quasi-static equilibrium, the stress at both interfaces is the same:

$$\sigma_1 = \sigma_2 \quad (3.8)$$

Using eqs. (3.6) and (3.7), the equilibrium condition can be expressed as:

$$\varepsilon_i + \varepsilon_r = \varepsilon_t \quad (3.9)$$

Based on equations (3.4), (3.5), (3.7), and (3.9), the average strain rate $\dot{\varepsilon}$, strain ε , and stress σ in the sample can be expressed as:

$$\dot{\varepsilon} = -2 \frac{C_b}{L_s} \varepsilon_r \quad (3.10)$$

$$\varepsilon = -2 \frac{C_b}{L_s} \int_0^t \varepsilon_r dt \quad (3.11)$$

$$\sigma = \frac{A_b}{A_s} \cdot E_b \cdot \varepsilon_t \quad (3.12)$$

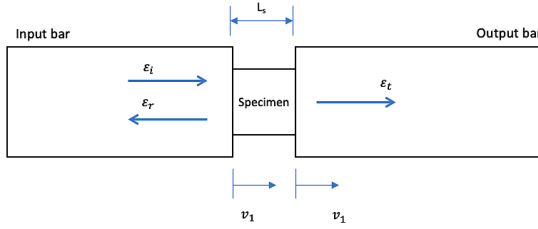


Figure 3.3. Analysis of compression experiment using the split Hopkinson bar

While the classical Hopkinson analysis presented above considered compression loading, it is also valid for tensile loading. The main differences are the method of application of load and sample clamping. In the case of a split Hopkinson tensile bar, the tensile wave can be generated either by the stored energy technique [18] – in which the input bar is clamped at a certain location, pulled and then the clamp is suddenly released – or by direct impact on a flange or an anvil attached to the end of the input bar using a pneumatic system [19,20]. Clamping of the tensile sample involves the modification of the bar interface to fix the sample either by adhesives [18,21], mechanical fixing [19,22,23], and form fit mounting [23,24]. In all cases, the additional modifications should be taken into consideration when performing the time shifting to the specimen/bar interfaces.

3.3.2. Wave dispersion and pulse shaping techniques

The stress wave which is generated from the impact of the impactor and the input bar is not ideally square. Instead, it is characterized by a very short rise time and, often, by the presence of high frequency oscillations, as seen in Figure 3.4 [10]. The presence of such high frequency oscillations is due to the complex three dimensional nature of the stress wave propagation in a long cylindrical bar, in which high frequency surface waves and radial waves are combined with the longitudinal waves. The presence of these oscillations causes wave dispersion when the wave propagates through the cylindrical bars. The wave dispersion can be clearly seen when the incident wave is compared to a reflected wave in an input bar without the output bar, see Figure 3.4. Any dispersion in the shape of the stress wave is considered a violation of the assumptions of the one-dimensional wave propagation theory, and consequently, the

Hopkinson bar analysis. Additionally, the very short rise time of the incident wave makes it difficult to achieve an early quasi-static stress equilibrium [9]. Pochhammer [25] and Chree [26] analyzed the three dimensional wave propagation in a cylindrical bar, and found that the high frequency waves lag behind the main longitudinal wave. Based on these findings, several analytical procedures for correction of wave dispersion were proposed [27–29]. Alternatively, wave dispersion effects can be experimentally reduced by reducing the high frequency components in the wave. This can be performed using a soft material – mainly copper – between the impactor and the input bar; a method generally known as pulse shaping [9,30,31]. Pulse shaping provides a longer rise time of the incident wave, which facilitates an early quasi-static equilibrium, in addition to reducing the high frequency oscillations. Nemat-Nasser et al. [32] proposed an analytical model to predict the shape of the pulsed waves and the optimum pulse shaper geometry. Alternatively, an impactor made of a soft material can be used as a pulse shaper [33], which was the approach adopted for the current research.

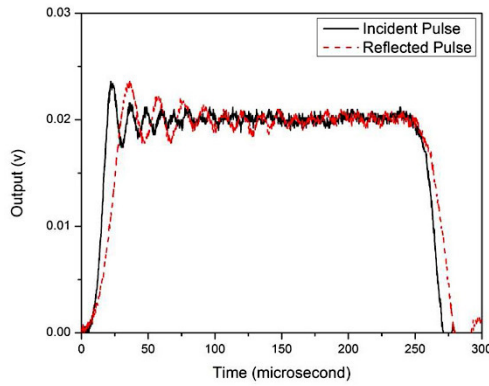


Figure 3.4. Initially rectangular incident wave after propagation in the input bar over a certain distance and reflected wave without output bar and without a pulse shaper [10]

3.4. The split Hopkinson bar facility at Ghent University

3.4.1. General description

The high strain rate dynamic experiments were carried out using the split Hopkinson tensile bar facility available at MST-DyMaLab of Ghent University, shown in Figure 3.5. This setup is a versatile setup, designed and constructed in the year 2000. It was optimized to test different materials such as advanced TRIP steels [33], titanium and titanium alloys [34], and ice [35], and to impose advanced loading conditions such as dynamic bending, strain rate jumps, and interrupted experiments [33]. The setup consists of two separate frames to reduce vibration effects; one frame supports the pneumatic impactor launching system, and the other supports the input and output bars. The setup also combines both tensile and compression loading modes in one facility. Figure 3.6 and Figure 3.7 show schematics of the tensile and compression loading configurations of the split Hopkinson bar facility, respectively.

The input and the output bars are made of high strength aluminum alloy (yield strength = 125 MPa), and have a diameter of 25 mm each. The length of the input bar is 6 m, while the length of the output bar is 3.25 m. Both bars are supported on lubricated roller supports to allow them to freely move in a horizontal position. Two momentum traps are mounted at the end of each bar to absorb the energy after impact. The tensile loading wave is generated by accelerating a cylindrical hollow impactor towards a flange at the end of the input bar, while the compression loading wave is generated by accelerating a cylindrical solid impactor towards the flange of the input bar.



Figure 3.5. The split Hopkinson bar facility at Ghent University

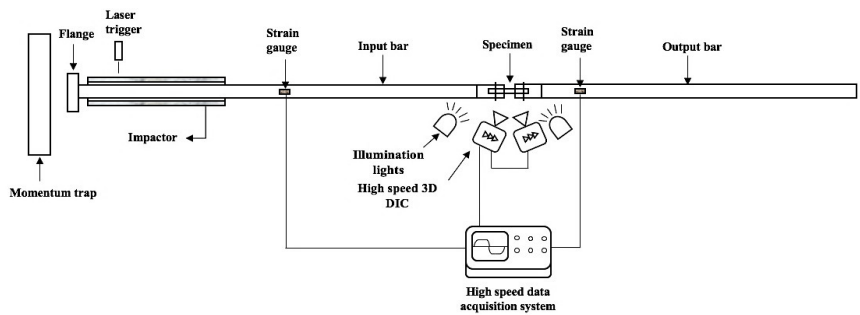


Figure 3.6. Schematic of the tensile split Hopkinson bar setup

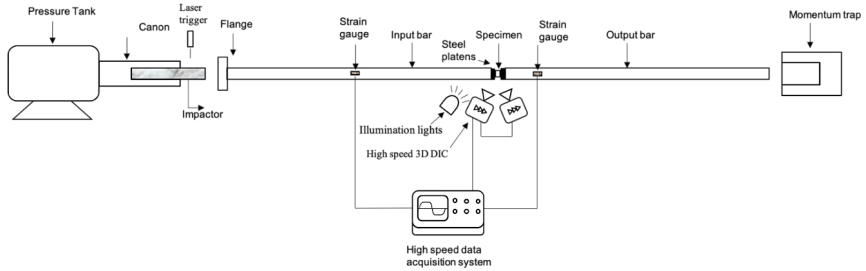


Figure 3.7. Schematic of the compression split Hopkinson bar setup

Both impactors are made of polyamide 6 (Ertalon 6 PLA), which acts as a natural pulse shaper to create a sufficiently long rising time of the loading wave in order to minimize wave dispersion effects in the bars, and to facilitate the stress equilibrium in the sample. The loading time for the tensile and compression loading waves are approx. 1.2 ms. Figure 3.8 shows a comparison between the incident and the reflected waves on the input bar using the polymer impactor in a tensile experiment, without the use of the output bar. It can be seen that both waves are nearly identical during the loading phase and are also free of high frequency oscillations. This indicates a minimum wave dispersion during the propagation of the wave in the bar. The ends of each bar at the sample interface are ground flat and parallel. Different types of end tabs – i.e., attachments, are attached to the end of the input and output bars by adhesives, in order to fix and introduce the load to the sample. These end tabs include a slot/pin end tab for tension tests, and a self-alignment attachment for compression tests. More details on the design of each end tab are given in chapter 5.

3.4.2. Strain measurement on the bars

The incident and the reflected waves were measured using two $120\ \Omega$ strain gauges (TML FLA-5-8) attached to the input bar. The transmitted wave was recorded using two $125\ \Omega$ semiconductor gauges (Kyowa KSP-2-120-E4) attached to the output bar. The semiconductor gauges are characterized by a high gauge factor of 130, in order to increase the signal-to-noise ratio compared to foil type gauges, and thus, increase the accuracy of the measured force signals, see Figure 3.9. The excitation voltage used for all strain gauges was 5 volts. It should be noted, however, that despite these advantages, the semiconductor gauges are very fragile and need extreme caution during handling and attaching to the bars. Additionally, the gauges are affected by some nonlinearity in the gauge factor and in the resistance at strain levels above $500\ \mu\text{strains}$ [36], which resulted in shifting of the signal baseline and scaling of amplitude. As such, foil type gauges were always used together with the semiconductor gauges for redundant measurement, and any difference in amplitude was corrected. These gauges are very sensitive to light, therefore, a layer of polyurethane and an opaque, putty-like coating was used to coat the semiconductor gauges. Each pair of the strain gauges on the input and the output bars was connected to a half Wheatstone bridge, as shown in Figure 3.10 (a) and (b). The gauges on both bars were attached in such a way to eliminate any possible bending waves, as shown in Figure 3.10 (c). It should be noted that the bridge connection of the semiconductor gauge –

although resulting in an unbalance of the Wheatstone bridge – helped reduce the fluctuations of the baseline signal during testing, and is implemented in this particular configuration following the guidelines of the manufacturer. The distance between the strain gauges on the input bar and the specimen/bar interface was 3275 mm, while the distance between the strain gauges on the output bar and the specimen/bar interface was 148 mm. The time histories of the strain signals on the input and output bar gauges were recorded using a high speed Gen 411 data acquisition system, at a sampling rate of 1 Ms/s and resolution of 16 bits.

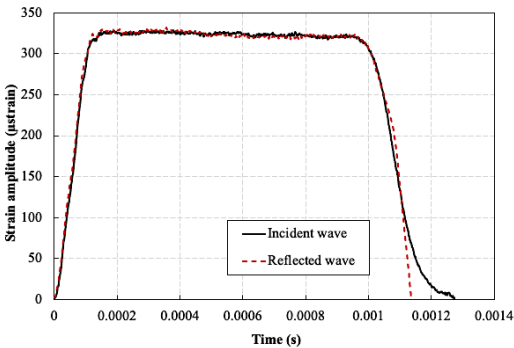


Figure 3.8. Comparison between the incident and the reflected waves with the polymer impactor

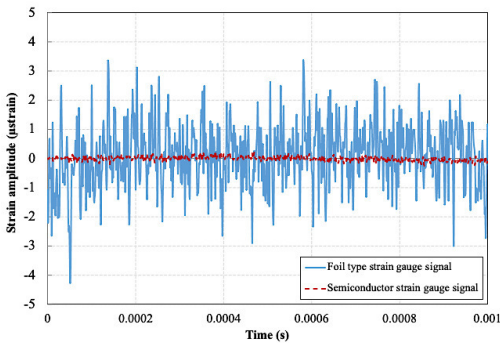


Figure 3.9. Comparison between the strain signals of the foil type and the semiconductor type strain gauges at zero load on the output bar

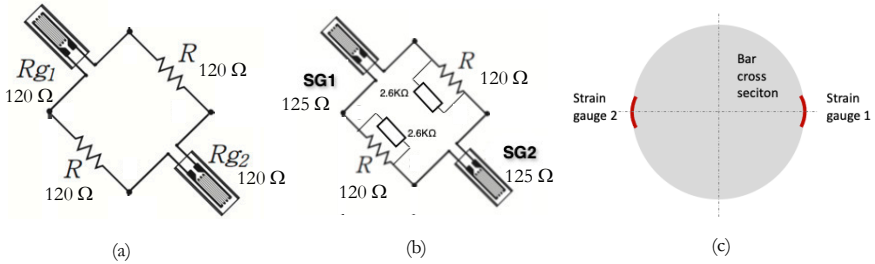


Figure 3.10. Different Wheatstone bridges configurations used: (a) half-bridge of the foil type gauges on the input bar, (b) half-bridge of the semiconductor gauges on the output bar, (c) orientation of the strain gauges on the bars

3.5. Quasi-static testing setup

Reference quasi-static experiments were performed using an Instron 5569 universal testing machine available at DyMaLab at Ghent University. The load was measured using a 50 kN load cell. A custom designed system of bars, made of steel alloy and having a diameter of 25 mm, was used to test the samples in tension and compression, as shown in Figure 3.11. The upper bar is directly connected to the load cell, while the lower bar is directly connected to the base of the testing machine. This reduces the influence of the standard – and typically heavy – grips on the small brittle samples, and keeps the same boundary conditions as in the split Hopkinson bar tests. The ends of the bars were also designed to have slotted/pinned connection and a flat connection in order to match the fixing conditions of the samples with these of the split Hopkinson bar experiments (see chapter 5 for more details).

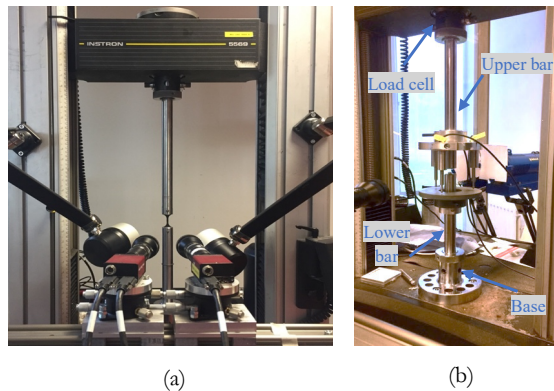


Figure 3.11. Bar systems used in quasi-static testing

3.6. Conclusions

This chapter provided an overview of the quasi-static and high strain rate testing methods used in the PhD research. The most commonly used methods for high strain rate testing at the strain rates of interest for present work – i.e. 100 s^{-1} up to 1000 s^{-1} – are servo-hydraulic machines and split Hopkinson bar setups. Unlike servo-hydraulic machines, split Hopkinson bar facilities do not suffer from the limitations of load cell ringing or of establishment of quasi-static equilibrium. Moreover, the highest strain rate that can be reached by hydraulic machines is limited to approximately 200 s^{-1} . As such, the split Hopkinson bar technique was considered the most suitable technique to test the polymers and brittle composites of present study at high strain rates. After presenting the theoretical background of the classical Hopkinson wave analysis, the split Hopkinson bar facility used in this research was described in detail. Special attention was paid to the experimental minimization of wave dispersion effects, facilitation of quasi-static equilibrium, and increasing the signal-to-noise ratio of strain measurements on the bars. The Hopkinson boundary conditions imposed to the sample, i.e., the load introduction and sample clamping, were kept the same in the quasi-static testing.

References

- [1] Nemat-Nasser, S., 2000, “Introduction to High Strain Rate Testing,” *ASM Handbook, Volume 8, Mechanical Testing and Evaluation*, H. Kuhn, and D. Medlin, eds., ASM International, pp. 427–428.
- [2] Sharpe, W. N., ed., 2008, *Springer Handbook of Experimental Solid Mechanics*, Springer US, Boston, MA.
- [3] Spronk, S. W. F., Verboven, E., Gilabert, F. A., Sevenois, R. D. B., Garoz, D., Kersemans, M., and Van Paepegem, W., 2018, “Stress-Strain Synchronization for High Strain Rate Tests on Brittle Composites,” *Polym. Test.*, **67**, pp. 477–486.
- [4] Xiao, X., 2008, “Dynamic Tensile Testing of Plastic Materials,” *Polym. Test.*, **27**(2), pp. 164–178.
- [5] Eriksen, R. N. W., 2014, “High Strain Rate Characterisation of Composite Materials,” Springer, Cham.
- [6] Daliri, A., Vijayan, A., Ruan, D., and Wang, C. H., 2017, “High Strain Rate Tensile Properties of Basalt-Fibre Reinforced Polymer Composites,” *17th Australian Aerospace Congress*, Melbourne.
- [7] Kolsky, H., 1949, “An Investigation of the Mechanical Properties of Materials at Very High Rates of Loading,” *Proc. Phys. Soc. Sect. B*, **62**(11), pp. 676–700.
- [8] Harding, J., and Welsh, L. M., 1983, “A Tensile Testing Technique for Fibre-Reinforced Composites at Impact Rates of Strain,” *J. Mater. Sci.*, **18**(6), pp. 1810–1826.
- [9] Ninan, L., Tsai, J., and Sun, C. T., 2001, “Use of Split Hopkinson Pressure Bar for Testing Off-Axis Composites,” *Int. J. Impact Eng.*, **25**(3), pp. 291–313.
- [10] Chen, W. W., and Song, B., 2013, *Split Hopkinson (Kolsky) Bar: Design, Testing and Applications*.
- [11] Koerber, H., Kuhn, P., Ploekl, M., Otero, F., Gerbaud, P. W., Rolfes, R., and Camanho, P. P., 2018, “Experimental Characterization and Constitutive Modeling of the Non-Linear Stress–Strain Behavior of Unidirectional Carbon–Epoxy under High Strain Rate Loading,” *Adv. Model. Simul. Eng. Sci.*, **5**(1), pp. 1–24.
- [12] Chen, W., Meng, Q., Hao, H., Cui, J., and Shi, Y., 2017, “Quasi-Static and Dynamic Tensile Properties of Fiberglass/Epoxy Laminate Sheet,” *Constr. Build. Mater.*, **143**, pp. 247–258.
- [13] Ou, Y., Zhu, D., and Li, H., 2016, “Strain Rate and Temperature Effects on the Dynamic Tensile Behaviors of Basalt Fiber Bundles and Reinforced Polymer Composite,” *J. Mater. Civ. Eng.*, **28**(10), p. 04016101.
- [14] Martin, A., Othman, R., and Rozycki, P., 2015, “Experimental Investigation of Quasi-Static and Intermediate Strain Rate Behaviour of Polypropylene Glass Fibre (PPGF) Woven Composite,” *Plast. Rubber Compos.*, **44**(1), pp. 1–10.
- [15] Bernard, C. A., Bahlouli, N., George, D., Rémond, Y., and Ahzi, S., 2020, “Identification of the Dynamic Behavior of Epoxy Material at Large Strain over a Wide Range of Temperatures,” *Mech. Mater.*, **143**(July 2019), p. 103323.
- [16] Lu, J., Zhu, P., Ji, Q., and Cheng, Z., 2017, “Experimental Study of In-Plane Mechanical Properties of Carbon Fibre Woven Composite at Different Strain Rates,” *Polym. Polym. Compos.*, **25**(4), pp. 289–298.
- [17] Schmack, T., Filipe, T., Deinzer, G., Kassapoglou, C., and Walther, F., 2018, “Experimental and Numerical

- Investigation of the Strain Rate-Dependent Compression Behaviour of a Carbon-Epoxy Structure,” *Compos. Struct.*, **189**(November 2017), pp. 256–262.
- [18] Gilat, A., Schmidt, T. E., and Walker, A. L., 2009, “Full Field Strain Measurement in Compression and Tensile Split Hopkinson Bar Experiments,” *Exp. Mech.*, **49**(2), pp. 291–302.
- [19] Taniguchi, N., Nishiwaki, T., Hirayama, N., Nishida, H., and Kawada, H., 2009, “Dynamic Tensile Properties of Carbon Fiber Composite Based on Thermoplastic Epoxy Resin Loaded in Matrix-Dominant Directions,” *Compos. Sci. Technol.*, **69**(2), pp. 207–213.
- [20] Xu, Y., Gao, T., Wang, J., and Zhang, W., 2016, “Experimentation and Modeling of the Tension Behavior of Polycarbonate at High Strain Rates,” *Polymers (Basel)*, **8**(3), pp. 15–63.
- [21] Eskandari, H., and Nemes, J. A., 2000, “Dynamic Testing of Composite Laminates with a Tensile Split Hopkinson Bar,” *J. Compos. Mater.*, **34**(4), pp. 260–273.
- [22] Li, X., Yan, Y., Guo, L., and Xu, C., 2016, “Effect of Strain Rate on the Mechanical Properties of Carbon/Epoxy Composites under Quasi-Static and Dynamic Loadings,” *Polym. Test.*, **52**(C), pp. 254–264.
- [23] Ledford, N., Paul, H., Ganzenmüller, G., May, M., Höfemann, M., Otto, M., and Petrinic, N., 2015, “Investigations on Specimen Design and Mounting for Split Hopkinson Tension Bar (SHTB) Experiments,” *EJ Web Conf.*, **94**, p. 01049.
- [24] Foroutan, R., Nemes, J., Ghiasi, H., and Hubert, P., 2013, “Experimental Investigation of High Strain-Rate Behaviour of Fabric Composites,” *Compos. Struct.*, **106**(C), pp. 264–269.
- [25] Pochhammer, L., 1876, “Ueber Die Fortpflanzungsgeschwindigkeiten Kleiner Schwingungen in Einem Unbegrenzten Isotropen Kreiscylinder,” *J. für die reine und Angew. Math. (Crelles Journal)*, **1876**(81), pp. 324–336.
- [26] Chree, C., 1889, “The Equations of an Isotropic Elastic Solid in Polar and Cylindrical Co-Ordinates, Their Solution and Application,” *Trans. Cambridge Philos. Soc.*, **14**, p. 250.
- [27] Gong, J. C., Malvern, L. E., and Jenkins, D. A., 1990, “Dispersion Investigation in the Split Hopkinson Pressure Bar,” *J. Eng. Mater. Technol. Trans. ASME*.
- [28] Follansbee, P. S., and Frantz, C., 1983, “Wave Propagation in the Split Hopkinson Pressure Bar,” *J. Eng. Mater. Technol. Trans. ASME*.
- [29] Li, Z., and Lambros, J., 1999, “Determination of the Dynamic Response of Brittle Composites by the Use of the Split Hopkinson Pressure Bar,” *Compos. Sci. Technol.*
- [30] Frew, D. J., Forrestal, M. J., and Chen, W., 2005, “Pulse Shaping Techniques for Testing Elastic-Plastic Materials with a Split Hopkinson Pressure Bar,” *Exp. Mech.*, **45**(2), pp. 186–195.
- [31] Vecchio, K. S., and Jiang, F., 2007, “Improved Pulse Shaping to Achieve Constant Strain Rate and Stress Equilibrium in Split-Hopkinson Pressure Bar Testing,” *Metall. Mater. Trans. A Phys. Metall. Mater. Sci.*, **38** A(11), pp. 2655–2665.
- [32] Nemat-Nasser, S., Isaacs, J. B., and Starrett, J. E., 1991, “Hopkinson Techniques for Dynamic Recovery Experiments,” *Proc. R. Soc. London. Ser. A Math. Phys. Sci.*, **435**(1894), pp. 371–391.
- [33] Van Slycken, J., 2008, “Advanced Use of a Split Hopkinson Bar Setup Application to TRIP Steels,” Ghent University.
- [34] Peirs, J., 2012, “Experimental Characterisation and Modelling of the Dynamic Behaviour of Ti6Al4V,” Ghent University.
- [35] Acx, S., 2015, “Impact Behaviour of Ice,” Ghent University.
- [36] “Characteristics of and how to use semiconductor gages”, KYOWA technical bulletin No. 1., KYOWA Electronic Instruments Co. Ltd.

Intentionally left blank

4

Development of Digital Image Correlation techniques

Parts of this chapter were rewritten based on the following article:

Elmahdy, A., and Verleysen, P., 2018, "The Use of 2D and 3D High-Speed Digital Image Correlation in Full Field Strain Measurements of Composite Materials Subjected to High Strain Rates," *Proceedings*, 2(8), p. 538. *(presented in the 18th International Conference on Experimental Mechanics, Brussels, Belgium, 2018)*

4.1. Introduction

In order to obtain a correct and reliable stress-strain curve when testing materials, accurate measurement of the local displacements and strains developing in the gauge section of the sample is of crucial importance. In particular, when split Hopkinson bar setups are used to characterize the dynamic behavior of (quasi-)brittle materials, special attention has to be paid to the strain measurement. Indeed, using the classical Hopkinson analysis to calculate the strain from the reflected wave, as will be seen in chapter 5, creates an unavoidable, though non-negligible, overestimation of the strain in a tensile sample, especially at low strains [1,2]. Due to the relatively low strain to fracture, accurate measurement of the specimen's strain directly from the classical Hopkinson analysis is therefore difficult to achieve in the case of tensile testing of brittle composites. Very often, strain gauges are used for local strain measurement on the surface of the sample [2–4]. However, strain gauges provide only average strain data, and do not provide full field strain information of the samples which might reveal strain heterogeneities – including strain localizations. Additionally, strain gauges could introduce some stress concentrations at the edges of the backing sheet, which might result in a premature failure of the brittle sample [4]. Furthermore, the use of very small strain gauges on the unavoidably small Hopkinson samples is practically very challenging, especially in terms of attaching multiple strain gauge to the sample for biaxial strain measurement and handling their delicate wiring. To overcome all these limitations, non-contact full field displacement and strain measurement techniques have been developed, such as holographic interferometry, speckle interferometry, shearography, Moiré interferometry, the grid method, and Digital Image Correlation (DIC) [5]. DIC relies on the tracking of a speckle pattern applied on the sample surface. Compared to the other full field measurement methods, DIC is considered relatively simple in terms of application and processing [5]. Additionally, the advancement of digital imaging, combined with the wide availability of high quality commercial digital cameras, allowed the DIC technique to become a mainstream experimental mechanics tool in a wide variety of applications [6–8]. Furthermore, the recent availability of commercial DIC software made it relatively easy to automate image capturing and post processing of the data. The DIC technique is capable of measuring full in-plane displacement and strain fields of planar objects with a high accuracy at a subpixel level. When used in a stereo imaging configuration, the technique is also capable of measuring the volumetric displacement and strain of virtually any irregular object under testing, including in-plane and out of plane information. However, the accuracy and precision of the displacement and strain measurements using DIC is highly sensitive to the choice of several hardware and software parameters. Sufficient attention should be paid to the selection of the suitable optical components, the calibration of the optical system, the speckling of the sample, and the selection of the post processing parameters. Concerning the latter, commercial DIC software should certainly not be used as a black box system.

This chapter covers the development of the low speed and high speed DIC setups used to measure the local displacements and strains throughout the PhD research. The critical and practical aspects of DIC experiments, which are typically not found in literature, are especially highlighted. The first part of the chapter covers the principles and theoretical background of

the digital image correlation technique and stereo vision. The overall principle of digital image correlation is described in section 4.2. The components of the DIC system such as the cameras, the speckle pattern, the subset and step sizes, the interpolation and the correlation algorithm are discussed in detail in section 4.3. The theoretical principles of stereo vision and correlation algorithms in 3D are discussed in section 4.4. The second part of the chapter covers the implementation of the theoretical concepts in the DIC systems developed for the current work. The developed DIC optical setups, calibration procedures, and processing software are described in detail in section 4.5. In section 4.6, the effect of the DIC processing parameters on the average displacement and strain noise levels for both 2D and 3D DIC systems are investigated. Additionally, a comparison between the 2D and 3D DIC systems is presented, and some remarks are given in section 4.7. The conclusions are finally presented in section 4.8.

4.2. Principles of the digital image correlation technique

DIC techniques involve several steps including iterative pattern matching, as shown schematically in Figure 4.1. Digital cameras record several images of the sample; at least one image at its initial state before the application of the load, i.e. completely static conditions at zero load, and several images during the deformation when the load is applied. The recorded image in the sample's initial state is referred to as "reference image", while the images recorded during deformation are referred to as "deformed images". The surface of the sample should have a unique randomized texture or a speckle pattern with high contrast. All recorded images are pre-processed to remove noise and obtain subpixel grey level values. During the processing of the images, a region of interest (ROI) is defined on the reference image where the displacement and strain fields are to be calculated. In the ROI of the reference image, an individual, square, group of neighboring pixels, called subset, is selected. The correlation algorithm performs an iterative matching of the subset between the reference image and every deformed image. In this iterative matching process, the algorithm searches for a group of pixels in the deformed image which matches that of the subset in the reference image, by minimizing the matching error. To increase the accuracy of this matching process, the subset is allowed to translate, deform, and change in shape. Once a matching subset is found in the deformed image, the iteration algorithm stops searching and the new position of the matched subset is registered at the subset's center. In order to obtain information in the full ROI, the initial subset is then shifted by a fixed number of pixels, called step, and the correlation algorithm reiterates the matching for the newly shifted subset. The full displacement field is obtained once the subset is shifted across the whole region of interest. After obtaining the full pixel positions of the deformed subsets in the deformed images, a straight-forward calculation of the strain field is performed. The calculated displacement field is first smoothed by a polynomial surface fit, in which a group of discrete displacement data points or a "strain window" is defined. The strain fields are finally calculated as derivatives of the displacement field. In the next section, each component and process of the digital image correlation technique will be discussed in more detail.

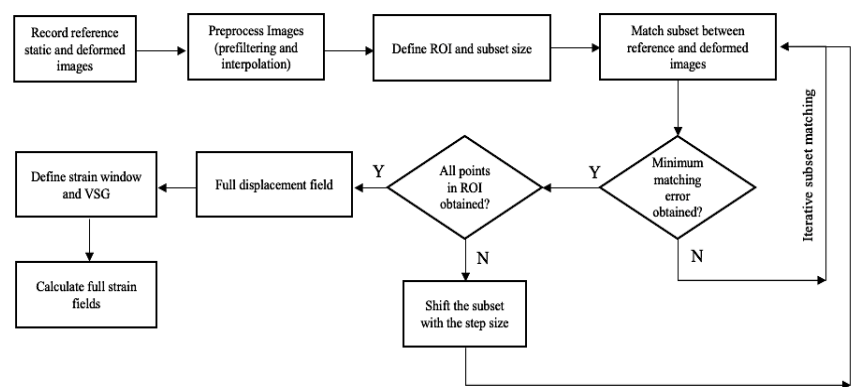


Figure 4.1. Schematic of the steps of the Digital Image Correlation technique (2D DIC)

4.3. Components of a digital image correlation system

4.3.1. Optical system

A typical DIC setup consists of a high quality digital camera, or two cameras in case of a stereo setup, which is fitted with a suitable lens and a light source directed to the speckled sample surface, as shown in Figure 4.2. Machine vision cameras are typically used for low speed testing, where a low frame rate is adequate. These cameras are usually equipped with Charge-Coupled-Device (CCD) image sensors, which are characterized by relatively low noise levels and high light sensitivity [9]. CCD sensors are generally small in size and have a high fill factor, which is the ratio between the active sensing area of the pixel to the total area of the pixel. This is due to the fact that the transistors and analog-to-digital conversion circuits are located outside of the physical pixels. This allows for packing many individual small pixels in the sensor area, which results in high image resolutions and high light sensitivity.

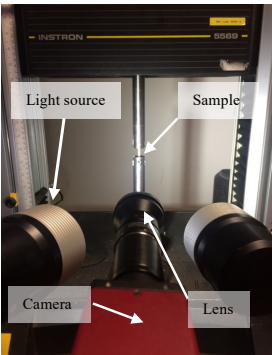


Figure 4.2. Typical DIC setup showing cameras and light source

For impact and high strain rate testing, very high frame rates (up to 100k frames per second) and a large number of recorded frames are necessary. Therefore, high speed cameras are used for such testing. These high speed cameras are generally equipped with Complementary-Metal-Oxide-Semiconductor (CMOS) image sensors. As opposed to CCD sensors, the CMOS sensors have a relatively low pixel fill factor. This is due to the presence of the transistors and analog-to-digital conversion circuits on the physical pixel. In order not to limit the light sensitivity because of the low fill factor, the pixels, and thus the sensor itself, are designed to be large in size compared to the CCD sensors. As such, only limited image resolutions (usually in the 1 megapixel range) can be obtained by these cameras. Only some ultra-high speed cameras are fitted with CCD sensors, such as rotating mirror, intensified CCD, and in-situ storage image sensor CCD. However, due to their technology, these ultra-high speed cameras usually have a very limited number of recorded frames. Additionally, they are much more expensive compared to high speed CMOS cameras. Consequently, the use of ultra-high speed cameras is outside the scope of this research work.

The selection of a camera lens is mainly dictated by the required magnification for the sample, and the mounting system of the used camera (C-mount or F-mount). Given the small size of the samples used in high strain testing using the split Hopkinson technique, a high magnification ratio is usually necessary. Based on the model of the standard simple lens system shown in Figure 4.3, the required magnification ratio M can be represented as:

$$M = \frac{\text{Image sensor size } (H)}{\text{Object size } (G)} = \frac{\text{Image distance } (h)}{\text{Object distance } (g)} \quad (4.1)$$

It can be seen from eq. (4.1) that the magnification can be increased either by reducing the object distance (which is the distance between the object and the lens), or by increasing the image distance (which is the distance between the lens and the sensor). From a practical point of view, reducing the object distance beyond a certain limit can affect the illumination of the sample, or damage the lens when the sample fractures. Increasing the image distance can be done simply by increasing the focal length of the lens, or by using extension tubes between the camera and the lens, or a combination of both. Additionally, the use of lenses with long focal length helps to reduce the in-plane strain error resulting from the out-of-plane displacement of 2D samples [10], and improves the overall accuracy of the stereo DIC systems (as will be seen in section 4.4). For the current work, only lenses with magnification ratio of at least 1:1 and focal length up to 100 mm were considered.

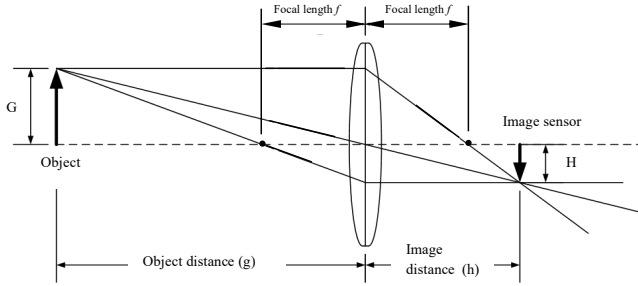


Figure 4.3. Standard simple lens model

Several sources of errors can be associated with the DIC optical components, such as random errors caused by the image sensor, and systematic errors caused by the lens distortion. The random errors caused by the image sensor are mainly caused by the signal amplification and thermal variations in the sensor [11,12]. This appears as high frequency variations in the grey levels of the individual image pixels. The camera sensor noise can be quantified by averaging several images at completely static, undeformed conditions and same lighting conditions, then calculating the standard deviation of the grey levels for all pixels [13]. This calculated standard deviation represents the camera sensor noise. The image noise can be reduced by various techniques such as image averaging and prefiltering using a gaussian low pass filter [12,14]. A kernel size of 5 pixels is considered suitable for gaussian filtering for DIC images. Larger kernel values generally increase the displacement and strain random errors [15]. Thermal variations can be reduced either by cooling the camera, or by using the cameras after a certain time interval to allow the camera to reach a thermal steady state [16].

Errors due to lens distortion result from the curvature of the glass lens. The distortion can become more pronounced in larger zoom lenses with shorter focal length and wide angle lenses. Figure 4.4 (a) shows a schematic of the distortions in an image. The position of a distorted point on an image can be divided into tangential and the radial distortion components. The radial distortion is considered more significant compared to the tangential distortion [17]. A positive radial distortion represents a barrel shape, while a negative radial distortion represents a pincushion shape, as seen in Figure 4.4 (b). Many correction techniques are available to correct for the systematic errors of the lens distortion [17,18]. For these techniques to work, a precise predefined object, i.e. a calibration target, is used to correct for the distortions (see section 4.4.2). For microscale strains, it is recommended to calibrate the cameras in 2D DIC in order to correct for the distortions [18].

It is worth mentioning that for all the DIC experiments in the PhD research, a calibration procedure was performed to correct for the distortion of the lenses. The calibration procedures will be detailed later in section 4.4.2. Additionally, the samples were placed at the middle of the field of view, and the region of interest was always taken in the gauge section of the samples in the middle of the field of view. Since the largest errors due to lens distortion are consistently present near the edges of the field of view [14,17,19], placing the sample in the middle of the field of view minimizes the errors due to the lens distortions.

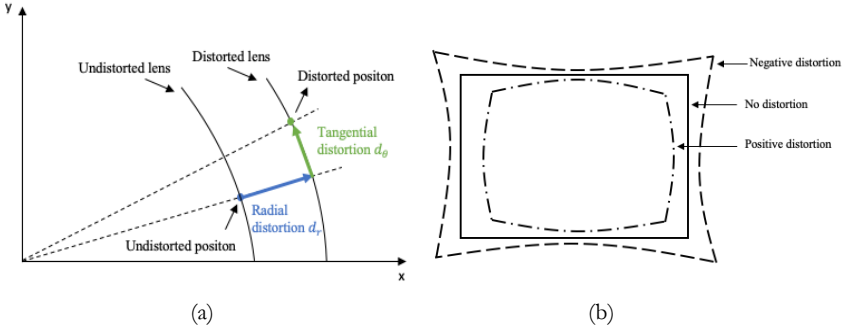


Figure 4.4. Schematic of lens distortions: (a) position of a point in a distorted image, (b) types of radial distortions (adapted from ref. [17])

4.3.2. Surface texture of the sample and speckle pattern

Tracking and matching of single pixels is virtually impossible, since the grey levels in one pixel would correspond to numerous other pixels in the recorded images. As a consequence, a group of pixels, i.e. the subset, is defined and matched instead of single pixels. Each subset should have a unique pattern, in order for it to be tracked across the different images. This can only be possible if the surface of the sample contains a natural, homogeneous, random texture. In case of the absence of such texture naturally on the sample's surface, a random pattern has to be artificially speckled on the surface of the sample. Speckling is typically performed by spraying a thin layer of black-on-white paint on the surface of the sample in order to create a high contrast pattern. Figure 4.5 shows an example of a painted random speckle pattern. It should be noted that the paint layer should fully adhere to the surface of the sample, and should be thin enough in order not to cause a deformation mismatch with respect to the sample. Therefore, careful cleaning and degreasing of the sample surface prior to the application of the paint is crucial. Matt type paints are preferred over other types of paints, as they reduce the light saturation on the sample surface.

The size of the speckle pattern is dependent on the pixel size of the image sensor. The minimum recommended size of each speckle is within the range of 3 to 5 pixels, so as not to cause under-sampling (aliasing) of the spatial signal [12,20]. This recommended size should cover both the black and white spots in the speckle pattern. Several methods can be used to quantify the size and density of the speckle pattern, such as autocorrelation [21,22] and segmentation analysis [23]. Visual qualitative analysis can also be used [23].

The speckled sample is illuminated using a non-flickering diffusive light source. Special attention should be paid to the achievement of a homogenous illumination of the speckled surface and the avoidance of saturated pixels. Grey level histograms are typically used to judge the quality of illumination of the sample, i.e. illumination intensity, contrast, and dark or saturated spots, as shown in Figure 4.6 by Hua et al. [24]

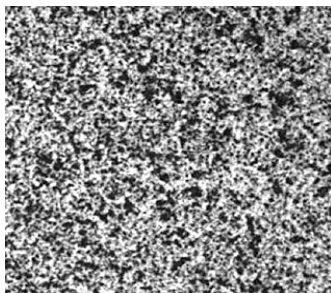


Figure 4.5. Example of a painted random speckle pattern

Figure 4.6 (b) represents the most suitable illumination and contrast conditions, since the range of grey levels covered is between 23 and 230 [21], and no saturated dark or bright pixels are present in the histogram. The histogram in Figure 4.6 (a) is an example of a shifted histogram, where the mean of the grey levels is shifted to the left, i.e., towards the darker pixels. This is due to the insufficient illumination of the speckle pattern, or due to the limitations in light sensitivity of the camera sensor, as with the case of high speed cameras at high frame rates. The histograms in Figure 4.6 (c) and (d) are examples of a scaled and shifted histogram, where the mean of the grey levels is shifted to the left or to the right, while also the contrast is scaled over a limited or large grey level range. The scaling and shifting of the grey levels can generally be mitigated by the correct choice of the correlation criterion, as will be seen in section 4.3.4.

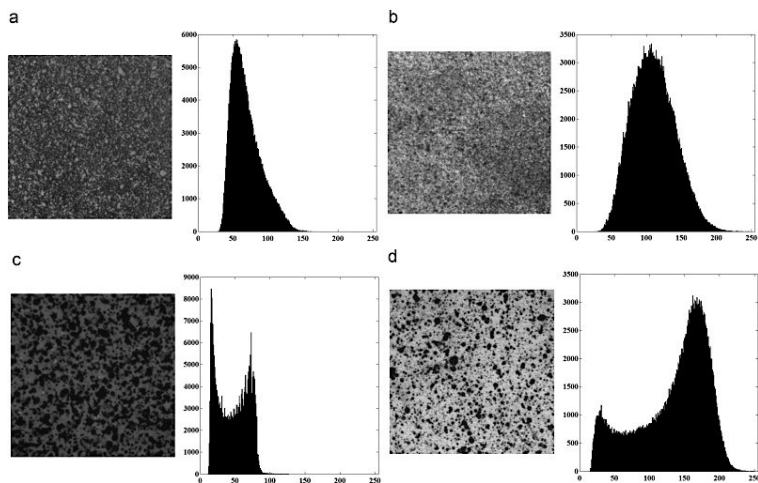


Figure 4.6. Examples of speckle patterns and corresponding grey level histograms: (a) left shifted, (b) most suitable, (c) scaled and left shifted, (d) scaled and right shifted [24]

4.3.3. Interpolation, subset size, and step size

Since the image is a discrete signal obtained from the image sensor, small displacements can take place at subpixel locations. Therefore, the continuous signal from the sensor needs to be reconstructed from the discrete image signal in order to determine the grey level values at non-integer pixel locations. This is performed using pixel interpolation.

Figure 4.7 shows an example schematic of a bilinear interpolation process. Interpolation uses the known grey level values of neighboring pixels to estimate the grey level values of the designed non-integer pixels. Several interpolants are typically used such as bilinear and bicubic polynomials and bicubic splines [25]. Since the reconstructed signal from interpolation typically follows a sinusoidal behavior, some grey level amplitude errors are associated with the interpolation process. To minimize this error, higher order interpolants are generally recommended [26], particularly higher order splines [27]. However, the computational cost of higher order interpolants is high compared to other basic interpolants. This can, indeed, be significant for high resolution images in low speed testing. Consequently, a compromise should be made between the required accuracy of the results and the computational time. For high speed images, the resolution of the image is much lower compared to the low speed case, therefore, the computational effort is not considered to be a limitation.

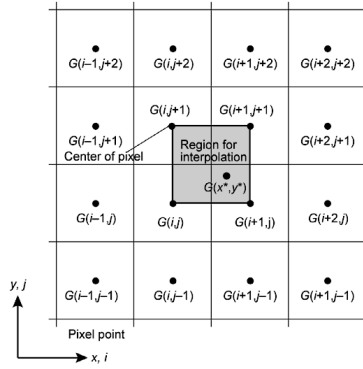


Figure 4.7. Schematic of the bilinear interpolation of grey levels between the subpixel locations [28]

Subset size is chosen so that the subset can be unique enough for correlation. On the one hand, increasing the subset size reduces the spatial resolution (which is defined as the minimum distance between any two independent data points in the full field), and small displacement and strain gradients will not be resolved. On the other hand, reducing the subset size will increase the displacement and strain random errors, i.e., noise floor [14,29]. Since the subset size is highly dependent on the speckle size, the optimum recommended subset size is 3 times the speckle size [21]. In other words, this means that the subset should contain at least three speckle features for it to be unique.

Step size is defined as the distance between the centers of each subset [30], and controls – together with the subset size – the amount of displacement and strain data points which can be calculated in the full field. The minimum allowable step size is 1 pixel [12]. Reducing the step size will increase the number of data points to construct the displacement and strain fields, however, at the expense of the computational effort and with relatively high noise levels [14]. On the other hand, increasing the step size will reduce the errors in displacement and strain estimations, however, at the expense of the number of available data points for full field construction.

4.3.4. Correlation criteria and subset matching

In order to match the subset between the reference image and the deformed image, the subset is allowed to, at least, translate in a rigid motion, rotate, and deform in normal and shear directions. If only rigid translations are considered for a subset that also deforms in shape, decorrelation will occur. A subset shape function is used to describe the deformation of the subset in the subsequent deformation images. This subset shape function should be able to describe the imposed displacement gradient on the sample, otherwise, decorrelation or biases can also occur. Figure 4.8 shows a general state of deformation of a subset, where the position of center of the reference subset P is moved to a new position P^* . The points Q and Q^* represent arbitrary points on the reference and the deformed subsets, respectively. The translation and deformation of the subset based on a first order (affine) polynomial shape function can be represented as follows [31]:

$$\begin{bmatrix} \zeta \\ \eta \end{bmatrix} = \begin{bmatrix} x_i \\ y_i \end{bmatrix} + \begin{bmatrix} u \\ v \end{bmatrix} + \begin{bmatrix} \frac{\partial u}{\partial x} & \frac{\partial u}{\partial y} \\ \frac{\partial v}{\partial x} & \frac{\partial v}{\partial y} \end{bmatrix} \begin{bmatrix} \Delta x \\ \Delta y \end{bmatrix} \quad (4.2)$$

Where ζ and η are the horizontal and vertical coordinates, respectively, of the center of the deformed subset P^* , x_i and y_i are the horizontal and vertical coordinates, respectively, of the undeformed subset, u and v are the horizontal and vertical translations, respectively, of the subset center P , $\frac{\partial u}{\partial x}$ and $\frac{\partial v}{\partial y}$ are normal strain components of the deformed subset, $\frac{\partial u}{\partial y}$ and $\frac{\partial v}{\partial x}$ are shear strain components of the deformed subset, Δx and Δy are the horizontal and vertical distances, respectively, measured from the subset center P to an arbitrary point Q within the undeformed subset area.

Higher order polynomial shape functions can also be used, however, they can be computationally intensive during correlation [21]. Additionally, second order polynomial shape functions are usually associated with large random errors in case of undermatched or overmatched subsets at the same subset size [32,33]. This can significantly affect the displacement results, especially in the low deformation range. Therefore, the first order polynomial shape function represents a good compromise between the computational effort and the correct representation of the deformation of general objects at relatively low strains [29,32,34]. However, it should be noted that optimizing the subset shape function for reducing

the displacement and strain random errors also compromises the spatial resolution, i.e., detection of large deformation gradients in the full field. As such, this recommendation is only valid when very small displacement and strain gradients are expected.

The best match between the deformed and undeformed subsets can be achieved by minimizing a cost function or a correlation criterion. The zero-mean normalized sum of square differences ZNSSD and the zero-mean normalized cross correlation ZNCC are the most used correlation criteria for DIC algorithms [21,31,35]. Unlike the classical correlation criteria such as normalized cross correlation and sum of square differences, the zero-mean normalized criteria takes into account the scaling of the grey levels (due to difference in contrast) and the shifting of the grey levels (due to difference in lighting) between the deformed and the undeformed images [21,36]. Compared to the ZNSSD correlation criterion, the ZNCC correlation criterion is characterized by a complex and time consuming calculation of their derivatives, which are required for the complete correlation algorithms [21]. Therefore, the ZNSSD correlation criterion is typically preferred over the ZNCC correlation criterion.

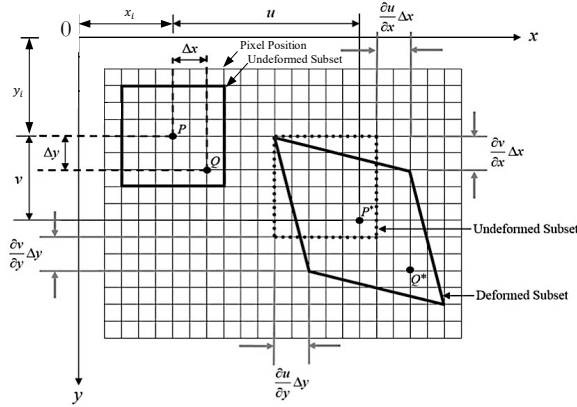


Figure 4.8. General state of deformation of a subset (adapted from Khoo et al. [31])

Considering an undeformed image F having n number of pixels, and a deformed image G with the same number of pixels, the zero-mean normalized sum of square differences ZNSSD correlation criterion can be expressed as follows [21]:

$$\chi^2_{ZNSSD} = \sum \left(\left(\frac{\sum \bar{F}_i \bar{G}_i}{\sum \bar{G}_i^2} G_i - \bar{G} \frac{\sum \bar{F}_i \bar{G}_i}{\sum \bar{G}_i^2} \right) - F_i + \bar{F} \right)^2 \quad (4.3)$$

Where χ^2_{ZNSSD} is the correlation parameter to be minimized, and the subscript i indicates the pixel in the subset. The terms \bar{F}_i and \bar{G}_i are expressed as:

$$\bar{F}_i = F_i - \bar{F} = F_i - \frac{\sum F}{n} \quad (4.4)$$

$$\bar{G}_i = G_i - \bar{G} = G_i - \frac{\sum G}{n} \quad (4.5)$$

The subset matching process is divided into two subsequent processes: coarse correlation and fine correlation. In the coarse correlation, the subset is only considered to be under rigid translation, i.e. only the zero degree polynomial part of the subset shape function in eq. (4.2) is considered. An initial guess of the horizontal and vertical translations (u and v) of the deformed subset is performed based on rigid translation after the minimization of the correlation coefficient. The fine correlation is performed using local optimization methods such as Newton-Raphson algorithm and Levenberg-Marquardt algorithm [12,35,37]. These algorithms also consider the normal and shear deformations of the subset based on the initial guess from the coarse correlation. The Levenberg-Marquardt algorithm is generally preferred over the Newton-Raphson algorithm, since it provides a better convergence performance without additional computational cost [35].

4.3.5. Strain calculation

The strain field can be directly obtained from the displacement field by calculating the deformation gradient, which contains the derivatives of the measured displacement fields. However, since the measured displacement field has inherent random errors, these errors will be amplified by differentiation, and hence, strain fields with large errors. Therefore, the measured displacement field is smoothed before calculating the strains. Local polynomial least square fitting, such as bilinear, quadratic, and biquadratic Lagrange polynomials, are usually used for surface fitting and smoothing of the displacement field [28,38]. The polynomial least square function considers a certain group of discrete displacement points called strain window, in which the fitting takes place.

Considering a quadratic quadrilateral polynomial, the horizontal displacement $u(x_i, y_i)$ and the vertical displacement $v(x_i, y_i)$ can be expressed as follows:

$$u(x_i, y_i) = a_u + b_u x_i + c_u y_i + d_u x_i^2 + e_u x_i y_i + f_u y_i^2 + g_u x_i^2 y_i + h_u x_i y_i^2 \quad (4.6)$$

$$v(x_i, y_i) = a_v + b_v x_i + c_v y_i + d_v x_i^2 + e_v x_i y_i + f_v y_i^2 + g_v x_i^2 y_i + h_v x_i y_i^2 \quad (4.7)$$

Where x_i and y_i are the pixel positions of the nodal displacement points in the strain window. Higher order polynomials can also be used, however, at the expense of the computational effort.

Based on eqs. (4.6) and (4.7), the deformation gradient \mathbf{F} can be calculated as follows [39]:

$$\mathbf{F} = \begin{bmatrix} 1 + \frac{\partial u(x_i, y_i)}{\partial x_i} & \frac{\partial u(x_i, y_i)}{\partial y_i} \\ \frac{\partial v(x_i, y_i)}{\partial x_i} & 1 + \frac{\partial v(x_i, y_i)}{\partial y_i} \end{bmatrix} \quad (4.8)$$

Based on the deformation gradient in eq. (4.8), the strain fields can be calculated based on various strain definitions such as Hencky ε^{Hencky} or the Biot undeformed $\varepsilon^{Biot\ undeformed}$ as follows [40]:

$$\varepsilon^{Hencky} = \ln(\sqrt{\mathbf{F}^T \cdot \mathbf{F}}) \quad (4.9)$$

$$\varepsilon^{Biot\ undeformed} = \sqrt{\mathbf{F}^T \cdot \mathbf{F}} - 1 \quad (4.10)$$

A more unified quantity which combines the strain window, the subset size, and the step size can be defined as the virtual strain gauge *VSG*. The virtual strain gauge size can be expressed as follows [41,42]:

$$VSG = \text{stepsize} \times (\text{strain window} - 1) + \text{subset size} \quad (4.11)$$

In a physical sense, the virtual strain gauge can be analogous to a physical strain gauge which is shifted along the region of interest to measure discrete strain points at its center. The virtual strain gauge size can directly affect the sensitivity of the strain fields to large strain gradients. Similar to the subset size behavior, larger virtual strain gauge size will result in a smoother strain field, and hence, less sensitivity to strain gradients. On the other hand, small virtual strain gauge size will result in better sensitivity to the strain gradients, but also higher random errors.

4.4. Stereo digital image correlation

Stereo DIC (or 3D DIC) is considered an extension to DIC, where 2 cameras are used simultaneously to generate a three-dimensional deformation map of the sample based on 2 images of different perspectives. As such, the same concepts of optical components, cameras, lenses, and speckle pattern which are discussed in the previous sections for the 2D DIC remains valid for the 3D DIC. The stereo DIC can overcome some of the limitations of the 2D DIC. For instance, the 2D DIC is well suited for flat sample, and requires the camera to be perfectly perpendicular to the sample, otherwise, errors could occur due to the lack of perpendicularity [39]. A well calibrated stereo setup can accurately measure the 3D position of a point in space, without the need for perfect perpendicularity of the cameras. Additionally, small out-of-plane displacements in case of 2D DIC can create apparent biaxial displacements when the sample is moving towards or further away from the camera, which can be a major source of error [10]. The 3D DIC can separate the in-plane displacement measurement from the out-of-plane measurements, and provided accurate in-plane strain fields which are not contaminated by the out-of-plane displacement effects [14]. Among the limitations of the 3D

DIC system are the higher initial cost, since at least two identical cameras and lenses need to be used. Moreover, on top of the standard 2D errors, additional errors are built-up due to calibration and triangulation.

Figure 4.9 shows the steps of the 3D DIC correlation. Two major differences can be seen when comparing the 3D correlation steps to the 2D correlation steps in Figure 4.1. The first difference is the calibration of the stereo test setup to obtain its intrinsic and extrinsic parameters, and quantification of the lens distortion. The second difference is the extended correlation, which includes the reconstruction of the 3D shape of the sample before and after deformation prior to calculating the full displacement field. In the next subsections, each of these differences will be discussed in more detail.

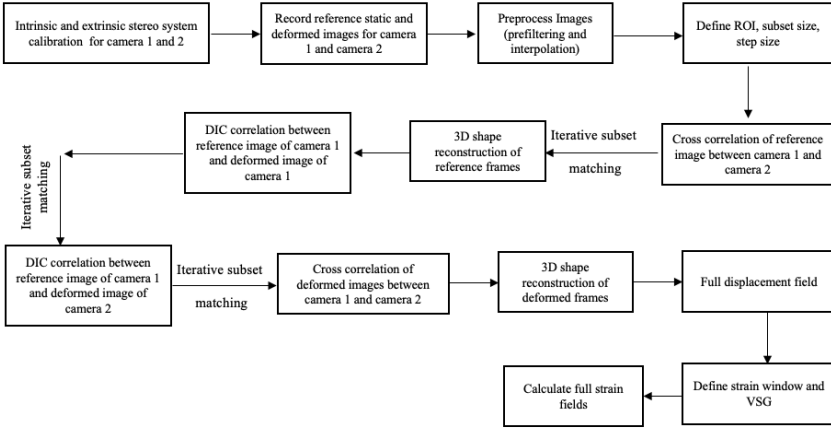


Figure 4.9. Schematic of the steps of 3D DIC

4.4.1. Basics of stereo vision and triangulation

Figure 4.10 shows the epipolar geometry for stereo vision based on the pin-hole camera model. The yellow triangle represents the epipolar plane, whose vertices include the point of interest X to be measured in 3D, and the symmetric optical centers O_L and O_R of both the left and the right cameras, respectively. The optical center represents the center point of both the camera sensor and the lens. Each camera observes a perspective projection of the point of interest X on each camera image plane, where X_L represents the perspective projection of point X on the left image plane and X_R represents the perspective projection of point X on the right image plane. The epipolar plane intersects both image planes in the epipolar lines $X_L e_L$ and $X_R e_R$, respectively. The two points e_L and e_R are referred to as epipoles, which both lie on the line $O_L O_R$ that connects both optical centers of both cameras. For the left camera image plane, the line $O_L X$ is observed as a single point, where points O_L , X_L , and X coincide on top of each other. However, the right camera image plane observes the line $O_L X$ as a line, which has a perspective projection on the right camera image plane as the epipolar line $X_R e_R$.

For each change in the 3D position of point X , a unique epipolar line is formed on the right camera image. If the position of point X_L on the left image plane is known, and the epipolar line $X_R e_R$ is known, then all other points which lie on the line $O_L X$ can also be seen as separate points coinciding on the epipolar line $X_R e_R$. This condition is referred to as the epipolar constraint. Moreover, if the positions of the optical centers of both cameras O_L and O_R are known, and the positions of both points X_L and X_R in their respective imaging planes are known, then the lines $O_L X_L$ and $O_R X_R$ should intersect at the point of interest X . This process is referred to as the triangulation, which is determined by the calibration of the stereo vision system.

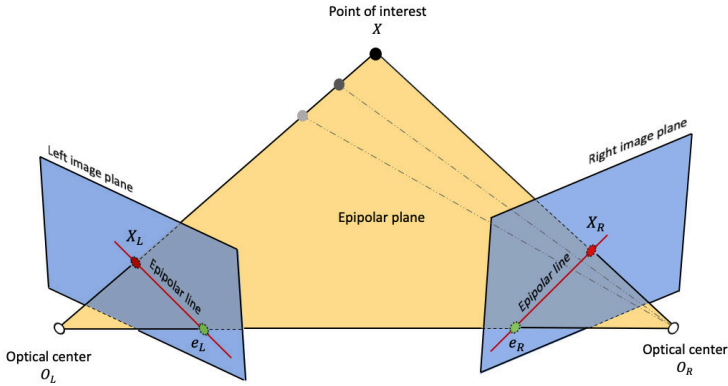


Figure 4.10. Schematic of the epipolar geometry for stereo vision

4.4.2. Calibration for stereo vision

The calibration for stereo vision allows the triangulation of the measurement point of interest on the deforming sample, which is translated into a set of intrinsic and the extrinsic camera parameters. In its simplest form, the calibration procedure translates and rotates a global coordinate system that is present at the point of interest to the respective local coordinate systems of each camera. This is performed by identifying the position of each camera with respect to the global coordinates and with respect to each other. Figure 4.11 shows a schematic of the different coordinate systems in a stereo setup, with the associated translations and rotations of the global coordinate system.

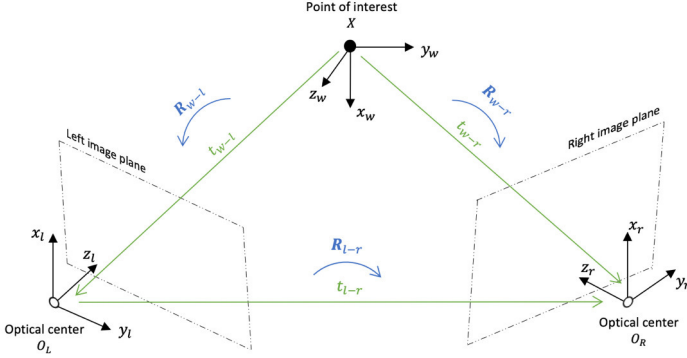


Figure 4.11. Schematic of the coordinate systems in the stereo setup

For a combined stereo system, the cameras are connected in a master/slave configuration. The determination of the local coordinates of the master camera is then performed with respect to the global coordinate system. The local coordinates of the slave camera is determined with respect to the master camera. The local coordinates of the master camera x_l, y_l, z_l and the slave camera x_r, y_r, z_r can be expressed in terms of the global coordinates x_w, y_w, z_w as follows [21]:

$$\begin{pmatrix} x_l \\ y_l \\ z_l \end{pmatrix} = [\mathbf{R}_{w-l}] \begin{pmatrix} x_w \\ y_w \\ z_w \end{pmatrix} + (t_{w-l})$$

$$\begin{pmatrix} x_r \\ y_r \\ z_r \end{pmatrix} = [\mathbf{R}_{l-r}] \begin{pmatrix} x_w \\ y_w \\ z_w \end{pmatrix} + (t_{l-r})$$

Where \mathbf{R}_{w-l} is the rotational matrix from the global coordinates to the local master camera coordinates, and \mathbf{R}_{l-r} is the rotational matrix from the local master camera coordinates to the local slave camera coordinates. The vector t_{w-l} is the translation vector from the global coordinates to the local master camera coordinates, and the vector t_{l-r} is the translation vector from the local master camera coordinates to the local slave camera coordinates. The rotational and translation matrices are called the extrinsic camera parameters.

To establish the global coordinates, a flat calibration target is typically used, based on the methodology of Zhang [43]. Figure 4.12 shows an example of a calibration target. The calibration target is made of a grid of a certain number of identical dots, which are equidistant by an accurate pitch. Additionally, the grid contains 3 distinct hollow markers, which represent the origin, the x_w axis and the y_w axis of the global coordinates. The z_w is taken perpendicular to the calibration target. The calibration target should be large enough to cover the field of view. During the calibration procedure, the target is carefully manipulated in different positions and several images are subsequently recorded. These positions are a result of translation movements along the $x_w - y_w$ plane, and rotation movements along the x_w and y_w axes of the global coordinates. The manipulation typically covers the field of view and the

depth of field required by the test. It should be noted that the calibration target should be held steady during the recoding of the calibration images. Additionally, all the calibration dots – including the 3 distinct hollow markets - should remain in focus during calibration. This becomes very important and challenging with very small targets and field of views. The depth of field is controlled by adjusting the aperture of the lens. In addition to the determination of the triangulation parameters of the stereo vision system, the calibration also allows to determine the intrinsic parameters of each camera. These parameters include the focal lengths and distortion coefficients of each camera, and the optical centers of each image plane.

Using the bundle adjustment technique [21] and the Levenberg-Marquardt global optimization algorithm to minimize the error between the measured coordinates and a predicted triangulation model, the intrinsic and extrinsic stereo system parameters can be obtained. These parameters are the following [39]:

- $C_{x(i)}$ and $C_{y(i)}$: which are the coordinates of the center of the image plane for each camera (i) in pixels, where (i) being camera 1 or camera 2,
- $f_{x(i)}$ and $f_{y(i)}$: which are the focal lengths in pixels of each camera (i) in the horizontal and vertical directions (coordinates of the focal point),
- k_1, k_2, k_3 : which are the radial distortion coefficients,
- t_x, t_y, t_z : which are the translations from the master camera coordinates to the slave camera coordinates,
- θ, ϕ, ψ : which are the rotations of the slave camera coordinates to the master camera coordinates.

The theoretical details of the calibration process and the calibration optimization can be found in reference [21]. It should be noted that changing the relative position of the cameras or the stereo system after calibration would result in the lack of triangulation, and thus, significant displacement and strain errors.

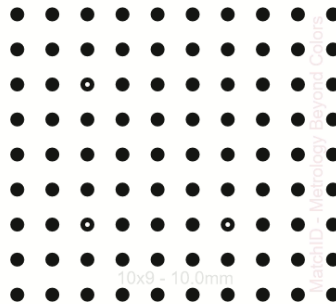


Figure 4.12. Example of a flat calibration target

An important parameter in the stereo calibration procedure is the stereo angle ϕ , which is the angle enclosed between the camera lines intersecting at the calibration target. The selection of the stereo angle directly influences the in-plane and out-of-plane measurement resolutions [44]. Smaller stereo angles generally provide a higher in-plane measurement resolution and a lower out-of-plane measurement resolution, whereas larger stereo angles increase the out-of-plane measurement resolution at the expense of the in-plane measurement resolution. Therefore, it is generally recommended that the stereo angle lies within the range of 10° and 35° for the best combination of in-plane and out-of-plane measurement resolutions [21,42].

Furthermore, the focal length of the lens also affects the stereo angle, and hence, the final measurement quality. When wide angle/short focal length lenses are used, larger stereo angles are also required in order to achieve the same out-of-plane error levels as in long focal length lenses [42]. The large stereo angle will limit the available depth of field and increase the relative perspectives of the camera, and hence, portions of the field of view will not be in focus. This will eventually limit the usable region of interest in the image. On the other hand, long focal length lenses can allow for smaller stereo angles without increasing the measurement errors, while also achieving a better depth of field [42]. Figure 4.13 illustrates the relationship between the stereo angle, the focal length of the lens, and the field of view on the sample surface.

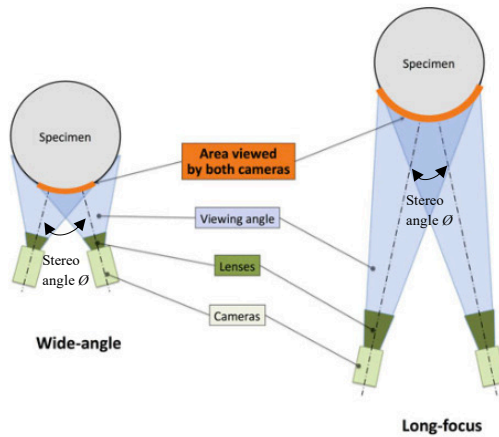


Figure 4.13. Relationship between the stereo angle, the focal length of the lens, and the field of view on the sample surface (adapted from ref. [12])

4.4.3. Correlation in 3D

The correlation in 3D DIC involves the reconstruction of the 3D shape of the measured sample before the calculation of the displacement and strain fields. This is performed by a combination of 2D subset correlation between the undeformed and the deformed images, and a subset cross correlation between both cameras to obtain depth information.

The procedure of 3D DIC correlation of several rectified images of a deforming sample from a master/slave stereo camera system is illustrated in Figure 4.14. The correlation is achieved by the following steps [18]:

1. A subset is selected on the rectified image of the undeformed sample (reference image) of the master camera. Using a simple subset shape function, the grey levels of this subset is matched in the rectified image of the slave camera such that the error in cross correlation criterion is minimum. From the calibration and the triangulation information of the stereo system, the position of the center of the subset in 3D space can be determined. This step is repeated for whole region of interest (i.e. shifting the subset with a step size) until a full 3D shape of the undeformed sample (x_0, y_0, z_0) is reconstructed.
2. The same subset from step 1 is matched between the rectified reference image of the master camera and the rectified deformed image of the master camera through a standard 2D correlation. The grey levels of the subset are matched such that the error in the ZNSSD correlation criterion is minimum. This results in the calculation of the center of the deformed subset in camera 1 perspective.
3. The same subset from step 1 is matched between the rectified reference image of the master camera and the rectified deformed image of the slave camera through a cross correlation. The grey levels of the subset are matched such that the cross correlation error is minimal. This results in the calculation of the center of the deformed subset in camera 2 perspective.
4. Using the centers of the deformed subset in camera 1 and camera 2 perspectives, and from the calibration and triangulation information of the stereo system, the position of the center of the deformed subset in 3D space can be determined. The steps 2, 3, and 4 are repeated for the whole region of interest until a 3D shape of the deformed sample (x_f, y_f, z_f) is reconstructed.
5. From the undeformed and the deformed 3D shape of the sample, the displacement field (u, v, w) can be obtained by subtracting the undeformed shape (x_0, y_0, z_0) from the deformed shape (x_f, y_f, z_f) . The obtained displacement field will then be represented by a 3D cloud of displacement data points. The same steps from 2 to 5 are repeated until the fracture of the sample to obtain its complete deformation history.

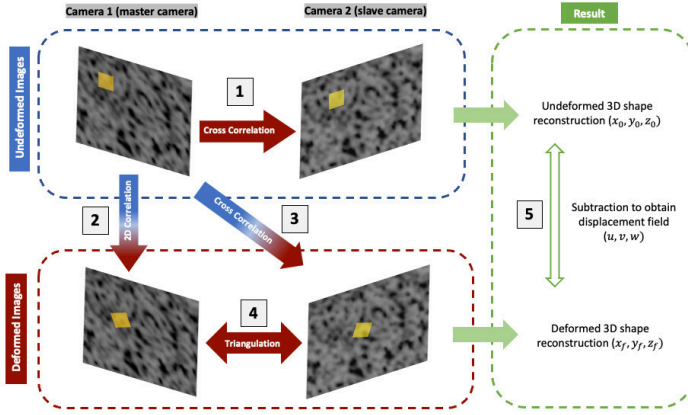


Figure 4.14. Schematic of the 3D correlation steps (adapted from Lava et al. [18])

From the calculated displacement field, the calculation of the strain can be done in a straightforward way as explained in section 4.3.5. The following steps summarize the calculation of the strain fields based on the 3D displacement points [21,45]:

1. A strain window is defined, consisting of a set of discrete 3D displacement points. A least square fit is applied to this strain window, where the strain at the center of the strain window is determined.
2. A set of local coordinates are established at the center of the strain window, which lies within a plane drawn tangent to the 3D surface at the center of the strain window.
3. The coordinates of the 3D displacement point based on the global coordinates at the center of the strain window are transformed to the local coordinate system at the center of the strain window.
4. Steps 1, 2, 3 are repeated in order to generate the complete strain field in 3D.

4.5. Development of low and high speed 2D and 3D DIC systems

Based on the theoretical concepts and principles of DIC elaborated in sections 4.2, 4.3 and 4.4, 2D and 3D DIC systems were developed for static and dynamic tests. Details on both setups and processing parameters are given in the sections below.

4.5.1. Low speed DIC setups

The low speed DIC setup in its 3D configuration consisted of two identical monochromatic 5 megapixel cameras (Allied Vision Stingray F-504b) connected in a master/slave configuration. The cameras could record images with a resolution of 2452 pixel \times 2056 pixels with an acquisition rate up to 9 images/s. The sensor of each camera was a 14-bit CCD sensor (Sony ICX655), with a physical pixel size of 3.45 μm \times 3.45 μm . The cameras were fitted with two identical low distortion c-mount fixed focus lenses (supplied by Edmund optics), having

a focal length of 100 mm each. Several extension tubes were used iteratively in combination with the lens in order to adjust the focus of each camera according to the tested sample. Extension tubes allow to focus on objects that are closer to the camera and to achieve a greater magnification by increasing the distance between the sensor to the lens. Each camera was securely mounted on a precision tilting head for adjusting the orientation. The complete setup was mounted on a rigid beam with tripod. Two high intensity LED lamps were used to illuminate the samples. The captured images from the camera, and other types of measurement signals such as strain gauge signal or LVDT signals were synchronized with the force signal obtained from the load cell of the testing machine using a NI 9215 data acquisition card. Figure 4.15 shows the components of the low speed 3D DIC setup. For the 2D DIC setup, only one camera is used while maintaining the same setup and signal synchronization. For all experiments in the PhD research where low speed DIC was used, samples were always placed at the middle of the field of view to minimize the errors due to lens distortion.

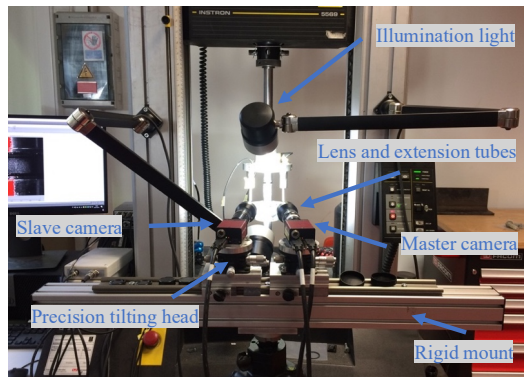


Figure 4.15. Components of the low speed 3D setup

For all samples tested using the low speed DIC systems, the speckle pattern was applied using airbrush technique with matt acrylic-based airbrush black and white paints (supplied by Golden Artists Colors, Inc., high flow titanium white PW6 and carbon black PBK7). The airbrush technique allowed to achieve a very small speckle size, which is suitable for the small pixel sizes and high resolution of the low speed DIC cameras. All the images recorded with the low speed DIC systems were exported in 8-bit resolution for post-processing.

4.5.2. High speed DIC setups

The high speed DIC setup in its 3D configuration consisted of two identical Photron mini AX200 high speed cameras configured in a master/slave configuration. These cameras are characterized by a high light sensitivity of ISO 40,000, and are capable of image acquisition speeds up to 900,000 frames per second. However, the image resolution is inversely proportional with the acquisition speed. The highest image resolution of 1024 pixels \times 1024 pixels can be achieved up to an acquisition speed of 6,400 frames per second, while the lowest image resolution of 128 pixels \times 16 pixels is achieved at 900,000 frames per second. The sensor

of each camera was a 16-bit CMOS sensor with a physical pixel size of $20\text{ }\mu\text{m} \times 20\text{ }\mu\text{m}$ with a fill factor of 58%, covering a grey level range from 0 to 65536. The cameras were fitted with two identical low distortion f-mount Tamron fixed focus lenses, which had a true 1:1 magnification, and a focal length of 90 mm each. Each camera was securely mounted on a precision geared tripod head for adjusting the orientation, and the complete setup was mounted on a rigid column. Figure 4.16 shows the components of the high speed 3D DIC system mounted on top of the split Hopkinson bar. Two high intensity Dedocool lamps were used to illuminate the samples. The exposure signal of the slave camera sensor and other measured signals (such as the strain gauge signals measured on the sample) were synchronized with the measured strain signals on the bars using a HBM high speed data acquisition system. Similar to the low speed DIC case, only one high speed camera was used in the high speed 2D DIC configuration, while maintaining the same setup and signal synchronization. A fan was also used to cool the high speed cameras, and was positioned in a way so as not to influence the stability of the system or affect the samples.

For all samples tested using the high speed DIC systems, the speckle pattern was applied using acrylic based aerosol matt white and matt black paints (supplied by Ambersel, Ral 9010 and Ral 9011, respectively). The aerosol technique allowed to achieve a sufficiently large speckle size, which is suitable for the large pixel sizes and limited resolution of the high speed DIC cameras. All the images recorded with the high speed DIC systems were exported in 8-bit resolution for post-processing. For all experiments in the PhD research where high speed DIC was used, samples were always placed at the middle of the field of view to minimize the errors due to lens distortion.

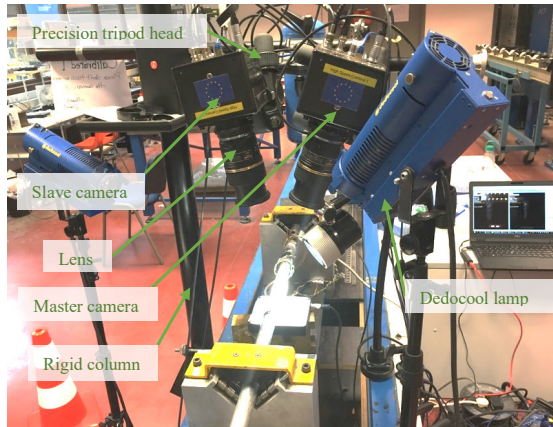


Figure 4.16. Components of the high speed 3D DIC setup

4.5.3. Calibration of the 2D and 3D DIC setups

The calibration for 2D and 3D low and high speed DIC systems was carried out using a special small etched glass calibration target (from Correlated Solutions Inc.), as shown in Figure 4.17. The calibration target contains 4 different grids with 9×9 dots with variable sizes and pitches between the centers of the dots, depending on the required field of view. This special calibration target was used instead of the typical paper printed targets due to the inability of the normal paper printers to achieve very accurate length resolution at a very small scale. The calibration target was backlit using an LED lamp. A magnetic base with a jointed lock arm was used to hold and carefully manipulate the calibration target in the millimeter range for the translation and rotation motions. For 2D DIC setups, the calibration allows to convert the image pixel to mm scale and to correct for the lens distortion, therefore, only translation motion in the image plane is required. As such, at least 25 images of translation motions of the calibration grid were recorded. The calibration of the high speed 2D and 3D DIC systems was performed at a resolution of $2452 \text{ pixel} \times 1024 \text{ pixels}$ and 50 frames per second, in order to achieve longer shutter times and allow more light to the camera sensor to recorded well illuminated calibration images. During the calibration of both low and high speed 3D DIC systems, at least 50 images of translation and rotation motions of the calibration grid were recorded. The calibration parameters were considered acceptable only if they achieved a maximum error of 0.01 pixels. For all the 3D DIC setups used in this PhD research, the cameras were adjusted such that a stereo angle of 10° to 30° is aimed at, so as to have a good combination between in-plane and out-of-plane measurement resolutions as previously mentioned in section 4.4.2.

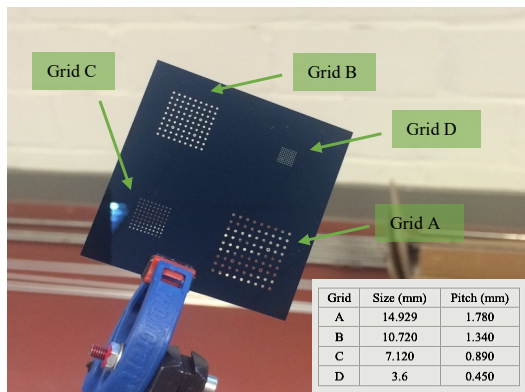


Figure 4.17. Glass etched backlit calibration target with grid sizes and pitch distances (bottom right)

4.5.4. Data processing software and processing parameters

MatchID commercial digital image correlation software package was used to process the recorded images and to generate the full displacement and strain fields. Additionally, the software was also used to automate the calibration processing and to estimate the camera noise and the speckle size. Full details of the software capabilities, theory, and implementation can be found in MatchID manual [46]. Given the theoretical information presented in sections 4.2, 4.3 and 4.4, and the processing capabilities of the computers available at DyMaLab at Ghent University, the following processing parameters were used and fixed for all the experiments in the PhD research:

- The zero mean normalized sum of square differences was used as the correlation criterion, in order to take into consideration the illumination heterogeneities during testing, i.e., scaling and shifting of the grey level histogram.
- A bicubic spline was used for image interpolation, since it provides higher accuracy and reduced errors during image reconstruction. The computation effort was mitigated by using a high end computing workstation with high computational power.
- A Gaussian prefilter of kernel size 5 was used for image filtering to reduce camera sensor noise in the image.
- A quadratic quadrilateral (Q8) polynomial was used for local least square fitting of the displacement field for higher accuracy of strain calculation. The computational effort was mitigated by using a high end computing workstation with high computational power.
- The selection of the subset and step size was mainly dependent on achieving a compromise between the number of data points in the full field, and reducing the displacement and strain noise, especially for small strain measurement. In all cases, the minimum subset size used for all tests was at least 3 times the speckle size. The maximum value of the step size was selected as half the subset size to limit the variability in strains, and to facilitate the convergence in the Levenberg-Marquardt algorithm [44]. The following section will shed more light on the selection of the appropriate range of subset and step sizes.

4.6. Comparison between 2D and 3D DIC setups

Since one of the objectives of the PhD research is to accurately and precisely measure displacements and strains of brittle composite materials with strains as low as 0.01, increasing the signal-to-noise ratio of the DIC displacement and strain measurements is very important. As seen in the previous sections, the selection of the DIC processing parameters has a significant effect on the measurement errors of displacements and strains. Measurement errors of DIC are classified into either systematic errors or random errors. Systematic errors result from interpolation errors in signal reconstruction [26], lens distortions [18,19], subset shape functions [32,34], and intensity gradients of the grey levels [47], and the processing parameters of the DIC (subset, step, and strain window) in case of heterogeneous displacement fields. Random errors usually result from camera noise [48], subset shape functions [33], intensity

gradients of grey levels, and the processing parameters of the DIC (subset, step, strain window, and subset shape function) [14]. The experimental quantification of the systematic measurement errors in DIC is difficult to perform because it requires a previously known displacement field which, in reality, is the quantity to be measured. Numerical deformation of images using a known finite element generated displacement field is one of the techniques used to quantify systematic errors [39]. However, this methodology does not take into consideration the unavoidable experimental effect such as changes in lighting conditions, boundary conditions, etc. Another technique used to quantify the systematic errors in homogeneous DIC displacement measurements is by applying in-plane and out-of-plane rigid translations using a precision translation stage [35]. Alternatively, a simple approach to quantify the measurement systematic errors is to compare the accuracy of the DIC measurements to another reference measurement technique [22,42]. Random measurement errors, on the other hand, can be quantified using images of a speckled sample at completely static conditions [49]. It should be noted that the random errors, i.e. noise floor, can also be considered as the minimum resolution of the measurement, considering the analogy of a DIC system with a purely analog measurement system.

In this section, a comparison between the 2D and the 3D DIC systems in terms of the displacement and strain random errors is presented. Only the vertical displacement and vertical strain components were considered in this study. The random errors were quantified using images recorded by both the 2D and the 3D DIC systems in completely static conditions (i.e. zero load), while maintaining the same speckling and lighting conditions for both DIC systems. The effect of several processing parameters such as subset size, step size, strain window, and subset shape function on the random displacement and strain errors is studied for both low and high speed DIC systems. The quantification of the systematic errors was done in the further experiments in the PhD research by comparing the DIC results with conventional measurement techniques such as LVDTs or strain gauges, as will be seen in chapter 6 and 7.

It should be noted, however, that the scope of this section is to provide a basic quantification of the random errors of displacement and strain measurements for the developed DIC systems (i.e. the noise floor of the measurements) as a function of certain processing parameters, and consequently justify the selection of those parameters (i.e. from a user perspective). As such, a full uncertainty quantification of the detailed errors in the DIC systems is out of the scope of this section and the PhD research. Detailed information on the uncertainty quantification of errors in 2D and 3D DIC can be found in references [41,44,47,50].

4.6.1. Experimental conditions and DIC processing

4.6.1.1. DIC systems and specimen geometry

The DIC setups used were the low speed and the high speed systems described in sections 4.5.1 and 4.5.2. Both systems were used in the 3D stereo configuration. Two cylindrical samples made of RTM6 neat epoxy resin were used in this study (one sample for each DIC system). The dimensions of each sample were 8 mm in diameter and 4 mm in height. The use

of cylindrical samples allows the direct comparison between the 2D and 3D systems using only the 3D DIC setup, while also using the same sample, nearly same field of view, same speckle pattern, and same lighting conditions. Since the surface of the sample is cylindrical, a 2D correlation can be possible using the images of the master camera only, where the region of interest is taken in a small area at the center of speckled sample. The lenses used in both low and high speed systems are long focal length lenses, which will allow small stereo angles and limit the perspective difference between both cameras. A small region of interest at the center of the sample would be nearly perpendicular to the master camera, from the master camera perspective view. Additionally, since the 3D DIC correlation uses the initial subset based on the master camera, a direct comparison between the 2D and the 3D DIC using the same 3D DIC system can be considered valid.

For the low speed 3D DIC system, samples were placed on the lower bar of diameter 25 mm and with a flat end (see chapter 3). The sample was positioned so that it occupies the center of the field of view, while maintaining the center part of sample in complete focus. An extension tube of length 55 mm was used to increase the distance between the sensor and the lens, and thus, increase the magnification. Images were recorded at an acquisition speed of 2 images/s, and with a resolution of $2452 \text{ pixel} \times 2056 \text{ pixels}$, covering a field of view of approx. $20 \text{ mm} \times 20 \text{ mm}$. For the high speed 3D DIC system, samples were placed between the input and the output bars of the split Hopkinson bar facility. The bars were in contact with the sample to fix it in place, however, no forces were applied to the sample. Images were recorded at an acquisition speed of 54000 images/s, and with a resolution of $384 \text{ pixel} \times 256 \text{ pixels}$, covering a field of view of approx. $20 \text{ mm} \times 14 \text{ mm}$. The speckle pattern was applied to each sample of the corresponding 3D DIC system using the techniques described in sections 4.5.1 and 4.5.2. The speckle size of the low speed DIC sample was approx. 6 pixels, corresponding to a physical size of approx. $48 \mu\text{m}$. The speckle size of the high speed DIC sample was approx. 3 pixels, corresponding to a physical size of approx. $155 \mu\text{m}$. Prior to recording of images (calibration and static images), the cameras were run in idle mode for at least 30 minutes in order to achieve a thermal steady state for the cameras' sensors.

4.6.1.2. Calibration of the 2D and 3D DIC setups

The calibration of the low and high speed 3D DIC systems was performed using the procedure described in section 4.5.3. Calibration grids A (14.92 mm in size and 1.78 mm in pitch) and B (10.72 mm in size and 1.34 mm in pitch) were used to calibrate the high speed and low speed DIC systems, respectively. Since the calibration grids are slightly smaller than the field of view of both setups, the series of rigid translations and rotations of the grid was performed across the complete field of view to fully cover it. In order to calibrate for the 2D DIC setup on the same 3D DIC setup, only the master camera was considered. The same calibration grids used for calibrating the stereo systems were also used to calibrate the 2D DIC setups. Table 4.1, Table 4.2, and Table 4.3 summarize the calibration parameters of the 2D and 3D DIC systems in low and high speed configurations. Additionally, the noise of each camera sensor was determined before correlation by calculating the standard deviation of the grey levels in the region of interest of the speckled sample, and averaging it over at least 10 images in completely static conditions (i.e. zero load), while maintaining the same lighting conditions. The camera

noise is reported as a percentage of the dynamic range of the camera, which is the ratio between the largest and the smallest measurable grey levels. The relatively high camera noise in the case of the low speed DIC system is due to the increased illumination of the sample.

Table 4.1. Calibration parameters of 2D DIC systems

Calibration parameter	Low speed 2D DIC	High speed 2D DIC
f_x, f_y (pixels)	62370, 62390	6830, 6835
k_1, k_2, k_3	1.199, 26.12, 0.01858	0.6068, -21.46, 1.097
C_x, C_y (pixels)	831.8, 1226	360.6, 401.3

Table 4.2. Calibration parameters of the low speed 3D DIC system

Calibration parameter	Master camera (camera 1)	Slave camera (camera 2)	Stereo
f_x, f_y (pixels)	62690, 62680	62870, 62820	-
k_1, k_2, k_3	1.568, 8.402, 0.005965	2.88, -330.9, 0.4442	-
C_x, C_y (pixels)	854.5, 1278	-387.1, 1100	-
t_x, t_y, t_z (mm)	-	-	132.8, 2.369, 14.27
θ, ϕ, ψ ($^\circ$)	-	-	0.2753, -14.56, 0.5682
Camera noise (% of the dynamic range)	2.39	1.29	-

Table 4.3. Calibration parameters of the high speed 3D DIC system

Calibration parameter	Master camera (camera 1)	Slave camera (camera 2)	Stereo
f_x, f_y (pixels)	5941, 5937	5965, 5969	-
k_1, k_2, k_3	0.3058, 4.031, 0.07011	0.2865, 11.21, 0.1584	-
C_x, C_y (pixels)	332.6, 312.7	287.8, 320.4	-
t_x, t_y, t_z (mm)	-	-	-139.3, -3.714, 18.05
θ, ϕ, ψ ($^\circ$)	-	-	-0.8166, 26.36, -0.52
Camera noise (% of the dynamic range)	0.615	0.636	-

Figure 4.18 shows the histograms of images of the illuminated speckled samples of the master camera in low and high speed 3D DIC systems in the region of interest indicated in red. The horizontal axis represents the grey levels of the 8-bit resolution sensor, where 0 represents a completely dark pixel and 255 represents a completely white pixel. For the image of the low speed DIC system, the median of the pixels is roughly centered in the mid grey levels (approx. 115), which indicates a good intensity of illumination. The range of grey levels covered are in a normal distribution, and within 20 to 230, which also indicates a good contrast [21]. Additionally, the histogram is free of saturated pixels at 255 grey level, or fully dark pixels are 0 grey levels. All the above histogram features indicate a good and homogenous illumination

for a good DIC correlation. In the case of the image of the high speed DIC system, the image is relatively darker and the median of the histogram is shifted to the left due to the limitations in light sensitivity of the high speed camera sensor at high frame rates, and the limitations in the light intensity of the light source. The scaling and shifting of the grey levels can generally be mitigated by the selection of the ZNSSD correlation criterion.

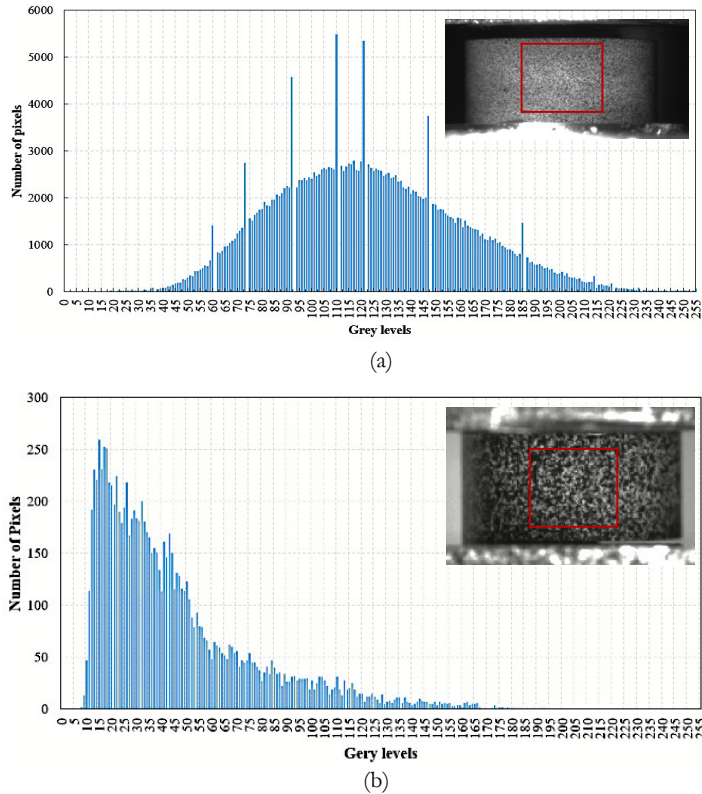


Figure 4.18. Example of grey level histogram of a speckled images in the region of interest:
(a) machine vision camera, (b) high speed camera

4.6.1.3. Data reduction and processing for DIC

In order to quantify the average random errors (i.e. the noise floor) of the displacement and strain measurements, at least 25 images were recorded at completely static conditions (i.e. zero load) using both the 2D and 3D low and high speed DIC systems, while maintaining the sample field of view and lighting conditions. For actual loading experiments, several images were also recorded during the deformation of the compression sample in both low and high strain rate tests. The recorded images were processed using MatchID commercial software in order to calculate the displacement and strain fields. The analysis was performed within a

region of interest at the center of the sample, as shown in Figure 4.18. The main processing parameters used are presented in Table 4.4.

To calculate the random errors, the standard deviation of the full field data points S_Q of the quantity of interest (vertical displacement or strain) was first calculated as follows:

$$S_Q = \sqrt{\frac{\sum_{i=1}^n (Q_i - \bar{Q})^2}{n - 1}} \quad (4.12)$$

Where Q_i is the value of the quantity of interest (displacement or strain) for each individual data point in the full field, \bar{Q} is the average value of the quantity of interest (displacement or strain) for the complete full field, and n is the number of data points in the full field. The average random errors \bar{S}_Q for the quantity of interest (the displacement or the strain) was then calculated as follows:

$$\bar{S}_Q = \frac{\sum_{j=1}^m (3S_Q)}{m} \quad (4.13)$$

Where m is the number of recorded static images. The use of 3 times the standard deviation is to ensure that the noise floor of the displacement and strain measurements is estimated within a confidence interval of 99%. Several values of subset size and step size were used to study their effect on the average displacement and strain noise. The minimum value of the subset size used was selected based on the speckle size of each low speed and high speed DIC sample, so that the subset size is 3 times the speckle size. The maximum value of the step size was selected as half the subset size to limit the variability in strains [44]. Additionally, a first order affine shape function and a second order quadratic shape function were considered.

Table 4.4. Common processing parameters of DIC systems

Parameter	value
Correlation criterion	Zero-mean normalized sum of square differences ZNSSD
Interpolation	Bi-cubic spline
Prefiltering	Gaussian prefilter (kernel size = 5)
Strain interpolation	Quadratic quadrilateral Q8
Strain convention	Biot undeformed
Stereo transformation	Affine transformation (for 3D DIC systems)

4.6.2. Results and discussion

4.6.2.1. Effect of subset size on the average vertical displacement and strain random errors

Figure 4.19 shows the effect of the subset size on the average vertical displacement noise in 2D and 3D low and high speed DIC systems. The remaining processing parameters were also kept constant as follows:

- For low speed DIC: step size = 8 pixels ($64\text{ }\mu\text{m}$), strain window = 15×15 pixels² ($120 \times 120\text{ }\mu\text{m}^2$), subset shape function = 1st order affine.
- For high speed DIC: step size = 4 pixels ($204\text{ }\mu\text{m}$), strain window = 15×15 pixels² ($765 \times 765\text{ }\mu\text{m}^2$), subset shape function = 1st order affine.

The solid lines indicate a power least square fit, with R^2 value higher than 98%. It can be seen that the average vertical displacement and strain noises decrease with increasing the subset size for both the 2D and the 3D systems in low and high speed setups. Increasing the subset size from 19×19 pixels² to 65×65 pixels² results in percentage reduction in displacement noise levels from 52% and 62% for low speed 2D and 3D systems, respectively, and approx. 85% for high speed 2D and 3D systems. The 3D DIC showed a lower average vertical displacement noise compared to the 2D DIC for both low speed and high speed system. At any given subset size, the 3D DIC system shows approx. 42% and 28% lower average vertical displacement noise compared to that of the low and high speed 2D DIC system, respectively. Only at a subset size of 19×19 pixels², the average displacement noise of the high speed 3D DIC system was comparable to that of the high speed 2D DIC system. The effect of the subset size on the average vertical strain noise in 2D and 3D low and high speed DIC systems also follows the same trend. Increasing the subset size from 19×19 pixels² to 65×65 pixels² results in a percentage reduction in average strain noise levels of approx. 66% and 62% for low speed 2D and 3D systems, respectively, and 80% and 83% for high speed 2D and 3D respectively. The low speed 3D DIC system also showed a lower average vertical strain noise compared to the low speed 2D DIC system. At any given subset size, the 3D DIC system shows approx. 52% to 40% and 25% to 37% lower average vertical strain noise compared to that of the low and high speed 2D DIC system, respectively. Similar results we obtained by several researchers such as Acciaoli et al. [51], Rajan et al. [29], Robert et al. [22], and Haddadi et al. [14]. Smaller subset sizes tend to have multiple local minima, which increase the displacement and strain noises during correlation [14]. For low speed DIC, subset size in the range of 35×35 pixels² to 60×60 pixels² provide the lowest displacement and strain noise for both 2D and 3D configurations.

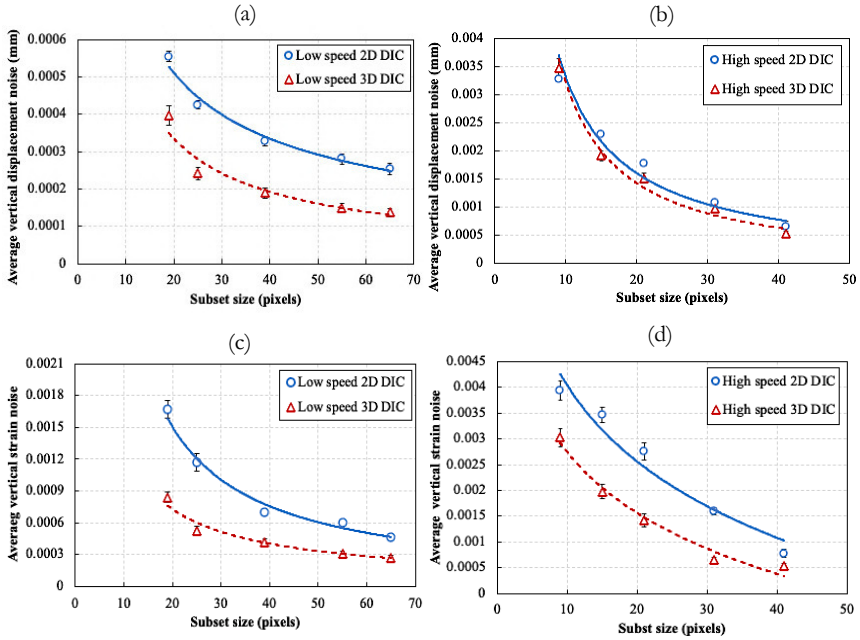


Figure 4.19. Effect of subset size on the average vertical displacement and strain noise: (a) average vertical displacement noise for low speed DIC, (b) average vertical displacement noise for high speed DIC, (c) average vertical strain noise for low speed DIC, (d) average vertical strain noise for high speed DIC. [For low speed DIC: step = 8 pixels, strain window = 15×15 pixels², first order affine shape function. For high speed DIC: step = 4 pixels, strain window = 15×15 pixels², first order affine shape function]

4.6.2.2. Effect of step size on the average vertical displacement and strain random errors

Figure 4.20 shows the effect of the step size on the average vertical displacement noise in 2D and 3D low and high speed DIC systems. The rest of the processing parameters were also kept constant as follows:

- For low speed DIC: subset size = 51×51 pixels² (408×408 μm^2), strain window = 15×15 pixels² (120×120 μm^2), subset shape function = 1st order affine.
- For high speed DIC: subset size = 37×37 pixels² (1.8×1.8 mm²), strain window = 15×15 pixels² (765×765 μm^2), subset shape function = 1st order affine.

The solid lines also indicate a power least square fit, with R^2 value higher than 98%. Similar to the subset size behavior, it can be seen that the average vertical displacement and strain noises also decrease with increasing the step size for both the 2D and the 3D systems in low and high speed setups. For the low speed DIC systems, increasing the step size from 5 pixels to 25 pixels results in percentage reduction in displacement noise levels of approx. 33% for 2D and

6.2% for 3D, and percentage reduction in strain noise approx. 83% for 2D and 79% for 3D. For the high speed DIC systems, increasing the step size from 5 pixels to 18 pixels results in percentage reduction in displacement noise levels of approx. 12.5% for 2D and 33% for 3D, and percentage reduction in strain noise approx. 33% for 2D and 47.5% for 3D. The 3D DIC also showed a lower average vertical displacement and strain noise compared to the 2D DIC for both low speed and high speed systems, with percentages ranging from 16% to 50% for the displacement noise and 5.2% to 62% for the strain noise. Similar results were obtained for the step size behavior by several researchers such as Rajan et al. [29], Robert et al. [22], and Haddadi et al. [14]. It should be noted that the higher noise at small step sizes is related to the high errors near the edges of the speckle pattern. For low speed DIC, step size in the range of 10 pixels to 20 pixels provide the lowest displacement and strain noise for both 2D and 3D configurations. Further increase beyond 20 pixels does not significantly affect the noise levels of the displacement and strain. For high speed DIC, step size in the range of 10 pixels to 15 pixels provide the lowest displacement and strain noise for both 2D and 3D configurations. Further increase beyond 15 pixels does not significantly affect the noise levels of the displacement and strain.

4.6.2.3. Effect of strain window on the average vertical displacement and strain errors

Figure 4.21 shows the effect of the strain window on the average vertical displacement noise in 2D and 3D low and high speed DIC systems. The rest of the processing parameters were also kept constant as follows: subset size = 21×21 pixels², step size = 10 pixels, subset shape function = 1st order affine. The solid lines also indicate a power least square fit, with R^2 value higher than 98%. Similar to the subset size and step size behavior, it can be seen that the average vertical displacement and strain noises also decrease with increasing the strain window for both the 2D and the 3D systems in low and high speed setups. For the low speed DIC systems, increasing the strain window size from 5×5 pixels² to 25×25 pixels² results in percentage reduction in strain noise levels of approx. 85% for 2D and 89% for 3D. For the high speed DIC systems, the percentage reduction in strain noise levels was approx. 14.2% for 2D and 16.6% for 3D. Additionally, the 3D DIC also showed a lower average vertical strain noise compared to the 2D DIC for both low speed and high speed systems, with percentages ranging from 2% to 14%. Similar results were obtained for the strain window behavior by Wang et al. [41]. The reduction in the strain noise when increasing the strain window size is related to the local smoothing of the displacement fields during the calculation of the strain fields. Larger strain windows include a large number of displacement points in the full field, which are then smoothed to one point at the center of the strain window. For both low and high speed DIC configurations, strain window in the range of 13×13 pixels² to 20×20 pixels² provide the lowest displacement and strain noise for both 2D and 3D configurations. Further increase beyond 20 pixels does not significantly affect the noise levels of the strain.

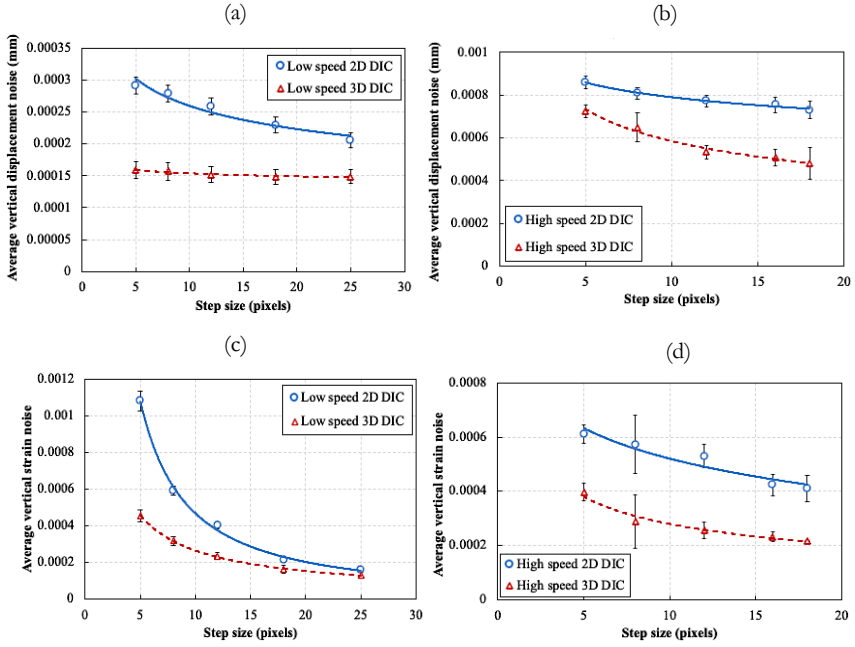


Figure 4.20. Effect of step size on the average vertical displacement and strain noise: (a) average vertical displacement noise for low speed DIC, (b) average vertical displacement noise for high speed DIC, (c) average vertical strain noise for low speed DIC, (d) average vertical strain noise for high speed DIC. [For low speed DIC: subset size = 51×51 pixels², strain window = 15×15 pixels², 1st order affine shape function. For high speed DIC: subset size = 37×37 pixels², strain window = 15×15 pixels², 1st order affine shape function]

4.6.2.4. Effect of subset shape function on the average vertical displacement and strain errors

Figure 4.22 shows the effect of the subset shape function on the average vertical displacement noise in 2D and 3D low and high speed DIC systems at different subset sizes. The rest of the processing parameters were kept constant as follows:

- For low speed DIC: step size = 8 pixels ($64 \mu\text{m}$) and strain window = 15×15 pixels² ($120 \times 120 \mu\text{m}^2$).
- For high speed DIC: step size = 4 pixels ($204 \mu\text{m}$) and strain window = 15×15 pixels² ($765 \times 765 \mu\text{m}^2$).

The lines also indicate a power least square fit, with R^2 value higher than 98%. It can be seen that the quadratic subset shape function shows a higher average vertical displacement noise for both the 2D and the 3D systems in low and high speed setups at different subset sizes

compared to the affine subset shape functions. For low speed 2D and 3D DIC systems, the displacement noise using the quadratic shape function was 20% to 47.3% higher than that of the affine shape function. For the high speed 2D and 3D DIC systems, these percentages were 45% to 60%. The same observation is also made for the strain noise. The strain noise using the quadratic shape function was 16% to 50% higher than that of the affine shape function for low speed 2D and 3D DIC systems, whereas for the high speed 2D and 3D DIC systems, the percentages were 11% to 70%. It is also seen that the 3D DIC achieved lower displacement and strain noise levels for both low and high speed systems at different subset shape functions. Only for the low speed 3D DIC system, the strain noise based on the affine and quadratic shape functions achieved almost the same results. Additionally, in order to achieve the same displacement and strain noise while using the quadratic shape function, a larger subset size should be used, compared to that using the affine shape function. Similar results were obtained by Schreier et al. [32] and Wang et al. [33]. On the one hand, both authors have shown that the second order shape function produces lower systematic errors compared to the first order subset shape function. In their argument, minimizing the systematic errors is more important for the measurement accuracy even at the expense of the large random errors. Consequently, they recommend the second order subset shape function for all DIC experiments, unless the displacement field is explicitly known to be first order. On the other hand, it can be argued that for testing of brittle composite materials, maximizing the signal-to-noise ratio is a more important objective in order to measure small strains compared to the large systematic errors, which can be corrected for. Additionally, a second order displacement field rarely occurs in real applications, and is not suitable for describing the displacement of brittle composites which generally have very small fracture strains [34]. Therefore, a first order subset shape function is more suitable in this case. Indeed, it was demonstrated by Rajan et al. [29] that for strains up to 5%, the systematic error in the displacement using a first order subset shape function remains constant and relatively low for different subset sizes.

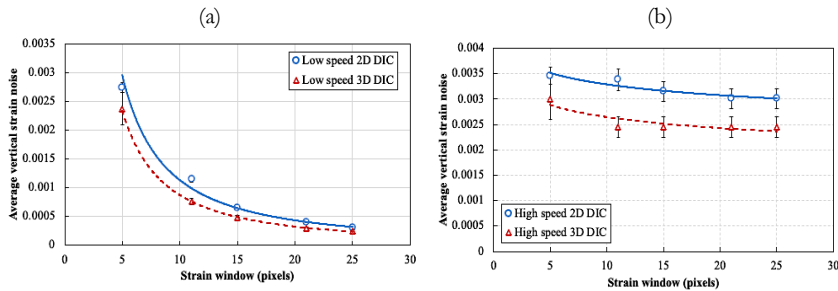


Figure 4.21. Effect of strain window on the average vertical displacement and strain noise: (a) average vertical displacement noise for low speed DIC, (b) average vertical displacement noise for high speed DIC, (c) average vertical strain noise for low speed DIC, (d) average vertical strain noise for high speed DIC. [subset size = 21×21 pixels², step size = 10 pixels, first order affine shape function]

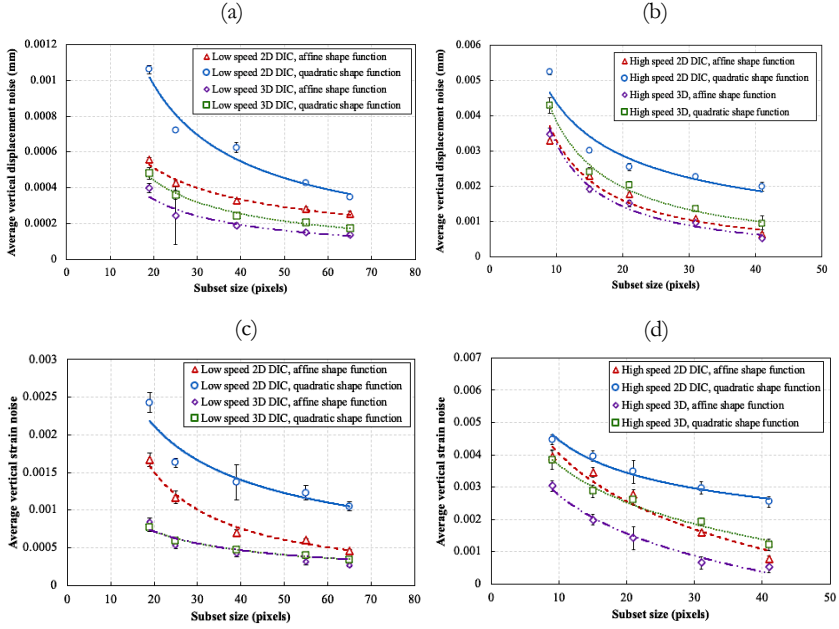


Figure 4.22. Effect of subset shape function on the average vertical displacement and strain noise: (a) average vertical displacement noise for low speed DIC, (b) average vertical displacement noise for high speed DIC, (c) average vertical strain noise for low speed DIC, (d) average vertical strain noise for high speed DIC. [For low speed DIC: step size = 8 pixels, strain window = 15×15 pixels². For high speed DIC: step size = 4 pixels, strain window = 15×15 pixels²]

4.7. Remarks on the 3D DIC technique

The results reported for this particular study and testing conditions indicated that the 3D DIC system achieved a lower displacement and strain noise (i.e. lower resolutions) at different processing parameters such as subset size, step size, strain window, and subset shape functions. The conclusion applies to both the low speed and high speed DIC systems, for which different camera sensors, different speckle patterns, different speckle sizes, and different lighting conditions had to be used. The obtained results go against the generally accepted conviction that the extra correlation steps and stereo calibration procedure required for 3D DIC become additional source of errors compared to 2D DIC [39]. One intuitive explanation for the lower noise would be the use of double the amount of data points in the stereo DIC due to the use of 2 cameras. However, as indicated in section 4.4.3, the correlation in 3D relies on one subset in the master camera with a specified amount of grey level intensities, and this particular subset in used in the 2D and cross camera correlation processes. The final amount of data points is essentially the same as in 2D DIC, with the exception of a 3D component in the out-of-plane direction. Therefore, this intuitive explanation cannot be considered valid.

Murienne et al. [52] reported similar results in which the 3D DIC showed lower displacement and strain noise levels compared to 2D DIC, but only considered the horizontal displacement and strain components in an inflating membrane experiment. However, in this inflating membrane experiment, the 2D DIC system was positioned to the side of the sample while the 3D system was positioned on top of the sample, thus, two completely different fields of view were considered. Therefore, the results obtained by Murienne cannot be directly compared to the current work. Moreover, if a flat sample is to be used for this comparison, 3 cameras have to be used on the same sample; a 2D camera positioned perfectly perpendicular to the flat sample, and a 3D camera system positioned in-line with the 2D camera, where both systems are viewing the exact same field of view. In this case, the requirement of perfect perpendicularity for the 2D DIC camera could be compromised if any tilting of the camera occurs, which could increase the displacement and strain noise levels of the 2D DIC. Indeed, it was shown by Lava et al. [39] that the oblique angle observation of the 2D DIC by values as small as 10° could increase the displacement and strain noise levels compared to the 3D DIC. However, in the current approach, a cylindrical sample is used. Not only does this approach guarantee that both cameras are operating with the same boundary conditions (i.e., speckling, lighting, etc.), but also guarantees that both cameras are viewing the exact same field of view. Indeed, the analysis of both 2D and 3D DIC systems is performed using the image of the master camera, in which the field of view is exactly the same. The use of the second camera in the 3D DIC – together with the triangulation information – gives the out-of-plane displacement component, but without changing the field of view. Therefore, additional research is required to understand why the stereo DIC system achieved lower noise levels compared to 2D DIC in these particular experiments.

Apart from the reduced noise shown in present study, 3D DIC system is still recommended by several authors since it reduces errors due to unavoidable out-of-plane displacements when calculating in-plane strains [10,14,39]. Moreover, the additional data provided by 3D DIC allows to obtain interesting information on the material response, such as the volume change of cylindrical samples during compression. Therefore, it was decided to use the 3D DIC technique for all the experiments performed in the framework of present PhD.

4.8. Conclusions

This chapter covered the development of the digital image correlation setups for local non-contact displacement and strain measurements in the PhD research. A theoretical background of the digital image correlation technique was first introduced, which covered the detailed components of the DIC technique and the effect of software and optical hardware parameter selection on the quality of measurements. Additionally, the practical aspects regarding the calibration of stereo systems, the judging of the quality of lighting conditions, and the application of speckle pattern were highlighted. The DIC 2D and 3D setups and the calibration procedures used in the PhD research were discussed in detail. The developed DIC systems were highly optimized for displacement and strain measurement of brittle composites with a high signal-to-noise ratio. Experiments were performed using the 2D and 3D low and high speed DIC systems in order to study the effect of the processing parameters such as subset

size, step size, strain window, and subset shape function on the average displacement and strain random error (i.e. noise levels). Considering the DIC systems, the samples, the experimental conditions, and the processing parameters used in this study, the following can be concluded:

1. The average displacement and strain random errors decreased with an increase of the subset size, the step size, and the strain window for both 2D and 3D low and high speed DIC systems.
2. The first order affine subset shape function achieved lower displacement and strain random errors at different subset sizes for both 2D and 3D low and high speed DIC systems
3. For low speed DIC systems, subset sizes ranging from 35×35 pixels² to 60×60 pixels² and step sizes ranging from 10 pixels to 20 pixels provided the lowest displacement and strain random errors for both the 2D and 3D setups. For the static DIC setup and sample used, a subset of 60×60 pixels² corresponds with $480 \times 480 \mu\text{m}^2$ on the sample. Further increase beyond these values did not have a significant reduction in the random errors.
4. For high speed DIC systems, subset sizes ranging from 20×20 pixels² to 35×35 pixels² and step sizes ranging from 10 pixels to 15 pixels provided the lowest displacement and strain random errors for both the 2D and 3D setups. For the dynamic DIC setup and sample used, a subset of 35×35 pixels² corresponds with $1.7 \times 1.7 \text{ mm}^2$ on the sample. Further increase beyond these values did not have a significant reduction in the random errors.
5. For both low and high speed DIC systems, strain window sizes ranging from 13×13 pixels² to 20×20 pixels² provided the lowest displacement and strain noise for both 2D and 3D configurations. For the DIC setups and sample used, a strain window of 20×20 pixels² corresponds with $1.4 \times 1.4 \text{ mm}^2$ and $8 \times 8 \text{ mm}^2$ on the sample for resp. the static and dynamic setups. A further increase beyond 20 pixels does not significantly affect the noise levels of the strain.
6. For this particular study and testing conditions, the 3D DIC system achieved lower displacement and strain random errors compared to the 2D DIC system at different processing parameters such as subset size, step size, strain window, and subset shape functions. This conclusion was also valid for both the low and high speed DIC systems.

It should be noted, that this study focused entirely on reducing the random noise levels of the displacement and strain measurements, rather than capturing strain heterogeneities. This was achieved by performing the measurements on undeformed samples (i.e., zero load). As such, the conclusions mentioned here do not take into account the heterogeneities in displacement and strain fields during actual deformation. As mentioned earlier, there is an inherent compromise between capturing strain gradients and reducing the random errors of the measurements. For a complete assessment of the optimum processing parameters, a complementary analysis should be performed on actual deforming samples to determine the sensitivity of the selected parameters to strain gradients. However, this was not included within the scope of this study.

References

- [1] Verleysen, P., and Degrieck, J., 2004, "Experimental Investigation of the Deformation of Hopkinson Bar Specimens," *Int. J. Impact Eng.*, **30**(3), pp. 239–253.
- [2] Eskandari, H., and Nemes, J. A., 2000, "Dynamic Testing of Composite Laminates with a Tensile Split Hopkinson Bar," *J. Compos. Mater.*, **34**(4), pp. 260–273.
- [3] Taniguchi, N., Nishiwaki, T., and Kawada, H., 2007, "Tensile Strength of Unidirectional CFRP Laminate under High Strain Rate," *Adv. Compos. Mater. Off. J. Japan Soc. Compos. Mater.*, **16**(2), pp. 167–180.
- [4] Gilat, A., Goldberg, R. K., and Roberts, G. D., 2007, "Strain Rate Sensitivity of Epoxy Resin in Tensile and Shear Loading," *J. Aerosp. Eng.*, **20**(2), pp. 75–89.
- [5] Grédiac, M., 2004, "The Use of Full-Field Measurement Methods in Composite Material Characterization: Interest and Limitations," *Compos. Part A Appl. Sci. Manuf.*, **35**(7–8), pp. 751–761.
- [6] Xing, H. Z., Zhang, Q. B., Ruan, D., Dehkhoda, S., Lu, G. X., and Zhao, J., 2018, "Full-Field Measurement and Fracture Characterisations of Rocks under Dynamic Loads Using High-Speed Three-Dimensional Digital Image Correlation," *Int. J. Impact Eng.*, **113**, pp. 61–72.
- [7] Hensley, S., Christensen, M., Small, S., Archer, D., Lakes, E., and Rogge, R., 2017, "Digital Image Correlation Techniques for Strain Measurement in a Variety of Biomechanical Test Models," *Acta Bioeng. Biomech.*, **19**(3), pp. 187–195.
- [8] Bing, P., Kema, Q., Huimin, X., and Anand, A., 2009, "Two-Dimensional Digital Image Correlation for in-Plane Displacement and Strain Measurement: A Review," *Meas. Sci. Technol.*, **20**(6), p. 62001.
- [9] Xing, H. Z., Zhang, Q. B., Braithwaite, C. H., Pan, B., and Zhao, J., 2017, "High-Speed Photography and Digital Optical Measurement Techniques for Geomaterials: Fundamentals and Applications," *Rock Mech. Rock Eng.*, **50**(6), pp. 1611–1659.
- [10] Sutton, M. A., Yan, J. H., Tiwari, V., Schreier, H. W., and Orteu, J. J., 2008, "The Effect of Out-of-Plane Motion on 2D and 3D Digital Image Correlation Measurements," *Opt. Lasers Eng.*
- [11] Kuroda, T., 2017, *Essential Principles of Image Sensors*.
- [12] Freddi, A., Olmi, G., and Cristofolini, L., 2015, *Experimental Stress Analysis for Materials and Structures*.
- [13] Reu, P., 2012, "Introduction to Digital Image Correlation: Best Practices and Applications," *Exp. Tech.*, **36**(1), pp. 3–4.
- [14] Haddadi, H., and Belhabib, S., 2008, "Use of Rigid-Body Motion for the Investigation and Estimation of the Measurement Errors Related to Digital Image Correlation Technique," *Opt. Lasers Eng.*, **46**(2), pp. 185–196.
- [15] Pan, B., 2013, "Bias Error Reduction of Digital Image Correlation Using Gaussian Pre-Filtering," *Opt. Lasers Eng.*, **51**(10), pp. 1161–1167.
- [16] Pan, B., Shi, W., and Lubineau, G., 2015, "Effect of Camera Temperature Variations on Stereo-Digital Image Correlation Measurements," *Appl. Opt.*, **54**(34), p. 10089.
- [17] Yoneyama, S., 2006, "Lens Distortion Correction for Digital Image Correlation by Measuring Rigid Body Displacement," *Opt. Eng.*, **45**(2), p. 023602.
- [18] Lava, P., Van Paepegem, W., Coppeters, S., De Baere, I., Wang, Y., and Debruyne, D., 2013, "Impact of Lens Distortions on Strain Measurements Obtained with 2D Digital Image Correlation," *Opt. Lasers Eng.*, **51**(5), pp. 576–584.
- [19] Pan, B., Yu, L., Wu, D., and Tang, L., 2013, "Systematic Errors in Two-Dimensional Digital Image Correlation Due to Lens Distortion," *Opt. Lasers Eng.*, **51**(2), pp. 140–147.
- [20] Lionello, G., and Cristofolini, L., 2014, "A Practical Approach to Optimizing the Preparation of Speckle Patterns for Digital-Image Correlation," *Meas. Sci. Technol.*, **25**(10), pp. 107001–107010.
- [21] Schreier, H., Orteu, J.-J., and Sutton, M. A., 2009, *Image Correlation for Shape, Motion and Deformation Measurements*, Springer US, Boston, MA.
- [22] Robert, L., Nazaret, F., Cutard, T., and Orteu, J. J., 2007, "Use of 3-D Digital Image Correlation to Characterize the Mechanical Behavior of a Fiber Reinforced Refractory Castable," *Exp. Mech.*, **47**(6), pp. 761–773.
- [23] Reu, P., 2014, "All about Speckles: Speckle Size Measurement," *Exp. Tech.*, **38**(6), pp. 1–2.
- [24] Hua, T., Xie, H., Wang, S., Hu, Z., Chen, P., and Zhang, Q., 2011, "Evaluation of the Quality of a Speckle Pattern in the Digital Image Correlation Method by Mean Subset Fluctuation," *Opt. Laser Technol.*, **43**(1), pp. 9–13.
- [25] Fadnavis, S., 2014, "Image Interpolation Techniques in Digital Image Processing: An Overview," *J. Eng. Res. Appl.*, **4**(10), pp. 70–73.
- [26] Schreier, H. W., Braasch, J. R., and Sutton, M. A., 2000, "Systematic Errors in Digital Image Correlation Caused by Intensity Interpolation," *Opt. Eng.*, **39**(11), p. 2915.
- [27] Cheng, P., Sutton, M. A., Schreier, H. W., and McNeill, S. R., 2002, "Full-Field Speckle Pattern Image Correlation with B-Spline Deformation Function," *Exp. Mech.*, **42**(3), pp. 344–352.

- [28] Yoneyama, S., 2016, "Basic Principle of Digital Image Correlation for In-Plane Displacement and Strain Measurement," *Adv. Compos. Mater.*, **25**(2), pp. 105–123.
- [29] Rajan, V. P., Rossol, M. N., and Zok, F. W., 2012, "Optimization of Digital Image Correlation for High-Resolution Strain Mapping of Ceramic Composites," *Exp. Mech.*, **52**(9), pp. 1407–1421.
- [30] Zdero, R., 2016, *Experimental Methods in Orthopaedic Biomechanics*.
- [31] Khoo, S.-W., Karuppanan, S., and Tan, C.-S., 2016, "A Review of Surface Deformation and Strain Measurement Using Two-Dimensional Digital Image Correlation," *Metrol. Meas. Syst.*, **23**(3), pp. 461–480.
- [32] Schreier, H., and Sutton, M. A., 2002, "Systematic Errors in Digital Image Correlation Due to Undermatched Subset Shape Functions," *Exp. Mech.*, **42**(3), pp. 303–310.
- [33] Wang, B., and Pan, B., 2015, "Random Errors in Digital Image Correlation Due to Matched or Overmatched Shape Functions," *Exp. Mech.*, **55**(9), pp. 1717–1727.
- [34] Bai, P., Xu, Y., Zhu, F., and Lei, D., 2020, "A Novel Method to Compensate Systematic Errors Due to Undermatched Shape Functions in Digital Image Correlation," *Opt. Lasers Eng.*, **126**(July 2019).
- [35] Min, H.-G., Kang, D.-J., Kim, K. J., and Park, J.-H., 2017, "New Non-Contact Measurement Method of Deformation at Tensile Test of Thin Film via Digital Image Correlation Technique," *Int. J. Precis. Eng. Manuf.*, **18**(11), pp. 1509–1517.
- [36] Pan, B., Xie, H., and Wang, Z., 2010, "Equivalence of Digital Image Correlation Criteria for Pattern Matching," *Appl. Opt.*, **49**(28), p. 5501.
- [37] Marquardt, D. W., 1963, "An Algorithm for Least-Squares Estimation of Nonlinear Parameters," *J. Soc. Ind. Appl. Math.*
- [38] Wattrisse, B., Chrysochoos, A., Muracciole, J.-M., and Némot-Gaillard, M., 2001, "Analysis of Strain Localization during Tensile Tests by Digital Image Correlation," *Exp. Mech.*, **41**(1), pp. 29–39.
- [39] Lava, P., Coppieters, S., Wang, Y., Van Houtte, P., and Debruyne, D., 2011, "Error Estimation in Measuring Strain Fields with DIC on Planar Sheet Metal Specimens with a Non-Perpendicular Camera Alignment," *Opt. Lasers Eng.*, **49**(1), pp. 57–65.
- [40] Hashiguchi, K., and Yamakawa, Y., 2012, *Introduction to Finite Strain Theory for Continuum Elasto-Plasticity*.
- [41] Wang, Y., Lava, P., Reu, P., and Debruyne, D., 2016, "Theoretical Analysis on the Measurement Errors of Local 2D DIC: Part II Assessment of Strain Errors of the Local Smoothing Method-Approaching an Answer to the Overlap Question," *Strain*, **52**(2), pp. 129–147.
- [42] Jones, E.M.C. and Iadicola, M.A. (Eds.), 2018, *A Good Practices Guide for Digital Image Correlation*. International Digital Image Correlation Society.
- [43] Zhang, Z., 2000, "A Flexible New Technique for Camera Calibration," *IEEE Trans. Pattern Anal. Mach. Intell.*
- [44] Ke, X.-D., Schreier, H. W., Sutton, M. A., and Wang, Y. Q., 2011, "Error Assessment in Stereo-Based Deformation Measurements," *Exp. Mech.*, **51**(4), pp. 423–441.
- [45] Grédiac, M., Hild, F., and Pineau, A., 2012, *Full-Field Measurements and Identification in Solid Mechanics*.
- [46] MatchID, 2020, "MatchID Manual."
- [47] Wang, Y., Lava, P., Reu, P., and Debruyne, D., 2016, "Theoretical Analysis on the Measurement Errors of Local 2D DIC: Part I Temporal and Spatial Uncertainty Quantification of Displacement Measurements," *Strain*, **52**(2), pp. 110–128.
- [48] Gao, Z., Xu, X., Su, Y., and Zhang, Q., 2016, "Experimental Analysis of Image Noise and Interpolation Bias in Digital Image Correlation," *Opt. Lasers Eng.*, **81**, pp. 46–53.
- [49] Sutton, M. A., Matta, F., Rigos, D., Ghorbani, R., Rajan, S., Mollenhauer, D. H., Schreier, H. W., and Lasprilla, A. O., 2017, "Recent Progress in Digital Image Correlation: Background and Developments since the 2013 W M Murray Lecture," *Exp. Mech.*, **57**(1), pp. 1–30.
- [50] Wang, Y.-Q., Sutton, M. A., Ke, X.-D., Schreier, H. W., Reu, P. L., and Miller, T. J., 2011, "On Error Assessment in Stereo-Based Deformation Measurements," *Exp. Mech.*, **51**(4), pp. 405–422.
- [51] Acciaoli, A., Lionello, G., and Baleani, M., 2018, "Experimentally Achievable Accuracy Using a Digital Image Correlation Technique in Measuring Small-Magnitude (<0.1%) Homogeneous Strain Fields," *Materials (Basel)*, **11**(5), p. 751.
- [52] Murienne, B. J., and Nguyen, T. D., 2016, "A Comparison of 2D and 3D Digital Image Correlation for a Membrane under Inflation," *Opt. Lasers Eng.*, **77**, pp. 92–99.

Intentionally left blank

5

Challenges in testing polymers and composites using the split Hopkinson bar technique

This chapter was rewritten based on the following articles:

1. Elmahdy, A., and Verleysen, P., “In-depth characterization of the dynamic behavior of RTM6 epoxy using digital image correlation” (*To be submitted to Polymer Testing in 2021*)
2. Elmahdy, A., and Verleysen, P., 2018, “Challenges Related to Testing of Composite Materials at High Strain Rates Using the Split Hopkinson Bar Technique,” EPJ Web Conf., 183, p. 02021. (*Presented in the 12th International DYMAT conference, Arcachon, France, 2018*)

5.1. Introduction

This chapter discusses the main challenges in testing polymers and composites in tension and compression using the split Hopkinson bar technique. In the first part of the chapter, the challenging aspects related to compression testing of polymers at high strain rates are discussed in section 5.2. In this section, important aspects such as the design of sample geometry to fulfil the testing requirements, and the aspects related to boundary conditions, load introduction, and general material assumptions are discussed in detail. The discussed challenges are illustrated with a compression test of RTM6 epoxy at quasi-static and high strain rates. The establishment of the quasi-static equilibrium, the uniformity of axial strains, and the effect of strain rate on interfacial friction are analyzed. Furthermore, the assumption of volume conservation during yielding of epoxy is also assessed. In the second part of the chapter, the challenges in tensile testing of brittle composites are discussed in section 5.3. Similar to the first part of the chapter, the aspects related to the design of a proper tensile sample geometry which can fulfil both the test requirements and the material requirements, in addition to clamping and fixing methods are first laid out. Based on the geometries used in the literature, two widely used geometries, namely dog-bone and straight strip, are then experimentally assessed based on the criteria of establishment of quasi-static stress equilibrium and the uniformity of the axial strain fields using the full field DIC strain measurement technique. The conclusions of the investigations for both tensile and compression testing are summarized in section 5.4.

5.2. Challenges in compression testing of polymers

5.2.1. Design of compression sample geometry

The design of a compressive sample geometry is a very important aspect in determining the correct stress-strain response of polymers. This becomes significant at high strain rate regimes, due to wave propagation inside the sample material. Normally, cylindrical and cubic shaped samples are used for compression testing in quasi-static conditions. In high strain rate conditions, several additional requirements have to be achieved:

- a. The compression specimen should be short enough to achieve an early quasi-static stress equilibrium and to increase the achievable maximum strain rate, yet the sample length should be long enough to be free of any influence from the loading interfaces,
- b. A state of uniform stress and strain has to be achieved in the sample,
- c. The design of the compression specimen should not promote failure due to buckling, and should reduce the inertia effects during dynamic compression.

Several studies were performed to determine the most suitable height to diameter ratio for cylindrical samples to achieve the abovementioned requirements [1–4]. A height to diameter ratio of 1 is most often recommended, in order to reduce the barreling effect due to interfacial friction [3]. Interfacial friction can significantly affect the accuracy of the measured stress and

strain. Indeed, it was shown by Morelle et al. [5] and Zhong et al. [4] that interfacial friction can increase the apparent strength of tested polymers due to boundary confinement. In addition, interfacial friction leads to a non-uniform stress state within the sample due to barreling. Therefore, sample design, combined with careful lubrication of the loading interface, are very important in reducing the errors due to interfacial friction. However, a height to diameter ratio of 1 might not be ideal for high strain rate compression tests, due to the additional requirements of quasi-static equilibrium and reduction of axial inertia effects [6]. This becomes more significant with polymers having low wave propagation speeds [7]. Therefore, a height to diameter ratio of 0.5 is usually applied in compression testing of polymers at high strain rates [6,8,9]. In this case, monitoring and studying the barreling effects on compression samples is important. The DIC technique has proven very useful in studying the interfacial friction effect in compression testing [10]. DIC can provide the full displacement field in 3D, and is free from the errors which are typically associated with other techniques such as LVDTs, when measuring the radial deformation of compression samples [1].

5.2.2. Boundary conditions and load introduction

In addition to the previous aspect of design of sample geometry, the boundary conditions and load introduction to the sample interfaces can significantly affect the final measured stress-strain curve and the validity of the split Hopkinson bar assumptions. High strength sample materials can indent into the more compliant bars, which can cause stress concentrations at the edges of the samples or a deviation from the assumption of flat loading interfaces, which will consequently lead to errors in stress and strain measurements [11]. A typical solution is the addition of high strength, hard metallic or ceramic inserts at both bar interfaces [11]. However, care should be taken to design such inserts in a way that does not introduce additional mechanical impedance mismatch and disturb the propagation of the waves [12]. Moreover, the contact conditions at the loading interfaces can significantly affect the accuracy of the results. The lack of parallelism and flatness can induce either an irregular stress-strain response at low strain levels or induce premature failure due to bending [1]. In addition, the lack of parallelism between the loading interfaces can result in tilting of the sample during high strain rate loading which can introduce errors in the determination of the dynamic elastic modulus in compression [13]. Spherical joints have been introduced to provide self-alignment capabilities at high strain rates [14]. However, the design of these spherical joints is susceptible to instabilities, especially if the centerlines of the sample and the bars are not perfectly aligned. Therefore, new design concepts for self-alignment attachment are required to provide both good contact conditions and good stability during dynamic testing.

5.2.3. Material assumptions

The conservation of volume is normally assumed for yielding and post yielding stages of deformation in polymers [9]. However, this assumption is applicable to metallic materials and cannot be directly extended to polymers, due to the difference in deformation mechanisms which involve molecular restructuring and entanglement of polymer chains. Indeed, it was shown by Jerabek et al. [1] that post yielding behavior at quasi-static strain rates can experience

either an increase or a decrease in volume. This indicates that the assumption of volume conservation during all stages of deformation should be validated, including at high strain rates considering the strain rate sensitivity of polymers [15].

In the following subsections, the above mentioned challenges are addressed when testing neat RTM6 epoxy in compression. Following the selection of a suitable sample geometry, a new concept of self-alignment attachment is introduced, and its effect on the measured waves is checked. The establishment of an early quasi-static equilibrium is also discussed. With the aid of 3D DIC techniques, the interfacial friction effects and sample barreling, the axial strain homogeneity, and the assumption of volume conservation during high strain rate deformation are analyzed in detail.

5.2.4. Experimental testing conditions in compression

5.2.4.1. Specimen material and geometry

The epoxy resin used in this study was the aeronautical grade RTM6, supplied by Hexcel Composites (Duxford, UK). It was made up of tetra-functional epoxy resin tetraglycidyl methylene dianiline (TGMDA) and two hardeners, namely 4,4'-methylenebis (2,6-diethylaniline) and 4,4'-methylenebis(2-isopropyl-6-methylaniline). The equivalent weight of the epoxy after mixing with the hardeners was 116 g/eq and the viscosity was 33 mPa.s at 120 °C. All the chemicals were used as-received. The RTM6 resin was prepared by first degassing the resin at 90 °C for 30 minutes in a vacuum oven, then the hardener was added and carefully mixed, according to the specified mixing ratio by the manufacturer. The resin was molded into a long, hollow metallic cylinder which was coated with a release agent (FREKOTE 70) to facilitate the extraction of the samples. The molded resin was then cured in an oven at 160 °C for 90 min, followed by a post-curing stage of 2 h at 180 °C, and left to cool to room temperature in the oven for 24 hours. Figure 5.1 shows the results of the Dynamic Mechanical Analysis (DMA) of the cured epoxy (performed by CNR-IPCB). The glass transition temperature which corresponds to the peak of the tan-delta curve was 226.6 ± 0.2 °C.

The fully cured cylindrical rods of the resin were finally cut into small cylindrical samples, having a diameter of 8 mm and a height of 4 mm, as shown in Figure 5.2. Based on the analysis of literature in section 5.2.1, the sample geometry was selected so that the height to diameter ratio is 0.5. The chosen sample geometry and dimensions fulfil the requirements of an early quasi-static equilibrium, minimize the inertia effects, and achieve a higher strain rate [6,8], however, sample barreling could become significant [1]. Therefore, in order to reduce barreling and interfacial friction, special attention was paid to the lubrication of the interfaces, as will be discussed later. To eliminate any discrepancies related to the sample geometry, the same sample geometry and testing boundary conditions were used for both reference quasi-static and high strain rate tests.

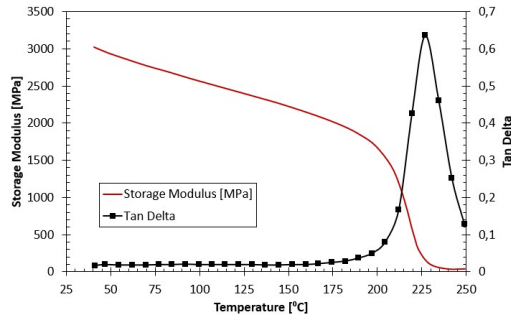


Figure 5.1. DMA results, i.e., tan delta and storage modulus, of the RTM6 epoxy resin

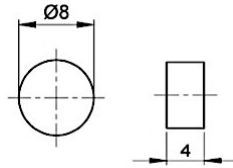


Figure 5.2. Dimensions of the cylindrical compression sample

5.2.4.2. Sample fixing and alignment

A special self-alignment attachment was developed for the quasi-static and high strain rates compression tests, as shown in Figure 5.3. This attachment was developed in order to provide a full contact between the loading surface of the bars and the specimen interfaces even if the specimen interfaces lack perfect parallelism. The attachment was based on a modified axial spherical plain bearing (INA GE30-AX), which was modified by changing its steel inner race to a blind aluminum spherical seat for the compression sample. The seat was cut from an aluminum ball and matched the spherical cavity of the bearing's outer race. The contact surface between the aluminum spherical seat and the bearing's outer race was made of a thin layer of glass fiber reinforced PTFE composite to minimize friction. The seat and the outer race were kept in contact by means of a back plate and a small set screw. This prevents the aluminum seat from falling off during loading. The contact surface between the backplate and the outer race was greased before assembly to minimize friction. The outer race was press fitted into an aluminum housing which was then attached to the output bar. Sufficient clearances were considered to allow the spherical seat to move and accommodate the sample. The side of the housing which is glued to the transmitted bar had the same diameter as the bar in order to minimize the impedance mismatch. Moreover, the housing and the spherical seat were made from aluminum also to match the material of the bars and minimize the impedance mismatch. However, due to the unavoidable difference in the cross section area in the housing and the different materials used, some small wave reflections were expected due to the impedance mismatch. For the quasi-static testing, the same self-alignment attachment configuration was used, however, the parts made of aluminum were replaced by steel parts to match the material of the quasi-static testing bars.

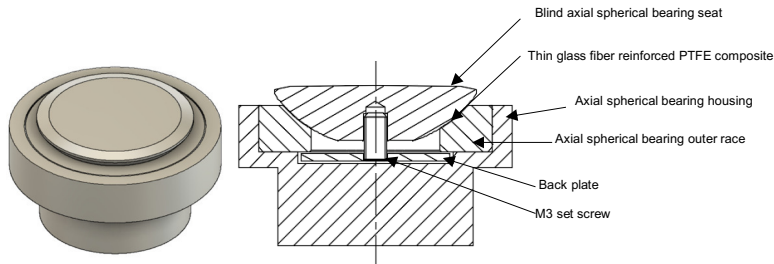


Figure 5.3. Self-alignment attachment for the compression tests as isometric view (left) and section front view (right)

Additionally, an alignment tool was developed in order to align the compression sample to the bars. Using this tool, the centerline of the sample can be aligned with the centerlines of the input bar, the output bars, and the self-alignment attachment. Figure 5.4 shows the developed sample alignment tool for compression tests.

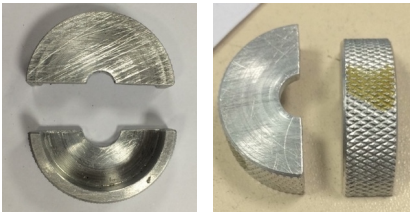


Figure 5.4. Top view (left) and side view (right) of the alignment tool for the compression sample on the bars

5.2.4.3. Quasi-static testing

Reference quasi-static experiments were carried out using the Instron 5569 universal testing machine described in chapter 3. Quasi-static compression tests were performed at speeds of 0.2, 2, and 20 mm/min, aiming at strain rates of 0.001, 0.01, and 0.1 s⁻¹, respectively, in the samples. Samples were placed between the two flat ended steel bars. The self-alignment attachment of the quasi-static tests was fixed at the interface of the lower bar. As for the dynamic tests, the loading interfaces with the sample were polished to a mirror finish, and carefully lubricated with a PTFE lubricant to reduce friction.

Global displacements and strains were measured using 3 LVDTs (supplied by RDP group) fixed on the bars close to the sample. The measurements obtained from the LVDTs were later corrected for the bar compliance during compression. Local full-field displacements and strains were measured using the low speed 3D DIC system described in chapter 4. The calibration procedure described in chapter 4 was used to determine the intrinsic and extrinsic calibration parameters of the DIC system. A 9×9 calibration grid of 10.72 mm in size and 1.34 mm in pitch was used for the calibration (see chapter 4). Table 5.1 presents the intrinsic and

extrinsic calibration parameters of the system. A black-on-white speckle pattern was applied to the surface of the samples prior to testing. Images of the speckled samples were recorded during testing at a resolution of 2452×2056 pixels and a rate of 1 images/sec for the testing speeds of 0.2 and 2 mm/min, and 3 image/sec for the testing speed 20 mm/min. The average speckle size of the samples tested at quasi-static speeds was approx. 0.09 mm, which corresponds to 10 pixels on the images. The captured images from the camera, and the strain measurements from the LVDTs were synchronized with the force signal obtained from the load cell using a NI 9215 data acquisition card. Figure 5.5 shows the quasi-static setup used. The average displacement resolutions were approx. 0.05 and 5 μm for in-plane and out-of-plane displacements, respectively, for the quasi-static 3D DIC system, 0.18 μm for the LVDTs.

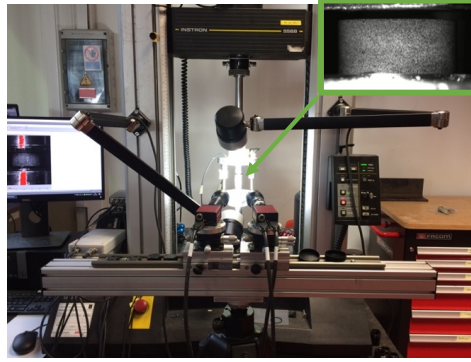


Figure 5.5. Quasi-static compression setup with a detail of the speckled sample (top right)

Table 5.1. Calibration parameters of the quasi-static 3D DIC setup

Parameter	Camera 1	Camera 2	Stereo setup
Focal lengths (pixels)	111900, 111000	81960, 81370	-
Distortion coefficients (K1, K2, K3)	1.599, -1.37, -0.000264	1.03, -411.3, -0.3179	
Optical centers (pixels)	1224, 1029	1267, 1806	
Stereo angles (degrees)	-	-	1.55, 18.85, -0.1085
Translation (mm)	-	-	303, 18.01, -214.6

5.2.4.4. High strain rate testing

The high strain rate compression experiments were performed using the split Hopkinson pressure bar setup described in chapter 3. To impose different strain rates to the sample, three impactor velocities were used: 8, 11 and 14 m/s. The incident bar had a length of 6 m which allows a loading time of approx. 1.2 ms. The time histories of the average axial strain rate $\dot{\epsilon}^{Hop}$, strain ϵ^{Hop} , and stress σ^{Hop} in the sample can be calculated using eqs 3.10, 3.11, and 3.12, respectively. The suffix “Hop” is added to relate these equations to the classical Hopkinson analysis.

Due to the impedance mismatch between the output bar and the self-alignment attachment, some wave reflections were expected. However, only very small, negligible oscillations were observed in the transmitted signal. Figure 5.6 shows an example of the incident, the reflected, and the transmitted waves recorded in one of the dynamic compression experiments. The loading interfaces of the sample were also lubricated with a PTFE based lubricant to minimize the interfacial friction.

The high-speed 3D DIC technique, described in chapter 4, was used to measure the local strains and strain rates on the surface of the sample. A black-on-white speckle pattern was applied to the surface of the samples prior to testing. Images were recorded at a resolution of 384×265 pixels and a rate of 54,000 images/sec. The intrinsic and extrinsic parameters of the DIC system were determined by the calibration procedure described in chapter 4. Table 5.2 presents the intrinsic and extrinsic calibration parameters of the high speed DIC system used. The calibration was performed using a small etched glass calibration grid, having 9×9 dots and a pitch of 1.78 mm between the centers of the dots. The exposure signal of the camera sensors was synchronized with the measured strain signals on the bars using the same high-speed data acquisition system. The average speckle size of the dynamically tested samples was approx. 0.16 mm, corresponding to a size of 3 pixels on the images. The average displacement resolutions were approx. 0.7 and 2 μm for in-plane and out-of-plane displacements, respectively. The better out-of-plane displacement resolution compared to the quasi-static optical system resolution is related to the use of a slightly larger stereo angle in the high-speed 3D DIC setup. Figure 5.7 shows the high-speed 3D DIC system used.

Table 5.2. Calibration parameters of the high speed 3D DIC setup

Parameter	Camera 1	Camera 2	Stereo setup
Focal lengths (pixels)	5941, 5937	5965, 5969	-
Distortion coefficients (K1, K2, K3)	0.305, 4.031, 0.0701	0.286, 11.21, 0.158	
Optical centers (pixels)	332.6, 312.7	287.8, 320.4	
Stereo angles (degrees)	-	-	-0.816, 26.36, -0.52
Translation (mm)	-	-	-1393, -3.714, 18.05

5.2.4.5. DIC data reduction and processing parameters

The images of the deforming samples recorded during the tests were processed and analyzed using MatchID commercial digital image correlation software. The processing parameters used for both quasi-static and dynamic tests are presented in Table 5.3. The parameters allowed to achieve a strain resolution of approx. 155 microstrains for quasi-static tests and approx. 400 microstrains for high strain rate experiments. Since the shape of the sample is cylindrical, only the central part of the sample lied in the cameras' focal plane. Therefore, at each moment during the quasi-static and dynamic tests, the average full field in-plane strains and out-of-plane displacements were extracted from an area of $3.5 \times 3.5 \text{ mm}^2$ at the center of the sample. The axial engineering strain ϵ^{DIC} was calculated based on the reference Biot strain convention,

while the axial true strain ϵ_t^{DIC} was calculated based on the Hencky strain convention (see eqs. 4.9 and 4.10).

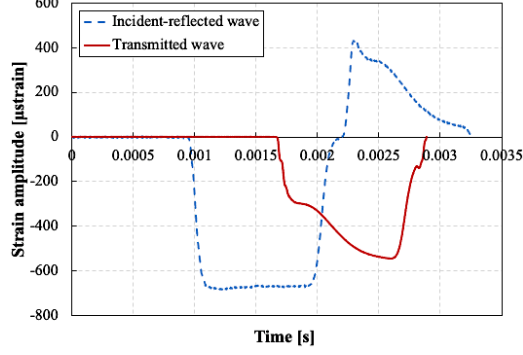


Figure 5.6. An example of the incident, the reflected, and the transmitted wave recorded on the Hopkinson bars during a dynamic compression experiment

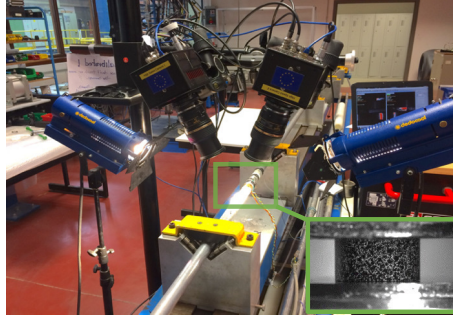


Figure 5.7. High-speed 3D DIC setup used, with detail of the speckled sample (bottom right)

Next to the axial strain, DIC processing also allowed to obtain the transverse component of the strain ϵ_{hoop}^{DIC} (also denoted as hoop strain). The hoop strain component was not straightforwardly taken from the DIC strain processing, since the strains in the DIC are calculated based on a local coordinate system at the sample surface. Instead, the hoop strain component was calculated at the center of the sample, so that the local coordinates coincide with the global (world) coordinates which increases the accuracy of the results. As such, the hoop strain was calculated using the radial displacement u_r obtained from the DIC measurements and the initial radius r_0 as follows:

$$\epsilon_{hoop}^{DIC} = \frac{u_r}{r_0} \quad (5.1)$$

True stresses are commonly calculated from engineering stresses assuming conservation of volume of the sample material during the deformation process. Using the DIC strain and engineering stress obtained by eq. (3.12), the true stress based on DIC strains and conservation of volume $\sigma_t^{DIC,Vol}$ can be calculated using the following relation:

$$\sigma_t^{DIC,Vol} = \sigma^{Hop} \cdot (1 + \varepsilon^{DIC}) \quad (5.2)$$

While the assumption of the conservation of volume might be a valid assumption for plastic deformation of metals, this might not be the case for polymers. Since the hoop strain was also measured in this study, the assumption of volume conservation becomes superfluous and the true stresses can be calculated based on the instantaneous cross sectional area using the following relation:

$$\sigma_t^{DIC} = \frac{F}{A} = \frac{F}{\pi r^2} = \frac{F}{\pi r_0^2 (1 + \varepsilon_{hoop}^{DIC})^2} = \frac{\sigma^{Hop}}{(1 + \varepsilon_{hoop}^{DIC})^2} \quad (5.3)$$

In order to further experimentally assess the assumption of conservation of volume, the total volumetric strain ε_V can be determined based on the ratio between the final volume V_f and the initial volume V_0 of the sample using the following relation:

$$\varepsilon_V = \frac{V_f}{V_0} - 1 = \left[(1 + \varepsilon_{hoop}^{DIC})^2 \cdot (1 + \varepsilon^{DIC}) \right] - 1 \quad (5.4)$$

The total volumetric strain includes both the elastic volumetric strain ε_V^{ela} and the non-elastic volumetric strain $\varepsilon_V^{non-ela}$. The non-elastic volumetric strain can be determined using the following relation:

$$\varepsilon_V^{non-ela} = \varepsilon_V - \varepsilon_V^{ela} = \left[\left[(1 + \varepsilon_{hoop}^{DIC})^2 \cdot (1 + \varepsilon^{DIC}) \right] - 1 \right] - [(1 - 2\nu) \cdot \varepsilon^{DIC}] \quad (5.5)$$

Where ν is the Poisson's ratio calculated in the elastic region, i.e., at the early stage of loading, using the following relation:

$$\nu = -\frac{\varepsilon_{hoop}^{DIC}}{\varepsilon^{DIC}} \quad (5.6)$$

In order to assess the validity of the classical Hopkinson stress and strain calculation, i.e., eqs. (3.11) and (3.12), the axial compressive true stress $\sigma_t^{Hop,Vol}$, assuming conservation of volume, was calculated from the stress obtained by eq. (3.12):

$$\sigma_t^{Hop,Vol} = \sigma^{Hop} \cdot (1 + \varepsilon^{Hop}) \quad (5.7)$$

The true compression strain is calculated based on eq. (3.11) using:

$$\epsilon_t^{Hop} = \ln(1 + \epsilon^{Hop}) \quad (5.8)$$

Table 5.3. Processing parameters for DIC for compression experiments

Parameter	Value
Correlation criterion	Zero normalized sum of square differences (ZNSSD)
Interpolation order	Bi-cubic spline
Shape function	Affine
Subset size (pixels)	55x55 (quasi-static) and 21x21 (high strain rate)
Step size (pixels)	10
Strain window	15

5.2.5. Results and discussion

5.2.5.1. Quasi-static force equilibrium and strain rate evolution in the SHPB tests

Figure 5.8 represents a comparison between the time histories of the forces at the input and output bar/specimen interfaces during a dynamic compression experiment. It can be seen that the input bar force signal shows an excellent agreement with the output bar force signal starting from approximately 100 μ s. This indicates the achievement of an early quasi-static force, and hence stress, equilibrium in the sample from the early stages of deformation. An early quasi-static equilibrium was achieved for all dynamically tested specimens. It should be noted that the oscillations resulting from the self-alignment attachment on the output bar were small in magnitude and occurred at stress levels in the sample below 100 MPa, which is well into the elastic stage [5].

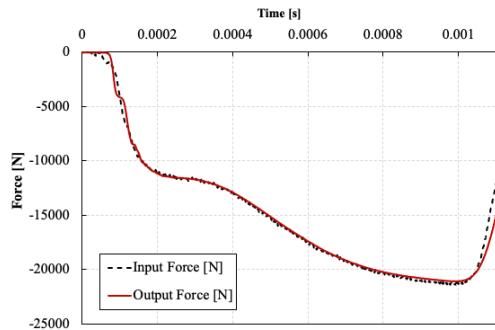


Figure 5.8. Comparison between the time histories of the forces at the specimen/bar interfaces during a SHPB test

Figure 5.9 (a) shows an example of the true axial strain time history for a high strain rate compression experiment, using the classical Hopkinson analysis (eq. 5.8) and the true DIC axial strain. It can be seen that the true axial strains measured using DIC show an excellent

agreement with the true axial strains measured using the classical Hopkinson analysis. It should be noted that due to the large deformations of the samples during compression, the speckle pattern could not follow the deformation of the samples beyond approx. 30 to 35 % true strain. Therefore, the true strains based on the DIC measurements were reported up to approx. 35%. In the dynamic tests, the samples were deformed during approximately 1 ms. The progression of the strain with respect to time consisted mainly of 3 stages: (1) a first stage with times ranging from 50 to 100 μs , corresponding to the viscoelastic response of the material, which comes after a time range from 0 to 50 μs in which the quasi-static force equilibrium is being established, (2) a second stage in which a fairly constant strain rate was established, starting from time 100 μs and up to 1 ms, and (3) a third stage, after 1 ms, in which the strain decreased corresponding to the unloading of the sample. None of the dynamically tested samples failed during the compression tests, and unloading was observed in all samples. Consequently, the maximum strain reached in the dynamic tests cannot be considered as the failure strain. For all dynamic tests, constant, though different, strain rates were achieved in the first and the second deformation stages which were explain earlier. As such, the average true strain rates corresponding to the elastic constants, i.e., elastic modulus and Poisson's ratio, were calculated in the first stage, while the average true strain rates corresponding to yielding were calculated in the second stage. The average true strain rates were calculated as the slope of the true strain-time curves in the first and second stages. The achieved average strain rates for all the dynamic compression tests were in the range of 285 s^{-1} to 1094 s^{-1} .

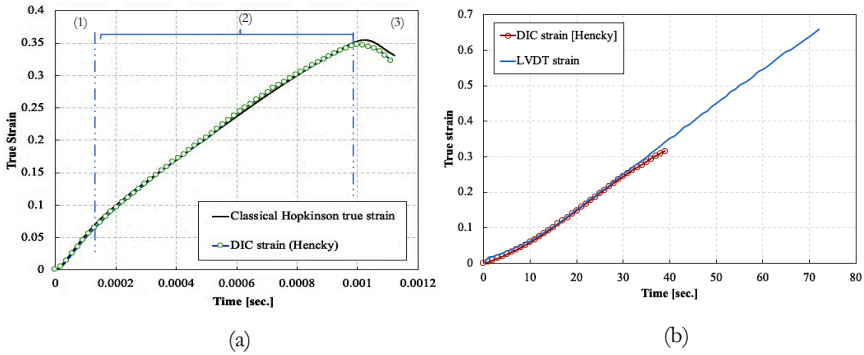


Figure 5.9. An example of the axial strain time history (a) during a high strain rate compression experiment, (b) during a quasi-static strain compression experiment

Figure 5.9 (b) shows an example of the true strain time history of a quasi-static compression experiment, using the LVDT and the DIC measurement techniques. The true strains measured using the LVDTs were corrected for the bar compliance, which is the compliance resulting from the compression of the portion of the bars contained within the LVDTs measurement section and the self-alignment device. The quasi-statically tested samples were compressed to failure.

Similar to the high strain rate case, the true strains measured using the DIC technique were in excellent agreement with the strains measured using the LVDTs. As with the dynamic compression tests, the speckle pattern could not follow the deformation of the samples beyond approx. 30% true strain. Therefore, the true strains based on the DIC measurements for the quasi-static tests were only reported up to approx. 30%.

5.2.5.2. Interfacial friction and sample barreling

As mentioned earlier, reducing the interfacial friction to limit sample barreling is crucial to ensure homogenous stresses and strains within the compression sample. Using the 3D DIC technique, it was possible to monitor the out-of-plane displacement during the deformation of the sample, and thus directly measure the barreling at the surface of the sample. This was performed by extracting the out-of-plane displacements on several points along a vertical center line on the surface of the sample during the deformation. Figure 5.10 shows an example of the extracted out-of-plane displacements for a quasi-static test and a high strain rate test at different levels of true axial strains. The vertical center line on the surface of the sample is indicated by a red dotted line. The upward movement of the curves which is observed in the dynamic tests is due to the relative movement of the input and the output bars, unlike in the quasi-static case in which the lower bar is fixed.

From a qualitative point of view, it can be seen that the barreling was nearly negligible up to 0.1 true axial strain for the quasi-static and dynamic tests. This is indicated by the nearly straight contour of the sample. The barreling was quantified by calculating the barreling ratio, defined as $(\Delta t_b/r_o)$, where Δt_b is the difference between the out-of-plane displacements in the middle of the sample and the most confined point close to one of the loading interfaces, and r_o is the initial radius of the sample. Figure 5.11 shows an example of the evolution of the barreling ratio as a function of true axial strain for several representative static and dynamic tests. The solid lines indicate a linear least square fit, with R^2 values higher than 82%. The mentioned strain rates correspond to the strain rate reached at the peak yield strength. It can be seen that the barreling ratio increases during the progression of the compression tests. However, the barreling significantly decreases with increasing strain rate. Indeed, at a true axial strain of 0.3, the barreling ratio of approx. 1% obtained in the sample tested at the lowest strain rate, i.e., 0.001 s^{-1} , was reduced with a factor of approx. 2.5 to 0.4% in the sample tested at a strain rate of 1011 s^{-1} . This phenomena can be simply explained in by friction concepts of tribology. At low strain rates, the lubricant film has enough time to dissipate between the asperities of the bar and specimen interfaces, thus increasing the apparent contact area and the friction between the two interfaces. However, at high strain rates, the lubricant film does not have enough time to dissipate between the asperities of the two interfaces. This decreases the apparent contact area between the two interfaces, and hence, the friction. The overall low barreling ratios indicate good lubrication conditions with minimum barreling up to 0.3 true axial strain in all compression tests.

5.2.5.3. Axial strain homogeneity and conservation of volume

Figure 5.12 shows the evolution of the true axial compressive strain fields during a quasi-static experiment at a strain rate 0.01 s^{-1} and a dynamic experiment with a strain rate of 428 s^{-1} at the peak yield strength. The images were recorded during the deformation from time 0 to 46 s for the quasi-static experiment, and 0 to $796\text{ }\mu\text{s}$ for the high strain rate experiment. The color map indicates the strain levels measured on the surface of the sample, blue corresponds to the highest true strain of 0.35 and red to a true strain of 0. It can be seen that homogeneous strain fields developed at both the quasi-static and the high strain rate. For the high strain rate tests, higher strains appear around the center of the sample, which then spread over the entire sample.

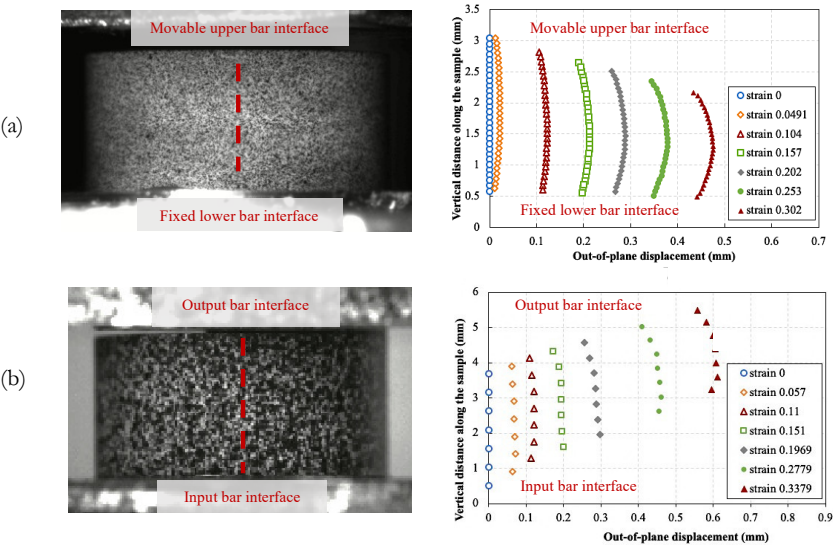


Figure 5.10. Out-of-plane (radial) displacement along a vertical center line on the sample surface at different levels of true axial strain: (a) during a quasi-static test, (b) during a high strain rate test

Figure 5.13 shows a comparison between the true stress-true strain curves of a SHPB experiment obtained using classical Hopkinson analysis (eqs. 5.7 and 5.8) and DIC data (eq. 5.2) assuming volume conservation, and direct DIC measurement (eq. 5.3). The true stress-true strain curves based on classical Hopkinson and DIC analysis with the conservation of volume show excellent agreement. However, both curves differ from the curve based on the direct measurement of DIC without conservation of volume. The latter shows higher stress levels in the yielding and post yielding stages, with approx. 20 MPa or 10% difference at a true strain of 0.15. Based on these curves, it is clear that the assumption of conservation of volume in the yield and the post yield stages cannot be considered valid. Assuming volume conservation gives rise to a non-negligible underestimation of the strength of the material.

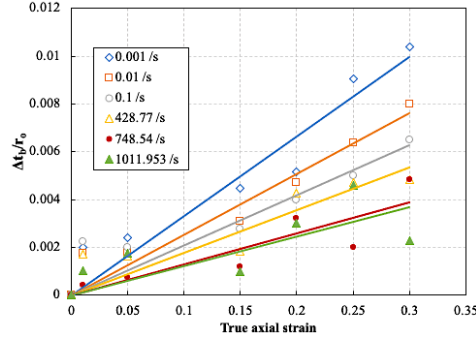


Figure 5.11. Example of the evolution of the barreling ratio during compression testing at different strain rates

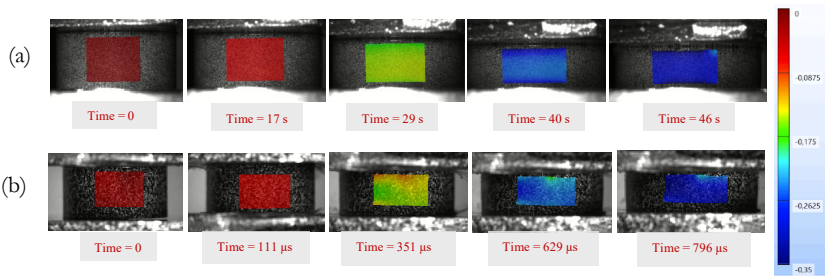


Figure 5.12. Evolution of axial true strain fields during compression testing for (a) a quasi-static test at 0.01 s^{-1} , (b) a high strain rate test at 428 s^{-1}

Figure 5.14 shows representative curves for the total and non-elastic volumetric strains (eqs. 5.4 and 5.5) obtained for quasi-static and high strain rate tests up to 0.2 axial strain. The solid lines represent a least square polynomial fit with R^2 values higher than 95%. The indicated strain rates correspond to the strain rates at the peak yield strength. As expected, the volume decreases as a function of imposed strain, for all strain rates. Additionally, the strain rate does not have a significant effect on the volume reduction. The volume of the sample is reduced by approx. 3% to 6% at an axial strain of 0.07, which is roughly the average strain level at which yielding of the material starts. At true axial strains higher than 0.07, the volume reduction rate is slightly reduced. The presence of this transition point indicates that the reduction in volume is different in the elastic-viscoelastic stage compared to the yield stage. The reduction in volume is attributed to the compaction of the material as a result of the compressive hydrostatic pressure. The non-elastic volumetric strains presented in Figure 5.14 (b) are quasi-zero up to true axial strains of approx. 0.02 for the static tests and 0.05 for the dynamic tests. Beyond these values of axial strain, the non-elastic volumetric strains increase to reach a maximum ranging between 1% to 3% of the total volume at all strain rates. The effect of strain

rate on the non-elastic volumetric strains is not significant. The volumetric strains indicate that in the yield stage, and contrary to what is often assumed, a permanent but limited volume change occurs. Similar results were reported by Jerabek et al. [1] for polypropylene in compression at quasi-static strain rates. However, in the yielding stage, the authors indicated that the material could experience either an increase or a decrease in the volume depending on the position at which the Poisson's ratio was measured on the sample, and the stage at which the Poisson's ratio was calculated. In present study, the Poisson's ratio used in eq. (5.6) was measured in the center of the sample, and extracted from the initial linear part of the stress-strain curve. Indeed, as evident from the DMA results in Figure 5.1, the tan delta – which is a direct measure of the viscous component of the material behavior – is nearly zero in the temperature range of 23 °C up to 150 °C. Additionally, as will be shown in chapter 7, the elastic modulus and the Poisson's ratio calculated in the linear part only seemed to be marginally affected by the strain rate. It is therefore assumed that the material response at the low deformation range is dominantly elastic rather than viscoelastic. Based on the previous analysis, the peak yield strength reported later in chapter 7 is based on the stress-strain curves without the conservation of volume.

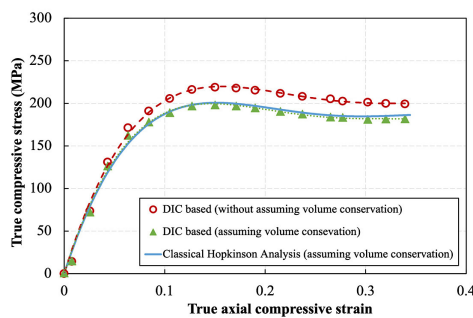


Figure 5.13. True stress-true strain curve of a high strain rate compression experiment on the neat epoxy resin

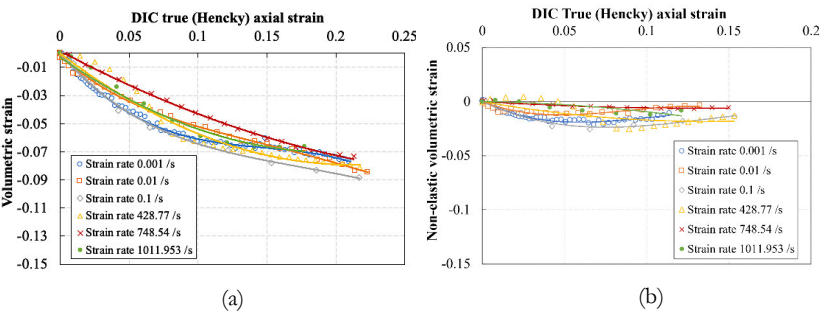


Figure 5.14. Variation of the relative volume change on the neat epoxy resin as a function of true axial strains at different strain rates during compression: (a) volumetric strain, (b) non-elastic volumetric strain

5.3. Challenges in tensile testing of brittle composites

5.3.1. Design of tensile sample geometry

Similar to the case of compression testing, the design of the sample geometry is a critical aspect in the high strain rate tensile testing of composite materials with the split Hopkinson tensile bar technique. Unlike quasi-static testing, there are no standardized sample geometries for the high strain rate tensile tests. Additionally, high strain rate testing involves dynamic stress waves traveling back and forth inside the specimen. The validity of such tests is closely linked to the establishment of a quasi-static stress equilibrium in the sample. The design of the tensile composite geometry, therefore, has to achieve the following main requirements:

- a. The specimen has to be short enough to achieve an early quasi-static force equilibrium and to increase the achievable maximum strain rate, yet the gauge section should be long enough to be free of any influence from the grips,
- b. A state of uniform stress and strain has to be achieved in the gauge section,
- c. The design of the specimen has to promote failure within the gauge section,
- d. The geometry has to be representative of the material constituents.

Dog-bone sample geometries can be designed to fulfill these requirements, in which a reduction in width is achieved compared to the shoulder, i.e., gripping, region. As a consequence, a transition zone is created between the gauge section and the shoulder section. For ductile metallic materials, the dog-bone geometry is highly effective since plasticity plays an important role in overcoming stress concentrations in the transition zones and promoting failure in the gauge section. However, Verleysen et al. [16] reported that the transition zones tend to introduce additional deformation attributed to the sample's gauge section, and thus overestimates the strain of the sample when using classical Hopkinson analysis. On the other hand, for brittle composite materials, the dog-bone geometry shows a tendency of failure in the transition zone due to stress concentrations [17]. A variety of dog-bone samples with different dimensions were typically used by several researchers [18–22]. Dog-bone samples which are reduced in the thickness direction rather than the width were also used by some researchers [23–25]. Despite its effectiveness, it has been argued that reducing the thickness will reduce the areas which are rich in resin, and therefore change the overall representativeness of the tested material [26]. In addition, a thick section is typically required for this type of samples. The above requirements highlights the difficulty of choosing a good sample geometry which can fulfill all the testing requirements. A compromise between the gauge length, width, and transition zone radius is, therefore, necessary to design a good dog-bone geometry for high strain rate tensile testing. The design of the gripping system (as mentioned in chapter 3) has to be considered as well when designing the tensile sample geometry. Based on the geometries available in the literature, it can be seen that the dimensions of the gauge section lies within the range of 6-30 mm for the gauge length and 3-25 for the width. Transition zones vary with radii of 2 to 50 mm. The variation of the section dimensions highly depends on the mechanical properties of the material being tested [22]. According to Foroutan et al. [18], larger transition zone reduces the tendency of failure at the transition zone. However, care should

be taken to limit the overall length of the sample to achieve the required quasi-static equilibrium.

To overcome some of the limitations of the dog-bone samples, rectangular (straight) strip samples were also used [26–28]. The rectangular strip sample is typically used in standard testing of composites [29], and has a parallel, uniform rectangular cross section with no transition zones, thus eliminates the failure tendency at the transition zones. However, the rectangular strip geometry introduces serious challenges related to the clamping of the sample on the input and the output bars for load introduction, especially when a large number of samples has to be tested. For example, if rectangular strip samples are gripped with a typical serrated wedge action grip (as in standard quasi-static testing), a soft tab material has to be used between the grip face and the sample to prevent the indentation of the grips to the sample and hence premature failure. In such case, stress concentrations at the tab ends arises which might also lead to failure [30]. Additionally, a straight strip sample with large width and/or thickness will require a relatively high force to reach failure. This can either cause a premature failure in the grips, or even exceed the yielding strength of the Hopkinson bars in some cases.

5.3.2. Sample clamping and load introduction

Clamping of tensile samples between the split Hopkinson bars should be carefully performed in such a way to provide correct load transfer the sample, without introducing unnecessary mechanical impedance mismatches with the bars or disturbing the wave propagation, also without causing premature failure at the grip area. Fixing the tensile samples by adhesives has been used extensively in the literature [22,31]. While this fixing method provides minimum interference with the waves and excellent load transfer, it is time consuming especially for a large testing program. This is due to the time required by the adhesive to cure at room temperature. Additionally, removing the fractured samples after testing is usually difficult to perform, and preparing the surfaces for reapplying the adhesive requires several cleaning and grinding processes. Alternatively, mechanical clamping was effectively used in testing metallic materials. Examples of mechanical clamping are pin/slot systems and form fitting systems [32]. Form fitting systems can only be used for large thickness composite dogbone samples which have woven fiber architecture or low longitudinal orthotropy (where the properties in the longitudinal and transverse directions are comparable) [18]. A pin/slot system was successfully used for fixing tensile composite samples at high strain rates [33,34], in addition to wedge action grips [27]. It should be noted that the use of pin/slot systems involves drilling the sample to accommodate the pin, which introduces some stress concentrations and possibly a premature failure in the grip section. This can be solved by the addition of a tab material to prevent premature failure at the pin hole.

In this part of chapter 5, the challenges of tensile testing of composites with the split Hopkinson bar technique are addressed. A preliminary assessment of two types of sample geometries, namely a dog-bone geometry and a straight strip geometry, is performed. The selected dog-bone sample geometry is based on the sample geometries used by Gilat et al. [21] and Del Rio et al. [22]. For the straight strip sample, a uniform cross section with the same

dimensions as the gauge section of the dog-bone sample was used. The criteria for the assessment include the achievement of the quasi-static force equilibrium and the achievement of a uniform strain distribution in the gauge section. For the latter, local full strain fields were measured using the 2D DIC technique for both geometries. The stress-strain response and strain rates obtained by classical Hopkinson analysis were compared to those measured using high speed 2D DIC for both geometries. Additionally, reference static experiments were also carried out to evaluate the use of these geometries at quasi-static strain rates. This study focuses on the linear elastic behavior of the basalt fiber reinforced composites up to a strain level of 2% for both static and dynamic experiments.

5.3.3. Experimental testing conditions in tension

5.3.3.1. Material and specimen geometries

The tested material was woven basalt fiber reinforced epoxy composite. Materials were supplied in the form of sheets with thickness 1.6 mm, made up of 10 cross ply laminates. The distance between each two consecutive fiber tows is 2 mm, therefore, the minimal width of the gauge section was chosen to include at least 2 repeated unit cells. This ensures a correct representation of the material constituents, as recommended by ASTM D6856/D6856M [35]. Dog-bone samples were cut to dimension using water jet cutting, while straight strip samples were cut using a water cooled cut-off wheel. Special precaution was taken to ensure that all sides of the straight strip sample were square and parallel. Figure 5.15 shows the dimensions of both the dog-bone and the straight strip samples, respectively. The gauge length and width for both geometries were 10 mm and 4 mm, respectively. All samples were extracted from the sheet in the fill direction (perpendicular to the main fiber warp direction). Aluminum tabs were glued at each side of the shoulders of the dog-bone specimens using a structural grade epoxy glue, to account for any possible premature failure in the shoulders. The straight strip samples were glued inside two slotted aluminum tabs using a structural grade epoxy glue. Each aluminum tab was designed so that it includes a chamfered edge to reduce the stress concentrations at the ends of the tabs. Significant effort was exerted to ensure that the center line of the parallel strip is carefully aligned with the centers of the holes for the pins. In order to avoid any discrepancies related to sample geometries or clamping technique, the same geometries and clamping technique were used for both reference quasi-static and dynamic tensile experiments.

5.3.3.2. Sample clamping and alignment

A pin/slot sample fixing technique was adopted for fixing the tensile samples between the input and output bars, as well as for quasi-static tests. This choice is particularly for the convenience of testing a large number of samples, and the effectiveness in load transfer from the bars to the samples. The tabs were made of aluminum and had the same diameter as the bars so as not to introduce any impedance mismatch. Figure 5.16 shows a schematic of the slotted end tabs with the pins.

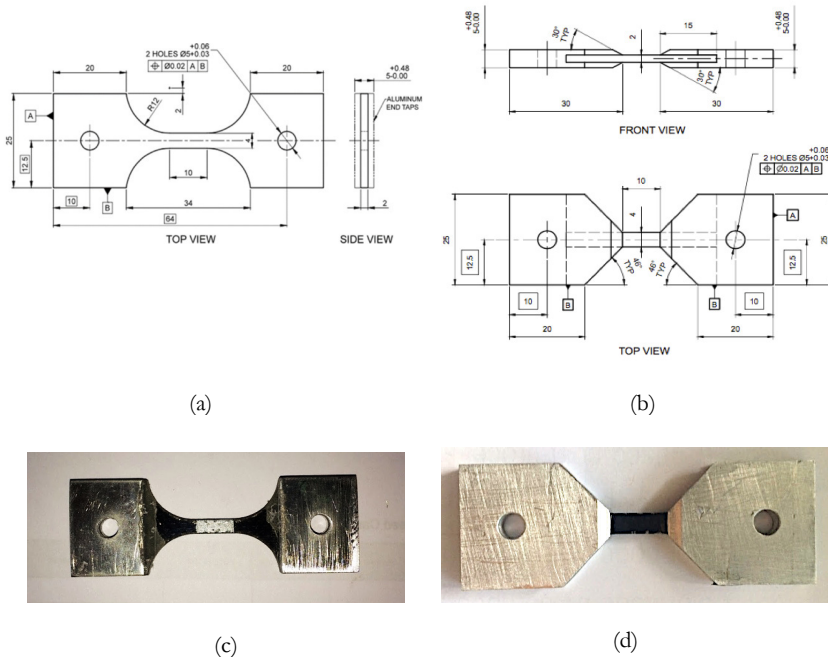


Figure 5.15. Sample geometries used: (a) dog-bone geometry, (b) straight strip geometry, (c) image of a dog-bone sample, (d) image of a straight strip sample

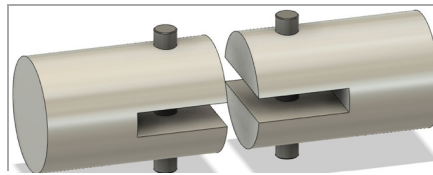


Figure 5.16. Slotted end tabs for the tensile samples

Each end tab was attached to each bar using adhesives. A special alignment tool was developed to align the end tabs to the bars, as shown in Figure 5.17. The use of this alignment tool also guarantees the alignment of the brittle samples with the pin holes and the bars.

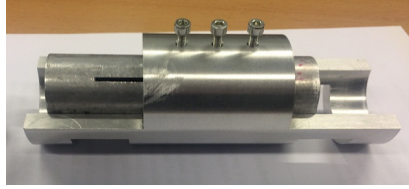


Figure 5.17. Alignment tool for slotted end tabs with the bars

5.3.3.3. *Quasi-static testing*

Reference quasi-static tests were carried out using the Instron 5569 universal testing machine at a testing speed of 2 mm/min, corresponding to a strain rate of 0.0006 s^{-1} in the gauge section. The load was measured using a 50 kN load cell. Samples were placed between 2 long slotted bars using two 5 mm diameter dowel pins. DIC technique was used to measure localized strain fields on the surface of the samples. To this purpose, a 5 megapixel camera was used to capture images of the speckled sample surface during the deformation at a rate of 2 images/second and in a 2D DIC configuration. In order to analyze the deformations in the transition zone of the dog-bone sample, the field of view was adjusted to include the transition zones in addition to the sample's gauge section. Figure 5.18 shows the quasi-static setup.

5.3.3.4. *High strain rate testing*

High strain rate tensile experiments were carried out using the split Hopkinson tensile bar described in chapter 3. The dynamic tensile stress wave was generated by accelerating an impactor towards a flange at the end of the input bar, at a speed of 8 m/s. Samples were placed and aligned between the two slotted aluminum tabs. The average stress, strain, and strain rate in the sample gauge section were calculated from the classical Hopkinson bar analysis (see chapter 3). Local strain in the gauge section were also measured using 2D DIC technique. For this purpose, a Photron AX200 Mini high speed camera was used to capture images of the speckled sample during deformation, at a speed of 86,400 frames per second, and at a resolution of 128x288 pixels. Due to the limited resolution available at the selected frame rate, only the gauge section of the sample was included in the field of view for both sample geometries. Figure 5.19 shows the high strain rate tensile setup with the optical setup used.

5.3.3.5. *Processing parameters for the DIC*

All captured images were analyzed and processed using MatchID commercial digital image correlation software, in order to obtain the full strain fields during the static and dynamic experiments. Table 5.4 indicates the different processing parameters and correlation criterion used. Localized strains in the direction of loading ϵ_{DIC} were calculated as average values taken at a gauge area of 8x4 mm. The chosen processing parameters allowed to achieve a strain resolution of approximately 100 microstrains for both quasi-static and dynamic experiments.

For the dynamic experiments, the strain rate based on DIC was calculated as the slope of the axial DIC strain-time curve in the range where nearly a constant strain rate was achieved.

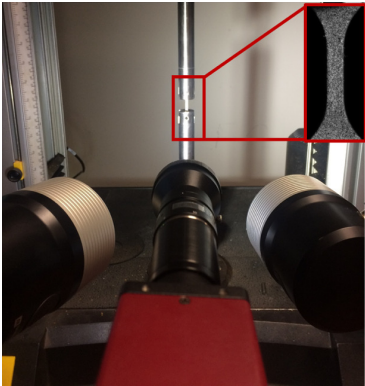


Figure 5.18. Quasi-static setup with 2D DIC

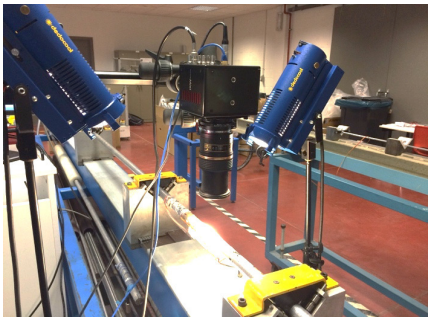


Figure 5.19. High strain rate setup with 2D DIC

Table 5.4. Processing parameters for the DIC for tensile experiments

Parameter	Value
Correlation Criterion	Zero normalized sum of square differences (ZNSSD)
Interpolation Order	Bicubic spline
Shape function	Affine
Subset size	21x21 pixels
Step size	10 Pixels
Strain window size	15 Pixels
Strain convention	Hencky

5.3.4. Results and discussion

5.3.4.1. Stress-strain response and evaluation of the axial strain homogeneities for both geometries in quasi-static conditions

As mentioned earlier, the axial strain fields were extracted from an area of $8 \times 4 \text{ mm}^2$ within the gauge section of the sample. In order to further study the uniformity of the axial strain fields within the gauge section of both geometries, the average strain fields were also extracted for a smaller gauge area of $5 \times 4 \text{ mm}^2$ and were compared to that of the larger area of $8 \times 4 \text{ mm}^2$. Figure 5.20 shows an example of the quasi-static stress-strain response for the dog-bone and the straight strip sample based on 2D DIC strain measurements for gauge area of $8 \times 4 \text{ mm}^2$ and $5 \times 4 \text{ mm}^2$. Additionally, the corresponding full field axial strain map is indicated at the corresponding points on the stress-strain curve. The blue color indicates a strain level of 0, while the red color indicates a strain level of 0.04. At least 2 experiments were performed for each condition, therefore, the curves shown are representative examples for each condition. It can be clearly seen that nearly identical stress-strain responses were obtained for both extraction areas for both geometries. Furthermore, the indicated axial strain fields up to 2% strain also show the strain uniformity within the gauge section. The strain fields at different stress levels also indicate a state of uniform strain within the gauge section for both geometries. For the dog-bone sample, the same strain field in the gauge section was extending even into the transition zone. Some strain concentrations were also observed in the transition zone at stress levels of approx. 280 MPa for the dog-bone geometry, and at the ends of the aluminum end tab for the straight strip geometry. These strain concentrations began to develop with the progression of deformation until fracture, as indicated in Figure 5.21. The developed strain concentrations eventually acted as initiators of fracture in the transition zone and at the end tabs, as indicated by the red arrows in Figure 5.21. This is due to stress concentration effects associated with the end tab and the transition zones, which is a well-known issue in standard quasi-static testing of composites [18,26,30].

Figure 5.22 shows a comparison between the stress-strain response obtained by the dog-bone and the straight strip samples geometries at quasi-static strain rates, based on 2D DIC strain measurements. It can be seen that the stress-strain response for both geometries shows very good agreement up to 0.02 axial strains.

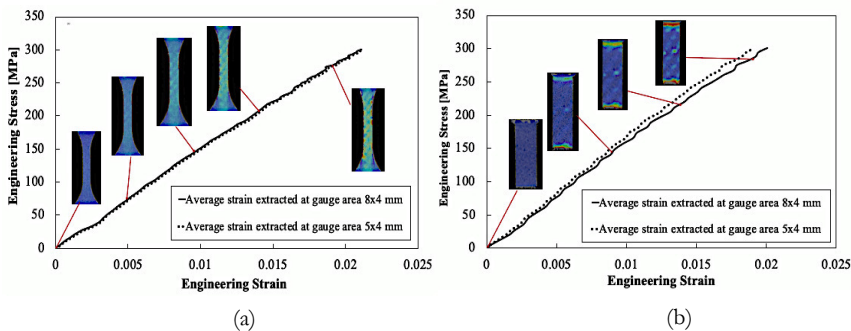


Figure 5.20. Quasi-static stress-strain response for different DIC extraction areas and with DIC strain fields up to 0.02 strain: (a) dog-bone geometry, (b) straight strip geometry

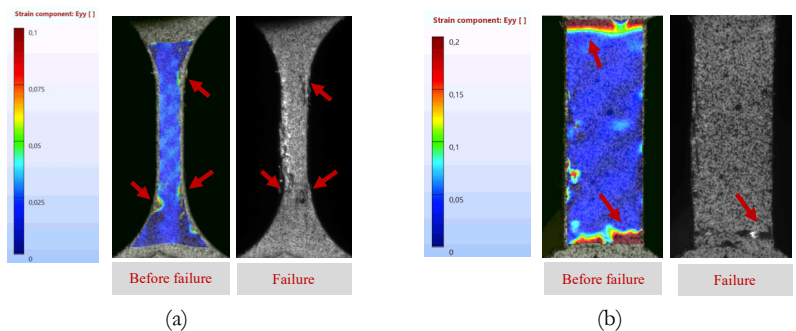


Figure 5.21. Concentrations of strains at the onset of fracture based on DIC axial strain fields: (a) dog-bone sample, (b) straight strip sample

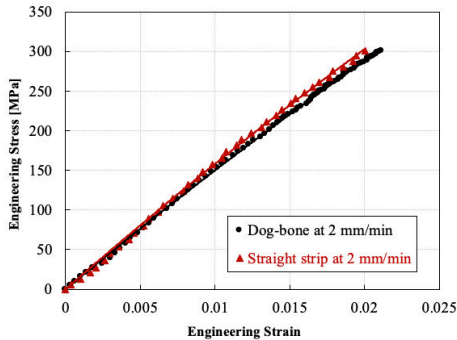


Figure 5.22. Comparison between the stress-strain response of dog-bone and straight strip geometries at quasi-static strain rates

5.3.4.2. Effect of the transition zone on the total deformation of the dog-bone geometry

To further study the contribution of the transition zone to the total strain of the deformed sample, axial strains were extracted along a vertical central line, which passes through the transition zones and the gauge section, as shown in

Figure 5.23. The contribution of the transition zone is nearly equal to that of the gauge section during the progress of the deformation. This is mainly related to the linear elastic behaviour of the basalt epoxy composite up to 2% strain, as opposed to metals where plasticity plays a role in concentrating the deformation within the gauge section. The observed waviness in the strain data is due the weaving (interlocking) nature of the fabric tows. Assuming that the same sample geometry will be used for dynamic tensile testing conditions under a quasi-static equilibrium, the deformation of the transition zones will also contribute to the total strain of the sample, resulting in an overestimation of the calculated strain based on classical Hopkinson analysis.

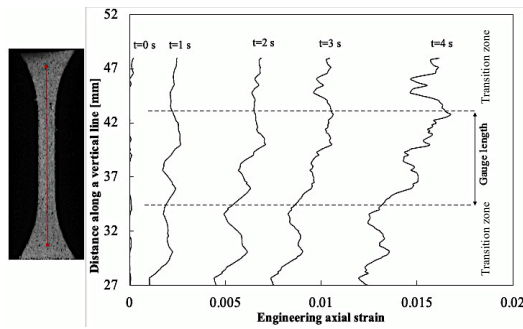


Figure 5.23. Distribution of the axial strain rates along a vertical centerline during deformation of the dog-bone geometry at quasi-static testing

5.3.4.3. Establishment of quasi-static equilibrium for both geometries at high strain rates

The achievement of the quasi-static stress equilibrium was experimentally verified for all dynamic experiments by comparing the forces at the interfaces of input and output bars. Figure 5.24 shows a comparison between the input and output bar forces for both dog-bone and straight strip sample geometries in one of the dynamic tensile tests. It can be seen that the input and the output bar forces show excellent agreement in both sample geometries. This indicates that both dog-bone geometry and straight strip geometry achieved the required quasi-static stress equilibrium throughout the high strain rate tensile experiments.

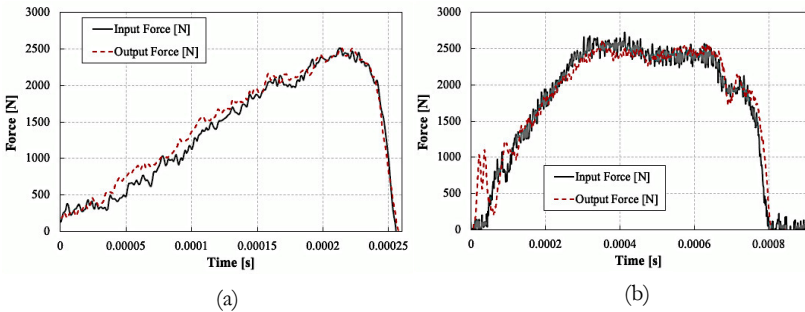


Figure 5.24. Comparison of the input and output forces equilibrium at the specimen/bar interface: (a) Straight strip geometry, (b) dog-bone geometry

5.3.4.4. Stress-strain response and evaluation of the axial strain homogeneities for both geometries at high strain rate conditions

Figure 5.25 represents the high strain rate stress-strain response of the basalt epoxy composites using both the dog-bone and the straight strip geometries, based on high speed 2D DIC strain measurements. Additionally, the corresponding full field strain map is indicated at the corresponding points on the stress-strain curve. The blue color indicates a strain level of 0, while the cyan color indicates a strain level of 0.02. Similar to the quasi-static strain rate conditions, the average axial strains were extracted at gauge areas $8 \times 4 \text{ mm}^2$ and $5 \times 4 \text{ mm}^2$ respectively to check the uniformity of the strains within the gauge section. It can be seen that the stress-strain responses for both extraction areas show very good agreement. The strain fields also indicate a good homogeneity along the gauge section for both geometries. Figure 5.26 shows a comparison between the stress-strain response of both the dog-bone and the straight strip tensile geometries at high strain rates. Considering the dynamic nature of the tests, the two geometries show good agreement in dynamic stress-strain response.

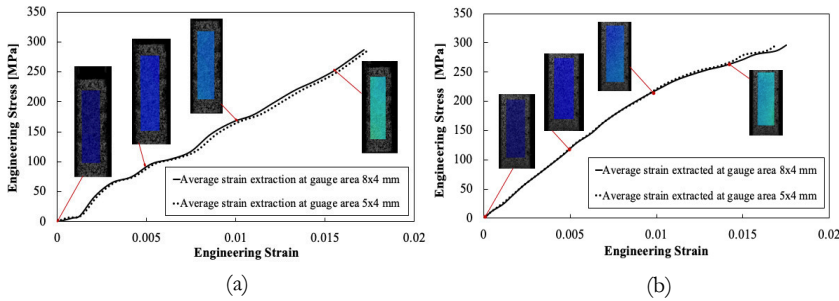


Figure 5.25. High strain rate stress-strain response for different DIC extraction areas and with DIC strain fields up to 0.02 strain: (a) dog-bone geometry, (b) straight strip geometry

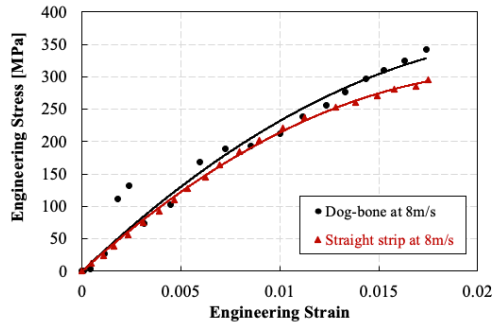


Figure 5.26. Comparison between the stress-strain response of dog-bone and straight strip geometries at high strain rates

Figure 5.27 shows a comparison between the high strain rate tensile behavior based on the classical Hopkinson analysis and the high speed DIC measurements for both sample geometry. It can be seen that the strains obtained by classical Hopkinson analysis are clearly overestimated by a factor of approx. 3 compared to the strains obtained by high speed 2D DIC technique for both geometries. In the classical Hopkinson analysis, the measured strain waves are shifted to the bar interfaces at the center of the dowel pins, where the actual transfer of the load to the sample takes place. As such, the length between the two centers of the dowel pins represents the effective gauge length. This effective gauge length includes not only the deformations within the gauge section, but also the deformations outside the gauge section in the pins and the transition zones. The use of a smaller actual gauge length in the calculation of strains results in the observed overestimation in the strains. In the case of the straight strip geometry, deformations of the pins and the aluminum tabs are also included within the apparent gauge length, resulting in the overestimation of strains.

Figure 5.28 shows the average strain rates achieved using the high speed 2D DIC technique and the classical Hopkinson analysis for both geometries. Using classical Hopkinson analysis, the average strain rate achieved was 300 s^{-1} for the dog-bone geometry and 310 s^{-1} for the straight strip geometry. However, the average strain rates achieved using the local, high speed 2D DIC technique were 80 s^{-1} for the dog-bone geometry, and 90 s^{-1} for the straight strip geometry. The average strain rates obtained by the classical Hopkinson analysis is also overestimated by a factor of approx. 3 compared to the strain rates achieved using the high speed 2D DIC technique for both geometries. It can be seen also that both geometries achieved very similar strain rates within the gauge section of the sample.

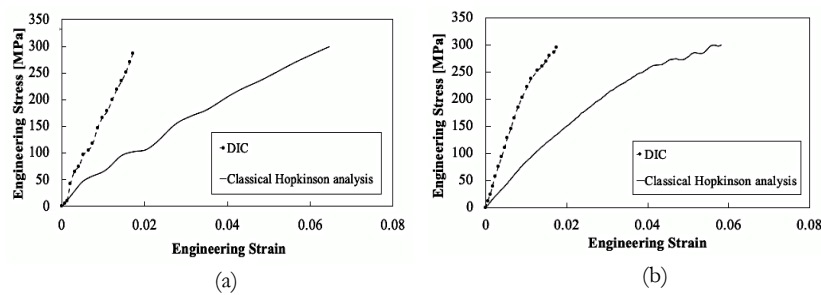


Figure 5.27. Stress-strain response of basalt epoxy based on 2D DIC and classical Hopkinson analysis: (a) dog-bone sample, (b) straight strip sample

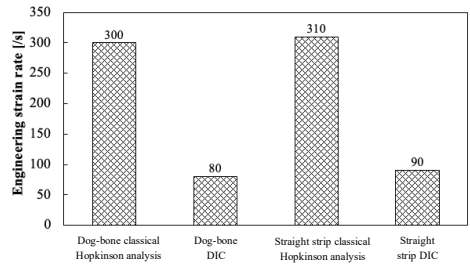


Figure 5.28. Achieved strain rates of basalt epoxy using dog-bone and straight strip geometries based on 2D DIC and classical Hopkinson analysis

5.4. Conclusions

In this chapter, the challenges in testing polymers and composites using the split Hopkinson bar technique were discussed. In the first part of the chapter, important aspects such as the design of a compression sample geometry which can fulfil the high strain rate testing requirements, the aspects related to boundary conditions, load introduction, and validating the testing and the material assumptions were discussed in detail. The challenges in compression testing were experimentally investigated using RTM6 neat epoxy resin at quasi-static and high strain rates. A novel alignment tool and a self-alignment attachment were developed specifically to provide good interfacial contact conditions at the start of the compression tests, and to align the samples between the bars. After selecting a suitable sample geometry, the establishment of the quasi-static equilibrium was studied. Additionally, the uniformity of axial strains and the effect of strain rate and lubrication on the interfacial friction were analyzed with the aid of 3D DIC. Furthermore, the assumption of volume conservation during yielding of epoxy was also validated by measuring the instantaneous cross section area of the deforming sample using the DIC. In the second part of the chapter, the challenges in the tensile testing of brittle composites using the split Hopkinson bar technique, such as design of the tensile sample geometry and clamping techniques, were investigated. In order to select the most appropriate sample geometry to study the tensile behavior of the basalt/epoxy composite, two of the most used samples geometries, i.e., namely dog-bone and straight strip geometries, were

compared and experimentally assessed. The criteria for the assessment were the establishment of the dynamic stress equilibrium and the achievement of strain homogeneity along the gauge section. To this purpose, the 2D DIC technique was used to measure the full strain fields developed locally along the gauge section at quasi-static and high strain rates. During testing, special attention and effort was paid to ensure the proper alignment between the bars and the samples, and the alignment of the straight strip sample components. The stress-strain behavior of the basalt material, up to 0.02 strain, obtained using both sample geometries was presented and compared. Moreover, for the dog-bone geometry, the strain contribution of the transition zone to the total strain of the sample was analyzed at quasi-static strain rates. Furthermore, a comparison between the strains and strain rates obtained using the classical Hopkinson analysis and the DIC technique was also presented. Considering the materials and testing conditions used, the following can be concluded:

1. The selected compression sample geometry with a height to diameter ratio of 0.5 fulfilled the requirement of an early quasi-static equilibrium, which can enable the extraction of the dynamic elastic constants, i.e. elastic modulus and Poisson's ratio, at high strain rates.
2. The novel self-alignment attachment provided good initial contact conditions which was evident from the stress-strain response of the epoxy resin. Additionally, the self-alignment tool which was used for the high strain rates tests introduced only negligible interference with the propagating stress waves.
3. The experimental assessment of the interfacial friction, defined by the barreling ratio, showed an increase in the barreling ratio during the duration of the test, i.e. with increasing the axial strains, but the ratio also decreased with increasing the strain rates. This was also evident from the nearly homogeneous axial strain fields by the DIC.
4. The assumption of volume conservation in yielding and post-yielding stages in brittle polymers cannot be considered valid. The volume of the sample is reduced during compression by approx. 3% in non-elastic volume change. Additionally, the difference in the peak yield strength with and without the assumption of volume conservation is nearly 10%, which cannot be neglected.
5. Both sample geometries fulfilled the required assessment criteria of the quasi-static stress equilibrium and axial strain field homogeneity along the gauge section up to 2% strain. This indicates that both sample geometries can achieve a valid split Hopkinson tensile bar test for the basalt/epoxy composite.
6. The stress-strain behaviors of the basalt/epoxy composite based on both geometries were in good agreement under both quasi-static and the high strain rate testing conditions.
7. For the dog-bone geometry at quasi-static strain rates, the contribution of the transition zones to the total strain of the sample was nearly equal to the deformation of the gauge section. Assuming that the same sample geometry will be used for dynamic tensile testing conditions under a quasi-static equilibrium, the deformation of the transition zones will also contribute to the total strain of the sample at high strain rates, resulting in an overestimation of the calculated strain based on classical Hopkinson analysis.

8. Classical Hopkinson analysis also overestimates the actual strains and strain rates in the sample by approx. a factor of 3 for both geometries. Local measurement of the strains along the gauge section is, therefore, crucial for the reliability of the characterization of the high strain rate behavior of composites.

The above mentioned conclusions suggest that either of the two geometries can be used in high strain rate tensile testing of woven composite materials using the split Hopkinson tensile bar. Both geometries will produce reliable results, provided that a local strain measurement system is used, so as not to cause overestimation in strains or strain rates. Both geometries will also suffer from stress concentrations, either in the transition zone (as in the case of the dog-bone geometry) or at the tab ends (as in the case of the straight strip geometry). In both cases, however, the same sample geometry should be used for all testing conditions, in order not to introduce discrepancies related to the sample geometry. As mentioned in section 5.3.3, the straight strip geometry required tedious effort to ensure the alignment of the centerline of the sample with the holes of the pin, in addition to the difficulties associated with gluing the sample to the aluminum tabs. The dog-bone sample, on the other hand, is produced in one step using automated water jet cutting, and therefore, parallel sections and aligned holes are automatically produced with a high accuracy. Gluing of the aluminum tabs is for the dog-bone sample easier compared to the end tabs in the straight strip geometry. Therefore, the dog-bone sample geometry was selected for the tensile testing of the woven composites.

References

- [1] Jerabek, M., Major, Z., and Lang, R. W., 2010, "Uniaxial Compression Testing of Polymeric Materials," *Polym. Test.*, **29**(3), pp. 302–309.
- [2] Pei, P., Pei, Z., and Tang, Z., 2020, "Numerical and Theoretical Analysis of the Inertia Effects and Interfacial Friction in SHPB Test Systems," *Materials (Basel)*, **13**(21), pp. 1–17.
- [3] Li, P., Siviour, C. R., and Petrinic, N., 2009, "The Effect of Strain Rate, Specimen Geometry and Lubrication on Responses of Aluminium AA2024 in Uniaxial Compression Experiments," *Exp. Mech.*, **49**(4), pp. 587–593.
- [4] Zhong, W. Z., Rusinek, A., Jankowiak, T., Abed, F., Bernier, R., and Sutter, G., 2015, "Influence of Interfacial Friction and Specimen Configuration in Split Hopkinson Pressure Bar System," *Tribol. Int.*, **90**, pp. 1–14.
- [5] Morelle, X. P., Chevalier, J., Bailly, C., Pardoën, T., and Lani, F., 2017, "Mechanical Characterization and Modeling of the Deformation and Failure of the Highly Crosslinked RTM6 Epoxy Resin," *Mech. Time-Dependent Mater.*, **21**(3), pp. 419–454.
- [6] Gorham, D. A., 1991, "The Effect of Specimen Dimensions on High Strain Rate Compression Measurements of Copper," *J. Phys. D: Appl. Phys.*, **24**(8), pp. 1489–1492.
- [7] Siviour, C. R., 2017, "High Strain Rate Characterization of Polymers," *AIP Conference Proceedings*, p. 060029.
- [8] Gerlach, R., Siviour, C. R., Petrinic, N., and Wiegand, J., 2008, "Experimental Characterisation and Constitutive Modelling of RTM-6 Resin under Impact Loading," *Polymer (Guildf)*, **49**(11), pp. 2728–2737.
- [9] Gómez-del Río, T., and Rodríguez, J., 2012, "Compression Yielding of Epoxy: Strain Rate and Temperature Effect," *Mater. Des.*, **35**(C), pp. 369–373.
- [10] Tuninetti, V., Gilles, G., Péron-Lühns, V., and Habraken, A. M., 2012, "Compression Test for Metal Characterization Using Digital Image Correlation and Inverse Modeling," *Procedia IUTAM*, **4**, pp. 206–214.
- [11] Chen, W. W., and Song, B., 2013, Split Hopkinson (Kolsky) Bar: Design, Testing and Applications.

- [12] Sunny, G., Yuan, F., Prakash, V., and Lewandowski, J., 2009, "Design of Inserts for Split-Hopkinson Pressure Bar Testing of Low Strain-to-Failure Materials," *Exp. Mech.*, **49**(4), pp. 479–490.
- [13] Miao, Y. G., Li, Y. L., Liu, H. Y., Deng, Q., Shen, L., Mai, Y. W., Guo, Y. Z., Suo, T., Hu, H. T., Xie, F. Q., Zhao, L., Mao, Y. J., and Qi, W., 2016, "Determination of Dynamic Elastic Modulus of Polymeric Materials Using Vertical Split Hopkinson Pressure Bar," *Int. J. Mech. Sci.*, **108–109**(July 2018), pp. 188–196.
- [14] Chen, W. W., Rajendran, A. M., Song, B., and Nie, X., 2007, "Dynamic Fracture of Ceramics in Armor Applications," *J. Am. Ceram. Soc.*, **90**(4), pp. 1005–1018.
- [15] Othman, R., 2018, *The Kolsky-Hopkinson Bar Machine: Selected Topics*, Springer International Publishing, Cham.
- [16] Verleysen, P., and Degrieck, J., 2004, "Experimental Investigation of the Deformation of Hopkinson Bar Specimens," *Int. J. Impact Eng.*, **30**(3), pp. 239–253.
- [17] Reyes, G., and Sharma, U., 2009, "Analysis of Woven Glass Fiber Reinforced Thermoplastic Composites under Varying Strain Rates," *Speautomotive.Com*, pp. 1–17.
- [18] Foroutan, R., Nemes, J., Ghiasi, H., and Hubert, P., 2013, "Experimental Investigation of High Strain-Rate Behaviour of Fabric Composites," *Compos. Struct.*, **106**(C), pp. 264–269.
- [19] Rodríguez, J., Chocron, I. S., Martínez, M. A., and Sánchez-Gálvez, V., 1996, "High Strain Rate Properties of Aramid and Polyethylene Woven Fabric Composites," *Compos. Part B Eng.*, **27**(2 PART B), pp. 147–154.
- [20] Ma, P., Hu, H., Zhu, L., Sun, B., and Gu, B., 2011, "Tensile Behaviors of Co-Woven-Knitted Fabric Reinforced Composites under Various Strain Rates," *J. Compos. Mater.*, **45**(24), pp. 2495–2506.
- [21] Gilat, A., Schmidt, T. E., and Walker, A. L., 2009, "Full Field Strain Measurement in Compression and Tensile Split Hopkinson Bar Experiments," *Exp. Mech.*, **49**(2), pp. 291–302.
- [22] Gómez-del Río, T., Barbero, E., Zazra, R., and Navarro, C., 2005, "Dynamic Tensile Behaviour at Low Temperature of CFRP Using a Split Hopkinson Pressure Bar," *Compos. Sci. Technol.*, **65**(1), pp. 61–71.
- [23] Harding, J., and Welsh, L. M., 1983, "A Tensile Testing Technique for Fibre-Reinforced Composites at Impact Rates of Strain," *J. Mater. Sci.*, **18**(6), pp. 1810–1826.
- [24] Welsh, L. M., and Harding, J., 1985, "Effect of Strain Rate on the Tensile Failure of Woven Reinforced Polyester Resin Composites," *Le J. Phys. Colloq.*, **46**(C5), pp. C5-405-C5-414.
- [25] Naik, N. K., Yernamma, P., Thoram, N. M., Gadipatri, R., and Kavala, V. R., 2010, "High Strain Rate Tensile Behavior of Woven Fabric E-Glass/Epoxy Composite," *Polym. Test.*, **29**(1), pp. 14–22.
- [26] Hodgkinson, J. M., 2000, *Mechanical Testing of Advanced Fibre Composites*, Woodhead Publishing.
- [27] Taniguchi, N., Nishiwaki, T., and Kawada, H., 2007, "Tensile Strength of Unidirectional CFRP Laminate under High Strain Rate," *Adv. Compos. Mater. Off. J. Japan Soc. Compos. Mater.*, **16**(2), pp. 167–180.
- [28] Suga, K., Okamoto, K., Takagi, K., Nakatani, H., Ogihara, S., and Kikuchi, M., 2012, "Numerical Validation of Split Hopkinson Pressure Bar Technique for Evaluating Tensile Mechanical Properties of CFRP Laminates," *Adv. Compos. Mater.*, **21**(3), pp. 221–232.
- [29] ASTM D3039 / D3039M-17, 2017, Standard Test Method for Tensile Properties of Polymer Matrix Composite Materials, West Conshohocken, PA, 2017.
- [30] Baere, I. De, Paeppegem, W. Van, and Degrieck, J., 2009, "On the Design of End Tabs for Quasi-Static and Fatigue Testing of Fibre-Reinforced Composites," *Polym. Compos.*, **30**(4), pp. 381–390.
- [31] Eskandari, H., and Nemes, J. A., 2000, "Dynamic Testing of Composite Laminates with a Tensile Split Hopkinson Bar," *J. Compos. Mater.*, **34**(4), pp. 260–273.
- [32] Ledford, N., Paul, H., Ganzenmüller, G., May, M., Höfemann, M., Otto, M., and Petrinic, N., 2015, "Investigations on Specimen Design and Mounting for Split Hopkinson Tension Bar (SHTB) Experiments," *EPJ Web Conf.*, **94**, p. 01049.
- [33] Li, X., Yan, Y., Guo, L., and Xu, C., 2016, "Effect of Strain Rate on the Mechanical Properties of Carbon/Epoxy Composites under Quasi-Static and Dynamic Loadings," *Polym. Test.*, **52**(C), pp. 254–264.
- [34] Lienhard, J., and Böhme, W., 2015, "Characterisation of Resin Transfer Moulded Composite Laminates under High Rate Tension, Compression and Shear Loading," *Eng. Fract. Mech.*, **149**(C), pp. 338–350.
- [35] ASTM International, 2016, ASTM D6856 / D6856M-03-Standard Guide for Testing Fabric-Reinforced "Textile" Composite Materials, West Conshohocken, PA, 2017.

Intentionally left blank

6

Mechanical behavior of basalt and glass epoxy composites at different strain rates

This chapter was rewritten based on the following articles:

1. Elmahdy, A., and Verleysen, P., 2019, "Tensile Behavior of Woven Basalt Fiber Reinforced Composites at High Strain Rates," *Polym. Test.*, 76, pp. 207–221.
2. Elmahdy, A., and Verleysen, P., 2020, "Mechanical Behavior of Basalt and Glass Textile Composites at High Strain Rates: A Comparison," *Polym. Test.*, 81, p. 106224.
3. Elmahdy, A., and Verleysen, P., 2019, "Comparison between the Mechanical Behavior of Woven Basalt and Glass Epoxy Composites at High Strain Rates," *Mater. Today Proc.*, 34, pp. 171–175. (*presented in The 12th International Conference on Composites Science and Technology, Sorrento, Italy, 2019*)

6.1. Introduction

This chapter discusses the experimental results for tensile and shear properties of the woven composite materials at different strain rates. Both types of materials were manufactured and supplied by Israel Aerospace Industries in Lod, Israel. First, the specimen materials and geometries used are presented in section 6.2. The experimental conditions for the reference quasi-static testing, the high strain rate testing, and the DIC parameters are presented in section 6.3. Section 6.4 presents and discusses the results and discussion on the obtained experimental data. In this section and prior to the formal analysis of the results, the verification of the establishment of the quasi-static equilibrium, the constant strain rate evolution, and the strain homogeneity in high strain rate tensile tests is first discussed. A detailed analysis of the results of the tensile and the shear behaviors of the woven basalt/epoxy composite is presented. Finally, a detailed comparison between the tensile and shear behavior of the woven basalt/epoxy composite and the woven glass/epoxy composite is presented. The main conclusions are finally presented in section 6.4.

6.2. Specimen materials and geometries

The materials considered in this study were woven basalt and woven glass fiber reinforced epoxy composites. The chosen glass epoxy composite is a typical composite used in the manufacturing of aircraft leading edges and aircraft secondary structures. The basalt epoxy composite was chosen to achieve similar fiber volume fraction, density, and stiffness at the quasi-static strain rate range compared to the glass epoxy composite. The same epoxy matrix was used for both composite types. The average diameters of the individual basalt and glass fibers were $13 \pm 5 \mu\text{m}$ and $6 \mu\text{m}$ respectively. Two plates of size 400 x 400 mm and 300 x 300 mm were manufactured from the basalt and the glass composites respectively, using the wet hand layup technique. Woven glass and woven basalt fibers were laminated such that the warp fibers are along the 0° direction and the fill fibers are along the 90° direction of the warp clock. The manufactured plates were cured in a two stage curing cycle at 60°C for 4 hours and 130°C for 3 hours respectively, according to the manufacturer's datasheet. Table 6.1 shows the details of the materials used, and the achieved properties after manufacturing. The void content for both composites was determined according to the ASTM D2734 standard [1]. Due to the selected manufacturing technique, the void content present in the basalt epoxy composite was relatively high, i.e., approx. 8%. Tensile samples with gauge section along the warp direction [0°] and the fill direction [90°], and off axis shear samples [$\pm 45^\circ$] inclined to the warp direction by 45° were cut from the plates using water jet cutting. Figure 6.1 shows the dimensions of the tensile and shear samples used. The chosen dimensions fulfill the requirements of a valid split Hopkinson bar testing (see chapter 5), while guaranteeing the presence of at least 2 repeated unit cells within the gauge section, according to the recommendations of the ASTM D6856/D6856M standard [2]. The gauge area of the shear sample of the basalt epoxy composite was slightly enlarged compared to that of the glass epoxy composite – see Figure 6.1 (b) and (c) – in order to increase the signal to noise ratio in the output bar of the split Hopkinson setup, and hence, increase the accuracy of the shear strength

measurement. Aluminum tabs were attached to the gripping area of all samples – indicated by hatched lines in Figure 6.1 – using a structural grade epoxy adhesive, in order to facilitate load transfer and prevent premature failure around the holes in the gripping area. A black-on-white speckle pattern was applied to the surface of the gauge section of the sample before testing to allow for displacement and strain measurements using the digital image correlation. For both composite materials, the same sample geometry which was used for the quasi-static testing was also used in the high strain rate experiments, in order to avoid discrepancies due to sample geometry when studying the effect of strain rate on the corresponding material behavior. The same boundary conditions were also used for all experiments on both materials.

Table 6.1. Properties of the woven basalt and woven glass epoxy composite materials used

Parameter	Glass epoxy composite	Basalt epoxy composite
Fiber type	Woven E-glass dry fabric (type 7781)	Woven basalt dry fabric (type BAS 220.1270.P)
Fiber manufacturer	Hexcel Corp., USA	BASALTEX™ NV, Belgium
Weave architecture	8 Harness satin weave	Plain weave
Fiber density (g/cm ²)	2.56	2.67
Warp and fill densities (ends/cm)	22.44 (warp) and 21.25 (fill)	7.2 (warp and fill)
Specific surface weight (g/m ²)	299	220
Matrix type	Epoxy (EPIKOTE resin L20 and EPIKURE curing agent 960)	Epoxy (EPIKOTE resin L20 and EPIKURE curing agent 960)
Matrix material manufacturer	HEXION Inc. USA	HEXION Inc. USA
Glass transition temperature (°C)	130 (measured using TMA)	130 (measured using TMA)
Fiber volume fraction	0.52	0.47
Density (g/cm ³)	1.80	1.78
Void content (%)	6	8
Number of plies	10	10
Nominal ply thickness (mm)	0.22	0.16
Nominal sample thickness (mm)	2.2	1.67

6.3. Experimental testing conditions

6.3.1. Quasi-static testing

Reference quasi-static experiments were carried out using the Instron 5569 universal testing machine at testing speeds of 2 and 20 mm/min, aiming at strain rates of 0.0006 and 0.006 s⁻¹ respectively in the sample's gauge section. Samples were placed between the two slotted steel bars, as detailed in chapter 5. Full-field displacements and strains were measured using the 3D DIC, as described in chapter 4, on one side of the gauge section of the sample. Additionally, for the tensile samples, a 120 Ω foil type strain gauge with a gauge length of 5 mm (TML FLA-5-8) was attached on the other side of the gauge section. Images of the speckled samples were

recorded at a resolution of 2452×2056 pixels and a rate of 1 and 3 images/s for the testing speeds of 2 and 20 mm/min respectively. The average speckle size of the samples tested at quasi-static conditions was approx. 0.046 mm, which corresponds to 4.6 pixels on the images. The captured images from the camera, and the strain measurements from the strain gauge on the sample were synchronized with the force signal obtained from the load cell using a NI 9215 data acquisition card. The intrinsic and extrinsic parameters of the 3D DIC system were determined using the procedure detailed in chapter 4. The calibration was carried out using a small etched glass calibration grid, having 9x9 dots and a pitch of 1.34 mm between the centers of the dots. Table 6.2 shows the calibration parameters of the quasi-static DIC system used. Figure 6.2 shows the quasi-static setup used. The average displacement resolution of the quasi-static 3D DIC system was approx. 344 μm .

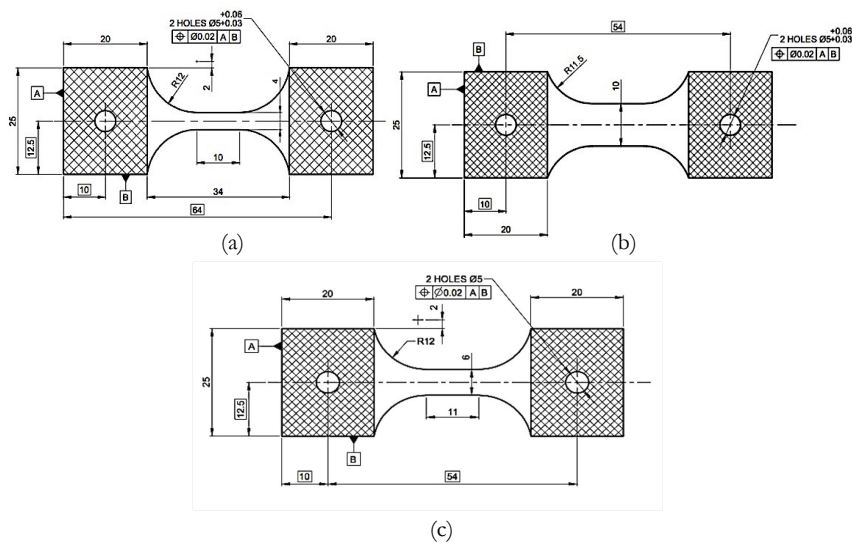


Figure 6.1. Dimensions of the specimens used: (a) tensile sample geometry for glass and basalt composites, (b) shear sample geometry for basalt composite, (c) shear sample geometry for glass composite

Table 6.2. Calibration parameters of the quasi-static 3D DIC setup

Parameter	Camera 1	Camera 2	Stereo setup
Focal lengths (pixels)	60055.1, 60013.75	55471.39, 55476.80	-
Distortion coefficients (K1, K2, K3)	-0.709, 754.19, 0.582	-0.643, 159.24, -0.00098	-
Optical centers (pixels)	1300.15, 1195.21	1273.42, 1871.34	-
Stereo angles (degrees)	-	-	0.72, 12.32, 0.460
Translation (mm)	-	-	-142.65, -0.577, -39.258

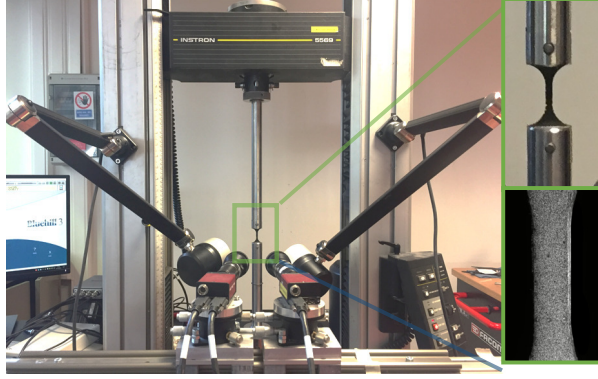


Figure 6.2. Quasi-static setup with detail of the sample gripping (top right) and speckle pattern for 3D DIC (bottom right)

6.3.2. High strain rate testing

High strain rate dynamic experiments were carried out using the split Hopkinson tensile bar, described in chapter 3. Samples were placed between the input and output bar in the slotted ends, as described in chapter 5. The same boundary conditions as in the quasi-static tests were used. The dynamic tensile wave was generated by accelerating the impactor towards the input bar flange at velocities of 8, 11, and 14 m/s. Figure 6.3 shows an example of the incident, the reflected, and the transmitted waves measured on the input and the output bars. The high speed 3D DIC technique (described in chapter 4) was used to measure the local strains and strain rates developed on the surface of the sample. A black-on-white speckle pattern was applied on one side of the sample, using aerosol technique, prior to testing. Additionally, for the tensile samples, on the other side of the gauge section, a $120\ \Omega$ foil type strain gauge with a gauge length of 5 mm (TML FLA-5-8) was attached. Images were recorded at a resolution of 128×265 pixels and a rate of 86,400 images/s. Similar to the quasi-static setup, the intrinsic and extrinsic parameters of the 3D DIC system were determined using the calibration procedure detailed in chapter 4. The calibration was carried out using a small etched glass calibration grid, having 9×9 dots and a pitch of 1.78 mm between the centers of the dots. Table 6.3 shows the calibration parameters for the high speed 3D DIC system. The exposure signal of the slave camera sensor and the strain gauge signals measured on the sample were synchronized with the measured strain signals on the bars using the same HBM high speed data acquisition system. Figure 6.4 shows the dynamic setup used. The average speckle size of the dynamically tested samples was approx. 0.53 mm, corresponding to a size of 5.8 pixels on the images, which is larger compared to the quasi-static 3D DIC system. This is because the individual pixel size of the high speed camera is physically larger than that of the low speed camera. The average displacement resolution was approx. 543 μm .

Table 6.3. Calibration parameters of the high speed 3D DIC setup

Parameter	Camera 1	Camera 2	Stereo setup
Focal lengths (pixels)	4748, 4740	5310, 5302	-
Distortion coefficients (K1, K2, K3)	0.3197, -43.64, 0.2241	0.2413, 16.79, 0.0142	-
Optical centers (pixels)	91.09, 192.9	142.2, 99.63	-
Stereo angles (degrees)	-	-	-0.937, 21.92, -0.8238
Translation (mm)	-	-	-129.2, 3.07, 63.1

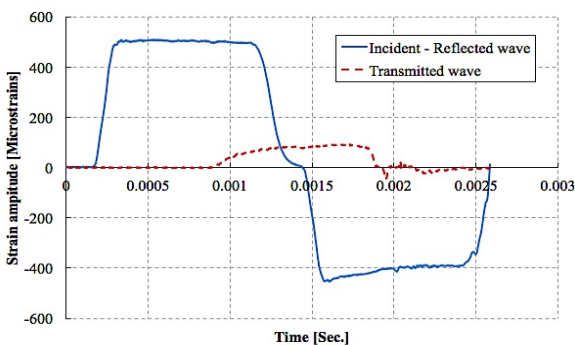


Figure 6.3. Example of the measured incident, reflected, and transmitted strain signals on the input and output bars

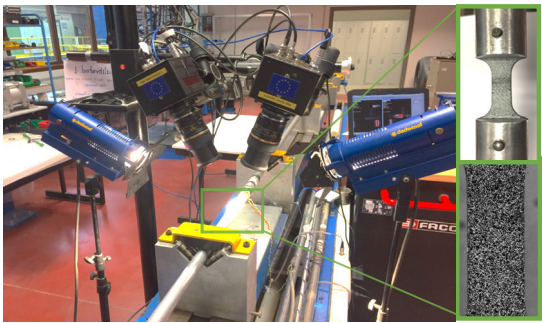


Figure 6.4. Stereo high speed digital image correlation used with detail of the shear sample gripping (top right) and speckle pattern for high speed 3D DIC (bottom right)

6.3.3. DIC processing parameters and data reduction

The different processing parameters used to process and analyse the captured images using MatchID commercial digital image correlation software for both quasi-static and dynamic tests are shown in Table 6.4. The parameters used in the processing of each image allowed to achieve a strain resolution of approx. 260 microstrains for quasi-static tests and approx. 322 microstrains for dynamic experiments. For both tensile and shear experiments, the average axial engineering strain ϵ_{yy} in the loading direction, and average transverse engineering strain ϵ_{xx} perpendicular to the loading direction were calculated from the generated DIC fields as the average strain fields in a gauge area of $8 \times 4 \text{ mm}^2$ at the centre of the sample. The average tensile stress σ in the sample was calculated using equation 3.3. The average engineering tensile strain rate for the static and the dynamic tensile experiments based on DIC measurements was calculated as the slope of the axial DIC strain-time curve in the range where nearly a constant strain rate was achieved. Considering the off-axis shear sample geometry, where the woven fibers are oriented at $\pm 45^\circ$ to the loading direction, the average engineering shear strain γ_{12} in the principal material directions (1-2 direction) was calculated with the transformation of axes using the following relation [3]:

$$\gamma_{12} = \epsilon_{yy} - \epsilon_{xx} \quad (6.1)$$

The average engineering shear strain rate in the principal material directions was calculated as the slope of the shear strain-time curve in the range where nearly a constant strain rate was achieved. Using the transformation of axes at $\pm 45^\circ$, the average engineering shear stress τ_{12} in the principal material direction at high strain rate was calculated using the following relation [3]:

$$\tau_{12} = \frac{\sigma}{2} \quad (6.2)$$

Table 6.4. Processing Parameters for DIC

Parameter	value
Correlation criterion	Zero normalized sum of square differences (ZNSSD)
Interpolation order	Bi-cubic spline interpolation
Shape function	Affine
Subset size (pixel)	35
Step size (pixel)	10
Strain window	15
Strain convention	Biot undeformed (engineering strain convention)

6.4. Results and discussion

6.4.1. Strain rate evolution

Figure 6.5 shows the stress and strain time histories in one of the tensile samples during loading up to failure, using the classical split Hopkinson bar analysis (eqs. (3.11) and (3.12)), the strain gauge measurements on the sample, and the high speed 3D DIC. It can be seen that the classical split Hopkinson bar analysis clearly overestimates the measured strain within the sample by approx. a factor of 5 during loading and up to failure compared to the strains measured locally on the gauge section using strain gauge and DIC technique. As explained in chapter 5, this is attributed to the contribution of: (1) the transition zone deformation to the total deformation of the sample, (2) some deformations around the hole in the grip area of the sample and (3) some deformations of the pin used to grip the sample. Moreover, it should be noted that the strains measured using the classical split Hopkinson bar analysis utilizes the relative displacement between the bar/specimen interfaces to measure the strains. As a consequence, an apparently continuous increase in strain can be seen after failure.

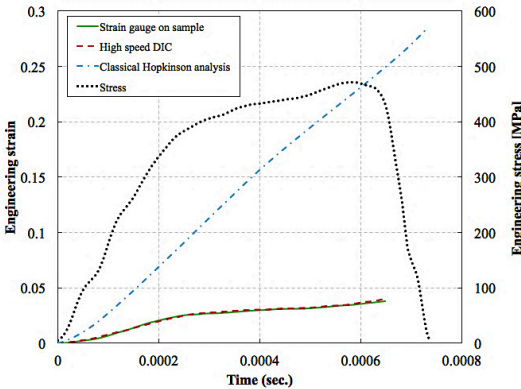


Figure 6.5. Stress and strain histories in the tensile sample during a dynamic test

Figure 6.6 shows a comparison between the strains obtained using the DIC technique and the strain gauge on the sample during a dynamic tensile test. The strains measured using the DIC technique show good agreement with the strains measured using the strain gauges. Consequently, the strains obtained using the DIC technique were used for the rest of reported results.

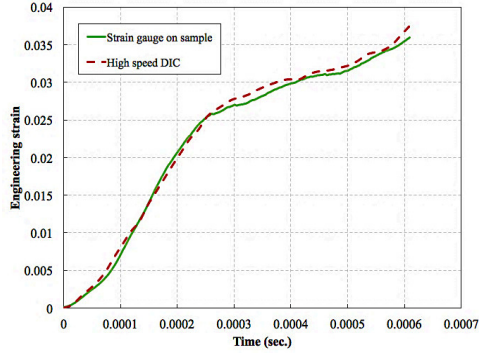


Figure 6.6. Comparison between the strain histories measured using high speed DIC technique and strain gauge on the sample in a dynamic tensile test

Figure 6.7 (a) shows typical time histories of the DIC strain averaged over the gauge section for both glass and basalt epoxy composites during a high strain rate tensile experiment. It can be seen that the progression of the strain over time can be divided into 3 regions: (1) a first region (at time range of 0 to 80 μs and a strain range of 0 to 0.0025 strain) characterized by a rapid increase of strain rate, i.e. slope of the curve, during which the quasi-static sample equilibrium was being established, (2) a second region (at time range of 80 to 310 μs and a strain range of 0.0025 to 0.02) with a quasi-constant strain rate, and (3) a third region (starting from time range of 310 μs and strain of 0.02 until failure) accompanied by a reduction in strain rate, which corresponds to the non-linear behavior of the tested composites before fracture. Figure 6.7 (b) shows the evolution of the strain for both glass and basalt epoxy composites during a high strain rate shear experiment with respect to time. Due to the high elongation of the off-axis [$\pm 45^\circ$] shear samples resulting from severe fiber rotations in the basalt epoxy composites, the speckle pattern could not follow the deformation beyond approximately 0.3 shear strain. Therefore, the shear strain based on the DIC measurements was reported up to approximately 0.3 only.

Similar to the strain rate evolution in tension, the progression of the strain over time in shear can be divided into 2 regions: (1) an initial region corresponding to the establishment of the quasi-static stress equilibrium, which started from time ranges 0 to approximately 130 μs and shear strain ranges of 0 to approximately 0.012 (shown in the magnified curve in Figure 6.7 (b)) and (2) a second region where a nearly constant shear strain rate was developed, starting from time ranges of 130 μs until 300 μs , and shear strain ranges of 0.012 up to approximately 0.33. For all dynamic tensile experiments, a constant strain rate was developed between strain ranges of 0.05 and 0.2, which was the same range used to calculate the average strain rate developed in the tensile samples using DIC. For all dynamic shear samples, a constant strain rate developed between strain ranges of 0.012 and 0.1, which was also the same range used to calculate the average strain rate developed in the shear samples using DIC. The achieved high strain rates for the dynamic tensile experiments were in the range of 74 – 148 s^{-1} for the basalt epoxy composites, and 75-154 s^{-1} for the glass epoxy composites, which are very close to each

other. The achieved high strain rates for the dynamic shear experiments were in the range of $235 - 505 \text{ s}^{-1}$ for the glass epoxy composite, and $335 - 645 \text{ s}^{-1}$ for the basalt epoxy composite.

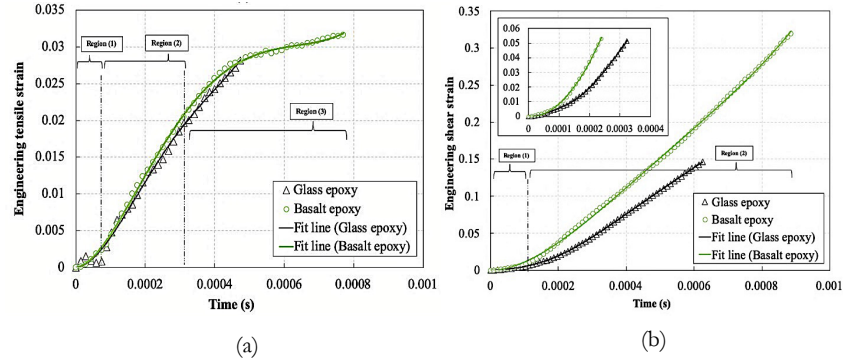
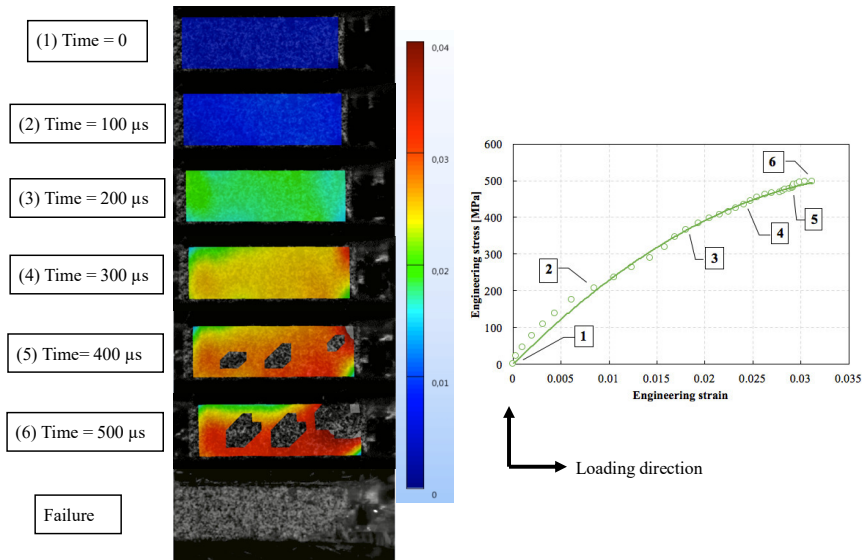


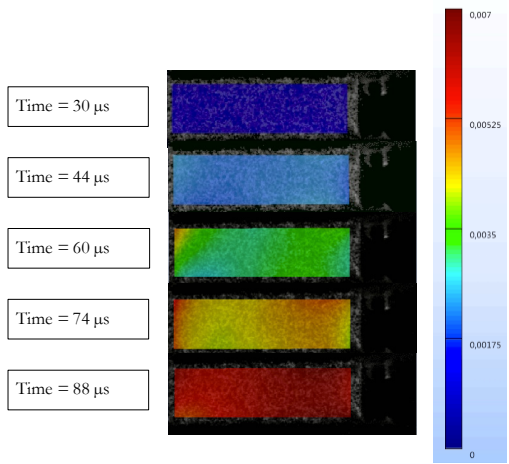
Figure 6.7. Strain evolution during a dynamic experiment for glass and basalt epoxy composites: (a) tensile experiment, (b) shear experiment

6.4.2. Evaluation of the axial strain homogeneity during high strain rate loading

Figure 6.8 (a) and Figure 6.9 (a) show examples of the evolution of axial strain field during a dynamic tensile experiment of the basalt/epoxy composite at a strain rate of 121 s^{-1} in the warp direction and at 116 s^{-1} in the fill direction respectively using DIC image analysis. Images 1 to 6 represent examples of images taken during the deformation. The locations are indicated on the corresponding stress-strain curve. The color map indicates the strain levels measured on the surface of the specimen, where blue indicates the lowest strain and red indicates the highest strain. It can be seen that a homogenous strain field was developed during the dynamic experiments in both the warp and fill directions. At $200 \mu\text{s}$, concentrations of strain along the center and at the top right end of the gauge section started to develop, then continued to spread along the gauge section until failure. Correlation was not possible at some regions within the gauge section in images 5 and 6 due to failure of the paint layer on the surface of the material, therefore some data could not be correlated in these regions. The strain fields obtained from the high speed DIC technique were also used to assess the establishment of homogenous strains during the early stages of loading, corresponding to the time range of the establishment of quasi-static stress equilibrium. Figure 6.8 (b) and Figure 6.9 (b) represent the evolution of the axial strain fields in time range of $30 \mu\text{s}$ to $88 \mu\text{s}$ during loading in the warp and fill directions respectively, and up to strain levels of 0.008. It can be clearly seen that nearly homogeneous strain fields developed during the early stages of loading. This also indicates a correct establishment of early quasi-static stress equilibrium.



(a)



(b)

Figure 6.8. Evolution of DIC axial strain field during a high strain rate test at 121 s^{-1} in the warp direction: (a) from time = 0 up to failure, (b) from time = $30 \mu\text{s}$ till $88 \mu\text{s}$ with a magnified strain scale

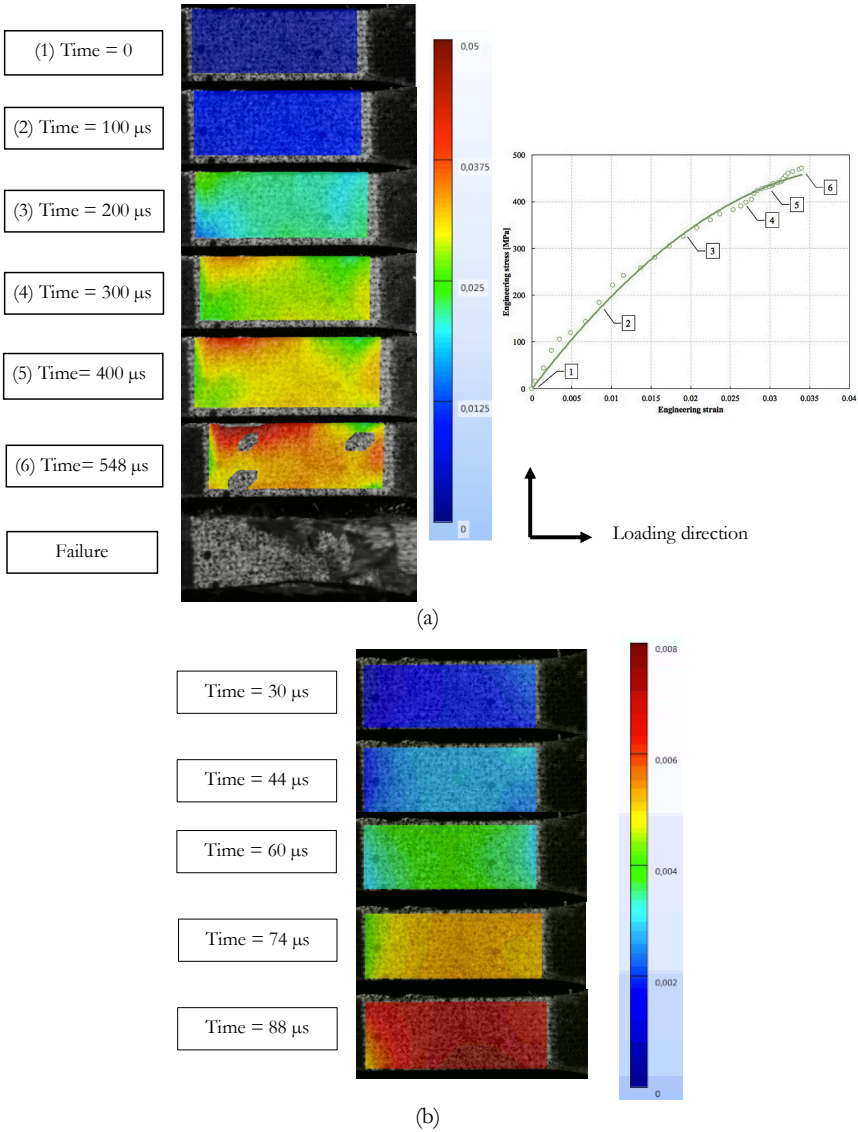


Figure 6.9. Evolution of DIC strain fields during high strain rate test at 116 s^{-1} in the fill direction: (a) from time = 0 up to failure, (b) from time = $30 \mu\text{s}$ till $88 \mu\text{s}$ with a magnified strain scale

6.4.3. Tensile stress-strain response of the basalt/epoxy and glass/epoxy composites in the warp (0°) direction

Figure 6.10 represents an example of the engineering tensile stress-strain curves for both basalt and glass epoxy composites at different strain rates. At least two experiments were carried out for each testing condition, therefore, the curves presented in Figure 6.10 are representative for each testing condition. The solid lines indicate the polynomial fit of the experimental data points, with R^2 values above 0.9. The static curves show that the initial stiffness of the basalt and glass composite are, as intended, very similar. Some oscillations were present in the initial loading stage of some of the high strain rate tensile experiments. These oscillations are due to the interaction of the loading wave with the pin used to fix the sample in the bars during testing. It should be stated, however, that the oscillations do not affect the state of uniform strain in the gauge section of the sample, as indicated from the developed full strain fields measurements using the high speed 3D DIC technique.

It can be seen that both basalt and glass epoxy composites are strain rate sensitive in the warp direction. For the glass epoxy composite, the maximum tensile strength and strain increased from approximately 324 MPa and 0.0197 at strain rate of 0.0006 s^{-1} to approximately 509 MPa and 0.0286 at strain rate of 154 s^{-1} . This corresponds to an increase of approximately 36.3% in tensile strength and approximately 50.5% in tensile strain with the increase of strain rate from quasi-static range to high strain range. Similarly, for basalt epoxy composite, the maximum tensile strength and strain increased from approximately 357 MPa and 0.0226 at strain rate of 0.0006 s^{-1} to approximately 503 MPa and 0.0359 at strain rate of 148 s^{-1} . This corresponds to an increase of approximately 40.8% in tensile strength and approximately 59% in tensile strain with the increase of strain rate from quasi-static range to high strain range. Similar results were reported for unidirectional basalt epoxy composites by Zhang et al. [4], and for woven and unidirectional glass epoxy composites by Naik et al. [5] and Shokrieh et al. [6] respectively. Both materials showed an initially linear behavior followed by a slight non-linearity until failure. The term “non-linearity” used in the context of this manuscript simply means a deviation from the linear elastic modulus line. The basalt epoxy composite generally showed higher maximum tensile strength and maximum tensile strain compared to the glass epoxy composite at all strain rates.

6.4.4. Tensile stress-strain response of the basalt/epoxy composites in the fill (90°) direction

Figure 6.11 represents an example of the engineering stress-strain response of the basalt/epoxy composite at different strain rates in the fill direction. Again, at least 2 experiments were carried out for each testing condition. As such, the curves represented in Figure 6.11 are also representative curves for each test condition. The solid lines also indicate a second degree polynomial fit with R^2 values above 0.9. Similar to the behavior in the warp direction, it can be clearly seen that the basalt/epoxy composite is also strain rate sensitive in the fill direction. The response of the material at quasi-static and high strain rates is initially linear followed by

a non-linear region until failure. An increase in stiffness, strength and strain can also be seen with increase of strain rate. The maximum strength and strain increased from 303.7 MPa and 0.0218 at 0.0006 s^{-1} strain rate, to 354 MPa and 0.0231 at 0.006 s^{-1} strain rate. This corresponds to approx. 16.5% increase in maximum strength and 6% increase in maximum strain at quasi-static strain rates. At higher strain rate (116 s^{-1}), the maximum strength and strain increase significantly to 460 MPa and 0.0323 respectively. This corresponds to an increase of approx. 51.4% in the maximum strength and 48% in the maximum strain compared to that at 0.0006 s^{-1} strain rate. Table 6.5 and Table 6.6 represent a summary of the tensile testing results at different strain rates for warp and fill directions.

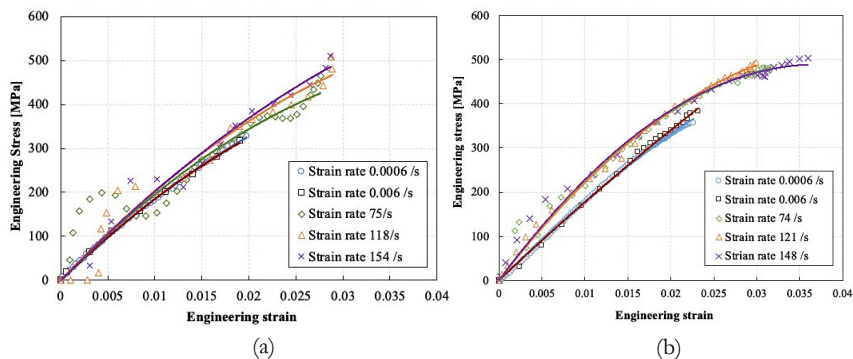


Figure 6.10. Example of the tensile engineering stress-strain response at different strain rates: (a) glass epoxy composite, (b) basalt epoxy composite

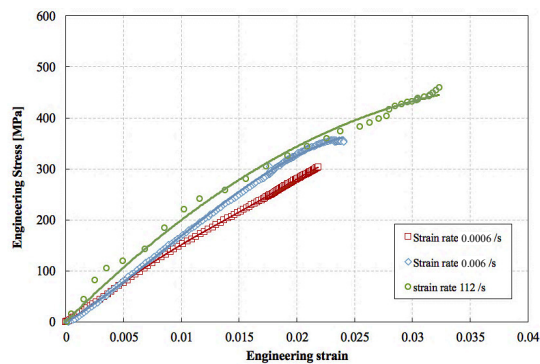


Figure 6.11. Tensile engineering stress-strain response of the basalt/epoxy composite in fill direction at different strain rates

6.4.5. Shear stress-strain response of the basalt/epoxy and glass/epoxy composites in the ($\pm 45^\circ$) direction

Figure 6.12 shows an example of the engineering shear stress-strain curve of both basalt and glass epoxy composites at different strain rates. At least three experiments were carried out for each testing condition. The solid lines also indicate the polynomial fit of the experimental data points, with R^2 values above 0.9. It can be clearly seen that both basalt and glass epoxy composites are also strain rate sensitive in shear. Both materials showed a highly non-linear shear response at low and high strain rates. Contrary to the tensile conditions, the basalt epoxy composite showed a lower shear stiffness and strength compared to the glass epoxy composite. However, the basalt epoxy composite tends to show larger strains to failure compared to the woven glass epoxy composite. The shear stress of the basalt epoxy composites showed a drop in value at approximately 0.2 shear strain at high strain rates. The same behavior was not observed at low strain rates. This drop in stress levels is associated with the onset of the progressive failure which takes place in the reinforcing fibers. During the initial stages of loading, the [$\pm 45^\circ$] laminate experience the maximum shear stress along the fibers (combined with a tensile stress component). With the progression of loading, the epoxy matrix eventually fails, and the fibers rotate towards the direction of the axial load, in a “scissoring” way. The tensile stress component along the fibers becomes relatively more significant. The fiber rotation phenomena causes the fibers to jam, introducing high levels of friction between the fibers, and eventually fail. At low strain rates, the deformation mechanism described above has enough time to be realized. At high strain rates, however, the fiber rotation and friction jamming is realized much faster, which leads to an increase in shear stresses and reduction in shear strains. Table 6.7 and Table 6.8 summarize the tensile and shear testing results at different strain rates.

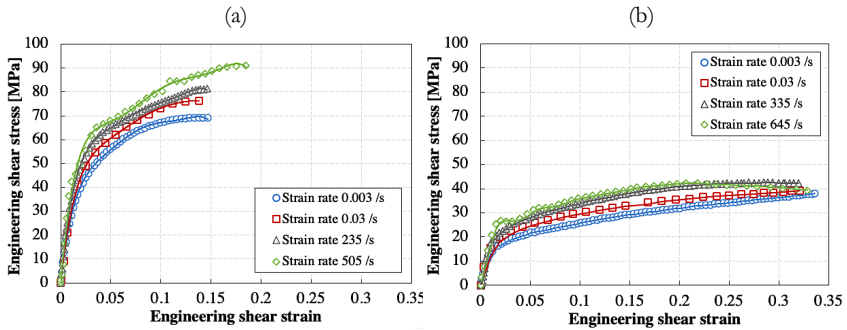


Figure 6.12. Engineering shear stress-strain response at different strain rates: (a) glass epoxy composite, (b) basalt epoxy composite

Table 6.5. Summary of tensile testing results of the basalt/epoxy composite in the warp (0°) direction

Average strain rate achieved (s ⁻¹)	Elastic modulus (GPa)		Ultimate tensile strength (MPa)		Ultimate tensile strain	
	Mean	Std. Dev.	Mean	Std. Dev.	Mean	Std. Dev.
0.0006	17.992	0.573	319.142	29.261	0.0214	0.00137
0.006	18.413	0.406	356.132	39.597	0.0221	0.00156
74	24.830	1.310	445.45	53.458	0.0279	0.00511
121	24.715	2.069	500.124	2.277	0.0303	0.00116
148	24.324	2.860	504.160	1.185	0.0336	0.00331

Table 6.6. Summary of tensile testing results of the basalt/epoxy composite in the fill (90°) direction

Average Strain rate achieved (s ⁻¹)	Elastic modulus (GPa)		Ultimate tensile strength (MPa)		Ultimate tensile strain	
	Mean	Std. Dev.	Mean	Std. Dev.	Mean	Std. Dev.
0.0006	17.966	0.537	318.918	48.366	0.0213	0.0027
0.006	18.512	0.547	357.023	53.104	0.0205	0.0038
112	21.089	0.570	483.545	12.55	0.0361	0.0018

Table 6.7. Summary of the tensile testing results for the glass/epoxy composites in the warp (0°) direction

Average strain rate Achieved (s-1)	Elastic modulus (GPa)		Ultimate tensile strength (MPa)		Ultimate tensile strain	
	Mean	Std. Dev.	Mean	Std. Dev.	Mean	Std. Dev.
0.0006	17.338	0.082	332.485	5.049	0.0198	0.0001
0.006	16.934	0.286	316.422	0.704	0.0193	0.0003
75	17.605	1.289	415.776	93.304	0.0270	0.0015
118	18.522	1.370	497.745	12.795	0.0270	0.0023
154	17.247	0.698	500.464	13.203	0.0278	0.0010

Table 6.8. Summary of the shear testing results for the glass/epoxy and basalt/epoxy composites

Glass epoxy composite					Basalt epoxy composite				
Average strain rate achieved (s^{-1})	Elastic shear modulus (GPa)		Shear strength at 5% shear strain (MPa)		Average strain rate achieved (s^{-1})	Elastic shear modulus (GPa)		Shear strength at 5% shear strain (MPa)	
	Mean	Std. Dev.	Mean	Std. Dev.		Mean	Std. Dev.	Mean	Std. Dev.
0.003	2.587	0.228	56.393	2.659	0.003	2.007	0.185	24.024	3.191
0.03	2.530	0.060	62.226	1.829	0.03	2.368	0.447	24.604	1.475
235	2.915	0.467	63.07	4.796	335	2.223	0.111	28.637	0.736
505	3.425	0.101	71.310	4.830	645	2.155	0.102	28.152	1.922

6.4.6. Effect of strain rate on the elastic modulus of the basalt/epoxy composite

Figure 6.13 represents the variation of the elastic modulus of the tested basalt epoxy composite as a function of the strain rate in both warp and fill direction. It can be seen that at high strain rate, the elastic modulus increased by approx. 33 % for the warp direction and by approx. 22% for the fill direction, compared to the value obtained at a static strain rate of $0.0006 s^{-1}$. Similar behavior was also reported by Ou et al. [7] for unidirectional basalt fiber epoxy composites at high strain rates, and Sun et al. [8] for woven basalt fiber vinyl ester composites at high strain rates. However, the difference in values is related to the different matrix materials and fiber configurations used.

The stiffness of the basalt fibers is known to be strain rate sensitive, and shows an increase with increasing the strain rate, as demonstrated by Zhu et al. [9,10]. In addition, similar epoxy resins also showed significant a strain rate dependency and an increase in stiffness with increasing the strain rate, as indicated by Gilat et al. [11], Littell et al. [12], and Gerlach et al. [13]. Therefore, the increase in the stiffness of the basalt epoxy composite at high strain rates is attributed to both the epoxy resin (due to its viscoelastic nature and its strain rate sensitivity of stiffness), and the basalt fibers (also due to their strain rate sensitivity). The increasing trend of the elastic modulus with the strain rate can be represented by the following equation for warp and fill directions:

$$E = A\dot{\epsilon}^d \quad (6.3)$$

where E is the elastic modulus of the material, A is the stiffness coefficient, and d is the strain rate sensitivity exponent. Using a least square power fit, for the warp direction, the stiffness coefficient and the strain rate sensitivity exponent were found to be 21.632 GPa and 0.0272 respectively, while for the fill direction, the stiffness coefficient and the strain rate sensitivity exponent were found to be 19.813 GPa and 0.0132 respectively. This indicates that the stiffness in the warp direction is more sensitive to strain rate compared to the stiffness in the fill direction.

6.4.7. Effect of strain rate on the ultimate tensile strength of the basalt/epoxy composite

Figure 6.14 shows the variation of the maximum tensile strength of the tested basalt epoxy composite at different strain rates in both warp and fill directions. An increasing trend in the ultimate tensile strength can be seen with increasing the strain rate. Similar findings were also reported by Zhang et al.[4] and Yao et al. [14] for their basalt epoxy composites. However, their materials were unidirectional basalt fibers and with different fiber volume contents compared to the woven basalt fibers used in this study.

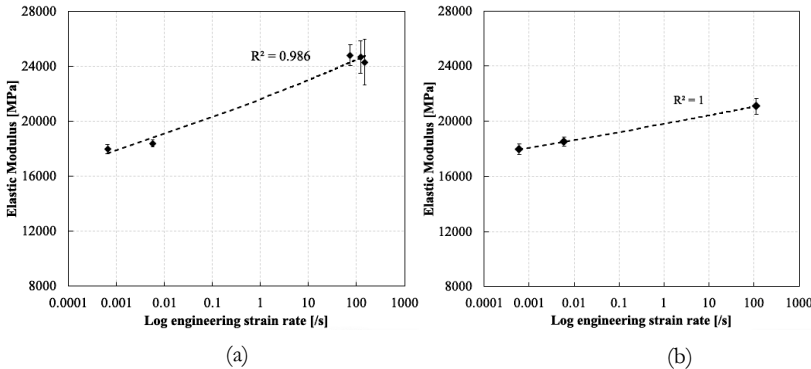


Figure 6.13. Effect of strain rate on the elastic modulus of basalt epoxy composites: (a) warp direction, (b) fill direction

The strength of basalt fibers is known to be dependent on surface defects and flaws [15], in addition to the inherent defects introduced by the manufacturing process of the composite itself. At low strain rates, the fracture has the time to find a path, connecting the flaws, of the weakest links in the material. At high strain rates, this is not the case and consequently higher stress levels and more energy are needed to initiate and propagate the cracks in the defect dominated material. In addition, the inter-fiber friction due to the weaving architecture of the fibers could also increase the apparent tensile strength. It has been demonstrated by Briscoe et al. [16] and Wang et al. [17] that the inter-fiber friction of woven fabrics increases their ballistic strength and tensile performance. However, these studies were carried out only on aramid and Kevlar fibers and the conclusions might not be directly extended to the basalt fibers or their composites. Therefore, further research is required to understand the effect of inter-fiber friction on the tensile strength of basalt composites at different strain rates. Moreover, similar epoxy resins have shown an increase in ultimate tensile strength with increasing the strain rate, as studied by Gilat et al. [11], Littell et al. [12], and Gerlach et al. [13]. Therefore, the strain rate sensitivity of the epoxy resin also contributes to the overall strain rate sensitivity of the ultimate tensile strain of the tested basalt epoxy composites.

The increasing trend of the ultimate tensile strength with the increase of strain rate can also be represented by the following equation for warp and fill directions:

$$S^{ult} = B\dot{\epsilon}^c \quad (6.4)$$

where S^{ult} is the ultimate tensile strength, B is the tensile strength coefficient, and c is the strain rate sensitivity exponent. For the warp direction, the tensile strength coefficient and the strain rate sensitivity exponent were found to be 418.69 MPa and 0.0304 respectively, while for the fill direction, the tensile strength coefficient and the strain rate sensitivity exponent were found to be 412.03 MPa and 0.0341 respectively. This indicates that while the warp direction has slightly higher ultimate strength compared to the fill direction, it is slightly less strain rate sensitive compared to the fill direction. The difference in the strength coefficient could be related to the pre-tension applied on the fibers during the manufacturing process of the plain weave basalt fabric itself, where the fibers along the warp direction are generally under more tension compared to the fibers in the fill direction.

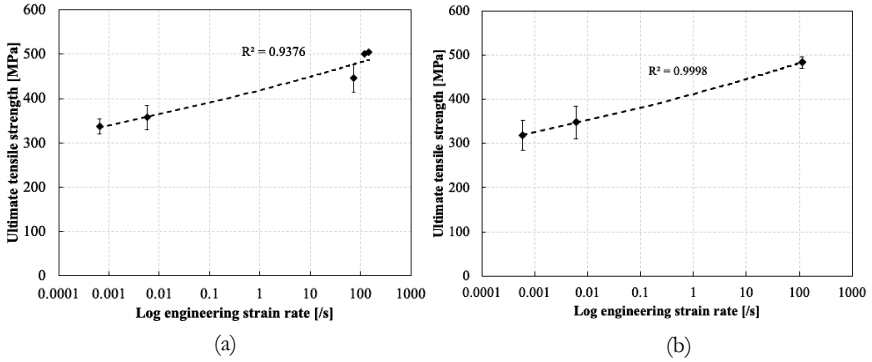


Figure 6.14. Effect of strain rate on the ultimate tensile strength of basalt epoxy composites: (a) warp direction, (b) fill direction

6.4.8. Effect of the strain rate on the maximum tensile strain of the basalt/epoxy

Figure 6.15 shows the variation of the maximum tensile strain of the tested basalt epoxy composite at different strain rates in both warp and fill directions. The term maximum tensile strain is used to indicate the value of the strain corresponding to the ultimate tensile strength of the tested material. An increasing trend in the ultimate tensile strain can be also observed with increasing the strain rate. A similar trend was also reported by Zhang et al. [4] and Yao et al. [14].

Further research is still required to understand why the ultimate tensile strains increase with the increase in strain rate. This observed behavior could again be attributed to the inter-fiber friction. The inter-fiber friction could introduce a “friction locking” to the fibers along the loading direction at early stages of loading. This could arise from the inability of the fibers perpendicular to the loading direction to realize the deformation at high speeds. At later stages of the loading, this “friction locking” would break which might result in the crimps producing

additional strain. The epoxy matrix does not significantly contribute to the total elongation of the composite, since the brittle matrix either fails earlier compared to the fibers (due to combinations of tensile and shear stresses), or debonds from the fibers at the fiber/matrix interface (due to shear). In both cases, the fibers carry the remaining load until failure.

Similar to the ultimate tensile strain dependency on the strain rate, the increasing trend of the ultimate tensile strain with strain rate can be represented by the following equation for warp and fill directions:

$$\varepsilon^{ult} = M\dot{\varepsilon}^n \quad (6.5)$$

where ε^{ult} is the ultimate tensile strain, M is the tensile strain coefficient, and n is the strain rate sensitivity exponent. For the warp direction, the ultimate tensile strain coefficient and the strain rate sensitivity exponent were found to be 0.0263 and 0.0321 respectively, while for the fill direction, the ultimate tensile strain coefficient and the strain rate sensitivity exponent were found to be 0.0272 and 0.0554. The fill direction shows higher ultimate tensile strain coefficient and higher sensitivity to strain rates.

6.4.9. Comparison of the tensile and the shear moduli for basalt and glass epoxy composites at different strain rates

Figure 6.16 (a) and (b) show a comparison of the elastic modulus and specific elastic modulus of both basalt and glass epoxy composites at different strain rates. The purpose of using the specific elastic modulus (which is the ratio of elastic modulus to the corresponding material density) is to provide a more meaningful comparison considering the slight difference in both material densities and the fiber areal weights. Both moduli of both materials were calculated as the slope of a line drawn from strain ranges of 0 to 0.01. The basalt epoxy composite showed a higher elastic modulus and specific elastic modulus compared to that of the glass epoxy composite at all strain rates, with differences ranging from 3.7% (4.7% for the specific modulus) at a strain rate of 0.0006 s^{-1} up to 41% (42.3% for the specific modulus) at a strain rate of 148 s^{-1} . The glass epoxy composite showed a nearly constant elastic modulus of approximately 17.3 GPa. Moreover, the elastic modulus of the basalt epoxy composite increased from approximately 17.9 GPa at a strain rate of 0.0006 s^{-1} to approximately 24.3 GPa at high strain rate of 148 s^{-1} , which corresponds to an increase of approximately 33%. Similar results were reported by Ou et al. [7,18] and Sun et al. [8] for the basalt and the glass epoxy composites, but with different fiber architecture and matrix material. As mentioned earlier, the increase in stiffness with the increase in strain rate for the basalt epoxy composite is attributed to the combined effect of the viscoelastic epoxy matrix [11,13], and the rate sensitive basalt fibers [9,10]. For the glass epoxy composite, with its relatively higher fiber volume fraction, the effect of strain rate on the elastic modulus is more dominated by the fibers compared to the epoxy matrix. The glass fibers do not show a strain rate sensitivity for the elastic modulus, as reported by Taniguchi et al. [19] and Ou et al. [20], and this results in a nearly constant elastic modulus for the glass fiber composites.

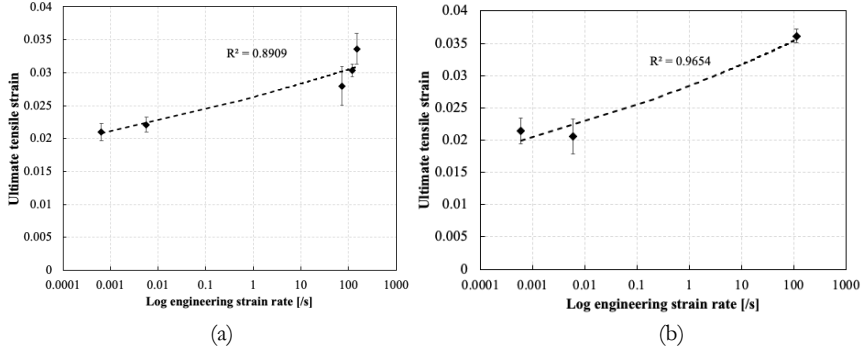


Figure 6.15. Effect of strain rate on the ultimate tensile strain for basalt epoxy composite: (a) warp direction, (b) fill direction

Figure 6.16 (c) and (d) show a comparison of the elastic shear modulus and specific shear modulus for both basalt and glass epoxy composites at different strain rates. Contrary to the tensile conditions, the basalt epoxy composite showed a lower elastic shear modulus and specific shear modulus compared to that of the glass epoxy composite at all strain rates, with a reduction percentage ranging from 28.8% (27.7% for the specific shear modulus) at a strain rate of 0.003 s^{-1} to 58.9% (57.5% for the specific shear modulus) at a strain rate of 645 s^{-1} . The elastic shear modulus of the glass epoxy composite increased from approximately 2.58 GPa at a strain rate of 0.003 s^{-1} to approximately 3.42 GPa at a strain rate of 505 s^{-1} , which corresponds to an increase of approximately 32%. The basalt epoxy, on the other hand, showed a nearly constant elastic shear modulus of approximately 2.1 GPa.

Given the slightly different fiber volume fraction for both glass and basalt epoxy composites, a normalized 0.5 fiber volume fraction (based on the rule of mixtures and the experimentally obtained fiber volume fractions) was interpolated for both materials [21], as shown in Figure 6.16 (e) and (f). This also provides a meaningful comparison between the behavior of both materials considering their different fiber volume fractions. The same trends of elastic and shear moduli for both materials can still be seen at different strain rates. Similar results were obtained by Gowtham et al. [22] for a glass epoxy composite with different fiber weaving type and matrix material. Similar results were also reported by Soares et al. [23] at quasi-static strain rates, but also with different matrix material and fiber architecture. To the author's knowledge, no results are available in entire literature to support the current findings of the elastic shear modulus of the woven basalt epoxy composite used in this study at high strain rates. The lower elastic shear modulus of the basalt epoxy composite compared to the glass epoxy composite used in this study is attributed to the insufficient adhesion between the basalt fibers and the epoxy matrix at the fiber/matrix interface (as will be seen in section 6.3.13), in addition to the relatively high void content compared to that of the glass epoxy.

6.4.10. Comparison of the tensile and the shear strengths for basalt and glass epoxy composites at different strain rates

Figure 6.17 (a) and (b) compares the ultimate tensile and the specific ultimate tensile strengths, respectively, of both basalt and glass epoxy composites at different strain rates. The ultimate tensile strength and the specific ultimate tensile strength of the basalt epoxy composite was approximately 8% higher than that of the glass epoxy composite at all strain rates. In addition, both materials showed an increasing trend in ultimate tensile strength with an increasing strain rate. Similar to the basalt epoxy composite, the increasing trend of the ultimate tensile strength with increasing the strain rates for the glass epoxy can be described by a same least square power fit, as in eq. (6.4). For the glass epoxy composite, the tensile strength coefficient and the strain rate sensitivity exponent were 398.49 MPa and 0.0343 respectively. As mentioned earlier, the increase of the ultimate tensile strength with the increase in strain rate for both materials is mainly attributed to the cracks not finding enough time to propagate and connect the weakest links in the material, therefore, more energy and higher stress are needed to break the sample. Additionally, the combined effect of the inter-fiber friction of the woven fibers [16,17] and the strain rate sensitivity of the epoxy matrix [11,13] also contribute to the increase in the tensile strength with increasing the strain rate.

Figure 6.17 (c) and (d) shows a comparison of the shear and the specific shear strengths, respectively, of both the basalt and the glass epoxy composites at different strain rates. It should be noted that the reported shear strength for both materials was taken as the stress corresponding to 5% shear strain, in order to limit the fiber rotation angle to approximately 1.5°, as recommended by the ASTM D3518/D3518M testing standard [24]. It can be seen that both materials showed an increase in shear strength with increasing the strain rate, albeit a modest increase for the basalt epoxy composite compared to the glass epoxy composite. The glass epoxy composite showed almost double the shear strength and the specific shear strength of that of the basalt epoxy composite at all strain rates. Similar results were reported for the woven glass epoxy composite by Gowtham et al. [22], and recently by Ganzenmüller et al. [25] for unidirectional basalt composites.

The increasing trend of the shear strength with the increase in strain rate can also be represented by a least square power fit relation as follows:

$$\tau_{12} = C\dot{\gamma}_{12}^d \quad (6.6)$$

where τ_{12} is the shear strength, C is the shear strength coefficient, and d is the strain rate sensitivity exponent. For the glass epoxy composite, the shear strength coefficient and the strain rate sensitivity exponent were 62.57 MPa and 0.0129 respectively. For the basalt epoxy composite, the tensile strength coefficient and the strain rate sensitivity exponent were 25.98 MPa and 0.0143 respectively. The increase in the shear strength with the increase of the strain rate for both materials is mainly affected by the strain rate sensitivity of both the fibers and epoxy matrix [11–13]. The lower shear strength of the basalt epoxy composite compared to

the glass epoxy composite is again attributed to the insufficient adhesion of the basalt fibers with the epoxy matrix (as will be seen in section 6.3.13) , and the relatively high void content.

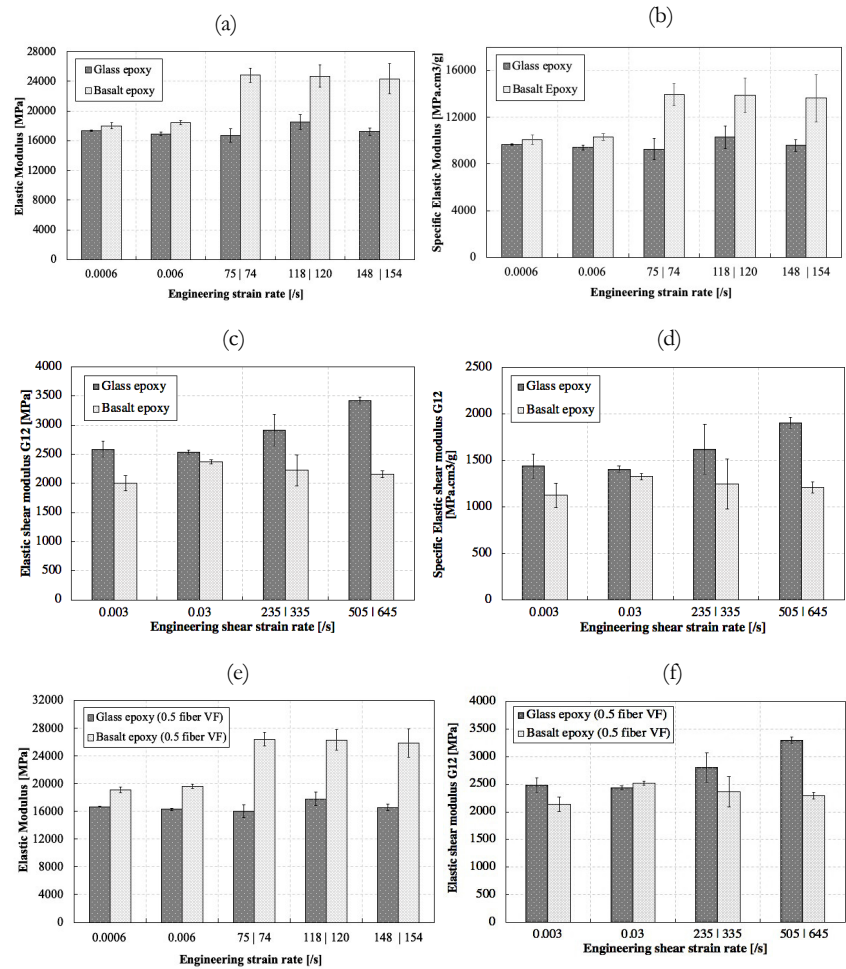


Figure 6.16. Elastic properties of basalt and glass epoxy composites at different strain rates: (a) elastic tensile modulus, (b) specific elastic tensile modulus, (c) elastic shear modulus, (d) specific elastic shear modulus, (e) elastic tensile modulus (0.5 fiber volume fraction)

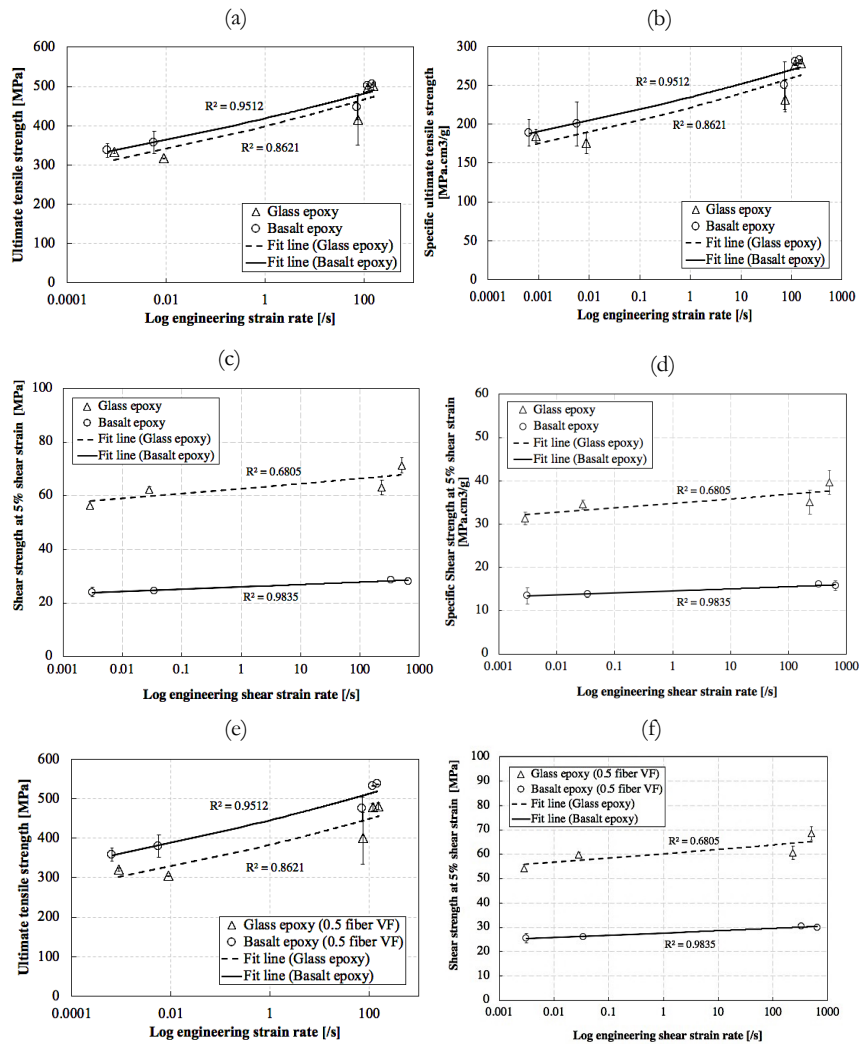


Figure 6.17. Tensile and shear strength of basalt and glass epoxy composites at different strain rates: (a) maximum tensile strength, (b) specific maximum tensile strength, (c) shear strength at 5% shear strain, (d) specific shear strength at 5% shear strain, (e) m maximum tensile strength (0.5 fiber volume fraction), (f) shear strength at 5% shear strain (0.5 fiber volume fraction)

Figure 6.17 (e) and (f) compares the ultimate tensile strength and shear strength at 5% shear strain for both basalt and glass epoxy composites, considering normalized data at 0.5 fiber volume fraction for both materials. It can be seen that the basalt epoxy composite still showed an approximately 23% higher ultimate tensile strength compared to that of glass epoxy composite. The glass epoxy composite still showed approximately double the shear strength values compared to these of the basalt epoxy composite.

6.4.11. Comparison of absorbed energy in tension and ultimate tensile strain for basalt and glass epoxy composites at different strain rates

Figure 6.18 (a) represents a comparison of the absorbed energy in tension per unit volume (which is the area under the tensile stress-strain curve) at different strain rates for both glass and basalt epoxy composites. It can be seen that both materials showed an increase in the absorbed energy in tension with the increase in strain rate, mainly due to their strain rate sensitivity in tension. The absorbed energy of the glass epoxy composite increased from approximately 3.4 mJ/mm³ at strain rate of 0.0006 s⁻¹ to approximately 7.7 mJ/mm³ at strain rate of 154 s⁻¹. For the basalt epoxy composite, the absorbed energy also increased from approximately 4.07 mJ/mm³ at strain rate of 0.0006 s⁻¹ to approximately 10.09 mJ/mm³ at strain rate of 148 s⁻¹. Compared to the glass epoxy composite, the basalt epoxy composite showed higher energy absorption capacity in tension at all strain rates, at approximately 17% at quasi-static strain rate of 0.0006 s⁻¹ and approximately 31% at high strain rate of 148 s⁻¹.

Figure 6.18 (b) shows a comparison of the ultimate tensile strain for both glass and basalt epoxy composites at different strain rates. The ultimate tensile strain is the strain corresponding to the ultimate tensile strength. It can be seen that the basalt epoxy composite showed a higher ultimate tensile strain compared to the glass epoxy composite at all strain rates, with percentages ranging from 6.2% at strain rate of 0.0006 s⁻¹ up to 20.8% at strain rate of 154 s⁻¹. Both basalt and glass epoxy composites showed an increase in ultimate tensile strain with increasing the strain rate. Similar results were also reported for the glass epoxy composite by Hufner et al. [26] and Ou et al. [20], and for the basalt epoxy composite by Zhang et al. [4] and Yao et al. [14]. As explained earlier, the increase in the ultimate strain for both material could be attributed to the inter-fiber friction caused by the weaving architecture. It should be noted that Wang et al. [27] suggested that the increase in the ultimate strain could be the result of the time delay in the load redistribution after the fibers are broken at the start of failure. However, this suggestion was based on a model utilizing unidirectional glass fibers, which cannot be directly extended to the woven fabric case. This indicates that further research is still required to understand the increase in the ultimate strain of woven fabric composites with increasing the strain rate, especially since this behavior is also observed for both composites regardless of the fiber type. The fact that basalt epoxy composite showed a higher ultimate tensile strains compared to the glass epoxy composite is due to the behavior of the individual fibers themselves. Indeed, it was shown by Deak et al. [28] that continuous basalt fibers possess higher fracture strain compared to glass fibers at the same strain rates. Given the relatively high fiber volume fraction for both composites, the epoxy matrix will not significantly contribute to the elongation of the material, and most of the load will be carried by the fibers

until fracture. The increasing trend in the ultimate tensile strain with the increase in strain rate for the glass epoxy composite can also be represented by eq. (6.5). For the glass epoxy composite, the tensile strain coefficient and the strain rate sensitivity exponent were 0.0236 and 0.00306 respectively. This indicates that the ultimate tensile strain for the basalt epoxy composite is more sensitive to strain rates compared to the glass epoxy composite.

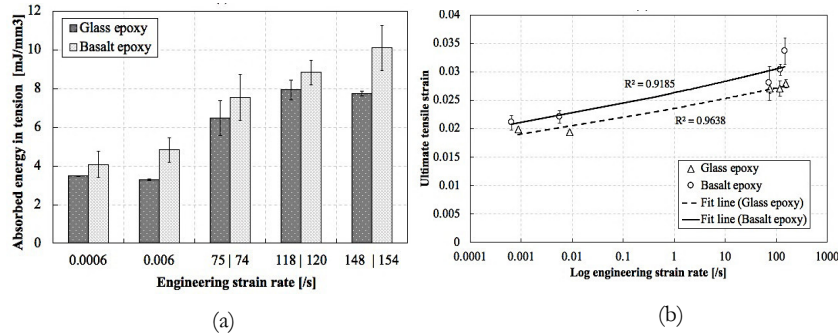


Figure 6.18. Absorbed energy and maximum strains in tension for basalt and glass epoxy composites at different strain rates: (a) absorbed energy per unit volume in tension, (b) ultimate tensile strain

6.4.12. Fractographic analysis and failure morphology

Figure 6.19 (a) and Figure 6.20 (a) show a fractured basalt epoxy composite specimen at quasi-static and dynamic conditions respectively. Failure in all samples took place either in the gauge section or at the interface between the gauge section and the transition zone. Scanning electron microscopy images of the fracture surface for the samples were taken, as shown in Figure 6.19 (b) and Figure 6.20 (b) respectively. No significant difference can be noticed in the failure nature between quasi-static and dynamic conditions for both material directions. Failure is dominated mainly by matrix and fiber failure. Some debonding between the fibers and the matrix can be seen, in addition to some fiber pullout. Significant amount of resin was concentrated between each ply due to the selected wet layup manufacturing technique. A magnification of a fractured fiber for both quasi-static and dynamic conditions is shown in Figure 6.19 (c) and Figure 6.20 (c) respectively. The failure of the basalt fiber is essentially brittle. Failure started at the indicated crack initiation locations, and spread across the entire cross section of the fiber.

Delamination was also observed in the failed samples at different strain rates. Figure 6.21 shows a side view of the thickness direction of the tested samples. Black lines along the thickness indicate the regions corresponding to delamination. With the increase of strain rate, delamination become more significant and spread along the gauge section. It could be that the pronounced delamination is caused by the free edge effects, in addition to the increase in strain along the loading direction. This increase in strain along the loading direction could lead to

some relative displacements between the layups, which could lead to interlaminar stresses and eventually an accelerated failure.

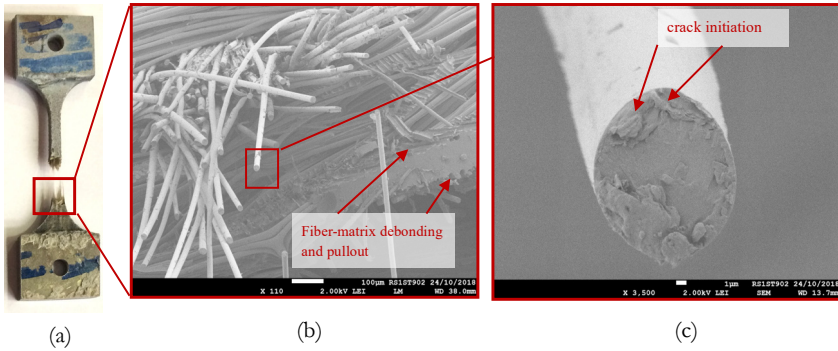


Figure 6.19. Fractured basalt epoxy sample tested at a quasi-static strain rate of 0.0006 s^{-1} : (a) failure shape, (b) SEM image of the indicated fracture surface, (c) magnified SEM image of a fractured fiber

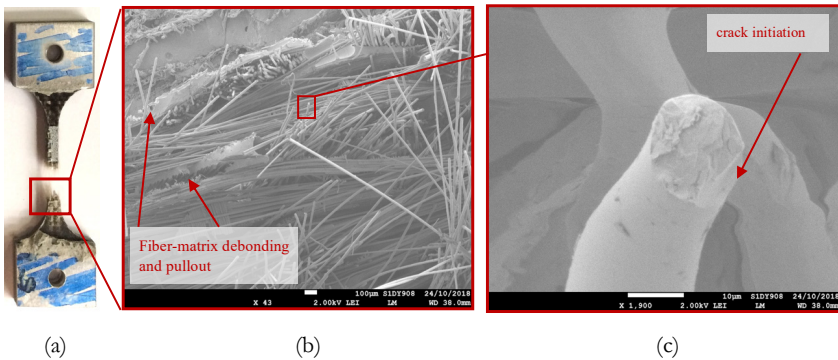


Figure 6.20. Fractured basalt epoxy sample tested at a dynamic strain rate of 74 s^{-1} : (a) failure shape, (b) SEM image of the indicated fracture surface, (c) magnified SEM image of a failed fiber

Fractured tensile specimens of the glass epoxy composite showed small localized delamination, in addition to fiber matrix debonding, fiber pull out, and fiber and matrix failure. Figure 6.22 shows some SEM images for the fractured glass epoxy composite in tension at different strain rates. No significant difference can be seen in the failure morphology between quasi-static and high strain rates.

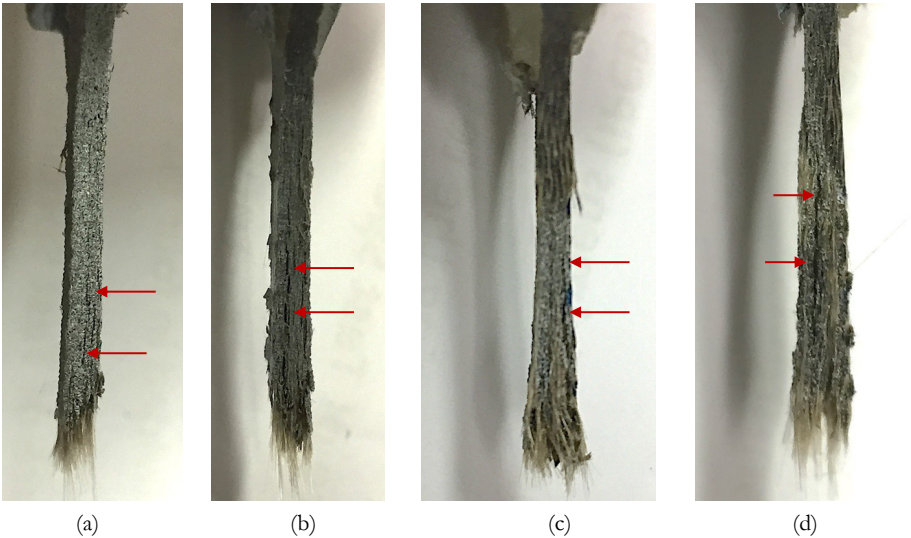


Figure 6.21. Delamination in the basalt epoxy samples at different strain rates: (a) 0.0006 s^{-1} , (b) 0.006 s^{-1} , (c) 74 s^{-1} , (d) 148 s^{-1}

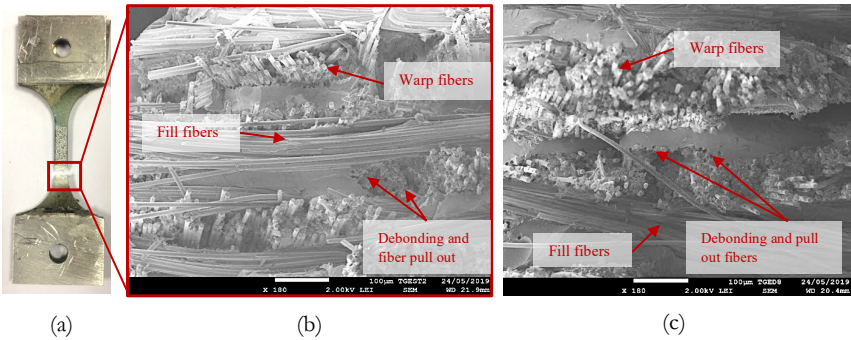


Figure 6.22. Fractured glass epoxy sample tested at a different strain rates: (a) failure shape, (b) SEM images of the fractured surface at strain rate 0.0006 s^{-1} , (c) SEM images of the fractured surface at strain rate 75 s^{-1}

Figure 6.23 (a) and (b) show the failure shape of the glass epoxy and basalt epoxy samples in shear. Similar to the fractured samples in tension, small localized delamination was observed in the fractured shear samples of the glass epoxy. Significant delamination, which spreads along the gauges section, was also observed for the fractured shear sample of the basalt epoxy composite. Figure 6.23 (c) and (d) show SEM images of the fractured shear samples for glass epoxy composites at different strain rates. Fiber pull out is clearly seen at quasi-static strain rates, while debonding can be seen at high strain rates. Figure 6.23 (e) and (f) also show SEM images of the fractured shear samples of the basalt epoxy composites at different strain rates. Unlike the glass epoxy composite, the basalt fibers are more spread with hardly any traces of the epoxy matrix on their surfaces. Debonding marks can also be observed in the traces of the fractured epoxy matrix. In general, a better fiber-matrix adhesion can be seen in the glass epoxy composites compared to the basalt epoxy composites at different strain rates.

6.4.13. Comparison with other conventional composite materials at similar high strain rates from literature

Figure 6.24 shows a rough comparison between the high strain rate tensile response of the currently tested woven basalt fiber epoxy composite and similar glass and carbon epoxy composites studied by Naik et al. [5] and Lu et al. [29], respectively, in the warp direction, and at strain rates of 200 s^{-1} . Table 6.9 shows the details of the tensile specimens used by both authors in comparison to the specimens used in the current study. The chosen examples of conventional composite materials have very similar epoxy resin properties, a similar fiber architecture (plain weave), and a comparable fiber volume fraction. However, the comparison presented here is only for representative and guiding purposes. It can be seen that the overall high strain rate response of the woven basalt epoxy composite is considered intermediate between the responses of both the woven glass epoxy and the woven carbon epoxy composites. The basalt material used in the current study showed higher ultimate tensile strain compared the glass and carbon epoxy composites studied by both authors, and showed a higher elastic modulus compared to the glass epoxy composite. The carbon epoxy composite showed the highest modulus and maximum tensile strength of all three composites.

The absorbed energy in tension (strain energy per unit volume) of the basalt epoxy composite in the current study was approx. 8.75 mJ/mm^3 , which is nearly double that of the reported carbon epoxy and glass composites which have the values of approx. 4.8, and 3.75 mJ/mm^3 respectively. This indicates that the tested basalt epoxy composites possess excellent energy absorption capabilities at high strain rates compared to the conventional glass and carbon epoxy composites tested by the authors mentioned above, which is an important criterion for designing impact resistant aeronautical and automotive components.

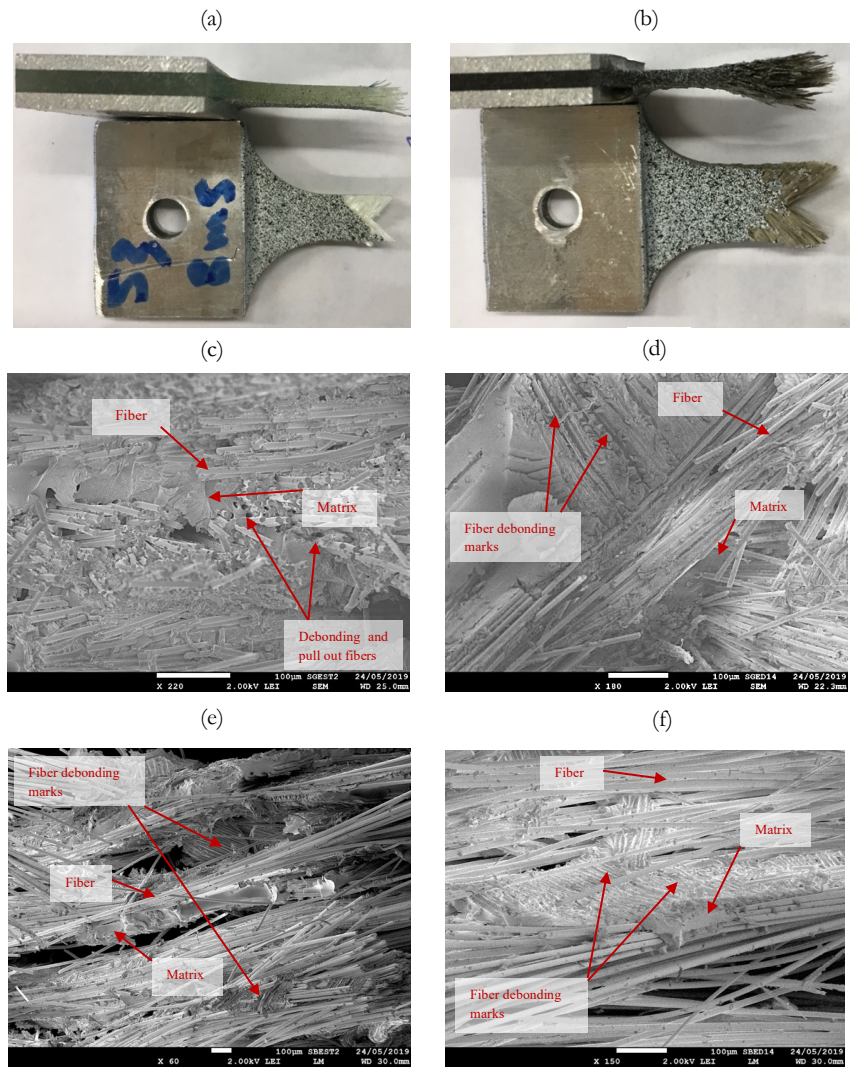
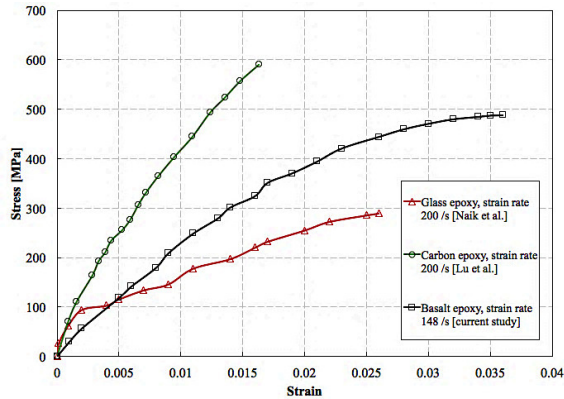


Figure 6.23. SEM images of the fractured shear samples: (a) failure shape of the glass/epoxy shear sample, (b) failure shape of the basalt/epoxy shear sample, (c) glass epoxy at 0.003 s⁻¹, (d) glass epoxy at 505 s⁻¹, (e) basalt epoxy at 0.003 s⁻¹, (f) basalt epoxy at 645 s⁻¹

Table 6.9. Properties of the specimens used by Naik et al. [40] and Lu et al. [41]

Property	Glass/epoxy (Naik et al. [5])	Carbon/epoxy (Lu et al. [29])	Basalt/epoxy (current study)
Weaving architecture	Plain weave	Plain weave	Plain weave
Fiber type	E-glass	Carbon fiber TC33–3K	Basalt fiber BAS 220.1270.P
Fiber volume fraction	0.52	-	0.47
Matrix type	Epoxy LY556 and hardener HY951	Epoxy LY1564 SP and hardener Aradur 3486	Epoxy EPIKOTE I20 and hardener EPIKURE 960
Void content %	0.75	-	8
Manufacturing process	Matched die molding	Vacuum infusion	Wet layup


Figure 6.24. Comparison between the behavior of comparable woven glass epoxy composite, woven carbon epoxy composite, and woven basalt epoxy at high strain rates

6.5. Conclusions

A comprehensive study was performed in order to study the tensile and shear behavior of woven basalt fiber reinforced epoxy composites at high strain rates. For the tensile behavior, both warp and fill directions were investigated. Additionally, a comparison between the high strain rate behavior of the woven basalt and a woven glass fiber reinforced epoxy composites was presented. For this comparison, the same epoxy matrix and manufacturing technique were used for both materials. Dynamic tensile and shear experiments were carried out using a tensile split Hopkinson bar facility and strains were measured using the 3D high speed digital image correlation technique. During test execution and result analysis, special attention was paid to the development of quasi-static stress equilibrium, the evolution of the strain rate, and the homogeneity of the strain fields in the sample's gauge section. Reference quasi-static tests were

also performed, using identical sample geometries and boundary conditions, allowing a comparison between the behavior of the material at low and high strain rates. The strain rates covered in this study were in the ranges of 0.0006 s^{-1} and 154 s^{-1} for tensile experiments, and 0.003 s^{-1} and 645 s^{-1} for shear experiments. Tensile and shear engineering stress-strain curves were presented and the effect of strain rate on the elastic modulus, ultimate tensile strength, and ultimate tensile strains of the basalt epoxy composite was discussed. Furthermore, a comparison between the tensile and shear elastic moduli, tensile and shear strengths, absorbed energy in tension, and ultimate tensile strains for both materials were discussed based on normalized data with respect to material density and fiber volume fraction. Scanning electron microscopy images of the fracture surfaces were taken to reveal the failure modes. Considering the tests, measurement results, and materials used in this study, the following can be concluded:

1. Both woven basalt and glass epoxy composites tested in this study were strain rate sensitive in tension and shear. Both materials showed a general increase in tensile strength, shear strength, and ultimate tensile strains with the increase in strain rate
2. The stiffness, ultimate tensile strength, and ultimate tensile strain of the tested woven basalt/epoxy composite increased with strain rate for both warp and fill directions.
3. The elastic modulus in the warp direction increased by approx. 33% at strain rate of 148 s^{-1} compared to quasi-static rate of 0.0006 s^{-1} , and in the fill direction, the elastic modulus increased by approx. 22% at high strain rate of 116 s^{-1} compared to quasi-static rate of 0.0006 s^{-1} .
4. The ultimate tensile strength and strain in the warp direction increased by approx. 41% and 59% respectively at high strain rate of 148 s^{-1} compared to quasi-static strain rate of 0.0006 s^{-1} , while in the fill direction, the increase is approx. 51% and 48% respectively at high strain rate of 116 s^{-1} compared to quasi static strain rate of 0.0006 s^{-1} .
5. In tensile testing conditions, the tested basalt epoxy composite showed up to 41% higher elastic stiffness, 8% higher ultimate tensile strength, and 28% higher ultimate tensile strain compared to the tested glass epoxy composite at high strain rates.
6. In shear testing conditions, the tested glass epoxy composite showed up to 58.9% higher elastic shear modulus, and double the shear strength compared to the tested basalt epoxy composite at high strain rates.
7. The absorbed energy in tension for the tested basalt epoxy composite was higher than that of the tested glass epoxy composite by approximately 31% at high strain rates.
8. The failure morphologies of both the woven basalt epoxy composite and the woven glass epoxy composite were to a high degree independent of the strain rate, except for the delamination which was significantly more spread along the gauge section at higher strain rates in the case of the woven basalt epoxy composite.
9. Analysis of the SEM microscopy images indicated that the failure is mainly dominated by fiber and matrix failure, debonding between the fibers and the epoxy matrix, and fiber pull out for both materials.
10. The tested basalt epoxy composite possesses excellent energy absorption capabilities compared to the tested glass epoxy composite and compared to conventional composites tested in literature, which makes it a good candidate material for impact resistant applications.

Despite the relatively high void content of the tested basalt epoxy composite and the insufficient adhesion between the basalt fibers and the epoxy matrix, the material still showed superior behavior in tension compared to the tested glass epoxy composites at different strain rates, considering the same volume fiber content. This suggests the possibility of replacing glass fiber composites with the cheaper and higher performant basalt fiber composites in some aircraft secondary structures, such as fairings, radomes, and wing tips. Nevertheless, further research is still required to improve the adhesion of the basalt fibers to the hosting epoxy matrix and to lower the void content through an improved manufacturing technique. This could increase the shear properties of the basalt epoxy composite, and allow the full exploitation of the promising properties of basalt composites in the design of aircraft secondary structures.

References

- [1] ASTM International, 2003, "Standard Test Methods for Void Content of Reinforced Plastics," Astm D 2734-94.
- [2] ASTM International, 2016, *ASTM D6856 / D6856M-03-Standard Guide for Testing Fabric-Reinforced "Textile" Composite Materials*, West Conshohocken, PA, 2017.
- [3] Byron, P., Leif, C., and Donald, A., 2010, *Experimental Characterization of Advanced Composite Materials, Fourth Edition*, CRC Press.
- [4] Zhang, H., Yao, Y., Zhu, D., Mobasher, B., and Huang, L., 2016, "Tensile Mechanical Properties of Basalt Fiber Reinforced Polymer Composite under Varying Strain Rates and Temperatures," *Polym. Test.*, **51**, pp. 29–39.
- [5] Naik, N. K., Yernamma, P., Thoram, N. M., Gadipatri, R., and Kavala, V. R., 2010, "High Strain Rate Tensile Behavior of Woven Fabric E-Glass/Epoxy Composite," *Polym. Test.*, **29**(1), pp. 14–22.
- [6] Shokrieh, M. M., and Omid, M. J., 2009, "Tension Behavior of Unidirectional Glass/Epoxy Composites under Different Strain Rates," *Compos. Struct.*, **88**(4), pp. 595–601.
- [7] Ou, Y., Zhu, D., and Li, H., 2016, "Strain Rate and Temperature Effects on the Dynamic Tensile Behaviors of Basalt Fiber Bundles and Reinforced Polymer Composite," *J. Mater. Civ. Eng.*, **28**(10), p. 04016101.
- [8] Yang, Y., Yu, J., Xu, H., and Sun, B., 2017, *Porous Lightweight Composites Reinforced with Fibrous Structures*, Springer.
- [9] Zhu, L., Sun, B., Hu, H., and Gu, B., 2010, "Constitutive Equations of Basalt Filament Tows under Quasi-Static and High Strain Rate Tension," *Mater. Sci. Eng. A*, **527**(13–14), pp. 3245–3252.
- [10] Zhu, L., Sun, B., and Gu, B., 2012, "Frequency Features of Basalt Filament Tows under Quasi-Static and High Strain Rate Tension," *J. Compos. Mater.*, **46**(11), pp. 1285–1293.
- [11] Gilat, A., Goldberg, R. K., and Roberts, G. D., 2007, "Strain Rate Sensitivity of Epoxy Resin in Tensile and Shear Loading," *J. Aerosp. Eng.*, **20**(2), pp. 75–89.
- [12] Littell, J. D., Ruggeri, C. R., Goldberg, R. K., Roberts, G. D., Arnold, W. A., and Binienda, W. K., 2008, "Measurement of Epoxy Resin Tension, Compression, and Shear Stress–Strain Curves over a Wide Range of Strain Rates Using Small Test Specimens," *J. Aerosp. Eng.*, **21**(3), pp. 162–173.
- [13] Gerlach, R., Siviour, C. R., Petrinic, N., and Wiegand, J., 2008, "Experimental Characterisation and Constitutive Modelling of RTM-6 Resin under Impact Loading," *Polymer (Guildf.)*, **49**(11), pp. 2728–2737.
- [14] Yao, Y., Zhu, D., Zhang, H., Li, G., and Mobasher, B., 2016, "Tensile Behaviors of Basalt, Carbon, Glass, and Aramid Fabrics under Various Strain Rates," *J. Mater. Civ. Eng.*, **28**(9), p. 04016081.
- [15] Wei, B., Song, S., and Cao, H., 2011, "Strengthening of Basalt Fibers with Nano-SiO₂-Epoxy Composite Coating," *Mater. Des.*, **32**(8–9), pp. 4180–4186.
- [16] Briscoe, B. J., and Motamedi, F., 1992, "The Ballistic Impact Characteristics of Aramid Fabrics: The Influence of Interface Friction," *Wear*, **158**(1–2), pp. 229–247.

- [17] Wang, Y., Miao, Y., Huang, L., Swenson, D., Yen, C. F., Yu, J., and Zheng, J. Q., 2016, "Effect of the Inter-Fiber Friction on Fiber Damage Propagation and Ballistic Limit of 2-D Woven Fabrics under a Fully Confined Boundary Condition," *Int. J. Impact Eng.*, **97**(C), pp. 66–78.
- [18] Ou, Y., and Zhu, D., 2015, "Tensile Behavior of Glass Fiber Reinforced Composite at Different Strain Rates and Temperatures," *Constr. Build. Mater.*, **96**(C), pp. 648–656.
- [19] Taniguchi, N., Arai, Y., Nishiwaki, T., Hirayama, N., Nakamura, K., and Kawada, H., 2012, "Experimental Study on Impact Tensile Property of Glass Fiber," *Adv. Compos. Mater.*, **21**(2), pp. 165–175.
- [20] Ou, Y., Zhu, D., Zhang, H., Huang, L., Yao, Y., Li, G., and Mobasher, B., 2016, "Mechanical Characterization of the Tensile Properties of Glass Fiber and Its Reinforced Polymer (GFRP) Composite under Varying Strain Rates and Temperatures," *Polymers (Basel)*, **8**(5), p. 196.
- [21] Lopresto, V., Leone, C., and De Iorio, I., 2011, "Mechanical Characterisation of Basalt Fibre Reinforced Plastic," *Compos. Part B Eng.*, **42**(4), pp. 717–723.
- [22] Gowtham, H. L., Pothnis, J. R., Ravikumar, G., and Naik, N. K., 2013, "High Strain Rate In-Plane Shear Behavior of Composites," *Polym. Test.*, **32**(8), pp. 1334–1341.
- [23] Soares, B., Preto, R., Sousa, L., and Reis, L., 2016, "Mechanical Behavior of Basalt Fibers in a Basalt-UP Composite," *Procedia Struct. Integr.*, **1**(C), pp. 82–89.
- [24] ASTM D3518, 2001, *D3518 - Standard Test Method for In-Plane Shear Response of Polymer Matrix Composite Materials by Tensile Test of a (-/+45) Degree Laminate*.
- [25] Ganzenmüller, G. C., Plappert, D., Trippel, A., and Hiermaier, S., 2019, "A Split-Hopkinson Tension Bar Study on the Dynamic Strength of Basalt-Fibre Composites," *Compos. Part B Eng.*, **171**, pp. 310–319.
- [26] Hufner, D. R., and Hill, S. I., 2017, "High Strain Rate Testing and Modeling of a Woven E-Glass–Vinylester Composite in Dry and Saturated Conditions," *J. Compos. Mater.*, **51**(21), pp. 3017–3039.
- [27] Wang, W., Makarov, G., and Shenoi, R. A., 2005, "An Analytical Model for Assessing Strain Rate Sensitivity of Unidirectional Composite Laminates," *Compos. Struct.*, **69**(1), pp. 45–54.
- [28] Deák, T., and Czigány, T., 2009, "Chemical Composition and Mechanical Properties of Basalt and Glass Fibers: A Comparison," *Text. Res. J.*, **79**(7), pp. 645–651.
- [29] Lu, J., Zhu, P., Ji, Q., and Cheng, Z., 2017, "Experimental Study of In-Plane Mechanical Properties of Carbon Fibre Woven Composite at Different Strain Rates," *Polym. Polym. Compos.*, **25**(4), pp. 289–298.

7

Compressive behavior of epoxy nanocomposites at different strain rates

This chapter was rewritten based on the following articles:

1. Zotti, A., Elmahdy, A., Zuppolini, S., Borriello, A., Verleysen, P., and Zarrelli, M., 2020, "Aromatic Hyperbranched Polyester/RTM6 Epoxy Resin for EXTREME Dynamic Loading Aeronautical Applications," *Nanomaterials*, 10(2), p. 188. *(First co-author)*.
2. Elmahdy, A., Zotti, A., Zuppolini, S., Zarrelli, M., Borriello, A., and Verleysen, P., "Effect of strain rate and filler content on the compressive properties of silica filled epoxy nanocomposites" *(To be submitted to Polymers in 2021)*
3. Zarrelli, M., Elmahdy, A., Zotti, A., Zuppolini, S., Borriello, A., and Verleysen, P., 2018, "Compressive Behavior of Epoxy Resin Filled With Silica Nanoparticles At High Strain Rates," *Proceedings of the 18th European Conference on Composite Materials ECCM18, Athens, Greece 24-28 June 2018*.

7.1. Introduction

This chapter presents the experimental results of the high strain rate compression tests which were performed on the RTM6 epoxy nanocomposites. Section 7.2 provides the procedure of the synthesis of the nanoparticles and the preparation of the nanocomposites. The synthesis of the nanoparticles, the preparation of the nanocomposites, the Dynamic Mechanical Analysis (DMA), and the SEM imaging of the silica nanoparticles were all performed by the National Research Council - Institute of Polymers, Composites and Biomaterials CNR-IPCB in Naples, Italy. Sections 7.3 and 7.4 provide the experimental conditions for the quasi-static and high strain rate testing, in addition to the processing information of the DIC systems. The effect of strain rate on the compressive stiffness, Poisson's ratio and peak yield strength of the tested epoxy nanocomposites is discussed in section 7.5. In addition, the effect of the weight content of all types of nanoparticles used on the compressive behavior of epoxy nanocomposite at different strain rates is presented. Furthermore, the effect of the size and the surface functionalization conditions of the silica nanoparticles on the compressive behavior of epoxy nanocomposites at different strain rates is also discussed. The chapter ends with the main conclusions in section 7.6.

7.2. Specimen materials

7.2.1. Synthesis of the silica nanoparticles

For the synthesis of the silica nanoparticles, Tetraethyl orthosilicate (TEOS), 3-aminopropyl triethoxysilane (APTES) and others solvents were used (supplied from Sigma-Aldrich). All the chemicals were used as received. Non-functionalized silica nanoparticles (NPsNF) were prepared by using the Stöber method [1] with TEOS as precursors. An amount of 19.6 ml of TEOS was added (dropwise and with stirring) to an alcoholic solution containing 50 ml of ethanol, 18 ml of water, and 6.3 ml of ammonia. The mixture was then refluxed at 78°C for 68 mins. The solution was filtered and washed with deionized water, then dried in vacuum oven overnight at 90°C. The same procedure was employed for the synthesis of the functionalized silica nanoparticles (NPsF), however, an equimolar mixture of 9.8 ml TEOS and 10.3 ml APTES was employed instead of the TEOS only [2]. Figure 7.1 shows the SEM images of both types of synthesized silica nanoparticles. The average diameter of the non-functionalized silica nanoparticles was 880 nm, whereas the average diameter of the functionalized silica nanoparticles was 300 nm. The reason of the size difference could be attributable to the functionality of the APTES precursor, which is characterized by only three reactive functional groups (O-CH₂CH₃) compared to TEOS (four reactive functional groups). Such reduced functionality of APTES limits the nanoparticles growth, thus, justifying the lower dimensions of functionalized silica nanoparticles. The nanoparticles and the nanocomposites manufacturing process is schematically illustrated in Figure 7.2.

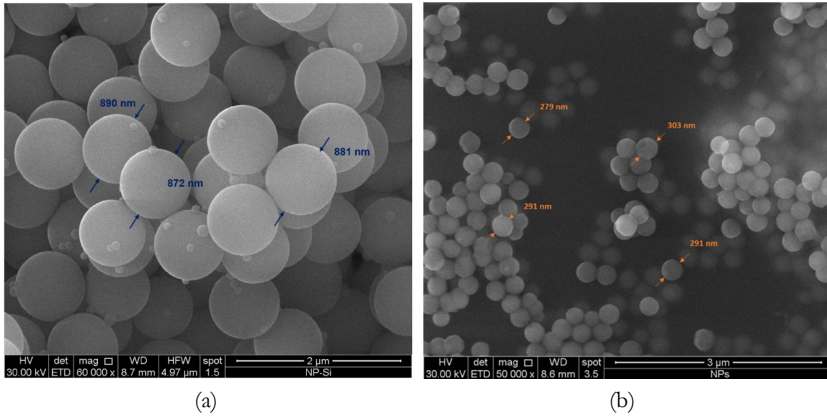


Figure 7.1. SEM images of the synthesized silica nanoparticles: (a) Non-functionalized and (b) Functionalized

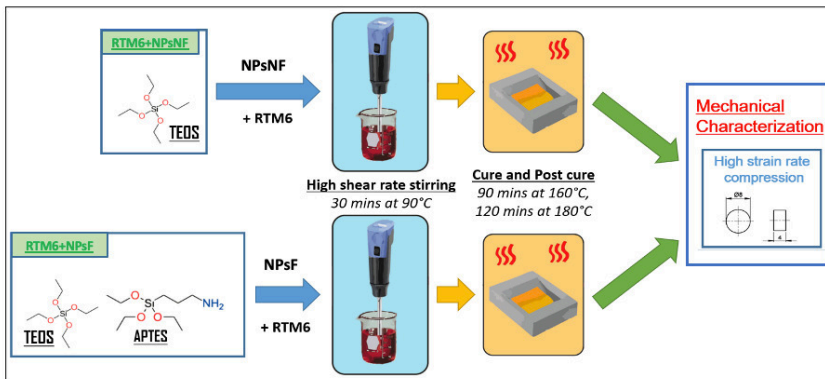


Figure 7.2. Manufacturing procedure of the silica/epoxy nanocomposites

7.2.2. Synthesis of the aromatic hyperbranched polyester nanoparticles

Aromatic hyperbranched polyester AHBP nanoparticles were synthesized according to the method of Zotti et al. [3], as illustrated in Figure 7.3. Five grams of Diphenolic acid and 60 μ l of $\text{Sn}(\text{Oct})_2$ were magnetically stirred in a three-necked round-bottom flask under nitrogen atmosphere for 3 hours at 190 $^{\circ}\text{C}$, in order to ensure the homogeneity of the mixture. The temperature was then increased to 225 $^{\circ}\text{C}$ to trigger the polymerization and the reaction was kept stirred for 3 h. The resulting product was dissolved in 10 ml of tetrahydrofuran (THF), and then the solution was poured in a large amount of deionized water (≈ 0.5 L) in order to precipitate the AHBP. Subsequently, the precipitate was filtered, washed with deionized water, and dried in an oven under vacuum at 100 $^{\circ}\text{C}$, for 24 hours. The obtained AHBP was characterized by a red/brown color.

The synthesized AHBP powder was dissolved in 5 mL of THF and the solution was mixed with the epoxy resin in a round-bottom flask. The solvent was removed by a rotavapor at 90 °C. Four filler contents of 0, 0.1%, 1%, and 5% were added to the neat epoxy resin.

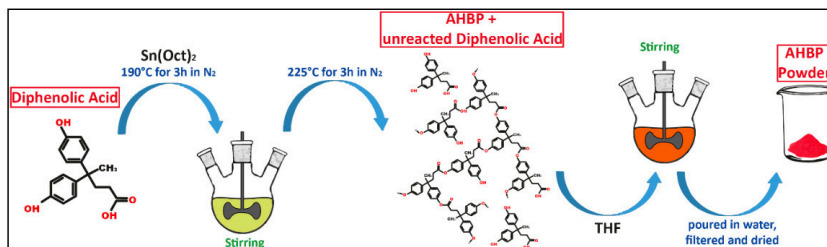


Figure 7.3. Schematic of the synthesis process of the aromatic hyperbranched polyester particles [3]

7.2.3. Preparation of the epoxy nanocomposites and testing specimens

The RTM6 neat resin was prepared according to the procedure described in chapter 5. Both types of nanoparticles were mixed with the neat resin with different weight contents using a high shear rate mixer (T25 digital ULTRA-TURRAX, Germany) to ensure uniform dispersion. For the silica nanoparticle filled epoxy, the weight contents of the non-functionalized silica nanoparticles were 0.1%, 1%, and 5%, and the weight contents of the functionalized silica nanoparticles were 0.1% and 1%. For the AHBP nanoparticle filled epoxy, the weight contents of the nanoparticles were 0.1%, 1%, and 5%. The unreacted mixes of the resin and the synthesized nanoparticles were casted into a cylindrical metallic molds which were coated with a release agent (FREKOTE 70) to facilitate the extraction of the samples. The resins were oven cured at 160°C , for 90 min, followed by a post-curing stage of 2 h at 180°C , and left to cool to room temperature in the oven for 24 hours.

The fully cured cylindrical rods of both neat and filled resins were finally cut into small cylinders of height 4 mm and diameter of 8 mm, as mentioned in chapter 5. To eliminate any discrepancies related to the sample geometry, the same sample geometry and testing boundary conditions were used for both reference quasi-static and high strain rate tests.

7.2.4. Dynamic mechanical analysis of the prepared nanocomposites

The dynamic mechanical analysis of both epoxy based nanocomposites was performed by CNR-IPCB using the DMA Q800 system (manufactured by TA Instruments). The dynamic mechanical properties of the nanocomposites were examined within the temperature range of 40°C to 250°C by using DMA analysis. Figure 7.4 and Figure 7.5 show the storage modulus and tan delta (loss factor) as a function of temperature for both silica and AHBP epoxy nanocomposites, respectively. The tan delta represented the damping component of the material. It can be seen that the addition of both types of silica nanofillers improved the storage modulus of the RTM6 epoxy resin. The largest increase in the storage modulus of approx.

11.6% was associated with the addition of 5% weight of non-functionalized silica nanoparticles to the neat resin. Moreover, the addition of the silica nanofillers also slightly increased the glass transition temperature of the RTM6 epoxy resin, as evident from the temperatures corresponding to the peak of the tan delta curves.

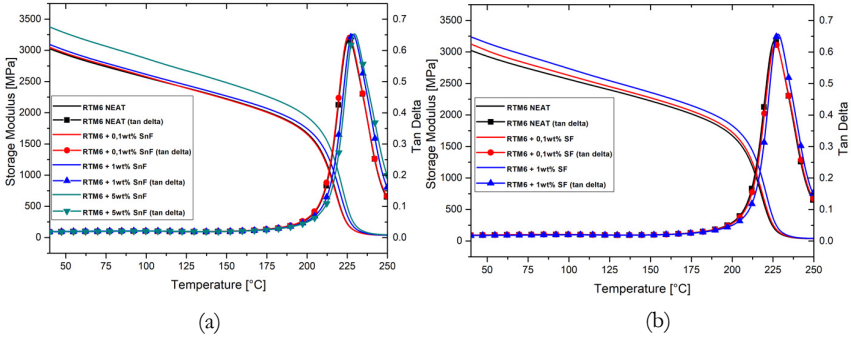


Figure 7.4. Dynamic mechanical analysis (DMA) curves of the silica/RTM6 epoxy nanocomposites in comparison with the neat RTM6 epoxy: (a) non-functionalized silica nanoparticles (b) functionalized silica nanoparticles

On the other hand, the addition of the AHBP nanoparticles to the RTM6 epoxy resin resulted in a slight reduction of its glass transition temperature and storage modulus. The glass transition temperature of the neat resin was 225 °C, while the glass transition temperature of the 0.1%, 1%, and 5% AHBP filled epoxies were 223 °C, 222 °C, and 212 °C respectively. It should be noted that the resultant glass transition temperature of the synthesized hyperbranched polyester AHBP particles was approximately 95 °C [3].

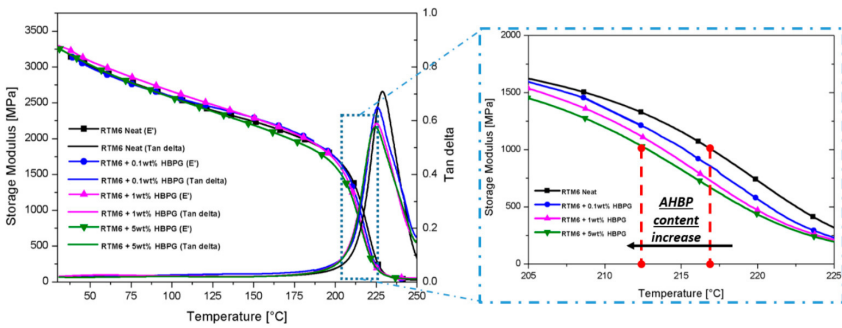


Figure 7.5. Dynamic mechanical analysis (DMA) curves of the AHBP/RTM6 epoxy nanocomposites in comparison with the neat RTM6 epoxy [3]

7.3. Experimental testing conditions

7.3.1. Quasi-static testing

Reference quasi-static experiments were carried out using the universal testing machine described in chapter 3. The tests were also performed with the same quasi-static testing conditions for the neat epoxy, as mentioned in Chapter 5. Tests were performed at speeds of 0.2, 2, and 20 mm/min, aiming at strain rates of 0.001, 0.01, and 0.1 s^{-1} respectively in the sample. Samples were placed between the 2 flat ended steel bars, where the self-alignment attachment was fixed at the interface of the lower bar. The loading interfaces were polished to a mirror finish, and carefully lubricated with a PTFE lubricant to reduce friction. The special alignment tool, described in Chapter 5, was used to position and align the sample between the bars, so that the centerline of the sample and the centerline of the bars are aligned. This also allows the sample to be always in same focus plane of the DIC cameras.

Global displacements and strains were measured using 3 LVDTs which were fixed on the bars. Local full-field displacements and strains were measured using the same 3D DIC setup and calibration conditions described in chapter 5. The speckle pattern was applied to the surface of the samples using airbrush technique prior to testing. Images of the speckled samples were recorded during testing at a resolution of 2452×2056 pixels and a rate of 3 images/sec for the testing speeds of 0.2 and 2 mm/min, and 1 image/sec for the testing speed 20 mm/min.

7.3.2. High strain rate testing

The high strain rate compression experiments were performed using the split Hopkinson pressure bar setup which was described in detail in chapter 3. The tests were also performed with the same high strain rate testing conditions for the neat epoxy resin, as mentioned in Chapter 5. The dynamic compressive wave was generated by accelerating the impactor towards a flange at the end of the input bar at velocities of 8, 11, and 14 m/s. The self-alignment attachment for dynamic testing, described in chapter 5, was fixed to the output bar. Two polished steel-platens of thickness 2 mm were attached to the loading interface of the input bar and to the inner race of the self-alignment attachment on the output bar. The same special tool was also used to position and align the sample between the bars. The loading interfaces of the sample were also lubricated with a PTFE based lubricant to minimize the interfacial friction.

The high speed 3D DIC technique with the same calibration parameters, which was described in chapter 5 for the neat epoxy resin, was used to measure the local strains and strain rates developed on the surface of the sample. A black-on-white speckle pattern was applied to the surface of the samples using aerosol technique prior to testing. Images were recorded at a resolution of 384×265 pixels and a rate of 54,000 images/sec. The average speckle size of the dynamically tested samples was approx. 0.16 mm, corresponding to a size of 3 pixels on the images.

7.3.3. Data reduction and processing parameters for the DIC

The recorded images were processed and analyzed using MatchID commercial digital image correlation software. The different processing parameters used for both quasi-static and dynamic tests were mentioned in chapter 5. The parameters used in the processing of each image allowed to achieve an in-plane strain resolutions of approx. 155 microstrains for quasi-static tests and approx. 400 microstrains for high strain rate experiments. Since the shape of the sample is cylindrical, and due to the limited depth of field available in the cameras, only the central part of the sample lies in the cameras' focal plane, while the outermost edges are out of focus. Therefore, at each moment during the quasi-static and the dynamic tests, the average full field in-plane strains and out-of-plane displacements were extracted from an area of $3.5 \times 3.5 \text{ mm}^2$ around the center of the sample.

7.4. Results and discussion

7.4.1. Compressive stress-strain response of RTM6 epoxy nanocomposites at different strain rates

Figure 7.6 and Figure 7.7 show examples of the true stress-true strain responses of the RTM6 epoxy nanocomposites at different strain rates and particle weight contents. These curves are based on the LVDT strain measurements (for the quasi-static strain rates) and the classical Hopkinson analysis (for the high strain rates). The purpose of showing these curves are only to show the complete stress-strain response of the materials, especially at large deformations. The indicated strain rates correspond to the strain rate at the peak yield strength. At least 3 experiments were performed for each testing condition. Therefore, the curves shown are representative curves for each testing condition. It can be seen that the compressive behavior of all tested epoxies (neat and filled) are strain rate sensitive. The true stress-true strain response for all materials follows 5 different regions as follows: (1) an initial region corresponding to the material's viscoelastic behavior, (2) a non-linear region corresponding to the yielding of the material, which reaches a maximum value at the peak yield point, (3) a strain softening region following the yielding, and (4) further strain hardening and (5) fracture for the quasi-static strain rates, or unloading for the high strain rates. All tested epoxies (filled and unfilled) showed an increase in strength with increasing strain rates. Both Gerlach et al. [4] and Morelle et al. [5] reported similar trends for RTM6 neat resin. It should be noted that only for the epoxy with AHBP weight content of 1%, a reduction in strength can be seen at a strain rate of 0.1 s^{-1} compared to that of 0.01 s^{-1} . Table 7.1, Table 7.2, and Table 7.3 summarize the results of the compression tests at different strain rates for the different types of nanoparticles used. The elastic modulus was calculated as the slope of the line on the true stress - true strain curve drawn between true axial strain ranges of 0 to 0.02. The Poisson's ratio was calculated as the slope of the line on the circumferential strain – axial strain curve drawn between true axial strain ranges of 0 to 0.02. It should be noted that the increase in strength at large deformations (i.e., beyond 35% strain) could be significantly affected by geometric nonlinearities. However, local strain measurements based on DIC were not obtained at these strain

levels as mentioned earlier. Alternative ways to measure the instantaneous cross section to calculate the true stress (such as measuring the diameter between the sample edges) were evaluated, though, because of the lack of focus at the sample edges, these resulted in a low accuracy and were not used.

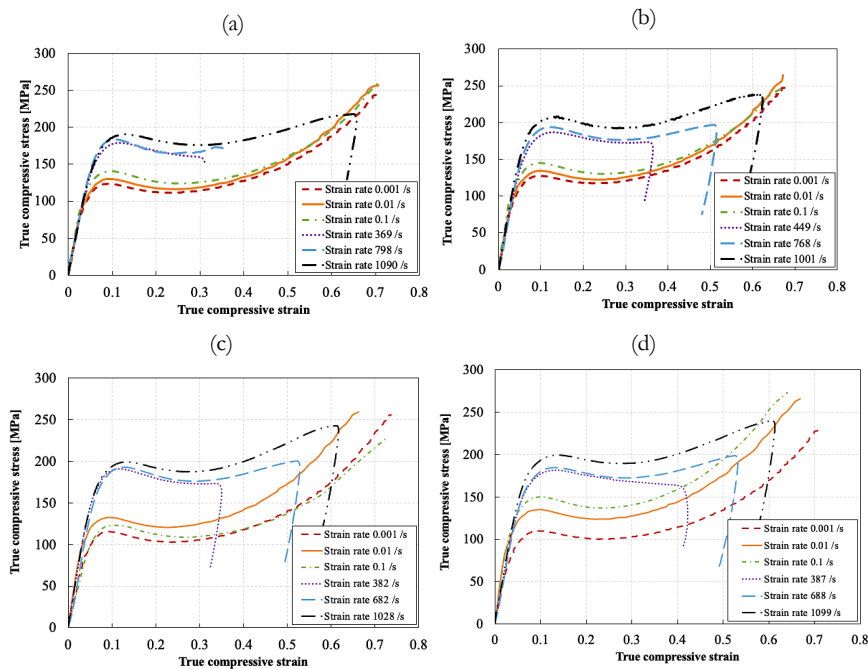


Figure 7.6. Example of the compressive true stress-true strain curves at different strain rates for the RTM6/AHBP nanocomposites at different AHBP weight contents: (a) 0% unfilled neat resin, (b) 0.1%, (c) 1%, (d) 5%

7.4.2. Effect of strain rate and weight content on the elastic modulus and Poisson's ratio of hyperbranched polyester filled RTM6 epoxy resin

Figure 7.8 shows the effect of strain rate on the elastic modulus and the Poisson's ratio of neat and AHBP filled epoxy resins at different particle weigh contents. The stiffness of the neat and AHBP filled resins generally showed a constant behavior with increasing the strain rate regardless of the weight percentages of the fillers. However, increasing the weight content of the AHBP particles lead to a slight decrease in stiffness across all strain rates. The lowest stiffness value was observed in the resin filled with 1% AHBP. The neat RTM6 resin and the resin filled with 5% AHBP particles achieved a nearly similar stiffness of approx. 3300 MPa. The resin filled with 0.1% and 1% AHBP particles achieved a stiffness of approx. 3100 MPa and 3000 MPa respectively. Gerlach et al. [4] reported an increase in stiffness with the increase

in strain rate for the neat RTM6 resin, which seems to contradict the current findings. This could be attributed to the fact that the strain rate range achieved in the current study was much lower compared to the range in Gerlach's work. Poisson's ratio, on the other hand, showed a nearly constant behavior with increasing the strain rates and weight percentages. The average value of the Poisson's ratio for the neat and the AHBP filled epoxies were approx. 0.32

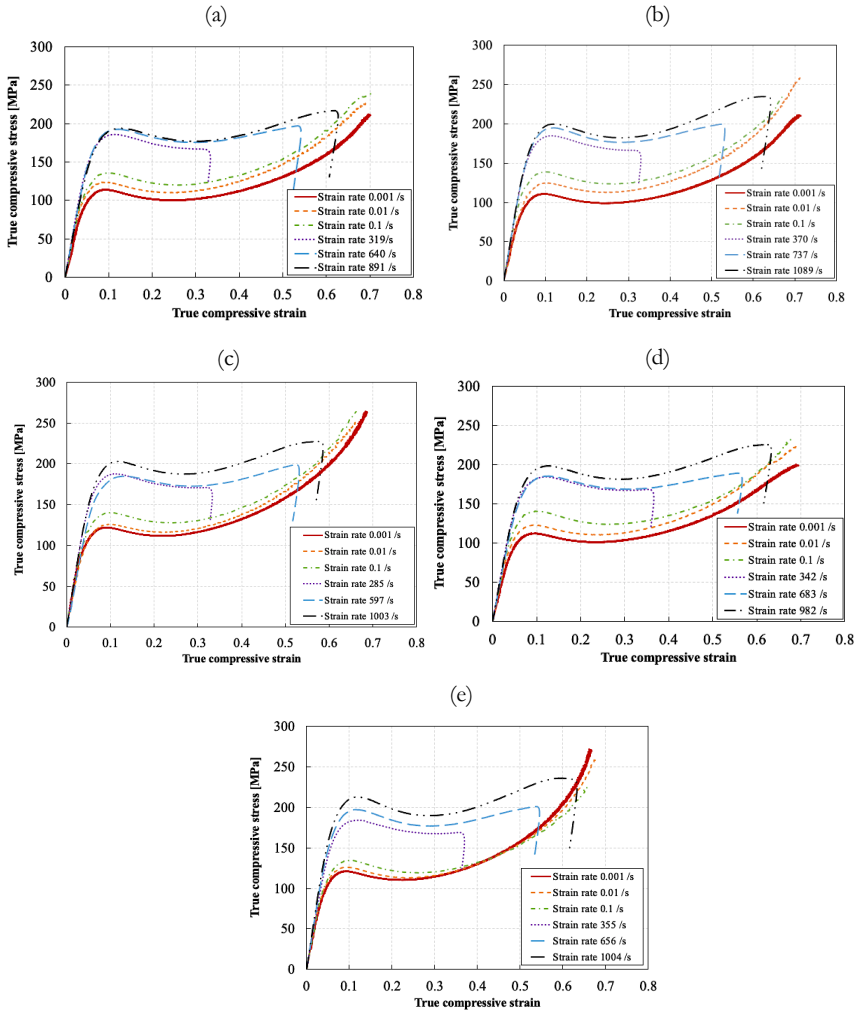


Figure 7.7. Example of the compressive true stress-true strain curves at different strain rates for the RTM6 epoxy/silica nanocomposite at different weight contents: (a) non-functionalized 0.1%, (b) non-functionalized 1%, (c) non-functionalized 5%, (d) functionalized 0.1%, (e) functionalized 1%

Table 7.1. Summary of the results of the neat RMT6 epoxy resin during compression at different strain rates

Material	Achieved strain rates for elastic modulus and Poisson's ratio (s^{-1})	Elastic Modulus (MPa)		Poisson's Ratio		Achieved strain rates for peak yield strength (s^{-1})	True peak yield strength (MPa)	
		Mean	Std. dev.	Mean	Std. dev.		Mean	Std. dev.
RTM6 neat resin	0.001	3242.733	256.889	0.3243	0.1256	0.001	116.403	6.2101
	0.01	3358.254	91.116	0.3208	0.0985	0.01	125.318	4.2153
	0.1	3250.859	314.344	0.2861	0.0178	0.1	135.196	7.8117
	478.638	3293.361	185.774	0.3683	0.09698	365.760	184.840	8.2448
	638.877	3307.398	251.415	0.3174	0.0017	527.334	191.603	11.305
	1034.972	3270.952	182.501	0.3608	0.0375	1017.751	192.295	1.774

Table 7.2. Summary of the results of the RMT6/AHBP epoxy nanocomposite during compression at different strain rates

Material	Achieved strain rates for elastic modulus and Poisson's ratio (s^{-1})	Elastic Modulus (MPa)		Poisson's Ratio		Achieved strain rates for peak yield strength (s^{-1})	True peak yield strength (MPa)	
		Mean	Std. dev.	Mean	Std. dev.		Mean	Std. dev.
RTM6 + 0.1% AHBP	0.001	3087.376	51.454	0.3038	0.0535	0.001	127.489	1.5249
	0.01	3168.662	39.370	0.2965	0.0331	0.01	135.789	1.2294
	0.1	3170.710	230.075	0.2673	0.0150	0.1	148.487	0.9944
	523.753	3138.723	67.298	0.4196	0.0099	449.168	201.065	6.900
	764.82	3112.810	94.101	0.3042	0.0374	768.025	205.430	7.846
RTM6 + 1% AHBP	1113.260	3271.245	302.182	0.2425	0.0286	1001.721	202.931	5.0199
	0.001	2863.227	439.298	0.3339	0.0686	0.001	114.667	2.1923
	0.01	3128.174	40.097	0.2790	0.0482	0.01	132.355	0.4847
	0.1	2891.366	67.166	0.3492	0.0156	0.1	129.811	1.3895
	522.691	2982.136	100.439	0.3950	0.1114	382.032	190.117	0.1477
	706.558	3109.570	56.636	0.2836	0.0258	681.985	190.899	3.389
RTM6 + 5% AHBP	1012	2855.602	334.261	0.3115	0.0766	1027.886	198.290	1.6847
	0.001	3375.550	110.633	0.3058	0.1344	0.001	116.516	0.9488
	0.01	3204.993	90.298	0.2772	0.1020	0.01	135.303	1.6714
	0.1	3264.327	252.327	0.3185	0.0369	0.1	144.308	1.4848
	525.962	3305.327	304.046	0.3505	0.0519	387.244	187.405	5.3024
	805.695	3218.091	174.332	0.3288	0.0608	687.926	195.717	4.4283
	1024.405	3082.614	83.6394	0.2886	0.0465	1099.499	200.196	5.1677

Table 7.3. Summary of the results of the RMT6/ silica epoxy nanocomposite (functionalized and non-functionalized) during compression at different strain rates

Material condition	Achieved true strain rates for elastic modulus and Poisson's ratio (s ⁻¹)	Elastic Modulus (MPa)		Poisson's Ratio		Achieved true strain rates for peak yield strength (s ⁻¹)	True peak yield strength (MPa)	
		Mean	Std. dev.	Mean	Std. dev.		Mean	Std. dev.
RTM6 + 0.1% NPsNF	0.001	3353.936	99.236	0.3471	0.0675	0.001	122.063	3.574
	0.01	3033.310	182.010	0.3175	0.0978	0.01	133.812	7.4526
	0.1	2922.217	141.158	0.3259	0.0045	0.1	143.187	1.1321
	454.339	3247.134	25.149	0.3046	0.0531	318.821	187.955	0.994
	750.6	3039.834	129.447	0.3398	0.0073	640.054	193.176	0.717
	946.35	2977.784	30.479	0.3846	0.0189	891	193.292	0.9457
RTM6 + 1% NPsNF	0.001	3084.413	230.726	0.3318	0.0325	0.001	126.242	0.873
	0.01	3214.713	162.226	0.3147	0.2677	0.01	132.376	0.0631
	0.1	3275.084	65.296	0.2677	0.0300	0.1	144.471	0.1899
	520.731	3120.626	196.823	0.3090	0.0013	369.592	188.867	3.8367
	786.096	3026.813	23.909	0.3172	0.0675	737.255	200.455	5.8581
	1093.333	3019.802	123.911	0.3516	0.0306	1089.456	199.829	3.6738
RTM6 + 5% NPsNF	0.001	2986.129	365.567	0.2324	0.0038	0.001	119.690	6.1066
	0.01	3310.217	130.112	0.3299	0.0240	0.01	133.717	1.6009
	0.1	2910.994	157.030	0.2516	0.0597	0.1	150.631	0.4492
	431.035	3270.771	70.508	0.3174	0.0607	285.279	189.522	2.3349
	670.14	3073.089	9.645	0.3031	0.0809	596.957	194.067	0.5062
	1015.2	3055.304	68.713	0.3341	0.0766	1003.242	202.986	2.6408
RTM6 + 0.1% NPsF	0.001	2910.187	132.380	0.3573	0.0028	0.001	121.454	2.6183
	0.01	3059.861	94.604	0.3300	0.0792	0.01	129.692	1.6139
	0.1	2844.310	238.876	0.2572	0.0465	0.1	152.510	0.6441
	476.222	3261.809	25.714	0.3439	0.0621	342.424	183.886	1.0950
	782.692	3009.674	80.688	0.2900	0.0068	683.038	187.785	3.3535
	991.71	2838.911	15.762	0.3723	0.072	982.414	200.873	3.3542
RTM6 + 1% NPsF	0.001	3367.566	10.616	0.3013	0.0457	0.001	124.687	0.9358
	0.01	3228.427	56.313	0.3707	0.0112	0.01	132.181	3.4609
	0.1	3011.124	160.050	0.3152	0.0189	0.1	143.443	3.0203
	524.656	3068.355	174.398	0.2990	0.0818	355.420	185.585	1.7706
	711.72	3071.298	286.803	0.3875	0.0334	656.1	195.882	2.0841
	1048.6	3128.0738	451.367	0.3576	0.1438	1004.4	210.579	3.1928

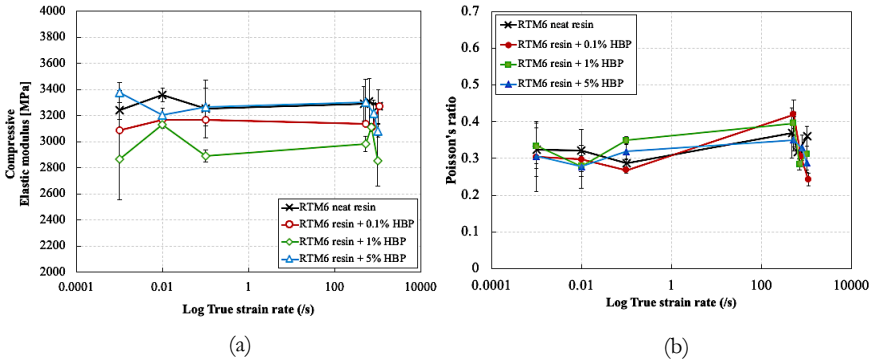


Figure 7.8. Effect of strain rate on the elastic modulus and Poisson's ratio of the AHBP filled epoxy at different particle weight contents: (a) elastic modulus, (b) Poisson's ratio

7.4.3. Effect of strain rate and weight content on the peak yield strength of hyperbranched polyester filled RTM6 epoxy resin

Figure 7.9 shows the effect of strain rate on the true peak yield strength for neat and AHBP filled epoxy resins at different particle weight contents. All tested materials showed an increase in the true peak yield strength at increasing strain rates. Similar results were obtained by Rio et al. [21] for a comparable epoxy resin. It can be seen that the addition of 0.1% and 5 wt% AHBP to the epoxy resin improved the true peak yield strength at different strain rates. The addition of 1 wt% AHBP to the epoxy resin improved the true peak yield strength slightly at high strain rates, while it had almost no effect at low strain rates. Compared to other filler contents, the most significant increase in the true peak yield strength was observed with the addition of 0.1 wt% AHBP. Indeed, at 0.1 wt% filler content, the true peak yield strength increased from 113 MPa for the neat resin to 128 MPa at strain rate of 0.0008 s^{-1} , and from 190 to 206 MPa at strain rate of 1000 s^{-1} . This corresponds to percentage increases of 13.2% and 8.4%, respectively, compared to the neat resin. On the other hand, a further increase in the AHBP content induced a reduction of the true peak yield strength compared to the sample loaded with 0.1 wt% of AHBP. The true peak yield strength at 5 wt% filler content decreased to approximately 120 MPa at a strain rate of 0.0008 s^{-1} and to approximately 200 MPa at a strain rate of 1000 s^{-1} compared to the respective values of 128 and 206 MPa at 0.1 wt% filler content. However, this still corresponds to percentage increases of about 6.2% and 5.3%, respectively, compared to the neat resin. Furthermore, for the 1 wt% filler content, the true peak yield strength increased to approximately 200 MPa at a strain rate of 1000 s^{-1} , which corresponds to an increase of only 4% compared to that of the neat resin. The relative decrease in the true peak yield strength at 1 and 5 wt% AHBP contents compared to the 0.1 wt% AHBP content is attributed to the softening effect associated with the addition of a relatively high AHBP content to the epoxy matrix, as explained earlier. In addition, since the true peak yield strength is realized at a compressive strain of approximately 10%, adiabatic heating effects cannot be neglected, especially at high strain rates [6]. Since the T_g of the AHBP is relatively

low, i.e., 95 °C (see section 7.2.4), the adiabatic heating induced in the sample during high strain rate deformation could transform the AHBP from their stiff glassy state to a soft rubbery state. This, in turn, might reduce the overall yield strength in the resulting AHBP filled epoxy loaded at higher strain rates. Indeed, Pan et al. [7] reported that the temperature rise in the sample due to adiabatic heating of epoxy at high strain rates can reach up to 90 °C. The increasing trend of the true peak yield strength of the AHBP filled epoxies with increasing strain rate can be described by a least square power fit relation as follows (R^2 values are greater than 0.9):

$$\sigma_t^{Peak\ yield} = A\dot{\epsilon}^b \quad (7.1)$$

Where $\sigma_t^{Peak\ yield}$ is the true peak yield strength in compression, A is the compressive strength coefficient, and b is the strain rate sensitivity exponent. For the unfilled epoxy resin, the compressive strength coefficient and the strain rate sensitivity exponents were 149.19 MPa and 0.0374 respectively. For the AHBP filled epoxy resin, the compressive strength coefficients for the 0.1%, 1%, and 5% weight contents were 161.2 MPa, 150.11 MPa, and 154.55 MPa respectively, while the strain rate sensitivity exponents for the same consecutive weight contents were 0.0352, 0.0383, and 0.0359 respectively.

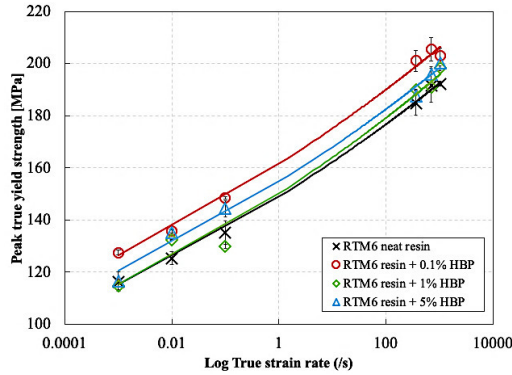


Figure 7.9. Effect of strain rate on the compressive true peak yield strength for the AHBP filled epoxy at different particle weight contents

7.4.4. Effect of strain rate and weight content on the elastic modulus and Poisson’s ratio of the silica nanoparticles filled RTM6 epoxy resin

Figure 7.10 and Figure 7.11 show the effect of strain rate on the elastic modulus and the Poisson’s ratio of silica nanoparticles filled epoxy resins at different particle weigh contents and functionalization conditions. The elastic modulus was slightly improved by the addition of the silica nanoparticles with different weight percentages of the particles across all strain rates. The elastic modulus of the neat resin was increased from approx. 3100 MPa to approx. 3300 MPa by the addition of silica nanoparticles. This corresponds to an increase of approx. 6.4%. Moreover, the elastic modulus was nearly constant with increasing the strain rates. Increasing the weight content of both particle types up to 5% also did not have a significant effect on the elastic modulus across all strain rates. The Poisson’s ratio also showed a nearly constant behavior with increasing the strain rates, at different weight percentages of the fillers and their functionalization conditions. The average value of the Poisson’s ratio for the neat and silica nanoparticle filled epoxies was approx. 0.32. The slight increase in the elastic modulus by the addition of the silica nanoparticles is due to the transfer of forces from the matrix to the higher stiffness particles. As mentioned earlier, the epoxy resin showed a predominantly elastic behavior rather than a viscoelastic behavior at the early stages of loading – i.e. small strains based on the DMA results. Consequently, the resin material is expected to show strain rate independency at small strains due to the lack of contribution of the damping component in the deformation behavior at high strain rates.

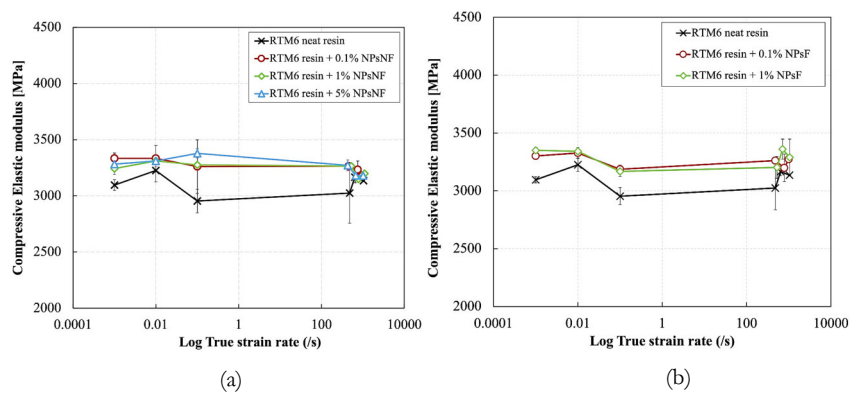


Figure 7.10. Effect of strain rate on the elastic modulus of the silica nanoparticle filled epoxy at different particle weight contents and functionalization conditions: (a) non-functionalized, (b) functionalized

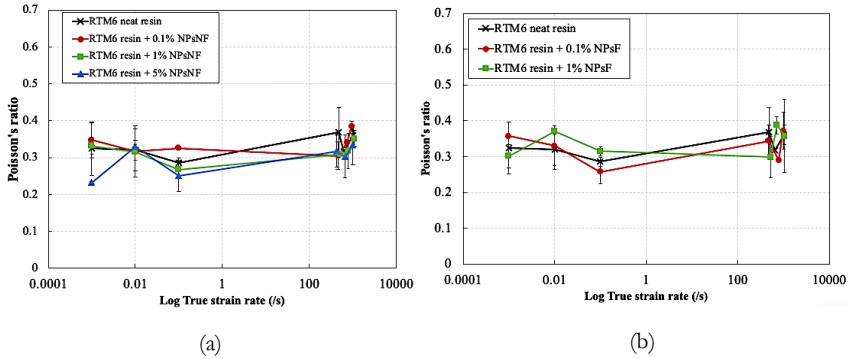


Figure 7.11. Effect of strain rate on the Poisson's ratio of the silica nanoparticle filled epoxy at different particle weight contents and functionalization conditions: (a) non-functionalized, (b) functionalized

7.4.5. Effect of strain rate and weight content on the peak yield strength of the silica nanoparticles filled RTM6 epoxy resin

Figure 7.12 shows the effect of strain rate on the true peak yield strength for functionalized and non-functionalized silica nanoparticle filled epoxy resins. Similar to the AHBP, the addition of the silica nanoparticles with different weight contents also improved the true peak yield strength at different strain rates compared to the neat resin. Hardly any change was observed in the trend of the true peak yield strength with increasing strain rate as a result of the surface functionalization conditions of the silica nanoparticles. Compared to the neat resin at low strain rates, the peak yield strength of the 0.1% silica content increased from 116.4 MPa to 122.42 MPa at strain rate of 0.0008 s^{-1} , and from 135.19 MPa to 143.18 MPa at strain rate of 0.08 s^{-1} . This corresponds to percentage increase of 5.2% and 5.9% respectively. This increase was almost the same regardless of the filler content in the low strain rate range up to 0.08 s^{-1} .

Moreover, it can be seen that the improvement of the peak yield strength was much more significant in the low strain rate range compared to the high strain rate range. Indeed, compared to the neat resin, the peak yield strength of the 0.1% silica nanoparticle content increased from 184.84 MPa to 187.95 MPa at strain rate of 277.5 s^{-1} and 303.7 s^{-1} respectively, and from 192.3 MPa to 193.39 MPa at strain rate of 1019.65 s^{-1} and 904.1 s^{-1} . This corresponds to percentage increases of 1.6% and 0.56% respectively, which are much lower compared to the percentage increases in the low strain rate range. Unlike the AHBP filled resin, the most significant improvement of the true peak yield strength was observed at silica weight contents of 1% and 5%, especially at low strain rates. Similar results were also reported by Tian et al. [8] and Miao et al. [9], but for a different epoxy formulation and a different size of nanoparticles. The increase in the true peak yield strength of the epoxy/silica nanocomposite is attributed mainly to the viscoelastic nature of the resin. However, further research is still required to

understand why the improvement of the yield strength is reduced at high strain rates compared to low strain rates. At low strain rates, the viscoelastic resin has enough time to deform. This allows the transfer of the forces from the matrix to the higher strength and higher stiffness silica nanoparticles, which further increase the yield strength. However, at high strain rates, the viscoelastic resin does not have enough time to fully deform due to the reduced molecular mobility of the polymer chains, as demonstrated by Chen et al. [10]. The reduced molecular mobility at high strain rates could reduce the interaction between the resin and the silica nanoparticles [11]. This behavior was also observed for the carbon nanotube fillers, as reported by Del Rio et al. [12]. Another contributing factor is the adiabatic heating effects at high strain rates, which cannot be neglected given the temperature increase of 90 °C as seen in the previous section. Indeed, it was reported by Del-Rio et al. [13] that an increase of 40 °C can reduce the yield strength of epoxy by 23% at high strain rates. It is worth mentioning that Miao et al. [9] suggested that the strain softening of the epoxy matrix is the main contributing factor of the reduction in the yield strength at higher strain rates regardless of the nanoparticle weight percentage added. However, this conclusion was based on a simple model which was validated only for silica nanoparticle content of 10%, and cannot be directly extended to other highly crosslinked epoxy resins and other weight percentages of silica nanoparticles.

The increasing trend of the true peak yield strength of the silica filled epoxies with increasing strain rate can be described by a least square power fit relation as follows (R^2 values are greater than 0.9):

$$\sigma_t^{Peak\ yield} = C\dot{\epsilon}^d \quad (7.2)$$

Where $\sigma_t^{Peak\ yield}$ is the true peak yield strength in compression, C is the compressive strength coefficient, and d is the strain rate sensitivity exponent. For the non-functionalized silica filled epoxy resin, the compressive strength coefficients for the 0.1%, 1%, and 5% weight contents were 154.85 MPa, 156.13 MPa, and 157.04 MPa respectively, while the strain rate sensitivity exponents for the same consecutive weight contents were 0.0335, 0.0353, and 0.0354 respectively. For the functionalized silica filled epoxy resin, the compressive strength coefficients for the 0.1% and 1%, weight contents were 155.09 MPa and 156.96 MPa respectively, while the strain rate sensitivity exponents for the same consecutive weight contents were 0.0331 and 0.0355 respectively.

7.4.6. Effect of the silica nanoparticles size and surface functionalization of on the elastic modulus, Poisson's ratio, and peak yield strength of RTM6 epoxy nanocomposite

Despite the different surface functionalization conditions of the silica nanoparticles used in this study, a rough estimate of the effect of the different sizes of these nanoparticles on the compressive behavior of the epoxy resin can still be studied. Figure 7.13, Figure 7.14, and Figure 7.15 show the effect of the silica nanoparticles size and surface functionalization conditions on the peak true yield strength, elastic modulus, and Poisson's ratio, respectively, for weight percentages of 0.1% and 1% at different strain rates. It can be seen that for a silica

nanoparticle content of 0.1%, the size of the particles and the surface functionalization conditions did not have a significant effect on the true peak yield strength and the elastic modulus all strain rates. Whereas for a silica nanoparticle content of 1%, a very slight increase in the true peak yield strength can be seen at the high strain rate range as a result of reducing the particle size from 880 nm to 300 nm and the functionalization of the particle surface. The size and the surface functionalization of the nanoparticles also did not show a significant effect on the elastic modulus and the Poisson's ratio at different strain rates for both filler contents. Similar results were reported by Dittanet et al. [14] for similar epoxy system at quasi-static strain rates and silica nanoparticle size range from 23 nm to 170 nm. Here, again, further research is required to understand why the change of the silica nanoparticle sizes in the range 300 nm to 880 nm does not significantly affect the compressive properties of the epoxy resin, particularly at high strain rate. As explained earlier in section 3.8, the combined effect of viscoelasticity and adiabatic heating could be the main contributing factors in that case.

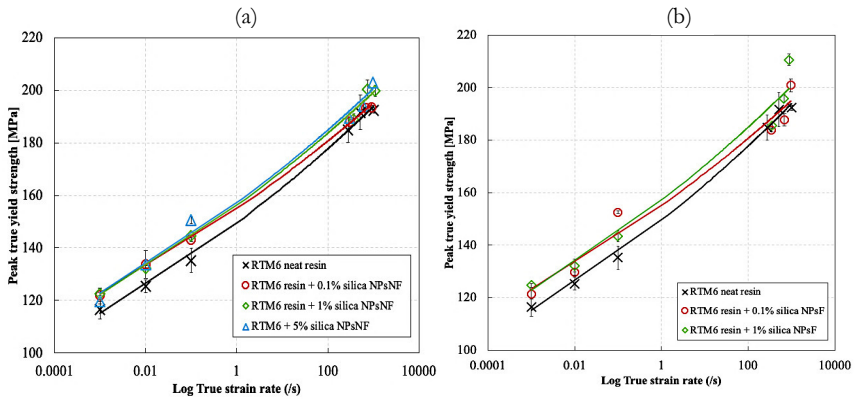


Figure 7.12. Effect of strain rate on the compressive true peak yield strength for the silica nanoparticle filled epoxy at different particle weight contents and functionalization conditions: (a) non-functionalized, (b) functionalized

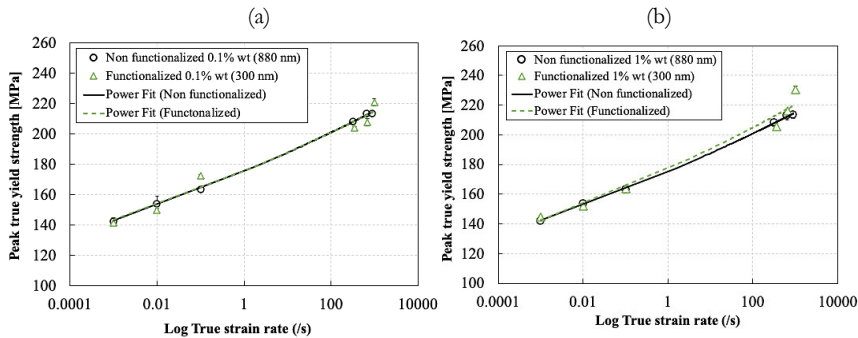


Figure 7.13. Effect of silica nanoparticles size and surface functionalization on the compressive true peak yield strength for the silica nanoparticle filled epoxy at different particle weight contents: (a) 0.1%, (b) 1%

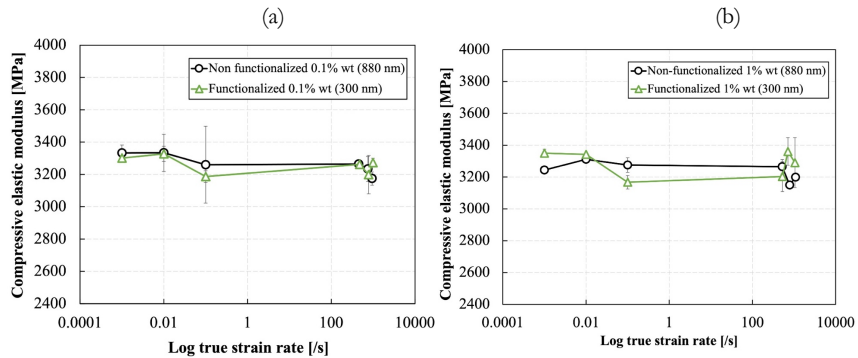


Figure 7.14. Effect of silica nanoparticles size and surface functionalization on the compressive elastic modulus for the silica nanoparticle filled epoxy at different particle weight contents: (a) 0.1%, (b) 1%

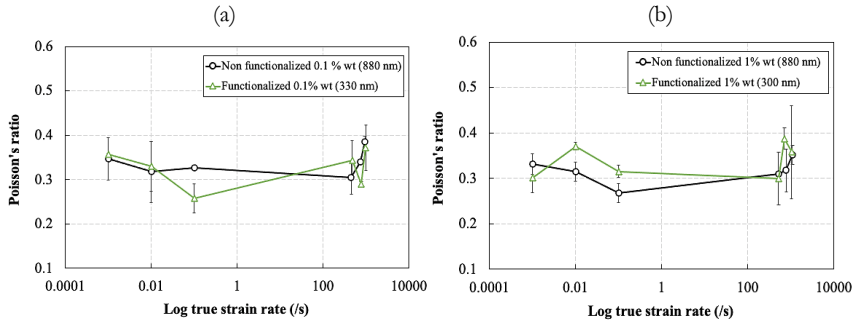


Figure 7.15. Effect of silica nanoparticles size and surface functionalization on the Poisson's ratio for the silica nanoparticle filled epoxy at different particle weight contents: (a) 0.1%, (b) 1%

7.5. Conclusions

Several experiments were performed in order to study the compressive behavior of several epoxy based nanocomposites at various strain rates. The matrix material was the aeronautical grade RTM6 epoxy, and the fillers were silica nanoparticles with a sizes of 300 nm and 880 nm and different surface functionalization conditions, and hyperbranched polyester nanoparticles. Three weight percentages were considered for the fillers: 0.1%, 1%, and 5%. High strain rate compression experiments were performed using the split Hopkinson pressure bar setup. Moreover, reference quasi-static compression experiments were also performed in order to study the compressive behavior of the RTM6 epoxy nanocomposites at a wide range of strain rates. Therefore, the strain rate range covered in this study was 0.001 s^{-1} up to 1099 s^{-1} . Local strains in the sample were measured using the 3D digital image correlation technique. During the execution of the experiments and the analysis of the results, a special attention was paid to experimentally improve the contact conditions and to reduce the interfacial friction conditions during compression. The effect of the strain rate, the size, the surface functionalization, and the weight percentage of the nanoparticles on the elastic modulus, the Poisson's ratio, and the true peak yield strength of the tested materials were discussed. Considering the tested materials, manufacturing techniques used, testing equipment and results, the following can be concluded:

1. The tested neat and nanoparticle filled RTM6 resins were all strain rate sensitive in compression. All materials showed an increase in strength and true peak yield strength with increasing strain rates for all the weight percentages and sizes of all nanoparticles.
2. The elastic modulus and the Poisson's ratio of the tested epoxy nanocomposites were independent of the strain rate, and showed a nearly constant behavior at different strain rates for all weight percentages and sizes of all types of nanoparticles.
3. The addition of silica and AHBP nanoparticles increased the true peak yield strength of the resin at all strain rates and all weight percentages and sizes of all the nanoparticles used. For the AHBP nanoparticles, the weigh percentage of 0.1 resulted in the highest improvement in the true peak yield strength. Further increase in the weight percentage

of the particles to 5% resulted in a decrease in the true peak yield strength but still higher than that of the neat resin. For the silica nanoparticles, it was found that increase in the silica nanoparticle weight percentage resulted in a slight increase in the true peak yield strength for all strain rates. Additionally, the improvement of the peak yield strength due to the addition of silica nanoparticles was more prominent in the quasi-static strain rate regime compared to the high strain rate regime.

4. The addition of AHBP nanoparticles to the epoxy resin lead to a decrease in the elastic modulus at all weight percentages of the particles, whereas the Poisson's ratio remained nearly constant with the addition of the AHBP particles. On the other hand, the addition of silica nanoparticles to the RTM6 epoxy resin generally improved both its elastic modulus and its peak yield strength at different strain rates for all the weight percentages of the particles. Increasing the weight percentage of both types the silica nanoparticles did not yield any improvement in the elastic modulus and the Poisson's ratio.
5. The sizes and surface functionalization conditions of the silica nanoparticles used (300 nm and 880 nm) did not significantly affect the compressive properties of the RTM6 epoxy resin, regardless of the weight percentages of the particles.

References

- [1] Fang, M., Volontinen, T. T., Kulkarni, S. K., Belova, L., and Rao, K. V., 2010, "Effect of Embedding Fe₃O₄ Nanoparticles in Silica Spheres on the Optical Transmission Properties of Three-Dimensional Magnetic Photonic Crystals," *J. Appl. Phys.*, **108**(10).
- [2] Zotti, A., Zuppolini, S., Borriello, A., and Zarrelli, M., 2019, "Thermal Properties and Fracture Toughness of Epoxy Nanocomposites Loaded with Hyperbranched-Polymers-Based Core/Shell Nanoparticles," *Nanomaterials*, **9**(3), p. 418.
- [3] Zotti, A., Elmahdy, A., Zuppolini, S., Borriello, A., Verleysen, P., and Zarrelli, M., 2020, "Aromatic Hyperbranched Polyester/RTM6 Epoxy Resin for EXTREME Dynamic Loading Aeronautical Applications," *Nanomaterials*, **10**(2), p. 188.
- [4] Gerlach, R., Siviour, C. R., Petrinic, N., and Wiegand, J., 2008, "Experimental Characterisation and Constitutive Modelling of RTM-6 Resin under Impact Loading," *Polymer (Guildf.)*, **49**(11), pp. 2728–2737.
- [5] Morelle, X. P., Chevalier, J., Bailly, C., Pardoën, T., and Lani, F., 2017, "Mechanical Characterization and Modeling of the Deformation and Failure of the Highly Crosslinked RTM6 Epoxy Resin," *Mech. Time-Dependent Mater.*, **21**(3), pp. 419–454.
- [6] Arruda, E. M., Boyce, M. C., and Jayachandran, R., 1995, "Effects of Strain Rate, Temperature and Thermomechanical Coupling on the Finite Strain Deformation of Glassy Polymers," *Mech. Mater.*, **19**(2–3), pp. 193–212.
- [7] Pan, Z., Sun, B., Shim, V. P. W., and Gu, B., 2016, "Transient Heat Generation and Thermo-Mechanical Response of Epoxy Resin under Adiabatic Impact Compressions," *Int. J. Heat Mass Transf.*, **95**, pp. 874–889.
- [8] Tian, Y., Zhang, H., Zhao, J., Li, T., Bie, B. X., Luo, S. N., and Zhang, Z., 2016, "High Strain Rate Compression of Epoxy Based Nanocomposites," *Compos. Part A Appl. Sci. Manuf.*, **90**(C), pp. 62–70.
- [9] Miao, Y. G., Liu, H. Y., Suo, T., Mai, Y. W., Xie, F. Q., and Li, Y. L., 2016, "Effects of Strain Rate on Mechanical Properties of Nanosilica/Epoxy," *Compos. Part B Eng.*, **96**(9), pp. 119–124.
- [10] Chen, L. P., Yee, A. F., and Moskala, E. J., 1999, "The Molecular Basis for the Relationship between the Secondary Relaxation and Mechanical Properties of a Series of Polyester Copolymer Glasses," *Macromolecules*, **32**, pp. 5944–5955.
- [11] Rose, S., Dizeux, A., Narita, T., Hourdet, D., and Marcellan, A., 2013, "Time Dependence of Dissipative and Recovery Processes in Nanohybrid Hydrogels," *Macromolecules*, **46**(10), pp. 4095–4104.

- [12] Gómez-Del Río, T., Rodríguez, J., and Pearson, R. A., 2014, "Compressive Properties of Nanoparticle Modified Epoxy Resin at Different Strain Rates," *Compos. Part B Eng.*, **57**, pp. 173–179.
- [13] Gómez-del Río, T., and Rodríguez, J., 2012, "Compression Yielding of Epoxy: Strain Rate and Temperature Effect," *Mater. Des.*, **35**(C), pp. 369–373.
- [14] Dittanet, P., and Pearson, R. A., 2012, "Effect of Silica Nanoparticle Size on Toughening Mechanisms of Filled Epoxy," *Polymer (Guildf)*, **53**(9), pp. 1890–1905.

Intentionally left blank

8

Conclusions and future perspectives

This chapter provides a summary of the conclusions presented in the previous chapters. Additionally, future research paths based on the findings of this PhD research are presented.

8.1. Summary of conclusions

Performed within the framework of the H2020 research project EXTREME, the aim of this PhD research was to study the mechanical behavior of new classes of epoxy based composite materials for aerospace applications at high strain rates. The materials considered in this research were woven basalt fiber reinforced epoxy and epoxy nanocomposites reinforced with silica nanoparticles and hyperbranched polymers. These new classes of composite materials were developed to address the challenges of implementing composite materials in modern aircrafts, such as the resistance to impact, the environmental aspects related to material recycling, and the costs of manufacturing, certification and airworthiness testing. For the basalt epoxy composites, the in-plane tensile and shear behaviors were studied. Additionally, due to the many similarities with glass epoxy composites, the mechanical behavior of the basalt epoxy composites was compared to the behavior of glass epoxy composites. For the epoxy nanocomposites reinforced with silica nanoparticles and hyperbranched polymers, the compressive behavior was studied.

A critical review of the state-of-the-art on the effect of strain rate on the mechanical behavior of basalt fiber composites and epoxy nanocomposites filled with silica nanoparticles and hyperbranched polymers was discussed in chapter 2. Additionally, the review was extended to include the effect of strain rate on the mechanical behavior of glass fiber composites, and a comparison between the mechanical behaviors of glass fiber composites and basalt fiber composites was presented. It was found that the effect of strain rate on the mechanical behavior of the considered materials is not very well understood, either due to the contradiction of the findings in the literature, or the lack of reliable results. The literature also lacks a meaningful comparison between the mechanical behavior of glass fiber composites and basalt fiber composites at different strain rates.

The most commonly used methods for high strain rate testing were summarized and critically discussed in chapter 3. It was found that servo-hydraulic machines have some limitations in high strain rate testing such as load cell ringing and the correct establishment of the quasi-static equilibrium, and therefore, not suitable for testing polymers and brittle composites at high strain rates. On the other hand, the split Hopkinson bar technique does not have these limitations due to its exploitation of wave propagation phenomena, and was therefore used for the high strain rate experiments in this research. Special attention was paid to the experimental minimization of wave dispersion effects and the facilitation of quasi-static equilibrium by using polymer impactors. Moreover, the quality of the measured strain signals on the bars and the signal-to-noise ratio were improved by using semiconductor strain gauges. Reference quasi-static testing was also performed using a universal testing machine. For these tests, a custom designed system of bars was used to reduce the influence of the heavy grips on the small brittle samples, while keeping the same boundary conditions as in the high strain rate tests.

The digital image correlation technique was utilized to accurately measure the strains in the samples, and to provide the full displacement and strain fields during testing, as discussed in chapter 4. State-of-the-art low and high speed digital image correlation setups were developed in 2D and stereo 3D configurations. The optical components and the processing parameters of both systems were optimized for measuring small strains in the small scale polymer and composite samples. The effect of the processing parameters such as subset size, step size, strain window, and subset shape function on the average displacement and strain random error (i.e. noise levels) were studied for both the 2D and 3D DIC systems. It was found that the average displacement and strain random errors, i.e., noise levels, decreased with increasing subset size, step size, and strain window, which was expected considering the smoothing effects of these parameters on the results. A first order affine shape function achieved lower displacement and strain errors compared to quadratic shape functions. Finally, the 3D DIC systems were selected to study the epoxy nanocomposites and the basalt/epoxy composites.

The challenges related to testing of polymers and brittle composites in tension and compression using the split Hopkinson bar technique were discussed in chapter 5. Important aspects such as the design of sample geometries which can fulfil the high strain rate testing requirements, aspects related to boundary conditions, load introduction, sample clamping, and validating the testing and the material assumptions were discussed in detail. The challenges in compression testing were investigated using RTM6 neat epoxy resin at quasi-static and high strain rates. New tools and attachments were developed specifically to provide good interfacial contact conditions at the start of the compression tests, and to align the samples between the bars. After selecting a suitable sample geometry, the establishment of the quasi-static equilibrium was studied. Additionally, the uniformity of axial strains and the effect of strain rate and lubrication on the interfacial friction were analyzed with the aid of DIC. Furthermore, the assumption of volume conservation during yielding of epoxy was validated by measuring the instantaneous cross section area of the deforming sample using the DIC. It was found that the selected compression sample geometry achieved an early quasi-static equilibrium at high strain rates, which enabled the extraction of the dynamic elastic modulus and the Poisson's ratio in compression. Sample barreling due to interfacial friction, quantified by the barreling ratio, showed a decrease with increasing strain rate. This was also confirmed by the nearly homogenous distribution of the axial strains in the compression sample. The assumption of volume conservation was found to be invalid in the yielding and post-yielding stages of compression deformation at low and high strain rates. Consequently, the DIC technique proved to be essential for the accurate determination of the stress-strain response of epoxy at low strains – and of polymers in general – in compression.

Moreover, the critical aspects related to tensile testing of brittle composites were studied based on basalt/epoxy composites using two sample geometries, namely a dog-bone and straight strip geometry. In this study, both geometries were assessed and compared based on the criteria of establishment of quasi-static force equilibrium and the uniformity of the axial strain fields with the aid of DIC measurements. Pin/slot end tabs were used to fix both samples to the bars. An alignment tool was also used to accurately align the brittle tensile samples between the end tabs and the bars. Results showed that both sample geometries fulfilled the requirements of an early quasi-static force equilibrium and homogeneous axial strain

distribution. Both geometries also showed similar stress-strain response for the basalt/epoxy material. However, the classical Hopkinson analysis overestimated the actual strains and strain rates in the sample by approx. a factor of 3 for both geometries. This overestimation resulted from the contribution of the transition zones to the total deformation. Local measurement of the strains along the gauge section was, therefore, crucial for the reliability of the characterization of the high strain rate behavior of composites.

Based on the previously discussed methodologies and aspects of the testing techniques, the materials under investigation were characterized. In chapter 6, the tensile behavior in the warp and fill directions and the shear behavior in the off-axis direction of the basalt epoxy composites were investigated. Additionally, a comparison between the tensile and shear behaviors of the woven basalt and a woven glass fiber reinforced epoxy composites at various strain rates was presented. For this comparison, the same epoxy matrix and manufacturing technique were used. The strain rates covered were 0.0006 s^{-1} up to 154 s^{-1} for tensile experiments and 0.003 s^{-1} up to 645 s^{-1} for shear experiments. Results showed that the woven basalt epoxy composite was strain rate sensitive in both warp, fill, and shear directions. An increase in tensile and shear stiffness, ultimate tensile and shear strengths, and ultimate tensile strain was observed with the increase of strain rate. Post mortem analysis of the fractured specimens using scanning electron microscopy revealed that the failure morphology was independent of the strain rate. Delamination was present at all strain rates, however, a more homogeneous distribution of delamination over the gauge section was observed with the increase of strain rate. Compared to conventional composites in the literature, the tested woven basalt epoxy composite showed excellent energy absorption capabilities at high strain rates. Furthermore, compared to the woven glass epoxy composites, the normalized results with respect to the material density and fiber volume fraction showed that basalt epoxy composite had a higher elastic stiffness, ultimate tensile strength, ultimate tensile strain, and absorbed energy in tension. However, the shear modulus and strength of the glass epoxy composite were higher than the values of the basalt epoxy composite. The results generally suggested a promising potential in replacing glass fibers composites with basalt fiber composites in aircraft secondary structures and, more generally, components prone to impact.

The effect of strain rate and filler content on the compressive behavior of RTM6 epoxy nanocomposites was investigated in chapter 7. The strain rates covered were $0.00a \text{ s}^{-1}$ up to 1113 s^{-1} . Results showed that the epoxy nanocomposites were strain rate sensitive in compression. The elastic modulus and the Poisson's ratio of the epoxy nanocomposites were independent of the strain rate, and showed a nearly constant behavior at different strain rates for all types, weight percentages, and sizes of the fillers used. However, the true peak yield strength showed an increase with increasing strain rate for all types, weight percentages, and sizes of the nanoparticles used. The addition of the silica nanoparticles to the RTM6 epoxy resin generally improved both its elastic modulus and its peak yield strength at different strain rates for all the weight percentages of the particles. Increasing the weight percentage of the silica nanoparticles up to 5% also reflected positively on the true peak yield strength. Moreover, both size and surface functionalization conditions of the silica nanoparticles did not show a significant effect on the compressive behavior of the resin at different strain rates. On the other hand, the addition of the hyperbranched polyester nanoparticles to the resin resulted in

an increase in the true peak yield strength of the resin, and a reduction in the compressive stiffness. The highest improvement in the peak yield strength was achieved at 0.1 % weight of the hyperbranched polyester. Further increase in the weight percentage did not result in further improvement in the true peak yield strength.

8.2. Future perspectives

The research performed within the framework of this PhD was an important step towards understanding of the dynamic mechanical behavior of the basalt/epoxy composites and epoxy based nanocomposites as new aerospace materials. However, as with any research project, many additional aspects still need to be understood, in order to qualify these materials as aerospace materials and to fully exploit their potential. Therefore, this section provides some suggestions and ideas for future research which were not included in the current research, but would build upon the work done.

8.2.1. Basalt fiber reinforced composites

As indicated in chapter 2, the behavior of the basalt fiber reinforced composites was not completely understood in the literature. The current PhD work covered only the effect of strain rate on the mechanical behavior of the basalt composite as a whole. However, understanding the effect of strain rate on the behavior of fiber/matrix interfacial bonding, and on the behavior of the basalt fibers, in particular, is very important to have an accurate understanding of the contribution of both the fiber and the matrix to the strain rate sensitivity. Moreover, the increase in ultimate tensile strain with increasing strain rates should be further investigated. In general, many composites have lower fracture strains with increasing strain rates. The unexpected, yet very interesting, result could be directly explained by the behavior of the basalt fibers themselves at high strain rates, since they are the main load carrying component in the composite. For this purpose, the use of miniaturized split Hopkinson bar setups with soft or hollow bars is essential for accurate measurement of the strength of the fibers. Furthermore, other loading conditions such as interlaminar shear and flexure behaviors are complementary towards the understanding of the structural behavior of these composites.

Understanding the influence of environmental conditions on basalt epoxy composites at high strain rates is also an important step towards certifying these material as aerospace materials. Most of the work reported in the literature regarding the effect of temperature and moisture on the mechanical behavior of basalt composites is focused on the low strain rate regime. In this case, new testing concepts should be developed to allow split Hopkinson bar tests at varying environmental conditions.

Manufacturing aspects should also be further investigated. Wet layup technique was used to manufacture both the glass and basalt epoxy composites used in the current study. However, the void content in the manufactured basalt composites was higher than the void content in the glass composites. This was reflected in the relatively low shear performance of the basalt epoxy composites compared to glass epoxy composites. The SEM investigation revealed

insufficient adhesion between the basalt fibers and the epoxy matrix, which were evident in the failure modes in shear. Of course, it should be mentioned that glass fibers have been used since many decades in the aerospace industry, and their manufacturing and adhesion properties to epoxy are highly optimized. In contrast, basalt fibers are relatively new to the aerospace industry, and a lot of research is still needed to optimize their manufacturing processes and surface treatment for better fiber/matrix adhesion. This way, the shear properties of the basalt epoxy composites can be improved compared to glass epoxy composites, and the full potential of basalt epoxy composites can be exploited in aeronautical applications. Some additional work within the EXTREME project was made to realize this goal, by comparing the performance of prepreg basalt epoxy composites with glass epoxy prepreps manufactured in an autoclave. Results revealed a similar performance of the basalt and glass epoxy prepreg composites in tension and shear. However, considering the manufacturing costs, attention should also be shifted to low cost methods such as resin transfer molding.

To compliment the abovementioned suggestions, modeling the behavior of these materials is crucial for accurate prediction of the behavior of structures made from basalt composites. It should be noted that important efforts were done within the EXTREME by the modeling partners (Dynamore, e-Xstream, and Brunel University) to provide multiscale models for the basalt composites.

8.2.2. Epoxy based nanocomposites

On the one hand, one of the main goals of modifying the RTM6 epoxy resin with silica and hyperbranched polyester nanoparticles was to increase its fracture toughness properties. On the other hand, the addition of these nanoparticles to the resin could influence other mechanical properties such as tension, compression, shear, etc. The current PhD research focused on the second aspect, particularly the effect of strain rate and the addition of the silica and AHBP nanoparticles on the compressive behavior of the RTM6 resin. In order to provide a full understanding of the effect of these nanoparticles on the mechanical behavior of the resin, tensile and shear testing should be performed at low and high strain rates. Within the duration of the EXTREME project, some first efforts were realized towards this purpose. At low strain rates, preliminary tensile testing results revealed that the addition of low content of silica nanoparticles to the RTM6 resin improved the tensile strength of the resin without influencing its elastic modulus. At high strain rates, the split Hopkinson bar technique was adapted for testing small scale dog-bone samples of the brittle RTM6 resin, together with the optimized 3D DIC setup. However, a full test campaign has yet to be carried out.

Furthermore, the fracture toughness performance of the modified resin was studied at low strain rates during the EXTREME project. Results indicated an improvement in the fracture toughness of the epoxy resin by the addition of both types of nanoparticles. The dynamic fracture toughness performance at high strain rates could also provide an important understanding of the effect of the strain rate on the fracture toughness behavior. A preliminary effort was made by adapting the split Hopkinson bar technique for measuring very low force

magnitudes, and by developing a special attachment to accommodate small notched samples on the output bar. However, a full testing campaign still has to be performed.

The compressive results of the silica nanoparticles filled epoxy showed that the improvement of the true peak yield strength was more pronounced in the quasi-static strain rate range rather than the high strain rate range. Additional research is still required to understand this behavior. Finite element modeling of the high strain rate behavior of the silica filled epoxy could provide a first step to understand this phenomenon. Regarding the hyperbranched polyester filled resin, although they have a potential to be good toughening additives to the epoxy resin, further research is still required to produce hyperbranched polymers which can limit the negative influence on the hosting resin, particularly with regard to the glass transition temperature and the stiffness.

Integrating these nanoparticles in the manufacturing of aerospace epoxy resins and certifying such materials as aircraft materials still need additional research, both by academia and industry. The modification of epoxy with nanoparticle additives is still in the experimental research phase with low technology readiness levels. Aspects such as homogeneous distribution of the nanoparticles in aerospace structures, intermediate handling of the nanoparticles, and recycling aspects should all be considered. The adhesives industry for example is already experienced with manufacturing epoxy resins with additives for special adhesives. However, addition efforts should be done to transfer this knowledge to the aerospace grade epoxy resins.

8.2.3. Methods

The digital image correlation technique proved to be a very important tool in testing of polymers and brittle composites in general, and at high strain rates in particular. Although stereo (3D) DIC was used for its ability to measure the in-plane and out-of-plane deformations of any given sample, the results of chapter 4 showed that the 3D DIC achieved lower displacement and strain noise levels compared to 2D DIC. These results go against the generally accepted conviction that the extra correlation steps and stereo calibration procedure required for 3D DIC become additional source of errors compared to 2D DIC. Therefore, additional research is required to evaluate and understand the reasons behind these results. In all cases, careful attention should be paid in maintaining the same lighting conditions and speckle pattern aspects when comparing 2D DIC with 3D DIC systems.

Finally, the use of the semiconductor strain gauges provided very low noise levels when compared to foil type strain gauges. This, in turn, proved very beneficial in testing brittle materials in general, and materials with very low force levels in particular. However, these gauges suffer from sensitivity to light and heat, and show some non-linearities in both the resistance and the gauge factor. Although foil type gauges were used as redundant measurements to correct for the shortcomings of the semiconductor gauges, further research is still required to understand and solve the issues related to the use of semiconductor gauges.

A close-up, low-angle shot of a jet engine fan blade. The blade is dark, metallic, and curved, with a prominent leading edge. It is part of a larger assembly, with other blades visible in the background. The lighting is dramatic, highlighting the texture and shape of the blade. A blue rectangular box is overlaid on the right side of the image, containing white text.

The LEAP jet engine fan blades are made of titanium leading edges and preformed 3D woven carbon fiber composites produced by resin transfer molding.